DEVELOPMENT OF REFLECTANCE IMAGING METHODOLOGIES TO INVESTIGATE SUPER-PARAMAGNETIC IRON OXIDE NANOPARTICLES

by

EMILY JANE GUGGENHEIM

A thesis submitted to
The University of Birmingham
for the degree of
DOCTOR OF PHILOSOPHY

Physical Sciences of Imaging in the Biomedical Sciences
College of Engineering and Physical Sciences
The University of Birmingham
September 2017

UNIVERSITY OF
BIRMINGHAM

University of Birmingham Research Archive

e-theses repository

This unpublished thesis/dissertation is copyright of the author and/or third parties. The intellectual property rights of the author or third parties in respect of this work are as defined by The Copyright Designs and Patents Act 1988 or as modified by any successor legislation.

Any use made of information contained in this thesis/dissertation must be in accordance with that legislation and must be properly acknowledged. Further distribution or reproduction in any format is prohibited without the permission of the copyright holder.

PUBLISHED WORK

Parts of Chapters 1-6 inclusive of this thesis contain material that has been published in a multi-author paper (Guggenheim *et al.* PLoS One. 2016.11(10)) and a multi-author mini-review paper (Guggenheim *et al.* Int. J. Biochem. Cell Biol. 83. pg 65-70.). The sections of that work presented here are my own with negligible contribution from the other authors unless otherwise stated. The details of the chapters containing published material is stated at the beginning of each chapter.

ACKNOWLEDGMENTS

I would first like to thank my primary lead supervisor, Iseult Lynch, for her constant help, support and knowledge throughout the PhD. I would also like to thank my original lead, Josh Rappoport, for his continued help even after moving to another continent! It would have been impossible to do it without you both! I would also like to thank my co-supervisor Iain Styles, for his valuable help and advice throughout the project, particularly for MATLAB, analysis and statistics support. I would also like to thank my final co-supervisor Mike Hannon for his ideas and input into the project.

I also want to thank all the people I have had the pleasure to work with in the various labs I have had the opportunity to work within. Starting with previous members of the once 'Rappoport lab', including Laura Mutch, Eric Pitkeathly, Phil Smith, Sarah Fletcher, Abdullah Khan and particularly Jeremy Pike for his initial help with MATLAB when I was (slightly more) clueless than I am now! I would also like to thank the Tomlinson lab, and the other lab groups on the 8th floor who became my adopted Biosciences group. Particularly Elis, Justyna, Zuhal, Angelos and Varvara for the breaks and fun times that we have had since you all joined the 8th floor! The nanogroup also require a special thanks, for adopting me entirely into the group, not only is it a great group of nice, conscientious scientists, but I have never experienced such enjoyable lab meetings (helped along by the pizza and wine parties!). I owe a particular thanks to Fatima, Laura and Sophie for the coffee breaks that keep me going on a weekly/monthly basis, and Tassos for his ability to find tequila at any time it is needed (and not needed). I also want to thank my colleagues on other floors of biosciences who always managed to brighten up my day when I needed

someone to talk to! Andy, thanks for being a great crossfit buddy, and Clement I will one day be able to have a conversation in French with you! A big thanks to my fellow PSIBS buddies, with a particular thanks to Mike, Chris and Hayley for entertaining me with board game nights and providing enough nerdiness to see me through.

I am very grateful to all the staff members of facilities I have had the pleasure to work alongside. Particularly the team at the Nikon Imaging Center in Chicago. Dina was always on hand to help whenever I popped in to ask her many questions about the N-SIM and the Confocal, and for providing a lunch buddy when I was in America. I also owe a special thanks to Lennel for his expertise in TEM sample preparation, and Farida, for their help and guidance with preparing and imaging TEM samples. I would also like to thank the BALM facility, in particular Alex Dimiao, he keeps the microscopes running and not only was a valuable source of knowledge, but also constantly making me laugh and smile in the lab (and hes a terrific bassist!).

Thanks to my amazing family for constantly supporting and encouraging me to keep going. I am constantly grateful to my mother who is always there whenever I need her and never more than a phone call or short drive away - and for proof reading this thesis! A special thanks to my sister and my beautiful nephew who always cheer me up when I pop in and visit. Lastly I would like to thank my house mates who have put up with me for the previous 3 years, particularly Emma who must have heard all of my presentations so many times over - doubt she wants to hear about a microscope or a SPION ever again!

Abstract

Engineered nanoparticles, such as Super Paramagnetic Iron Oxide Nanoparticles (SPIONs) offer significant benefits for the development of various diagnostic and therapeutic strategies. These include the targeted delivery of drugs, hypothermia treatment and contrast enhancement in magnetic resonance imaging (MRI). However with the increased growth in production and the therapeutic benefit SPIONs offer, there is a paralleled increase in concerns associated with exposure. It is critical to improve the understanding of the interactions that occur following cellular exposure to these particles to ensure the safe and efficacious use of these particles within biomedicine in the future.

The limitations of existing imaging methodologies in the study of NPs, such as the effects of fluorescent labeling and diffraction limited resolution, and the advantages that visualization of spatial localization can offer in studies, increases the demand for new and optimized imaging routines. Within this thesis, existing Reflectance Confocal Microscopy (RCM) methods were optimized and Reflectance Structured Illumination Microscopy (R-SIM) was introduced, offering a two fold increase in resolution - particularly advantageous for NP quantification and localization studies. Analysis routines were developed to enable the automated quantification of NP presence within cells via the different methodologies. Correlative procedures were also established for imaging the same sample with different reflectance methods and TEM, maximizing the information attainable from a single sample and allowing comparisons between the techniques for specific applications.

These aforementioned optimized techniques were then applied to the determination of NP uptake in four different cell lines, and, in combination with siRNA, to ascertain proteins that are involved in the uptake process. Preliminary work aimed at the translation of these studies into 3D culture models, and confirmation of the applicability of reflectance

for imaging these 3D spheroid cultures was achieved. Reflectance imaging methods were applied to SPION and cerium trafficking studies, and analysis methods were extended to include fluorescent segmentation and quantitative colocalization measures, determining the eventual fate of SPIONs and cerium dioxide NPs within cancer cells. Mock dissolution studies were performed in a fluid that simulated the lysosomal compartment within cells. These studies aimed to model the degradative process of SPIONs within this mock fluid as measured by the analytical technique Inductively Coupled Plasma Mass Spectrometry (ICP-OES). This thesis thus provided several important tools for the future assessment of the efficacy and safety of NPs for clinical use, enabling quantitative analysis of uptake route, sub-cellular localization and NP intracellular fate.

SUMMARY

The fields of Nanomaterial (NM) research and nanomedicine have erupted over the last few decades. Nanoparticles (NP)s are currently incorporated into a larger number of everyday items. Initially it was assumed that NP properties would resemble those of the bulk material which, in some cases, have been previously defined and intensively characterized. However it is becoming increasingly apparent that NP do not behave in the same way as materials of the same composition with different dimensions. Additionally, modifications are often made to the core material to manipulate the particles to fulfill the different needs within the application area, altering their physical properties and effects. Magnetic particles have received much attention in part due to their inducible magnetization, which can enhance MRI images to aid the diagnosis of disease, allow magnetic targeting to a particular region and allow magnetic field modulated drug release, or field modulated heating to selectively kill cancer cells. This permits an increase in therapeutic effect and drug action at the site of interest, and decreases the off-target toxicity. Despite all the apparent advantages displayed by such NPs, clinical phase trials often do not result in the expected outcomes.

NPs interact with a variety of different constituents within the body, and these interactions are often ill-defined. This not only leads to a lack of efficacy, but also raises concern over the safety of these particles. This has led to an increased drive for thorough characterizations of NPs and their effects within biological systems. Including the physical characteristics that change upon and during exposure to various bodily fluids to the interactions that occur within different cell populations. One problem is the lack of

effective and standardized means of quantifying the uptake, localization and fate of NPs both *in vitro* and *in vivo*. Transmission electron microscopy provides the gold standard method for evaluating and quantifying the presence and localization of particles within cells and determining sub-cellular characteristics such as size. However TEM has several limitations for these studies. It is a destructive technique that is performed under vacuum, and it cannot provide temporal information unless samples are prepared and imaged separately at different time points. Therefore investigations into new methodologies to allow characterization of these particles and their effects is an area of high priority and investment.

A subset of NPs provide high levels of contrast using reflected light microscopy methods, and these provide opportunity to visualize the particles, both live and fixed, in conjunction with fluorescent labeling This provides a cost and time effective method to facilitate NP investigations. However reflectance methods are not well defined or optimized at present, and there is a lack of superresolution reflectance methods. Additionally NP are not the only cellular constituents that reflect light, therefore the resultant image is comprised of high level background signal arising from cellular constituents and high intensity reflectance signal associated with NP. Images therefore require a preprocessing step to facilitate the extraction of meaningful information from within. Manual based image analysis of any type is often user dependant, time consuming and easily biased. There is therefore a focus on the automation of such processing and analyses to increase result consistency and quality, in addition to decreasing processing times.

This thesis introduces new methods for the visualization and quantification of intracellular NPs as a means to support translation from lab to clinic in a responsible manner to understand the fate of particular metallic oxide NPs and their impact on a range of cell types. This includes the optimization of reflectance confocal microscopy for the acquisition of high quality reflectance images, and the development of superresolution reflectance mi-

croscopy to facilitate high resolution nanoscale investigations. Computational work-flows for the preprocessing of reflectance (and fluorescence) images are described within, facilitating the automated removal of background effects and segmentation of reflectant signal of interest. These imaging and preprocessing methodologies have been applied to the characterization of cellular effects following metallic NP exposure, including the uptake amount and route in four different cancer cell types, the cell-specific trafficking of the NPs and their eventual fate. This is important to facilitate the safe, efficacious and selective application of these NP to the diagnosis and treatment of disease. Computational work-flows have been devised to quantify these different experiments automatically, leading to an unbiased quantification of signal. Automated analysis methods give increased confidence in the observed effects, improving reproducibility and greatly improving throughput. This is crucial for making accurate conclusions in a time efficient manner that can facilitate future developments in the clinical applications of these NP.

CONTENTS

LIST OF FIGURES

LIST OF TABLES

ABBREVIATIONS

AFM - Atomic Force Microscopy; ALF - Artificial Lysosomal Fluid; Amp - Ampicillin; AP2 - α-Adaptin-2; Cav1 - Caveolin-1; CB - Cacodylate Buffer; CLEM - Correlative Light Electron Microscopy; CLSM - Confocal Laser Scanning Microscopy; CME - Clathrin-Mediated Endocytosis; CPD - Coherent Point Drift; CREM - Correlative Reflectance Electron Microscopy; CT - Computerized Tomography; CTO - CellTracker Orange; CTR - CellTracker Deep Red; CTV - CellTrace Violet; CTxB - Cholera Toxin Subunit B; CytD - Cytochalasin D; DAPI - 4',6-Diamidino-2-Phenylindole, Dihydrochloride; DF - Darkfield; DNA - Deoxyribonucleic Acid; EMR - Electromagnetic Radiation; EPRE - Enhanced Permeability Retention Effect; FBS - Fetal Bovine Serum; FFT - Fast Fourier Transform; FID - Free Induction Decay; Field Free Point - FFP; FITC - Fluorescein isothiocyanate; FT - Fourier Transform; FWHM - Full Width at Half Maximum; FWM - Four Wave Mixing; GA - Gluteraldehyde; GST - Glutathione-S-Transferase; ICP - Inductively Coupled Plasma; ICP - Iterative Closest Point; IRM - Interference Reflection Microscopy; ISO - International Organization for Standardization; IV - Intravenous; Kan - Kanamycin; LA - Laser Ablation; LDI - Laser Desorption Ionization; LM - Light Microscopy; MDM - Monocyte Derived Macrophages; MDR - Multidrug Resistance; MPI - Magnetic Particle Imaging; MPS - Mononuclear Phagocyte System; MRI - Magnetic Resonance Imaging; MS - Mass Spectrometry; MSI - Mass Spectrometry Imaging; NA - Numerical Aperture; NIR - Near Infrared; NMR - Nuclear Magnetic Resonance; NP - Nanoparticle; NSC - Non-Silencing Control; OECD - Organization for Economic Co-operation and Development; OES - Optical Emission Spectroscopy; OsO4 - Osmium Tetroxide; P - Penicillin; PAGE - Polyacrylamide Gel Electrophoresis; Pak1 - Protein Activated Kinase 1; PALM

- Photo-Activated Localization Microscopy; PBS - Phosphate Buggered Saline; PET - Positron Emission Tomography; PFA - Paraformaldehyde; PMA - Phorbol 12-Myristate 13-Acetate; PPB - Parts Per Billion; PPT - Parts Per Trillion; RCM - Reflectance Confocal Microscopy; RF - Radiofrequency; RFP - Red Fluorescent Protein; RI - Refractive Index; RNA - Ribonucleic Acid; RT - Room Temperature; S - Streptomycin; SCM - Serum Containing Media (Complete); SDS - Sodium Dodecyl Sulfate; SERS - Surface Enhanced Raman Spectroscopy; SFM - Serum Free Media; SIMS - Secondary Ion Mass Spectrometry; Sienna^{+} - a clinically used SPION; siRNA - Small Interfering RNA; SOC - Super Optimal Catabolic repression; SPECT - Single-photon emission computed tomography; spICP-MS - Single Particle Inductively Coupled Mass Spectrometry; SPIONs - Super Paramagnetic Iron Oxide Nanoparticle; SPR - Surface Plasmon Resonance; STORM - Stochastic Optical Reconstruction Microscopy; TBST - Tris-Buffered Saline with Tween; TEM - Transmission Electron Microscopy; TF - Transferrin; TIRF - Total Internal Reflection Fluorescence; TIRM - Total Internal Reflectance Microscopy; Tub - Tubulin; UA - Uranyl Acetate; USPION - Ultrasmall Superparamagnetic Iron Oxide Nanoparticle; UWT - Undecimated Wavelet Transform; VD3 - 1,25-dihydroxyvitamin D3; VEGF - Vascular Endothelial Growth Factor; VS - Vectashield; Wave2 - Wiskott-Aldrich syndrome protein family member 2; XRF - X-Ray Fluorescence.

CHAPTER 1

INTRODUCTION

Parts of this chapter are published as part of a multi-author mini-review paper (Guggenheim *et al.* Int. J. Biochem. Cell Biol. 83. pg 65-70.).

1.1 Nanomaterials and nanotechnology

A Nanomaterial (NM) is commonly defined as a material with at least one dimension on the nanoscale (1-100 nm). A nanoparticle (NP) is defined as a material with all three external dimensions on the nanoscale [1]. However the definition is not formally agreed between international bodies such as International Organization for Standardization (ISO) and Organization for Economic Co-operation and Development (OECD). The term 'NP' encompasses a broad range of particles and applications including natural, incidental, engineered and manufactured NPs. Naturally occurring NPs arise through an array of environmental processes including volcanic eruptions, dust storms and weathering. In some cases these NPs are central to natural processes such as in the nano-sensing of the earths magnetic field by certain bacteria [2]. NPs are also released as incidental by-products of industrial processes such as coal, oil and gas boilers, and through diesel exhaust [3, 4, 5]. The effect these NPs have on the complex systems they interact with following release depends largely upon the NP's physicochemical properties. These same properties also provide a great potential for manipulation in a variety of commercial and medical fields.

There is a growing realization of the opportunities offered by nanotechnology within areas such as electronics, environmental remediation, diagnostics and therapeutics. Therefore recent years have seen an increase in the quantity and diversity of NMs and NPs that we are concurrently exposed to [6, 7]. NPs are now regularly incorporated into a range commercial goods, including sun screen, chewing gum, tennis rackets, and iron free shirts [8, 9, 10]. The increasing use of NPs has subsequently driven the need for an in-depth understanding of the associated biological behaviors, effects and fate following release and exposure.

1.1.1 Potential risks and regulations associated with NP production

NPs have the potential to cause short term effects from direct exposure, but they also carry risk of long term toxicity. The consequences of bodily, environmental and ecological exposure is largely unknown and therefore a cause for concern. Although NPs and their potential for toxicity is a fairly new concept, the basic principles stem from well-established particle toxicity studies. These studies originated from the occurrence of toxicity following human exposure to two hazardous materials, alpha-quartz and asbestos, and the study of particle toxicity associated with air pollution [11]. These particular cases highlighted that although sometimes the mechanisms of toxicity are not fully elucidated, measures must still be taken to ensure that substances with potential to cause harm are regulated. This is particularly true for those NPs that are considered as potential diagnostic or treatment tools for use in humans. These NPs must be held to the highest safety standards and thoroughly characterized with the potential deleterious interactions understood. This includes their potential for bio-accumulation and slow release.

It is assumed that as particle diameter decreases and surface area increases, the associated potential toxicity can increase [12, 13]. However, currently there is a lack of definitive epidemiological evidence for the causal relationship between exposure to NPs below 100

nm and different pathologies. There is, however, an increasing number of studies that are beginning to link particular effects to NP exposure *in vivo* and *in vitro* [11]. Several studies have determined links between, for example, NPs in diesel exhaust and increased risks of coronary disease, however the mechanisms were unclear [14, 15]. There is also significant concern regarding the environmental impact of engineered NPs. The short and long term toxicity of NPs to complex organisms is largely unknown. Studies have found correlations between NP (silver) uptake / degradation and deleterious cellular effects in aquatic organisms such as *Daphnia Magna* [16]. Therefore it is imperative to determine the potential risk posed by different NMs. One of the major problems with ascertaining these risks associated with non-biomedical NP exposure is the inadequate information available regarding the exposure quantity. The amount of NPs included in different products and released during specific processes at various stages of production and use into the environment is not necessarily readily available. This is partly because there is currently no requirement to disclose particular quantities of NPs within products. There has also been a distinct lack of regulatory requirements introduced for NP containing products. The safety regulations applied to the NP form of a material can be identical to those given for the bulk material, and the NP form is not classified as a 'new' material. Large particles can simply be replaced by NPs with no additional studies or disclosure. Although EU REACH regulations do not have explicit requirements for NMs, they are currently developing additional requirements for both NPs and NMs. This involves discussing the best practices for assessing and managing the safety of NMs, and funding research projects to assess the impacts of NP [17, 18]. The issues with regulatory aspects of nanotechnology have been reviewed [19].

1.1.2 Nanoparticles for use in biomedicine

The use of man-made NPs for diagnostics and therapy is a key application area of nanotechnology. In order to be of use within biomedical applications NP must fulfill particular criteria, for example they must outperform the conventional method, have minimal tox-

icity, reach the target site of interest and avoid non-specific unwanted effects. NPs offer unique properties to aid fulfillment of these criteria; their small size allows them to be targeted to and accumulated at particular areas of interest. Their large surface area to mass ratio also provides a platform for the conjugation of small molecules to the NP's surface. These small molecules can include therapeutic drugs, targeting molecules or imaging probes.

Chemotherapeutic drug delivery

The non-specific action of drugs in non-target tissue is a major limiting factor during chemotherapy treatment. NPs have received considerable attention for use as directed nanovectors, either loaded with, or conjugated to therapeutic agents. NPs aim of fulfilling the two most important criteria for successful treatment: temporal delivery and spatial placement [20]. Currently around 80% of NPs in clinical phases focus on anti-cancer strategies [21]. Several drugs have been combined with NPs for cancer therapy, including paclitaxol, doxorubicin and methotrexate [22, 23, 24]. NPs that are between 10-100 nm can be passively targeted to, and accumulated at, solid tumor micro-environments by exploiting the surrounding 'leaky' vasculature in a phenomena known as the Enhanced Permeability Retention Effect (EPRE), depicted in Figure 1.1 [25, 26, 27]. This effect can be manipulated and augmented by the induction of hypertension which causes an increase in blood flow to the tumor due to the lack of smooth muscle in the defective vasculature, thereby enhancing the drug accumulation at the target site [28]. Furthermore, under the hypertensive state the accumulation of NPs at other sites is decreased. This in turn decreases the associated off-target toxicity increasing the potential for this technique for chemotherapeutic delivery [28].

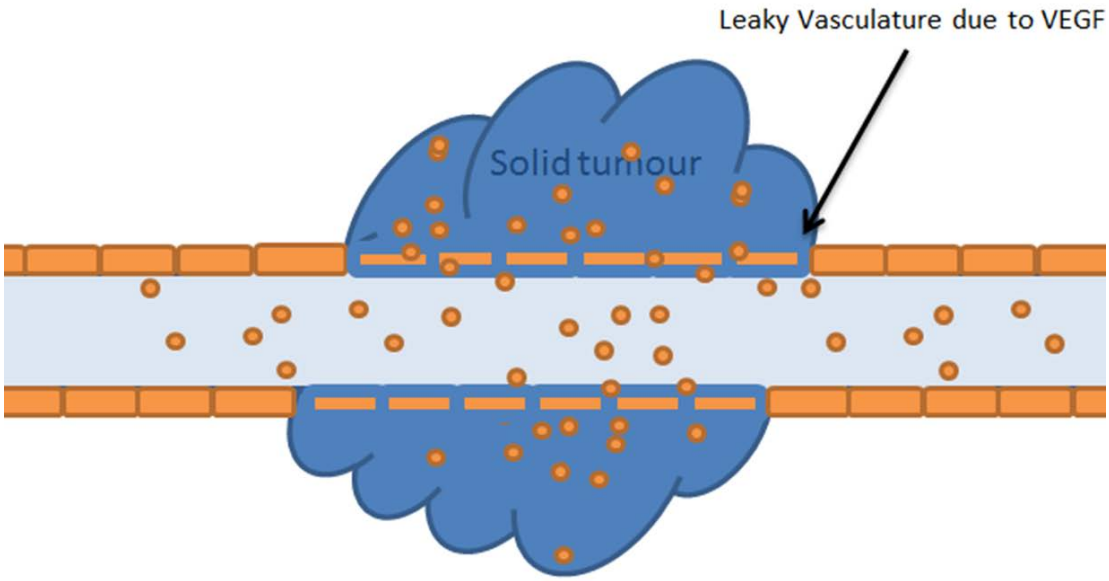

Figure 1.1: Enhanced permeability retention effect. Angiogenesis in tumors, stimulated by the release of Vascular Endothelial Growth Factor (VEGF), leads to the formation of vasculature surrounding the tumor, however they are normally irregular in shape, leaky or defective, lack organized structure. Often the basement membrane or smooth muscle layers are absent. This leads to the extravasion and accumulation of NPs (between 10-100 nm in size). Due to poor lymphatic drainage these are often retained for longer periods of time than molecular drugs which are subject to diffusion across concentration gradients

Active targeting

Not only must nano-therapeutics reach the desired tissue location but then they must also be successfully internalized within the cells of interest, and localize to the required sub-cellular destination. There are therefore two stages of targeting required for successful therapy - biodistribution to the region of interest (such as a tumor site by EPRE), and accumulation within the desired cell populations (such as the particular cancer cells using active targeting). The latter will be revisited in more detail in Section 1.2.1 and Chapter 5. Despite the potential they appear to hold, NPs often exhibit an unexpectedly low targeting specificity. This can lead to a high false positive rate in diagnostics, lack of drug efficacy in therapeutics and product withdrawal [29, 30].

The specificity of NPs can be amplified through surface modification, such as the attachment of targeting moieties directed towards tumor specific markers. This offers the

potential for unique personalized therapies that direct the nanocarriers to particular cell types, in addition to aiding evasion of clearance via the Mononuclear Phagocyte System (MPS) [31, 23, 24]. A host of different targeting methodologies have been employed. These include attachment of receptor ligands, attachment of antibodies and magnetic targeting [32, 33, 31, 34]. Magnetic NPs conjugated with HER2/nu targeting ligands displayed accumulation within cancer cells over-expressing the Her/nu receptor were visualized by MRI. These NPs, in combination with paclitaxol, led to the *in vivo* tumor cell killing in mice [35, 36]. Specific cancer cells have also been targeted by folate conjugation. This facilitated the successful tumor accumulation both *in vitro* and *in vivo* [24, 37]. Comprehensive reviews published in the literature regarding the specific cellular targeting and subsequent internalization of NPs based on surface ligands are available [38, 39]. One important factor to consider in NP targeting is the formation of a protein corona around NPs within biological media [40]. The protein corona will be discussed in more detail in Section 1.2.1 and Results Chapter 3. NPs acts as scaffolds for attachment of biological proteins that bind and alter the NPs surface considerably. This leads to modification of the biologically 'perceived identity', introducing a new layer of complexity with regards to the accumulative potentially and toxicity of these NPs. It is therefore crucial to consider this 'corona' effect in terms of subsequent protein interactions, targeting and clearance when designing particular engineered particles with a desired function [40].

Accumulation at target site

Not only can NP delivery systems provide opportunity for delivery to the desired site but they also may help to retain them at the target by bypassing Multi-Drug Resistance (MDR). MDR is a major factor in the failure of conventional therapeutics [41]. Tumors are normally heterogeneous with some populations sensitive to certain chemotherapeutics and some populations that are resistant. Chemotherapy removes those that are sensitive, leaving behind those that are resistant which then expand. This leads to the formation of a tumor that is completely insensitive to the previous treatment. MDR is characterized by

an increase in specific efflux pumps in the cell membrane. Most notably increases in the MDR1 gene product, p-glycoprotein, and MDR-associated protein (MRP) [41, 42]. NPs loaded with drug molecules can accumulate within the cell through receptor mediated endocytosis and travel through the endo-lysosomal system. It is theorised that this may allow the complex to evade removal by p-glycoprotein and related efflux pumps, resulting in increased accumulation in previously resistant tumor cells [43].

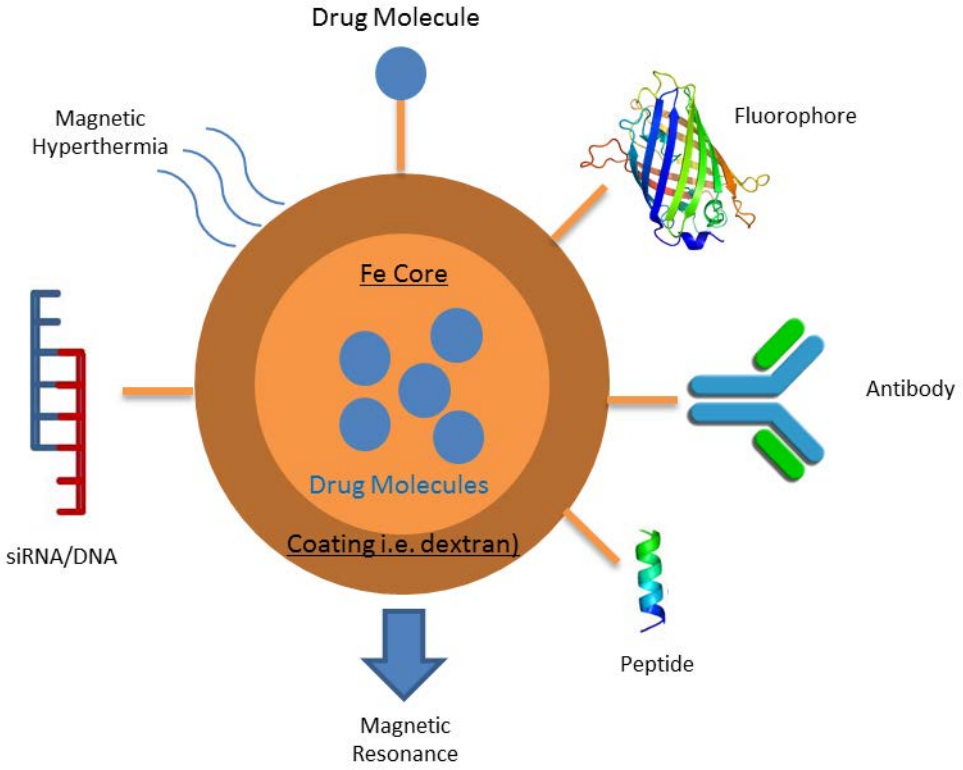

Figure 1.2: Example of a multi-functional SPION that could be applied for diagnostic and therapeutic applications. Various bioactive molecules can be attached at the surface of the NP, such as targeting moieties, imaging probes and therapeutic agents.

Advantages are clearly offered by the incorporation of drugs, targeting ligands and imaging molecules in so called 'multi-functional NP' (depicted in figure 1.2). However, issues exist with the paralleled increase in NP size, due to the number of conjugated functional groups. This can lead to altered clearance of NPs, increased bioaccumulation potential, decreased aqueous solubility and limited increase in specific localization at the target site. NPs with drugs grafted to the surface can also experience the burst release effect. The

burst effect occurs when the diffusion of the drug from the NP occurs at a faster rate than the degradation of the matrix leading to significant premature drug release [44]. The burst rate was found to be reduced by 21% by using cross-linkable tamoxifen NPs compared to non-cross-linked [45]. It has been suggested that the protein corona, (see Section 1.2.1), can decrease the burst effect and alter the drug release profile of nano-carriers [46].

In addition to the interest in NPs for cancer therapy, there is also a significant interest in the utilization of special characteristics exhibited by certain NPs in other areas of biomedicine such as diagnostic imaging. Examples include the use of gold NPs for use as contrast enhancement agents with Computerized Tomography (CT) scanning, magnetic NPs for Magnetic Resonance Imaging (MRI) and the use of quantum dots for cancer cell labeling [47, 48, 49]. The following section will introduce magnetic NPs and their use as MRI contrast agents and therapeutic tools.

1.1.3 Super-paramagnetic iron oxide nanoparticles

Super-paramagnetic iron oxide NPs (SPIONs) typically consist of an iron oxide core with a central moiety of Fe^{2+} or Fe^{3+} and a polymer coating [50]. The polymer coating can prevent agglomeration of particles, decrease the potential for toxicity or confer a specific function. For example, the use of Polyethylene Glycol (PEG) coatings can lead to the evasion of opsonization and macrophage recognition, whereas coating with bio-compatible dextran can lead to increased uptake by endocytosis [51]. The effect of coatings on the biological identity of NP is discussed in more details later on in Section 1.2.1. Following Intravenous (IV) injection SPIONs are rapidly taken up by circulating macrophages leading to accumulation in organs rich in reticulo-endothelial cells. Thus, current and previous biomedical applications of SPIONs involve the 'imaging' of macrophage phagocytic activity (or loss thereof). The liver and spleen are the organs that generally dominate removal of SPIONs from the blood stream, but in high doses SPIONs can accumulate in other macrophage rich tissues (Table 1.1) [52]. The biodistribution of SPIONs can be

manipulated by the size of the SPION itself, some examples are shown in Table 1.1 [53].

SPION size	Distribution
<2nm	Passive diffusion through cell membranes; therefore unsuitable for biomedical use. [55,59]
<20nm (Feruglose NC100150)	Renal clearance. Bone marrow imaging. Perfusion Imaging. MR angiography. [55,60]
10-50 (Combidex / Sinerem)	Accumulate predominantly in the lymph nodes, and therefore used for lymph node imaging. Can also be found in other organs including liver, spleen, bone marrow, heart and kidney.[55, 56, 57]
50-200nm (Ferumoxides – Resovist / Endorem)	Found exclusively in the liver and spleen – cleared in 2-4 hours. Liver metastases and lesion imaging. [55,58]
>300nm (Ferumoxsil)	Used for bowel contrast [54, 55]

Table 1.1: Biodistribution of various sizes of clinical SPIONs used with MRI. This table summarizes the biodistribution of some clinically used SPIONs based on their size, generated based on the associated references shown in the table. Smaller SPIONs accumulate in bone marrow and pass renally, slightly larger SPIONs accumulate in the lymphatic system, and as size increases they are preferentially accumulated moreso in the liver. Those larger than 300 nm accumulate in the bowel following ingestion [54, 55, 56, 57, 58, 59, 60].

Magnetic NPs, such as SPIONs, have attracted large amounts of attention within biomedicine as they fulfill some of the criteria necessary for use. Firstly they are assumed to be fairly biocompatible due to their iron core and dextran coating, which is discussed later in Chapter 3 and Chapter 5). Secondly, due to their magnetic properties, they can be spatially placed using external magnetic fields and visualized non-invasively by MRI *in vivo* [61, 62, 63, 64, 34, 65]. This magnetic property is termed super-paramagnetism [66]. Ferromagnetic iron oxides such as maghemite and magnetite lose their permanent magnetization when they are smaller than 30nm in diameter. Therefore, SPIONs do not exhibit spontaneous magnetic moments in the absence of an applied field, but exhibit high magnetic susceptibility [20]. This is due to the small size of the NPs. Unlike their larger counterparts, they contain only a single magnetic domain that orients randomly [59]. Upon application of an external magnetic field, magnetization can be induced [67]. Following removal of the magnetic field the particles no longer show magnetization, which

is important for the prevention of SPION agglomeration and subsequent embolization of vessels. This makes SPIONs particularly attractive candidates for use in diagnostic imaging such as MRI for contrast enhancement, hypothermia tumor therapy and directed drug delivery systems [68]. SPIONs have also been employed in a variety of other areas that cannot all be introduced within this thesis, therefore the most relevant biomedical applications (diagnosis with MRI, magnetic hyperthermia and magnetically guided drug delivery) will be discussed. Other applications, for example, within the fields of electronics and environmental remediation fall outside the remit of the thesis and are reviewed elsewhere [69, 70, 71].

1.1.4 MRI imaging

Basics of MRI imaging

The first biomedical application of SPIONs was to enhance tissue contrast in Magnetic Resonance Imaging (MRI). MRI is a non-invasive, non-destructive technique widely employed in medical imaging to investigate internal structures within the body, particularly soft tissues, in health and disease. Within the field of cancer diagnostics, MRI aims to provide early cancer detection with the eventual aim of improved prognosis [72].

Figure 1.3 shows a schematic explaining signal generation using MRI. When placed in a strong magnetic field, B_0, unpaired protons (^1H) align to the magnetic field; giving a net magnetization in the direction of the applied field (Figure 1.3B). Upon application of an oscillating radio-frequency at the Larmor frequency, orthogonal to the magnetic field, tilts the net magnetization, which was along B_0 (Z axis) into the transverse (XY) plane where the signal is detected (Figure 1.3C) [73]. Upon removal of the radio-frequency signal the protons begin to relax back to equilibrium with B_0, and in doing so release their own radio-frequency signal, referred to as the Free Induction Decay (FID) response signal (Figure 1.3D). It is this signal that induces a corresponding oscillating voltage in the

receiver coil surrounding the sample, this detected signal gives information regarding the proton environment. The net magnetization recovers mainly through two processes. T_1 spin-lattice relaxation is the rate at which the longitudinal magnetization of the magnetization vector recovers towards its thermodynamic equilibrium. T_2 or spin-spin relaxation is the irreversible exponential decay of the transverse or X-Y component of the magnetization vector. The relaxation process consists of another component that arises due to loss of phase between protons caused by field inhomogeneities (called the inhomogeneous contribution to relaxation). The homogeneous contribution to T_2 relaxation can be measured using a spin echo (SE) sequence, which re-phases the protons, removing the contribution from inhomogeneities [74]. Conversely gradient echo (GRE) sequences do not eliminate the dephasing therefore relaxation is a combination of both true relaxation (T_2) and relaxation due to field inhomogeneities, this is called (T_2*) [75]. The localization of signal in 3D space can be obtained by varying three gradients (slice, phase and frequency) in the three spatial directions (X Y and Z); each voxel can therefore be matched to a signal that is characterized by its frequency and phase (X and Y)[76]. Acquisition gives rise to a matrix (slice) of spatial frequencies termed 'K-space' in the Fourier domain, where each signal $S_{(x,y)}$ represents one voxel within the imaged slice; the 2D inverse Fourier transform (FT) converts the K-space matrix from the frequency domain into the spatial domain [76].

Contrast agents for MRI: SPIONs

Hydrogen protons are abundant in water and lipids of tissue. Since the relaxation time is directly linked to the environment of the protons, different proton environments in different tissues will lead to varied relaxation times, providing image contrast, allowing differentiation between tissues. However the intrinsic MRI sensitivity is low in comparison to other optical imaging techniques, due to the relatively small difference in the low and high energy states of protons. Often selective contrast agents are employed in order to manipulate the relaxation processes, amplifying the MR signal and thus providing increased contrast [77, 35]. These contrast agents typically fall into two categories: paramagnetic

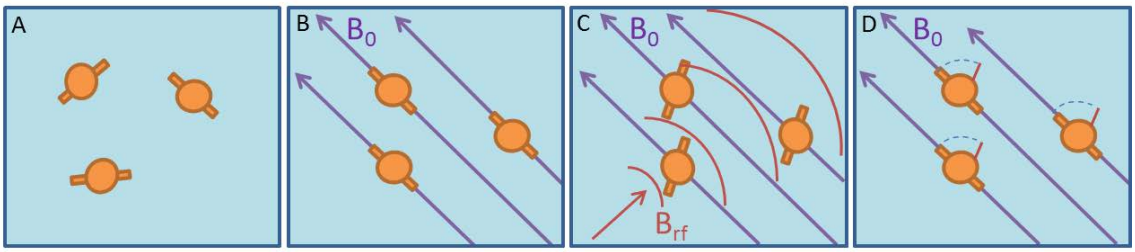

Figure 1.3: Schematic of how proton (^{1}H) MRI uses magnetic fields and radio-waves to produce spatial images of tissue. MRI utilizes the directional magnetic field associated with charged particles in motion. Hydrogen atoms have an odd number of protons (1) and therefore have a characteristic 'precession'. (A) In the absence of a magnetic field, nuclei are randomly aligned. When placed in a strong magnetic field (B_0) (such as within a superconducting electromagnet) protons become aligned with the magnetic field inducing net magnetization in the direction of the field; the nuclei then 'precess' about the field at the Larmor frequency (B). A radio-frequency pulse (B_{rf}) is applied perpendicular to the magnetic field, with a frequency equal to the Larmor frequency, this disturbs the aligned nuclei causing the net magnetization (M_{xz}) to tilt away from B_0(C). Upon removal of B_{rf} the nuclei return to equilibrium and realign in parallel with B_0, in a process called 'relaxation' (D). A radio-frequency signal is produced as the protons return to their aligned positions during the relaxation process.

species, which includes gadolinium chelates, and super-paramagnetic agents, such as SPIONs. Gadolinium agents have commonly been used for cell and molecular imaging with MRI, and they act to decrease the T_1 relaxation time of surrounding protons therefore leading to hyper-intensive regions [78]. However, in addition to having a comparatively low magnetic moment, gadolinium is not bio-compatible and the free ion is extremely toxic. Chelation with various ligands can greatly reduce this toxicity, but the potential release of gadolinium from its chelate within the body gives cause for concern; the potential for toxicity from gadolinium based contrast agents is reviewed [79, 80]. Conversely, SPION-based contrast agents mainly effect the T_2 and T_2* relaxation of surrounding protons particularly in Gradient Echo (GRE) techniques, introducing a hypo-intensive region at their location [77]. The alteration in T_2 relaxation, and consequently signal intensity between different SPIONs depends on a variety of factors, including size, composition and crystallinity; however SPIONs have significantly increased relaxivity when compared to gadolinium [81, 82]. Generally larger SPION cores have increased relaxivity, however the core is constrained to below 20 nm to retain the super-paramagnetism [82]. Ultra-small (U)SPIONs, such as resovist, have an increased effect on T_1 weighted images, due to their

smaller size [81].

The first clinical application of SPION enhanced MRI was for hepatic lesion imaging [83]. This was due to the excellent uptake of SPIONs by macrophages, particularly in the liver. Specialized liver macrophages, called Kupffer cells, rapidly take up SPIONs; however Kupffer cells will not be present at sites of liver damage. SPIONs will therefore cause hypo-intensive regions at the location of normal healthy liver, whereas at a diseased or liver tumor site the intensity will remain the same, providing excellent T_2/T_2^* contrast, resulting in increased lesion visibility and detectability [77, 84]. Reimer *et al* found SPION enhanced MRI to be more accurate than other non-enhanced MRI and spiral CT for the detection of lesions [84]. Two particle formulations were introduced specifically for liver imaging, ferumoxide (Feridex - USA, Endorem -Europe; 120 - 180 nm Hydrodynamic Size (HDS - the important of which is discussed in Chapter 3) and Ferucarbotran (Resovist - HDS 60 nm), shown in Table 1.1 [81]. However, Resovist was withdrawn from the market in 2009 and ferumoxide in 2008, due to commercial reasons and possible safety concerns [81].

SPIONs smaller than 50 nm (USPION) are cleared though the lymphatic system and transported to lymph nodes. Lymph node status is an important part of clinical staging for a variety of cancer types, and evaluation of lymph node metastasis can provide the basis for therapy decision and prognosis. In healthy nodes, macrophages will internalize SPIONs, introducing contrast. In neoplastic nodes, where tumor cells have replaced healthy cells, macrophage activity will be lost leading to a loss in hypo-intensity [85, 86]. USPIONs are therefore ideally suited to lymphography [85, 86]. MRI was previously relatively insensitive for the detection of lymph node metastases, however one study found that USPION-enhanced MRI increased the sensitivity of metastasis detection, on a person to person basis, from 45.4% up to 100% [85]. Choi *et al* found that USPION-enhanced MRI led to increased diagnostic accuracy in lymph node metastasis when compared to

PET/CT (in rabbit models) [87]. One USPION, ferumoxtran, (Combidex / Sinerem; HDS 20 - 40 nm) was in development for lymph node imaging, however production was ceased due to the lack of additional clinical trials, and controversy regarding the risk/benefit of these SPIONs [30]. Other types of SPIONs include those larger than 300 nm (such as GastroMark), for bowel MRI contrast, and below 20 nm for bone marrow and perfusion imaging [88].

Other diseases that are characterized by an increase, or decrease, in macrophage activity have the potential to be imaged with SPION-enhanced MRI. In this way, the technique has been used for the detection of macrophage activity in kidney nephrotoxicity, encephalomyelitis, arthritis, macrophage recruitment to atherosclerotic plaques and graft rejection monitoring [77, 89, 81]. There are numerous methods of NP modification for contrast in a variety of MRI applications; these are reviewed [90, 91]. Several SPIONs were approved for use with MRI imaging, however subsequent concerns over the safety and efficacy led to Sinerem, Feridex and Resovist being withdrawn from the market [92, 93].

1.1.5 SPIONs for magnetic hyperthermia

Magnetic hyperthermia is a promising new cancer therapy in clinical phase trials that relies on local heat induction at the site of a tumor. Magnetic NPs can be introduced at the site of tumor, either targeted systemically or inserted as an implant. External electromagnetic energy is then converted by the particles to heat (41-46 ℃) at the tumor site, delivering toxic amounts of thermal energy to cancer cells. This causes successful selective cancer cell death and tumor shrinkage in *in vivo* models of cancer [94, 95, 96, 97, 98]. Zhao *et al* demonstrated that head and neck cancer cells in rodent models were killed within 30 minutes of hyperthermia treatment, while delivering no damage to healthy cells [99] Hyperthermia treatment has been particularly successful when used adjuvant to radiotherapy. In radiotherapy the limiting factor is the effects of damage to healthy tissue [100]. Hyperthermia sensitizes the cells to death by radiotherapy in a variety of

mechanisms that are not fully understood. The effect has been partially attributed to the fact that heat alters protein structures and decreases the cells DNA damage repair response [100].

SPIONs for other uses

SPIONs have also been used in conjunction with a hand held magnetometer, which is a detection device for use in sentinel lymph node biopsy [101, 102]. SPIONs offer a promising alternative to the current gold standard, radioisotope guided localization, which carries obvious drawbacks due to the reliance on radioactive material [101, 102]. Other uses for SPIONs include magnetofection, a method of deliberately introducing genetic material into cells, gene delivery, stem cell labeling and tissue engineering to allow monitoring of cell delivery in vivo [103, 104].

1.1.6 Magnetic targeting

As previously mentioned, targeting is an important aspect of successful NP based therapies, and NP based diagnostics. One physical targeting method, first proposed by Freeman *et al*, utilizes the magnetic properties of NPs such as SPIONs [34]. SPIONs can be guided to a pathological site by an applied external magnetic field, ensuring significant accumulation of a conjugated drug without the need for targeting ligands; the applied field can then be altered to modulate drug release, or drug release can be initiated enzymatically by changes in physiological conditions such as pH [105, 106, 34, 20, 59]. Kumar et al successfully showed that use of an external magnetic field was capable of delivering a target drug to its specific site of action [65]. The removal of the field leaves no remaining magnetization, reducing the chance of particle agglomeration, decreasing risks of thrombosis and increasing biological half-life [59]. Issues remain with using magnetic fields to target deep into the body; currently only areas at the surface can be targeted due to the need for sufficient magnetic field strength at the desired site [59]. Concerns exist over the

directed delivery of a large concentration of NPs to a localized area. This can lead to iron overload and high levels of Fe ions which can lead to cellular toxicity including Reactive Oxygen Species (ROS) induction, and DNA damage [107]. This could be particularly problematic in areas such as the heart, where RES cells are less abundant, leading to slower clearance of NPs and therefore increased potential for accumulation, iron overload and toxicity [108]. If these NPs are to be safely used in biomedicine every effort needs to be made to establish the potential effects associated with their use, and the metabolism and clearance of the NPs in the target, and non-target, tissues.

1.2 SPIONs in biological systems

Numerous potential benefits and problems have been highlighted with the use of NPs, such as SPIONs, in different areas of biomedicine. Lack of efficacy and specificity led to the withdrawal of some SPIONs following clinical trails, and other issues exist regarding the possible clearance, toxicity and side effects. This is particularly true if the target tissue is not well equipped for the removal of these NPs. Underlying all of these issues is the inadequate understanding of NP-cell interactions and the post-internalization fate of the NPs. These crucial factors limit the successful use of NPs in biomedicine. This section will aim at introducing the interactions that occur between NPs and specific bodily fluids, and the subsequent cellular uptake that may occur. NP are often very efficiently internalized within a variety of cell types through a combination of uptake routes. However it is the specific discrimination between cell types and cell pathways that is required to provide successful diagnosis and treatment and mitigate unwanted side effects. There are a combination of factors that determine if NPs gain entry into cells and by what mechanisms. The outcome is largely dependant upon the intrinsic NP properties themselves, the properties of the media they are exposed to and the internalization properties of the cell populations being targeted or exposed. This offers the great advantage of tailoring design to suit the need, but also provides a vast landscape of potential interactions and effects

that are largely unknown and unpredictable without thorough investigation. Therefore it is crucially important that the physical properties of NP's are extensively studied and characterized, in order to understand the subsequent biological effects and make accurate conclusions within nanoscale investigations. Some of the most important factors that modulate cellular uptake will be discussed and the different cellular mechanisms that can be exploited for selective entry will by introduced; these will be discussed in more detail in the relevant results chapter, i.e. Section 5.

1.2.1 NP properties and protein corona formation

When NPs enter a biological system, they come into direct contact with bodily fluids containing various biomolecules; blood plasma alone contains several thousand different proteins [109]. Some of these biomolecules will adsorb rapidly to the surface of the NP's forming a dynamic protein corona [110]. Proteins bound tightly at the NP surface are termed the 'hard corona'. These proteins form strong bonds with the NP surface and exhibit a slow exchange rate with other proteins. The hard corona also interacts weakly with other proteins, forming the 'soft corona'. The exchange kinetics of the soft corona are much faster, leading to a dynamic NP surface. Proteins that exist in the corona will be dependant, at least in part, on the availability of proteins in the fluid. Therefore the corona composition will vary according to the exposure environment providing an opportunity to modify the NP surface composition. Grafe *et al* saw that by changing the concentration of FBS in the NP exposure media, the molecular weight (MW) of proteins present in the NP corona could be modified. Increasing the concentration of FBS increases the fraction of low MW proteins present in the corona [111]. It was initially thought that the protein corona changes in composition over time, an effect described as the 'Vroman Effect'. According to the Vroman Effect, high abundance, low affinity proteins first bind to the surface with weak interactions and then over time these are replaced by lower abundance higher affinity proteins [112]. However it has also been suggested that these changes may be quantitative, rather than qualitative [112, 113]. Some studies have found

a lack of detectable Vroman effect, such as in the protein corona of USPIONs [114].

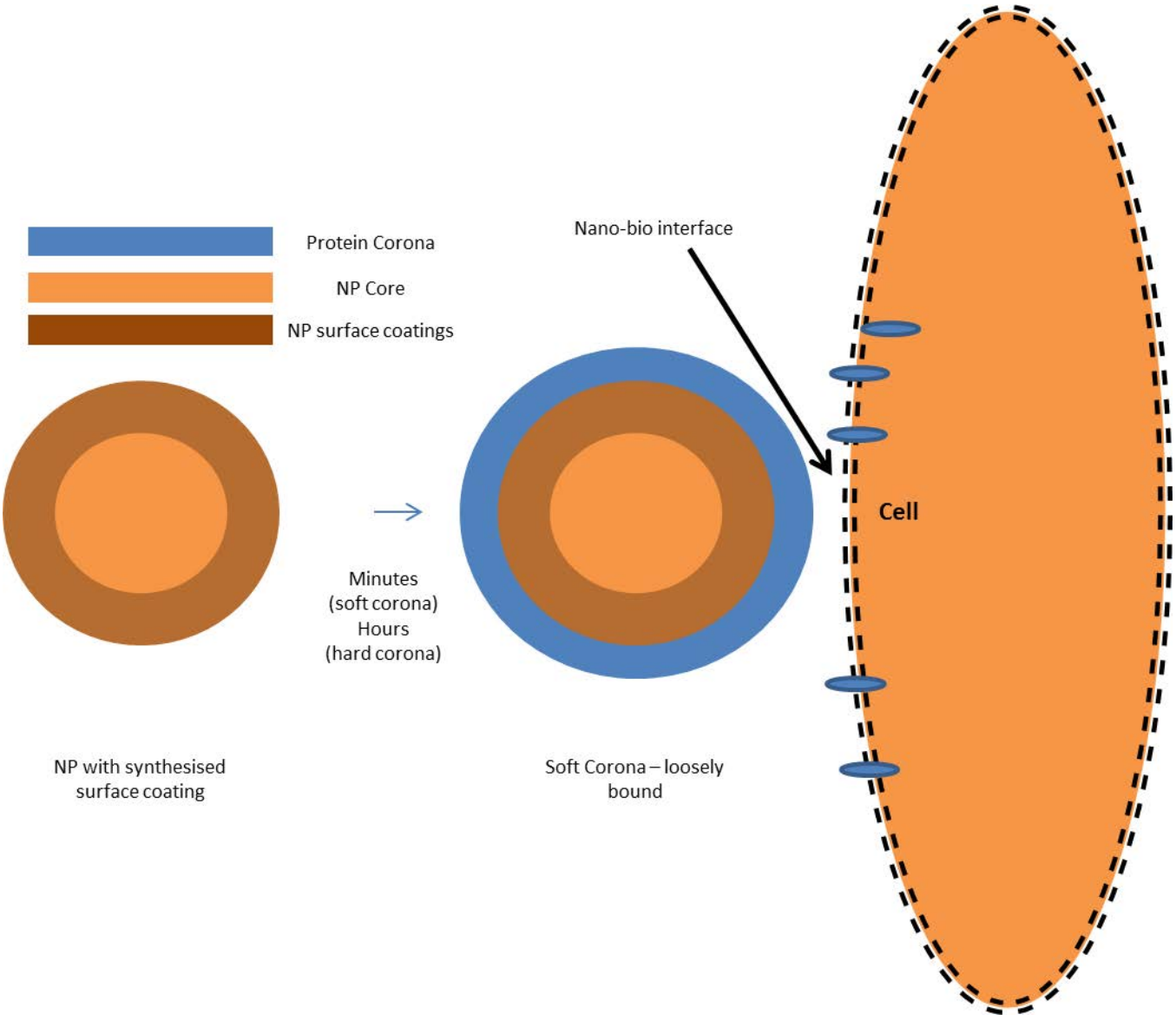

Figure 1.4: Depiction of the formation of a protein corona around an NP and the nano-bio interface when the NP is 'seen' by the cell. A NP exposed to biological media experiences adsorption of proteins to the NP surface. These proteins effectively mask the NP surface, including any targeting ligands unless specific steps are taken to prevent this, providing a new interface that the cell will 'see'. This can lead to interactions at cell membranes, and subsequent internalization and biological effects. Adapted from [115].

The intrinsic physical properties of NP's, at least partially, determine the formation of the protein corona. Properties such as size, surface charge and surface functionalization all have been shown to effect the constituents of the corona [116, 20, 117]. Therefore

it is vital that these different properties are characterized fully before, during and after exposures. Common methods used to characterize NPs include Transmission Electron Microscoy (TEM) to investigate the size, shape, monodispersity and agglomeration state of NP solutions, dynamic light scattering (DLS) to investigate the hydrodynamic size and size distribution, and zeta potential to measure surface charge. These methods have therefore proven indispensable for monitoring NP suspensions and protein adsorption during exposure experiments (Discussed more during Section 3). As an example, different sized NPs will have different extents of surface curvature, leading to the preferential binding of different proteins. The coronas of smaller NPs have been found to have a higher percentage of low MW proteins when compared to larger NPs which have a larger percentage of high MW proteins. It is likely that at a certain amount of surface curvature protein adsorption will cease completely [110]. Deng *et al* found that particularly small NP (7 nm) bind specifically to proteins, rather then proteins to them; facilitating cooperative binding of multiple NPs to a single protein molecule [118]. This leads to different possibilities of the NP-protein conformation, illiciting different cellular responses in each case [118].

Surface coatings are also an important determinant in protein binding. The surface coating can alter the stability of the NPs, and change the interactions that occur between biological components and the NPs. Often the coating stabilizes the suspension preventing agglomeration, weak interacting forces that occur between NPs that are broken apart easily by mechanical forces, and aggregation, the stronger bonds that form between NP which are more difficult to break apart. A huge range of surface coatings are available for NPs and can be used to modulate, to an extent, which proteins bind following immersion in protein containing fluids [119, 120]. Zeta potential provides a measure of the magnitude of surface charge or attraction between NPs in solution [121]. This provides a measure of the colloidal stability of the NP formulation, facilitating the determination of potential interactions, including agglomeration, repulsion and protein binding. Briefly, the environment surrounding an NP in a colloidal solution follows a double layer model

as depicted in Figure 1.5, comprised of a strongly bound inner layer (Stern Layer) and a loosely bound outer layer (Diffuse Layer). The zeta potential is a measure of the charge or membrane potential (mV) at the 'Slipping Distance' (the boundary between the double layer and surrounding ions in solution) from the NPs surface [122]. A strong negative or positive (<-30 mV / >+30 mV) indicates electrostatic stabilization, due to the strong repulsive forces that will occur between particles, preventing interactions. A more neutral charge can indicate steric stabilization or, alternatively, instability of the colloid if there is nothing present that could provide steric stabilization. Although it has been suggested that negatively charged NP may attract positively charged proteins, other studies have suggested that the corona is negatively charged regardless of initial surface charge [113, 109].

The protein corona that forms is unique to each NP and the exposure environment. This leads to a new 'biological identity' of the NPs, with different size, charge, and surface properties. All of these properties must therefore be characterized post-protein adsorption, in addition to prior. This newly formed corona constitutes the primary point of interaction between the NPs and biological components, such as cell membranes. This point of contact is known as the nano-bio interface, depicted in figure 1.4. Therefore the interactions that occur at this interface ultimately influence the biological response to the NPs, and the eventual outcome [115]. Several thorough reviews have been published regarding the protein corona formation, and the impact this has on cellular interactions [115, 123]. A complete understanding how the properties of NPs modulate the corona formation will aid advancements for NP targeting immensely and be crucial in understanding and predicting the biological effect and fate of the NPs. This will facilitate the intelligent, rational design of selective NPs that will have the required properties and desired cellular outcome *in vivo*. For example, if a specific high MW protein was required on the NP surface to allow selective uptake by particular cell types, and was known to adsorb to positively charged SPIONs, then a SPION of a larger size and positive charge would be

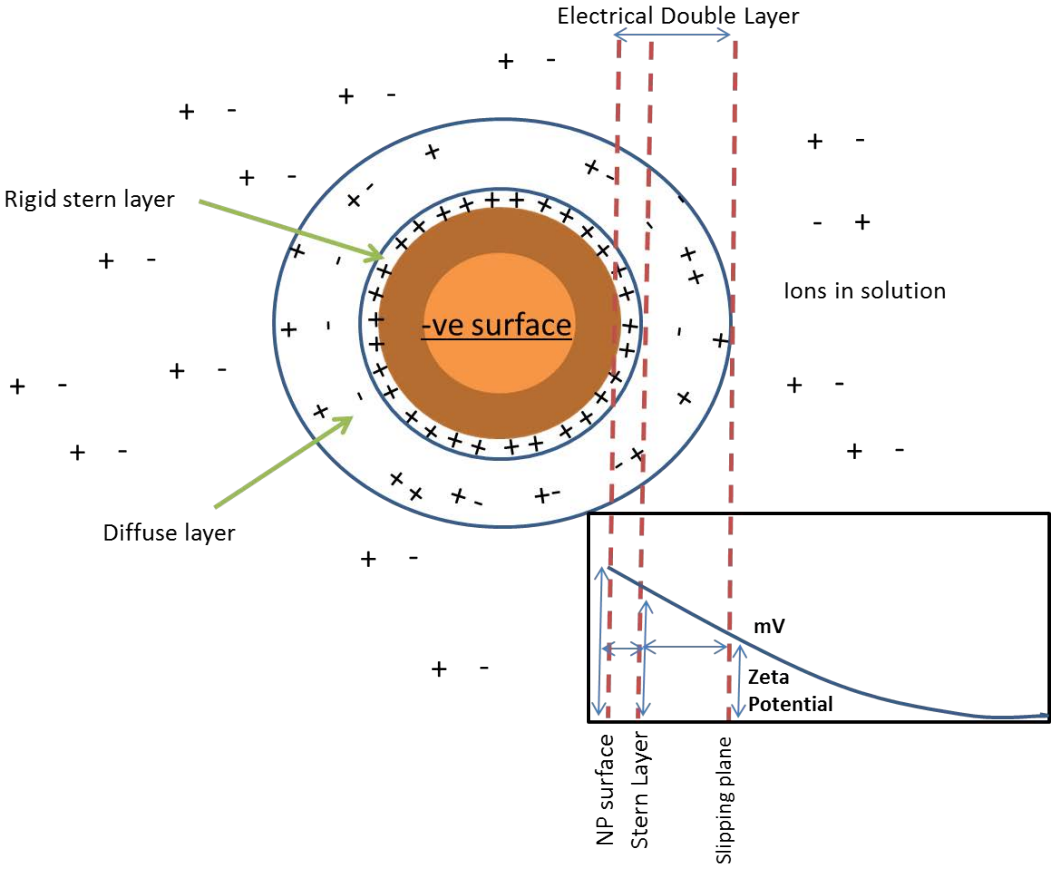

Figure 1.5: Depiction of the measurement of zeta Potential. The charge at a NP surface follows a double layer model (indicated on figure). A rigid layer of charge will form adjacent to the NP surface, called the stern layer, and a second layer forms, that is slightly further from the surface but still attracted to and associated with the NP. The boundary between the electric double layer and the ions in equilibrium is called the slipping plane. Zeta potential is defined as the potential that is measured in mV at the slipping plane distance from the NP surface. Adapted from [122]

used. Not only does the adsorption of biomolecules lead to alterations in the NPs cellular effects, when proteins bind to the surface of an NP they can undergo conformational changes. This can lead to irreversible inactivation of the protein. For example SPIONs have been shown to irreversibly alter the conformation of transferrin. If necessary cellular proteins are damaged through NP modification or by NP interaction, cellular function may be restricted, changed or inhibited [124].

Protein binding and surface effects on cellular uptake

Following interactions at the nano-bio interface, NPs may become internalized within the cell they interact with. The eventual extent of cellular accumulation depends upon the internalization mechanism utilized and the properties of the NPs and cells themselves. The protein corona has been shown to reduce the uptake of NPs into some cells when compared to the bare NP core. Smith *et al* saw a 20-fold reduction in the cellular internalization of polystyrene NPs into HeLa cells in the presence of proteins when compared to serum free conditions [5]. This is likely due to a reduction in the non-specific cell surface interactions that occur between NPs and the cell membrane. Experiments performed in the absence of proteins is not a biologically relevant condition. Bare, uncoated NPs will not be present in biological fluid *in vivo*, as protein adsorption occurs almost instantaneously. The protein corona can modulate cellular internalization, and lead to increases or decreases in uptake in a cell specific manner. Vogt *et al* saw an increase in NP uptake by macrophages when the protein corona was present in Silica coated SPIONs [125]. This is presumably due to opsonization of the NPs with proteins that are recognized by macrophages. If the protein corona contains proteins that reduce macrophage recognition, termed dysopsonins, such as serum albumin or IgA, the circulation time can be increased and macrophage uptake reduced [126].

Alternatively if the proteins bound at the surface of the NPs are recognized by cell surface receptors, NPs may be taken up through the specific protein or receptor internalization

pathways, introduced in Section 1.2.2. Many of the so far identified proteins within NP coronas are of the lipoprotein family, which have comparable nanoscale size. These lipoproteins are often involved in the cellular process of cholesterol metabolism. This could determine a route of NP entry within certain cell populations [127]. Lipoprotein E, for example, is known to be involved in the trafficking of PEG coated NPs to the brain. This gives an opportunity for the delivery of NPs through the Blood Brain Barrier (BBB) but also raises the potential neurotoxicity [127]. Proteins at the cell surface can also mask targeting ligands, leading to loss of selectivity. The transferrin receptor is over-expressed in a variety of cancer cells, and is often associated with poor prognosis, and therefore transferrin is often incorporated at the NP surface to target these cells specifically for drug delivery [128]. However, Salvati *et al* observed that transferrin coated NPs lost their specificity following protein corona formation [129]. It is clear that the ultimate fate and effect of NPs in biological systems is a complex interplay between the NP properties and the environments it is exposed to and the specifics of the targeting site.

NP surface charge and coating were found to be influential in governing the extent of NP uptake; extensive reviews have been published on the effects of various surface functionalisations and modifications of SPIONs [130, 131, 132, 133, 59, 134]. Modification with certain coatings alters the surface properties and therefore the behavior of the NP, such as reducing agglomeration and aggregation, or altering their uptake kinetics in different exposed cells. NP coated with neutral coatings such as polyethylene glycol (PEG) display reduced agg and reduced opsonization therefore they exhibit reduced non-specific macrophage internalization, facilitating NP evasion of circulating macrophages and increased blood circulation time [135]. Cationic (positively charged) NPs tend to show good cellular internalization, even if coated with opsonins, thought to be due to the interaction between the positively charged particle and the negatively charged cell surface [126]. However, anionic NP have shown better distribution than cationic NP through tumors. This provides a rational for creation of a negatively charged NP, that can distribute

through tumor cells, with the incorporation of a surface coating that becomes positive at low pH (i.e. in the tumor micro-environment) facilitating enhanced cellular uptake by the induced cationic NP [120].

1.2.2 Mechanisms of cellular internalization

The two main mechanisms for extracellular material, such as NPs, to be transported into a cell can be broadly classified as phagocytosis and pinocytosis. These processes exist within cells to tightly control the response of the cell to its extracellular environment. In general, first the cargo is engulfed in membrane invaginations that are 'pinched off' to form intracellular endosomes or phagosomes that are subsequently internalized and trafficked to various different target locations within the cell [136]. Phagocytosis, first discovered by Ilya Mechnikov, is involved in the uptake of large particles (up to 20 µm) by professional phagocytic cells, such as macrophages following opsonization with proteins [136]. NPs present in the blood stream are phagocytosed by circulating cells of the MPS and tissue specific macrophages. This leads to an accumulation of NPs in macrophage containing organs, notably the liver, spleen, bone marrow, lymph nodes, lungs and brain [52, 81, 85]. Most non-specialized cells do not perform phagocytosis. Rather, they rely on pinocytosis to internalize extracellular materials. Pinocytosis can be further split into subgroups according to the specific proteins involved in the internalization process. NPs can hijack these pathways to gain entry into cells, either non-specifically through fluid phase endocytosis, or through association with ligands that interact with cell surface receptors [137, 138, 5, 139, 140]. NPs have also been seen to directly permeabilize membranes [141].

Clathrin mediated endocytosis (CME) was the first endocytosis pathway discovered and is by far the most well studied. CME relies on the Clathrin triskalial comprised of three Clathrin Heavy Chains (CHC) for internalization events [142]. CME is involved in a plethora of different cellular functions, including turnover of membrane lipids and proteins, uptake of extracellular nutrients, polarized cell migration and neurotransmitter re-

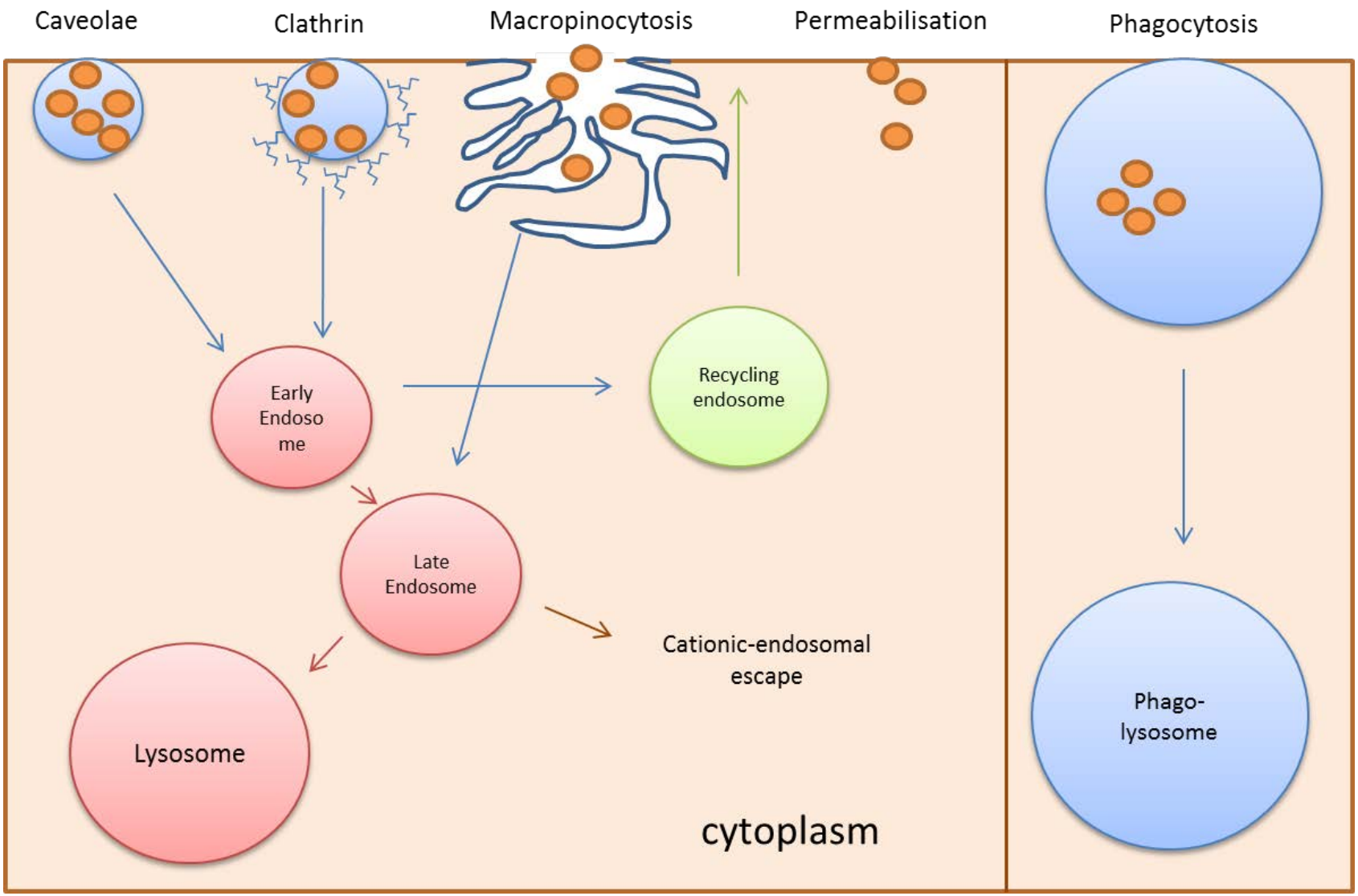

Figure 1.6: Depiction of the main internalization mechanisms that NP can exploit to gain entry into cells. The main routes for cellular internalization of foreign molecules and surface receptors are shown. CME and Caveolar endocytosis both are dynamin dependant and converge with the endosomal transport system. Macropinocytosis and Phagocytosis methods converge later with the lysosomal pathway.

lease. The first stage in CME is the recruitment of different proteins or cargo molecules, such as Adaptor Protein 2 (AP2), to Clathrin coated pits [143]. These pits are formed due to the polymerization of Clathrin to form Clathrin coated vesicles (CCVs), roughly 100 nm in diameter. The subsequent CCVs are released intracellularly by the action of the GTPase, dynamin. Dynamic pinches off the CCV in an energy dependant process. The vesicles and their cargo are then trafficked in an actin dependant manner to their specific sub-cellular destinations. Usually the vesicles lose their Clathrin coat and fuse with early endosomes, where they can be sorted for the lysosomal pathway, recycling to the plasma membrane or to the golgi network [144, 136]. Many different receptors/ligands are internalized through CME, including transferrin, which is often used as a marker for CME. The presence of transferrin in the NP protein corona has been suggested to lead to a CME route of internalization for that NP [138].

The other major cellular method of endocytosis involves caveolae and is defined by its dynamin dependence and Clathrin independent mechanism [145]. Caveolae are a subset of lipid rafts and were first identified as membrane invaginations around 60 - 80 nm in diameter [145]. Caveolae are important in a number of processes including virus entry to host cells and regulated signal cascades. There are three caveolin proteins, of which, caveolin-1 (cav-1) is the most abundant in caveolae. Depletion or removal of cav-1 leads to the formation of few to no caveolae in cells, this can be rectified by the reintroduction of cav-1 into the cell [146]. This is indicative of the requirement for cav-1 in caveolae formation [139, 146]. Cav-1 forms oligomers and co-assembles with cavins, these structures are stabilized by fatty acids and cholesterol [147]. Depletion of cholesterol leads to flattening of these caveolae structures, therefore caveolae is suggested to be involved in cholesterol and lipid homeostasis and metabolism [148, 143]. The mechanism of caveolae endocytosis is less well studied than CME, however studies suggest that caveolae are static structures, and budding is thought to be triggered by ligand binding to cargo receptors, and regulated by various phosphatases and kinases [147]. The GTPase dynamin releases

the caveolae vesicle into the cytoplasmic side of the cell. This pathway was once thought to have a distinct endocytotic sorting compartment, termed the 'caveosome'. This was later retracted due to insufficient evidence, and the caveolae vesicles have now been shown to converge with the Clathrin pathway at the early endosome, where they can be sorted [149, 150].

It has been suggested that caveolae internalization takes longer than CME, and has the ability to bypass the lysosome pathway [136]. Fewer known cargo exist for caveolae mediated endocytosis, some specific cargo include pathogens and sphingolipid binding toxins such as shigatoxin and Cholera Toxin Subunit B (CTxB) [151]. The dysopsin albumin is also a cargo that requires interactions with its receptor, gp60 to facilitate internalization via caveolae [151]. Albumin is known to promote evasion of macrophages, and its presence in the protein corona of NPs could lead to a mechanism of internalization through cavaolar endocytosis [126]. The abundance of lipoproteins in the coronas of NP may also indicate a mechanism for caveolae in the internalization of some NP. Caveolar endocytosis has been determined as the route of entry for silica coated SPIONs into HeLa cells [152]. Other Clathrin and caveolin independent pathways exist within cells including the less well studied Arf-6-dependent, flottilin-dependant, cdc42 dependant and RhoA-dependant [136]. All these pathways appear to be dependant upon cholesterol, and are likely dynamin dependant. They also seem to bypass Rab5 trafficking, however the sub-cellular trafficking and fate of these pathways is not well studied or elucidated [136].

Internalization can also occur through macropinocytosis, and its morphology which was first observed in 1931 [153]. Macropinocytosis normally occurs through growth factor stimulation that causes extensive actin-mediated membrane ruffling, which extends around large regions of extracellular fluid that is subsequently internalized. Therefore uptake by macropinocytosis is often non-specific fluid phase uptake. Due to the actin involvement, it has been suggested that macropinocytosis plays a role in motility, and

potentially tumor metastasis [154]. Macropinosomes are generally larger than 200 nm, and can be up to 10 µm in diameter, and are therefore much larger than CCV or caveolae vesicles [154]. Following internalization macropinosomes mature and recruit Rab7, a late endosome marker and then eventually fuse with the lysosome, or recycle to the plasma membrane. However the macropinosome maturation process has been found to be distinct in different cell types [154]. Macropinocytosis can be investigated using markers such as high MW dextran, and is sensitive to some forms of the Cytochalasin drugs [136]. It is likely that macropinocytosis can play a role in NP internalization, due to the lack of specificity required.

Various NPs have been found to utilize a variety of mechanisms to enter different cell types, including membrane permeabilization and dynamin dependant pathways, Clathrin mediated endocytosis and caveolae mediated clathrin-independant endocytosis [155, 137, 138, 5, 139, 140, 156]. However there is still no clear factor that determines which route is preferentially employed. Various properties have been suggested to be key in determining this uptake route, including size, shape and surface coating [139, 157, 158, 152]. The route of polystyrene NP uptake was size specific and NP smaller than 200 nm were preferentially internalized through CME [139]. Dos Santos *et al* found that NP pathway utilized by polystyrene NPs of size 40 nm and 200 nm was cell line dependant [159, 160]. Inhibition of CME in HeLa cells led to similar inhibition of both 40 nm and 200 nm NPs (around ∼25%), however with inhibition in A549 cells, the entry of 200 nm NPs was inhibited to a greater extent (∼50% compared to ∼25%) [159, 160]. The inhibition of caveolae endocytosis led to a stronger inhibition of 200 nm NPs entry into A549 cells (∼50%) and in HeLa cells (∼30%), compared to the smaller NP (∼24% and ∼7% respectively). Larger polystyrene NPs (up to 500 nm) also appeared to rely on caveolae mediated endocytosis [139]. These examples are interesting as caveolae are normally reported to be small invaginations of around 60 - 80 nm. Another study by Zu *et al* found that small NP (55 nm) internalize through CME, caveolar endocytosis and dynamin independent pathways

[140]. Computation modeling was performed to determine size limits for internalization via CME. The outcome indicated that NPs below and above two specific critical sizes (10 nm, 1000 nm respectively) would not be internalized via this route [161]. Charge also appears to have an effect on internalization. Positively charged particles appear to preferentially accumulate within cells via CME and macropinocytosis whereas negatively charged particles however have been found to utilize other internalization routes, possibly explaining the slower uptake observed [162]. It is therefore likely that complex interplays of the NP characteristics, exposure medium and the active cellular internalization machinery and surface protein expression modulate the entry of NPs into cells.

1.2.3 Fate and toxicity of internalized NPs

Following internalization, little is known about the subsequent biotransformation steps of the core and coatings of particular NPs. Suggested mechanisms include distribution to daughter cells during mitosis (only applicable in dividing cells), potential exocytosis and intracellular degradation [157, 163, 164]. Uptake pathways can converge to a common transport system regulated in part by Rab proteins, which will be introduced in more details later in Section 6. Vesicles recruit Rab-5 proteins and fuse with other vesicles to form late endosomes, with the ultimate fate of degradation in the acidic lysosomal compartment. Mono-crystalline iron oxide has been shown to accumulate within perinuclear vesicles which may represent terminal lysosomes [165]. NPs may also escape a degradative fate if they are recycled back to the plasma membrane in Rab11 positive vesicles or if they are released from the endo-lysosomal system into the cytoplasm. Particular surface coatings can lead to escape from the endo-lysosomal system following uptake in a process termed 'cationic-endosomal swelling and escape'. The integration of the amine PEI can illicit the ability to free the NPs from the endosomal system, which could be advantageous for some applications such as the release of drugs or siRNA into the cytoplasm [120, 166].

Once NPs are within the lysosome degradation may occur. It has been suggested previ-

ously that surface coatings of dextran are not very firmly attached at SPIONs surfaces. Therefore dextran coatings are prone to detachment. This could lead to potential agglomeration of the iron cores following dextran removal during degradation [91]. The effect of this has been seen to result in similar toxicities to those associated with the uncoated SPIONs. Indeed this was observed in studies where both coated and uncoated SPIONs led to cell death in fibroblasts [91]. The iron core is thought to be metabolized by the innate iron metabolism pathways [167]. Arbab postulated that the NPs may dissolve in the lysosome via metallic chelates (such as citrate) leading to release of iron into the cytoplasm through divalent cationic transport. This degradation is associated with subsequent release of Fe^{3+} into the cytoplasm, followed by storage aided by ferritin and hemosiderin, increasing total cellular iron content by 1.25-5% [157, 168, 167].

An increase in Fe^{3+} or Fe^{2+} ions within the cell is associated with problems, including iron overload and disturbed iron homeostasis. This may lead to symptoms of iron toxicity. This is particularly relevant in the case of targeting NPs, where the local concentration is expected to be exceptionally high. A variety of investigations have indicated that cells treated with SPIONs go on to later exhibit characteristics resembling that of iron overload, the effects of iron overload have briefly been discussed [169]. Iron ions themselves can interact with a variety of cellular components, can alter DNA, induce ROS and lead to epigenetic change; iron overload has also long been associated with carcinogenesis [107, 170]. For example an increase in free iron can lead to the production of reactive oxygen species (ROS) via fenton reaction with oxygen and hydrogen peroxide, leading to protein damage, membrane damage, formation of reactive mutagenic compounds and DNA damage [168, 170, 107, 59, 135, 171]. However it has been suggested that, with successful specific targeting, the production of ROS at a desired target (i.e. cancer cells - which are more sensitive to ROS) can be therapeutically advantageous, enhancing cancer cell death [171].

Some *In vitro* studies have indicated that below 100µg/mL SPIONs show low toxicity [107, 62]. Although other groups have reported that SPIONs with different coatings are toxic at this concentration in specific cell lines [172, 173]. In contrast, Lunov *et al* studies the effect of Resovist treatment on human macrophages for longer time periods and noticed toxic responses. Within the first 24 hours no cytotoxic effects were observed, but following the degradation of the dextran coating, ROS induction occurred leading to delayed apoptosis and loss of viability [174]. Macrophages may be particularly susceptible to iron overload following high levels of internalization, due to their limited differentiation capacity. These results indicate the cell and NP specific effects of various NP preparations and highlight the importance of thorough evaluation in different cell types and conditions.

There exists controversial information regarding the toxicity of NP's, in part due to the lack of specific endpoint assessments for toxicological response particularly in *in vivo* studies [175, 176]. No obvious signs of toxicity were observed following a long term SPION clearance study in mice [176]. There has also been an apparent lack of side effects observed in the few patient trials that have been carried out. It appears that the administration of SPIONs was well tolerated by most patients with only very mild side effects [63, 64]. There has however been reported cases of dextran itself causing anaphylactic shock [177]. Therefore it is not only the NPs themselves that must have safety testing - most NP suspensions are a combination of ingredients and the dispersing agents must also be considered. Teratogenicity in rabbits and rats has also been observed [178]. The measure of biocompatibility in such studies often focuses on observed effects *in vivo*. It is likely that different toxic effects are associated with different surface coatings, which as indicated above can lead to quite different fates in terms of uptake and retention by different tissues and cells. It is clear from *in vitro* studies that there needs to be clearly defined criteria and end points for measuring and describing the occurrence and extent of toxicity associated with various NP. This will allow the standardization of toxicity testing to properly ascertain the hazards, risks and benefits of particular NPs.

1.3 Quantifying NP uptake and localization

There is obviously a complex interplay of factors that determine the uptake, trafficking and toxicity of different NP preparations. More investigations are required to thoroughly understand the cellular interactions that occur during and following NP uptake in order to facilitate safe and efficacious use in biomedical applications. It is clear that rather than being one entity, each NP preparation with different characteristics exhibit different interactions within cellular systems and therefore biological outcomes. These outcomes must be completely characterized to facilitate progression of NP-based therapies to ensure efficiency and reduce the risk of subsequent product withdrawals from the market. One common factor in all of these necessary investigations is the requirement for reliable, fast detection and quantification of NP internalization within different cell types. There is therefore an increasing drive for the development of robust and implementable methods and algorithms with resolution and throughput sufficient to facilitate these investigations. These could then be used as part of clinical developing and testing strategy to enable NPs to deliver their full potential as diagnostic and therapeutic agents.

A variety of methods are available for the detection and characterization of NPs. NPs have distinct physico-chemical characteristics such as size, shape, charge, composition and refractive index that can be manipulated to facilitate characterization and identification. A subset of techniques revolve around the interaction of NP samples with Electromagnetic Radiation (EMR). DLS, for example, is based on light scattering by NP in solution. Therefore, the size and size distributions of these NPs can be determined by intensity fluctuations that occur due to Brownian motion [179]. Spectroscopic methods are often employed, mainly for quantitation purposes. These methods generally have very sensitive detection limits, but are often limited in terms of the spatial resolution or localization information. The range of NPs that these methods can be applied to is also limited. Imaging strategies are particularly popular for studying the localization and effects of NPs. Light (fluorescence and reflectance), X-ray and electron microscopies all offer dif-

ferent advantages and disadvantages in terms of sample preparation time, imaging time, cost and resolution. A simplified decision tree is depicted in Figure 1.7 to indicate where elemental analysis may be preferred over microscopical examination and vice versa.

The method of choice will therefore greatly depend on the hypotheses in question. Figure 1.7 gives an example of the methods that may be employed under certain situations. Reviews exist that discuss the most popular detection and imaging methods [181]. For the purpose of this discussion, the focus will be on the detection of NP within biological matrices, and the localization of the NP within cellular systems. A brief overview of the main analytical techniques and label-free microscopic approaches available is provided subsequently. The resolution of these are summarized in Table 1.2 [182, 183, 184, 185, 186, 187, 188]. These values however can vary with parameters and values given are rough guides due to their large variability in available configurations for experimental procedures.

	Resolution X-Y	Resolution Z	Additional info
(Nano)SIMS imaging	100 nm	10 nm	High mass accuracy, time consuming
MSI (e.g. LA-ICP-MS)	>1-5 µm	>1.2 µm	Elemental concentration, limited by laser spot size
Raman Confocal Imaging	~250 nm	~1.7 µm	Spectral information; Resolution can be enhanced using TERS
Magnetic Resonance Imaging	>120 µm	>600 µm	Can measure large areas in 3D (deep tissue imaging), soft tissue contrast
Electron Microscopy	>1 nm	>90 nm	Tomography, sectioning (determines 'Z resolution'), cellular contrast and single particle resolution
Light Microscopy	>300 nm	>700 nm	Fluorescence and reflectance, light diffraction limited
Super-resolution Light Microscopy	4 – 150 nm	>50 nm	Several variations available with speed / live / different resolution capabilities

Table 1.2: Summary of the resolution capabilities of different imaging tools. Different techniques offer different capabilities in terms of resolution. These are summarized within the table and are given as rough guides based on references [182, 183, 184, 185, 186, 187, 188], due to the variability in instrumental set-ups these may vary slightly.

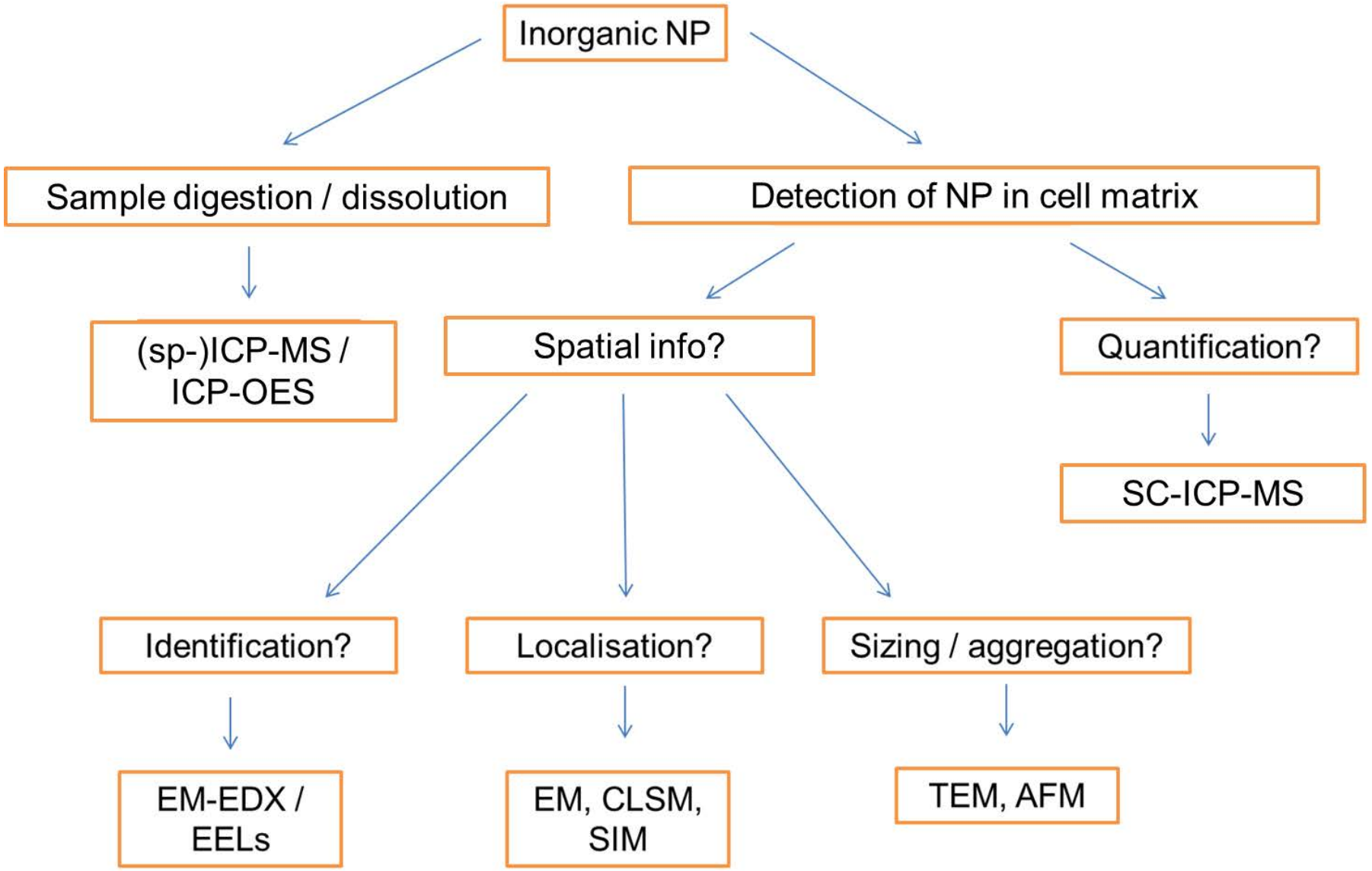

Figure 1.7: Decision tree for the techniques used to measure NPs within a sample. The decision tree shows examples of situations where certain methods would be chosen over others for the investigation of NPs within a sample. This focuses on inorganic NP, as this is the major focus of the research presented in this thesis. This figure was adapted from [180]. For example, if an NP was in solution and required quantification of dissolved fraction after a specified length of time, such as during dissolution studies, this could be analysed with ICP-OES or ICP-MS. If an inorganic NP is in a biological matrix, but the matrix can be digested by enzymes then sp-ICP-MS could be used for quantification following matrix digestion. Alternatively if an NP is in a cellular matrix then, for quantification, SC-ICP-MS could be used. Where spatial information is required, generally, LM or EM would be used, unless combining some form of sampling with spectroscopy such as in MALDI-MSI.

1.3.1 Spectroscopy techniques

Spectroscopy involves the measurement of a specific wavelength of EMR emitted, scattered or absorbed by a sample. Spectroscopy encompasses a wide range of different measurements and instruments. Inductively Coupled Plasma (ICP), in combination with either Mass Spectrometry (MS) (separation by mass) or Optical (atomic) Emission Spectroscopy (OES separation by light emission), is one of the most utilized techniques for elemental detection and quantification. Both OES and MS are capable of the rapid, simultaneous multi-elemental quantification of trace Parts Per Billion (ppb) or µg/mL amounts of metallic, and some non-metallic, elements. ICP-MS, however, is more sensitive for ultra-trace Parts Per Trillion (PPT) or ng/mL detection limits. ICP-MS also provides mass and isotopic information [189]. Some cellular constituents can complicate analysis, or are not compatible with particular instruments. For example in conventional ICP-OES and MS you cannot introduce a solid biological sample directly into the mass spectrometer. Therefore sample digestion is necessary, such as enzymatic digestion of a biological tissue, and acid digestion for solid NPs prior to analysis. These types of analyses cannot distinguish the NPs from the elemental ionic form, a limitation that can be overcome in Single Particle (sp)ICP-MS. The cellular matrix also contributes a complicating factor. Complex matrices often have several different components within and this can lead to spectral overlapping and spectral interferences. New techniques that can overcome this type of problem are emerging, including Single Cell (SC)-ICP-MS which allows the introduction of whole cells in suspension into a MS, revolutionizing the way cellular uptake is quantified. One limitation of these techniques is the loss of any sub-cellular spatial information. Additionally, NP on the cell surface and those that are intracellular cannot be distinguished. To combat these problems, isolated cellular fractions can be lysed and digested in concentrated HNO_3 acid. Thus, elemental quantification can be obtained to indicate the localization of particles within different compartments in this way [190, 191, 156].

1.3.2 Spectroscopy imaging

Although traditionally spectrometry methods provide information regarding the concentration and elemental compositions of the constituents in digested fluids, they can be used for imaging purposes when combined with particular spatial acquisitions that usually involve the destructive removal of consecutive small sample regions. This allows the acquisition of particular regions, building up an image map of constituents. The spatial resolution therefore usually depends upon the size of the sampling area (such as a laser or ion beam) [192, 193] An example of this is Laser Ablation (LA) which can be coupled with ICP-MS providing a quantitative method of imaging or mapping the elemental distribution within tissues and tumor sections with microscale resolution at trace concentrations [194, 193]. This can also be applied to the imaging of the distribution of NPs in single cells [182]. Drescher *et al* successfully demonstrated this technique for the imaging and quantification of the uptake of silver and gold NPs within human fibroblasts, determining their cellular localization [182]. One disadvantage is the complex cellular matrix within which the imaging takes place, leading to a lack of accepted reference standard and complicating the identification of different constituents [182]. Other techniques include the use of secondary ion mass spectrometry (SIMS) using MS-Imaging(I) and Laser Desorption Ionization (LDI)-MS [191, 195, 196]. Not all spectroscopy imaging techniques are destructive however; X-Ray Fluorescence (XRF) allows acquisition of elemental maps of individual cells. XRF, which detects the emission of secondary X-rays following bombardment with high energy gamma or X-rays, has been used to quantify the distribution of uptake of TiO_2 NPs in single cells [190].

1.3.3 Raman spectroscopy imaging

Raman scattering is capable of providing highly resolved vibrational information regarding a sample. Raman detects the inelastic scattering of EMR by NP; the effect of this can be enhanced by the use of a metal surface also known as Surface Enhanced Raman

Spectroscopy (SERS) increasing the Raman intensity. This is thought to be due to the particular scattering interactions that certain NPs, such as gold and silver, undergo with certain wavelengths of light. This effect is termed Localized Surface Plasmon Resonance (SPR) [197]. SERS has therefore been used extensively to characterize preparations of gold and silver NPs [198]. SERS has also facilitated the differentiation between different sized NPs of the same composition, enabling the simultaneous detection of sub-cellular structures differentially labeled by the two different AuNPs [198, 199]. Raman can also be applied *in vivo* for the detection of NP contrast agents. Raman scattering using SERS of gold NP with a silica shell has been shown particularly useful for tumor imaging in mice liver tumor models [200]. Another, related technique termed 'Four Wave Mixing' (FWM) is also based around SPR of gold and silver NPs [201]. Three pulsed incident laser fields illuminate a sample to generate a new signal field that is detected [202]. This technique can be sensitive to electronic transitions and vibrational properties of the sample. This renders FWM a versatile technique with a variety of applications, particularly in NP and NM studies, especially when combined with spatial sampling and imaging [202]. FWM has also recently been optimized to provide superresolution information, with a spatial resolution of 130 nm [203]. CARS is a subset of FWM techniques, where the difference in frequency of two illuminating lasers matches a Raman transition in the metal, increasing the FWM mixing signal [202]. This CARS technique has been shown useful for the 3D imaging of large intracellular iron oxide microparticles (1 µm) with both on and off resonant CARS imaging, confirmed using bright-field [204].

1.3.4 Magnetic resonance and electron paramagnetic resonance

As previously mentioned, some NPs, such as SPIONs, have particular super-paramagnetic properties that give rise to signal using resonance based techniques such as MRI. As previously described in Section 1.1.4, this is the basis for their use as *in vivo* MRI contrast agents for use in diagnostics. MRI and related techniques can also be used for the *in vitro* detection of NP in solution or single cells. Magnetic Particle Imaging (MPI), first intro-

duced by Gleich and Weizenecker in 2005, is rapidly gaining significant interest [205, 206]. Although it has similar concepts to MRI and NMR it has a distinct physical signal generation process. A sensitive focal point is created by two magnetic fields, called the Field Free Point (FFP), and only SPIONs at this location will induce a response signal [205]. As with MRI, no depth attenuation occurs, and no background signal is observed, This renders MPI a powerful, high contrast method for monitoring of cells and NPs localized within cells, such as stem cells, *in vivo* and *in vitro* [205].

Electron Paramagnetic Resonance (EPR) is an emerging technique that selectively and directly measures the magnetization of SPIONs allowing absolute quantification. It is a spectroscopy method based, again, on similar principles to those of MRI and Nuclear Magnetic Resonance (NMR). EPR involves the application of a radio-frequency (RF) at the resonant frequency, and the retrieved signal indicates the amount of SPIONs present in the sample. However in EPR it is the electron spin, rather than the proton spin that are excited. This provides a much greater sensitivity due to the high gyromagnetic ratio (γ), which is the ratio of the magnetic moment to the angular momentum [207]. This technique can be used to quantify NPs, such as SPIONs *in vitro* and *ex vivo* [207, 208]. Danhier *et al* compared EPR to fluorescence for the detection of SPIONs following uptake into different cell lines [207]. EPR was shown to be able to discriminate between endogenous and exogenous iron offering advantages for the detection and quantification of SPIONs over fluorescence and ICP-OES. EPR could therefore be a useful technique following MRI scanning to confirm the hypo-intensity is observed due to NPs and not endogenous iron, thus reducing the false positive rate in clinical applications [209, 207].

1.3.5 Microscopy

Microscopy remains one of the most utilized techniques for NP imaging, particularly for *in vitro* investigations. This is due to the resolution achievable and the ability to directly visualize signal in context with other cellular components when coupled with labeling or

staining. Although other microscopy methods are available, including XRD and Atomic Force (AFM), this intro will focus particularly on Light Microscopy LM and EM as these are the approaches utilized extensively within subsequent chapters.

1.3.6 Electron microscopy

Transmission-EM (TEM) remains the current gold standard for NP imaging. Electro-dense NPs, such as gold, have often been used to increase contrast within TEM micro-graphs, such as in immunogold labeling of proteins of interest [210, 211]. TEM provides ultrahigh resolution capable of distinguishing individual mono-disperse intracellular NPs with a resolution of 2-4 nm depending on the core material. Therefore TEM provides a means of quantifying NP number inside cells and this has been applied to multiple NP types including SPIONs, silica, zinc and gold [212, 213, 214, 215, 216]. When used in conjunction with counter staining, such as lead citrate and uranyl acetate, the localization of NPs to sub-cellular compartments can be determined. Despite the advantages that TEM offers, conventional sample preparation is extensive. This leads to the alteration of cellular structure and morphology during the dehydration and resin embedding processes, restricting investigations to fixed samples [217]. TEM is therefore limited in it's capacity to provide the high throughput studies necessary for the investigation of NP cellular interactions, and data interpretation can be complicated due to poor contrast arising from soft materials [218].

1.3.7 Light microscopy

Transmission LM employs a white light source that illuminates through a sample, projecting an image based upon inherent contrast that is determined by differing Refractive Indices (RI). Fluorescence imaging involves the excitation of fluorophores, often attached to a particular sub-cellular protein, lipid or structure of interest, with specific wavelengths of light and the collection of the subsequent emitted light. Fluorescent NP labeling and

subsequent imaging can be used for investigation of NP internalization and sub-cellular location of intracellular NPs. This method requires little sample preparation; however the use of fluorescent tags has known limitations, including low sensitivity, difficult bio-conjugation, low quantum efficiency and photo-bleaching effects, in addition to potential alteration of NP surface chemistry if the label is surface-attached, a factor known to influence biological activity [219, 220, 221, 222, 223]. Fluorescent tags can also dissociate from the NP following uptake, complicating the experimental analysis and results [224]. An alternative technique that can be used in conjunction with fluorescent imaging is reflected light imaging, in which metallic NPs give rise to significant contrast [225].

1.3.8 Reflected light imaging

Reflectance imaging, like transmission microscopy, exploits the inherent RIs within samples, providing label free contrast. There are a large number of interfaces with differing RIs in biological samples. Therefore the scattering of light is inevitable, generating contrast within reflectance images. The tissue or cellular structure and spatial distribution of RIs is linked, and RI is known to depend on the local macromolecule density. Therefore, imaging the light scattered provides a tool for interrogation of the cell or tissue architecture. NPs act as light reflective probes, akin to fluorescent labeling, enhancing the scattering of light and introducing strong contrast at their location within samples [226]. The use of reflectance imaging therefore obviates the need for NP fluorescent labeling, and provides an alternative platform for visualizing NPs [225]. Reflective features are not affected by photo-bleaching and therefore remain constant throughout imaging, unlike fluorescence signal which degrades over time. Detecting the reflected signal offers advantages over the detection of transmitted light. Transmitted light microscopy involves the collection of light passing through a sample, leading to a large amount of signal detection. The detection of slight alterations in the transmitted light signal arising from small features in the sample can therefore be obscured. Collection of only reflected light increases the detection of small changes in light scatter [227].

The reflected signal can be generated and detected in a variety of modalities, including standard epi- illumination, or using contrast enhancement measures such as a confocal pinhole configuration, oblique angle illumination or interferometry [228, 229, 230, 231, 225]. Other methods focus on selective illumination of a thin region close to the coverslip in order to provide high contrast information regarding interactions at the membrane, or use structured illumination to double the spatial resolution [232, 233]. Reflectance Confocal Laser Scanning Microscopy (CLSM) has proven indispensable in *in vivo* and *ex vivo* diagnostics, and may eventually facilitate eradication of some invasive surgical biopsy procedures, enabling earlier, more accurate diagnosis and staging of disease progression; however this will not be discussed in detail for the purpose of this thesis [234, 235, 236, 237].

1.3.9 Interference reflectance microscopy

Reflectance imaging was first applied to the interrogation of cellular structures closely opposed to a glass surface, and was termed Interference reflectance microscopy (IRM) [230, 238]. In IRM the interference between light reflected from different interfaces is imaged. The intensity within the IRM image increases with separation distances between the cell and the coverslip up to a depth of 100 nm (Figure 1.8). This allows quantitation of the separation distance of cell contacts and the coverslip directly from the pixel intensities [239]. Therefore, IRM can identify areas of attachment sites such as focal adhesions, which will appear dark in the IRM image due to close contact with the coverslip [239]. Curtis first applied this to imaging the contacts between chick heart fibroblasts and a glass substrate. IRM has since been applied extensively to imaging of the contacts between cells and a substrate [238, 230, 240, 241].

These investigations have provided information relevant to the understanding of many different cellular processes including the maintenance of the cell cytoskeleton, cell motility

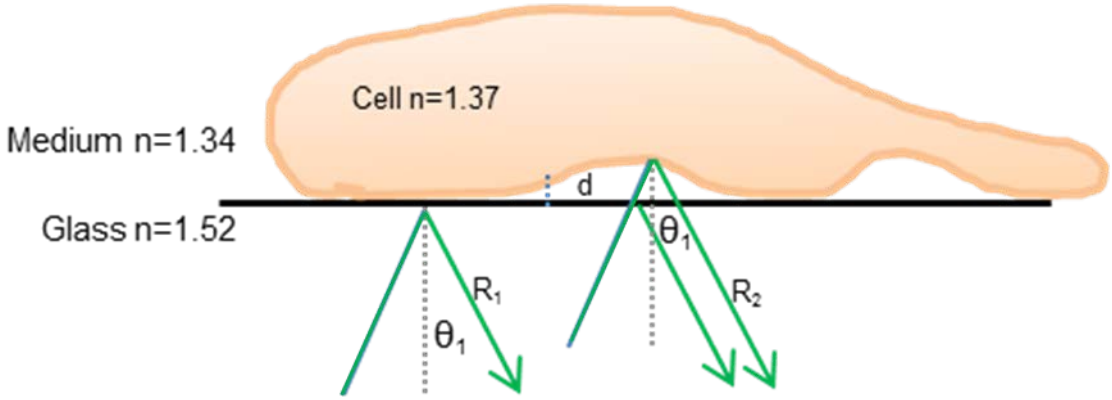

Figure 1.8: Schematic of the sample illumination and collection of reflected light using IRM. Depiction of the reflected rays generated from incident light hitting a biological sample. R1 is generated at the glass medium interface. R2 is generated at the medium-cell interface. The length of d (path distance) dictates the phase in which the light hits the detector, thus influencing the intensity of the image due to constructive (d = 100 nm or more) or destructive(d approaching 0) interference. Regions in close contact of the coverslip therefore appear dark and intensity increases with distance from the coverslip.

(which is important in wound repair, immune response, tumor formation and metastasis) and multicellular structure and function in organs such as the liver and the vascular network. Different methods have been employed to try and reduce the stray reflections that arise due to other cellular constituents in IRM, including the use of an anti-flex immersion objective that circularly polarizes light and as well as an annular to block 90% of the illumination light creating an oblique incident angle [242]. These methods allow selective collection of light reflected from the sample reducing stray reflections. Alternatively, some recently developed IRM techniques specifically rely on the collection of all the available light including background scatter. An optimized interferometric microscope setup, called iSCAT, utilizes this configuration to facilitate single molecule detection and tracking of nanoscopic lipid domains [243, 244].

1.3.10 Dark-field microscopy

Dark-field (DF) microscopy utilizes wide-field oblique angle illumination to enhance reflectance image contrast by selectively capturing only the light scattered by the specimen. Oblique angle illumination is achieved using a specialized condenser which contains a light

block comprised of an annulus with a narrow aperture [245]. If a sample is present a portion of the illumination the light will be scattered back into the objective. This introduces contrast against a dark background leading to the characteristically high Signal to Noise (SNR) DF image with reduced potential for artifact. However, sample preparation must be rigorous as dust on the coverslip can lead to unwanted reflections. High intensity illumination light is often necessary due to the low intensity signal, which may cause sample damage. DF is mainly used for the interrogation of semi-opaque samples that are unable to be imaged via transmitted light microscopy. DF is also well-suited for the visualization of reflective NPs, and has been combined with CLSM (DF-CLSM) for the detection and characterization of NP uptake in cultured cells [231]. NPs serve as light reflective probes and AuNP labeling (so-called immuno- labeling) of NPs targeted towards the HER2 receptor showed sufficient NP accumulation within target cells to facilitate thermal therapy [236]. DF can be coupled with a specialized condenser that improves the SNR up to 7-fold compared to conventional DF. This enhanced DF has been applied in numerous investigations, including the identification and localization of metal oxide NPs within different anatomical regions of rat organs following inhalation studies [246].

1.3.11 Confocal microscopy

Confocal microscopy utilizes a conjugate pinhole system to block out of focus light allowing collection of light from a plane of interest. This allows contrast and resolution enhancement (compared to epi-illumination) in biological imaging of cells or sub-cellular structures. Conventional Fluorescence Confocal Microscopy (FCM) can provide a maximum X-Y resolution of 250 nm; Reflectance Confocal Microscopy (RCM) is reported as higher at 200 nm [247]. Due to the removal of out-of-plane signal by the pinhole system, confocal microscopy allows optical sectioning through a sample which is advantageous for 3D imaging. Operating in confocal reflectance mode, rather than fluorescence, requires only the addition of a transmission / reflectance dichroic to facilitate collection of reflected incident light. This makes RCM an accessible technique that can provide information re-

garding a sample either alone or in combination with fluorescent imaging. No additional labeling is necessary providing sufficient contrast is generated from the endogenous RI mismatches within biological samples. For example, the lipid droplets in the developing drosophila primordia provide a good example of inherent contrast with RCM [248].

NPs, such as those made of metals or metal oxides, can be used to label cells or subcellular components such as specific proteins or biomarkers of interest from a variety of tissues for imaging with RCM [225]. Alternatively, the NPs can be the subject of investigation. RCM can be employed in conjunction with other labeling methods to provide insight into the cellular entry, trafficking, fate and toxicity of these NP [249, 5, 250]. It is important to note, most studies conducted on NP trafficking utilize only fluorescent labeling, rather than fluorescent label free RCM. Quantifications can be obtained from the resultant images. RCM can also be used in conjunction with other techniques to provide absolute quantitative information at a single cell level, including with spectroscopic methods such as ICP-MS [251]. RCM was used in conjunction with ICP-MS to quantify the uptake of gold NP within the endo-lysosomal system and an apparent linear relationship between reflectance intensity and particle size was established [251]. Determining the exact relationship between reflectance data and elemental NP quantification is essential for the translation of *in vitro* experiments into efficacy within a clinical setting. The short and long term toxicity of NPs to complex organisms that may be exposed as a result of increased NP use and release is largely unknown. RCM is ideal for assessing such toxicity associated with this NP exposure in whole organisms, such as the model aquatic organism Daphnia Magna, as it is non-destructive and capable of 3D imaging [16].

Two-photon fluorescence, using Near-Infrared (NIR), offers superior tissue penetration, lower photo-toxicity and suppressed background when compared to confocal imaging, and therefore is often employed for *in vivo* studies [252]. Collection of the backscattered laser light from *in vivo* investigations allows visualization of haemodynamic events and pro-

vides structural information to contextualize fluorescent signal [252, 253]. This emerging combination of two-photon and RCM imaging can be employed to visualize blood flow and anatomical tissue structure in regions such as the brain cortex [253]. Axonal myelin gives rise to contrast in the reflectance image, providing a means of monitoring axonal de-myelination, a critical event in a host of neurodegenerative pathologies [252]. A novel methodology, termed *in vivo* microcartography, also employs this combination method to visualize the architecture and haemodynamics of *in vivo* tumor angiogenesis [254].

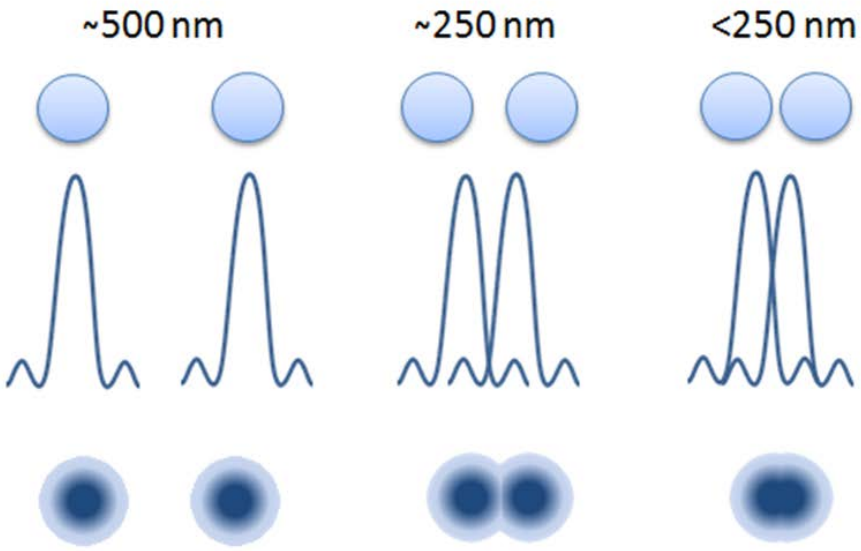

Figure 1.9: The resolving capability of diffraction limited imaging. The Point Spread Function (PSF, airy disk) represents the intensity distribution of sub-diffraction emitting sources (left). We can resolve a pair of sources (middle) if the central peak of the diffraction pattern is no closer than the airy disk; this is known as the Rayleigh criterion. If two point sources are closer than the Rayleigh Criterion together their airy disks (center of the airy pattern to the first minimum) will overlap (right) and will not be resolved.

Despite the advantages RCM methodologies provide, the resolution is fundamentally constrained due to the finite wavelength of the incident light [255, 256]. Therefore NPs and NP clusters appear as blurred spots, this effect is depicted in Figure 1.9 [250]. Diffraction prevents the resolution of two objects if their separation distance is less than the Full Width at Half Maximum (FWHM). FWHM is therefore often quoted as the resolution

limit. Light microscopes, such as RCM, can resolve objects laterally that are separated by roughly 250 nm, and axially by approximately 600 nm. This, however, relies on perfect experimental conditions and the concept of an infinitely small pinhole. Therefore these resolutions will not be achieved in practice, particularly in fluorescence microscopy where light intensity is a limiting factor [247]. Therefore structures separated by less than the resolution limit of the system will not be resolved. To overcome this limitation, novel superresolution methods are necessary for accurate NP studies under label free conditions.

1.3.12 Structured illumination microscopy

All the aforementioned reflectance techniques, despite having distinct advantages for certain applications, lack the superresolution afforded by some fluorescence techniques. Superresolution methods break the diffraction limit and bridge the gap between light and electron microscopies [257, 258, 259]. One method, first proposed by Neil *et al* called Structured Illumination Microscopy (SIM) falls into the category of 'Optical Transfer Function' (OTF) modulation methods [258, 257]. SIM was first developed collaboratively between the labs of John Sedat (University of California, San Francisco) and the late Mats Gustafsson (formerly of HHMI Janelia Research Campus) [257]. In SIM, a physical grid is used to structure the illumination light to effectively increase the resolution limit imposed by diffraction [258]. In an entire SIM acquisition, the grid projects illumination structures onto the sample in several different orientations. The spatial emission pattern of the sample at the grid positions can interfere with the excitation light, producing Moiré fringes. A Moir pattern, depicted in Figure 1.10, is a secondary, visually evident superimposition pattern created when two identical patterns are overlaid while displaced/rotated (i.e. phase shifted).

When the grid structures are applied in several directions, high frequency variations in the light emitted / reflected from a sample occur as a function of grid position and time. As the grid pattern is known, the resulting Moir interference pattern contains otherwise non-

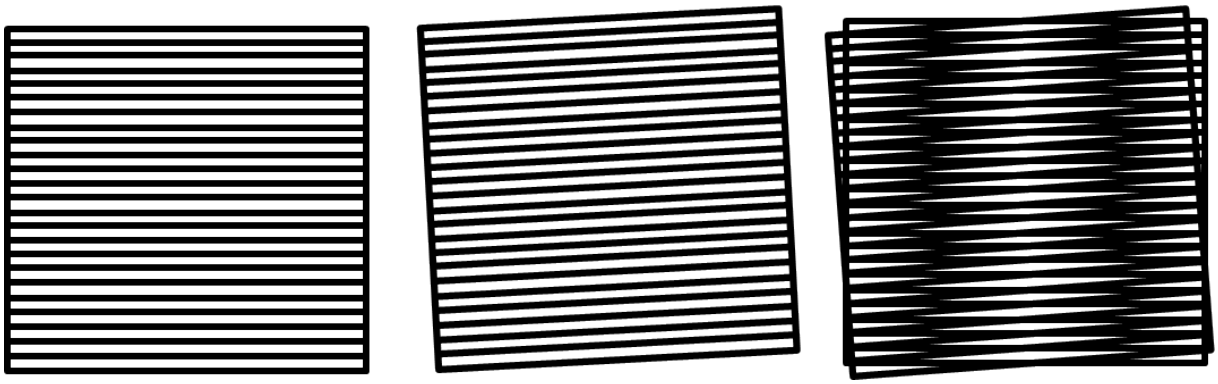

Figure 1.10: Example of moiré fringes. Depiction of Moiré fringes that result from the interference of two patterns (in SIM this is the structure in the sample and the grid).

resolvable sub-diffraction structural information about the sample. In a single acquisition typically 3 different grid orientations and 3 to 5 different positions together generate the final SIM image. Image reconstruction takes place in reciprocal space to separate sharp image signals and generate the Fourier transform (FT) the inverse of which is the super-resolution image. The theory of SIM reconstructions is described in detail in references [258, 257]. If there is a large amount of unfocused light, the reconstruction may be unsuccessful. The Fast Fourier Transform (FFT) of the image can give an indication of a successful reconstruction. SIM can increase resolution two-fold, enabling the identification of previously unresolvable cellular structures such as individual nuclear pore complexes [260, 261]. SIM is generally only associated with superresolution fluorescence imaging. There are a limited number of examples of superresolution reflectance methodologies, all involving the use of structured illumination. Chang *et al* used a custom built SIM microscope to image the light scattered by gold AuNPs using 3D-SIM, to obtain optical sections with nearly double the lateral and axial resolution achieved with conventional reflectance techniques [233]. Similar imaging methods using two frame acquisitions with just two grid positions have been used successfully with reflectance mode to increase the depth resolution when deep tissue imaging [262].

1.3.13 Summary of reflectance methods

Other modalities exist that use reflected light, including Total Internal Reflectance Microscopy (TIRM) and Optical Coherence Tomography (OCT). These will not be discussed in detail in this thesis, but are reviewed [263]. A summary table of the major reflected light methods is presented (Table 1.3). Each reflectance technique offers different advantages and disadvantages, in terms of resolution and imaging capabilities for different types of investigations within a host of different biomedical applications. Therefore, for different types of biological investigations, different modalities would be more appropriate. Collectively reflectance offers a wide range of experimental opportunities to probe a variety of different sample types in a label free manner.

	X-Y resolution	Z resolution	Penetration Depth	Advantages	Disadvantages	Applications
R-SIM	~115 nm	~685 nm (measured)	~100 µm (fluorescence)	Increased lateral resolution, can be coupled with fluorescence acquisition, optical sectioning	Suffers high levels of background, acquisitions of >1s	*In vitro* live 3D studies (e.g. NP), Colocalisation studies, potential for high resolution tissue imaging
RCM	~250 nm	~500 nm	350 µm	Accessible, optical sectioning, can be coupled with fluorescence acquisition	Limited depth penetration in tissues, limited by diffraction	*In vitro* live 3D studies / *In vivo* dynamic studies (e.g. NP), *In vivo* diagnostics (dermatology, endoscopy, ophthalmology, blood flow), complimentary structural information, (semi)-transparent substrate
TIRM	250 nm	100 nm	~200 nm	High SNR, sub diffraction limit in Z	Small penetration depth	Endocytosis studies, (single)-particle tracking, cell dynamics and trafficking
IRM	250 nm	NA*	100 nm	Quantification of separation distances	Limited by diffraction, No optical sectioning unless coupled to CLSM,	Imaging surfaces (cell surface) and cell contact dynamics, quantifying separation distances, complimentary structural information
Darkfield	~250 nm	NA*	NA	High SNR, High detection capabilities	No optical sectioning unless coupled to CLSM, limited by diffraction, sensitive to dust / dirt on coverslip	Opaque substrate, NP studies, imaging surfaces
OCT	~ 5 µm	>1 µm	>1 mm	Deep tissue penetration	Limited by diffraction, limited X-Y resolution	*In vivo* diagnostics (dermatology, endoscopy, ophthalmology, blood flow), deep tissue imaging

*Can be combined with CLSM to obtain optical sections and Z-resolution akin to that available for confocal

Table 1.3: Summary of the capabilities of the most commonly used reflected light methods. Different techniques offer different capabilities in terms of resolution, penetration depth, and sample type. These are summarized within the table.

1.3.14 Correlative microscopy

Recently there has been a drive for the development of sequential methodologies that allow the acquisition of multiple data types (quantification, high resolution, live images) from a

single sample. Reducing the error introduced by variable cell culture experiments and decreasing the number of samples required to obtain various information. Correlative Light Electron Microscopy (CLEM) can encompass a wide range of experimental techniques. CLEM can include microscopical investigations that are either acquired sequentially on separate instruments, or as completely integrated solutions [264, 265, 266]. CLEM often involves FLM to capture the occurrence of a rare event, followed by ultra-structural investigation at high resolution with TEM. CLEM has been successfully applied in multiple fields of cell biology. This includes the ultra-structural characterization of Golgi carriers, the discovery of the invadopodia organelle in metastatic cells, and characterization of endothelial cells involved in angiogenesis sprouting [**?**, **?**, 267]. CLEM has also been used to investigate gold and iron nanoparticle internalization within cells [224, 268, 214]. Böse et al imaged the uptake of gold NPs with a fluorescent coating using FCM, followed by imaging of the gold core with SEM and TEM. This enabled them to determine that some of the fluorescent tags were detaching from the NP following and during uptake, indicating a clear limitation of the technique for fluorescent NP imaging [224]. Difficulties arise in CLEM protocols; they are often complex, time consuming and technically demanding. A single CLEM experiment involves the treatment of a biological specimen, imaging by light microscopy, lengthy EM preparation, EM imaging and image realignment. EM preparation often leads to changes in cell morphology, and alteration of cell orientation, increasing the complexity of cell relocation and co-alignment [269]. Various techniques have been developed to increase accessibility and ease of performance in CLEM investigations. This includes integrated systems released to perform all imaging steps, and software that bridge the two modalities including Corr Sight, MAPS and iCorr, are now emerging. The integrated techniques are used to provide a faster and more accurate approach to CLEM, however these are often costly and are mostly applicable only to SEM and/or employ low magnification/Numerical Aperture light microscopes without optical sectioning or super-resolution capabilities. New computational measures could facilitate higher throughput methodologies, more accurate cell relocation methods, in addition to

increasing the accuracy of image alignment. This would be beneficial to assist the complex CLEM work-flows and would reduce the cost associated with buying integrated platforms [270].

1.3.15 Summary of detection methods

There are numerous detection methods each with their own advantages and caveats for specific applications and investigations. Spectroscopic methods offer absolute quantification for sample elemental compositions, but often at the expense of spatial resolution. When spatial resolution is required, it typically involves destruction of the sample to attain sub-cellular resolution, normally not approaching the resolution achievable with microscopic methods. Microscopy, particularly TEM, provides high resolution information, but again is limited to destructive, lengthy sample preparation and imaging of fixed cells. Reflectance imaging, such as RCM, provides resolution sufficient to distinguish different cellular compartments and NP clusters, and facilitates semi-quantitative analysis. Despite the advantages offered by RCM, such as fast acquisition of large sample areas with optical sectioning capabilities, the resolution is not as high as superresolution techniques, and there is a distinct lack of information regarding the optimization of RCM for NP investigations. Superresolution is a necessity for accurate internalization and colocalization studies to determine the precise uptake, localization and trafficking routes of NPs. Often combinations of techniques, such as in CLEM methodologies, can offer the maximum information regarding a sample.

A drawback of microscopy compared to analytical methods is the lack of absolute quantitation. In microscopy, often the quantification of a specific signal of interest from images involves the manual delineation of a region followed by the measuring of mean intensity of a signal. This methodology has associated problems, particularly for reflectance microscopy. When utilizing reflectance microscopy to detect small optically reflective objects, a high level of unwanted, non-uniform background signal can occur. This is es-

pecially problematic within highly scattering environments such as within a cell; optical elements within the microscope can also generate reflectance patterns [227, 271]. Optimization of the imaging procedure is therefore necessary but this is not well documented in the literature. This background also leads to associated problems when attempting to quantify relative signal intensities, which compared to noise components, is a relatively small portion of the total signal [227]. This is documented in Results Chapter 4. The mean signal across an entire cell is therefore skewed by the contribution from the cellular background. Manual processing is time consuming, user dependent, and contains inherent natural bias. In reality, to make accurate (relative) quantitative conclusions about signal the analysis must first be optimized both during the acquisition and in the processing stages to allow a non-biased, user independent and automated analysis to facilitate more accurate, reproducible quantifications to allow high throughput investigations. This will be introduced and discussed more in Chapter 4, however a brief introduction of image analysis is discussed below.

1.3.15.1 Introduction of image analysis

Often the quantification of a specific signal of interest from microscopy images involves the manual delineation of a region followed by the measuring of mean intensity of a signal. This mean signal is skewed by the high level of background present in the image, therefore even when using a manual method, some form of pre-processing is necessary. This process also tends to be time consuming, user dependant, and contains inherent natural bias. In reality, to make accurate relative quantitative conclusions about a specific signal, the work-flows must first be optimized during the acquisition and processing stages. This allows non-biased, user independent, automated analysis to facilitate more accurate, reproducible quantifications in high throughput investigations.

An image is made up of an array of pixel values corresponding to different regions. Microscopy images are inherently noisy, therefore, the associated pixel values can loosely be

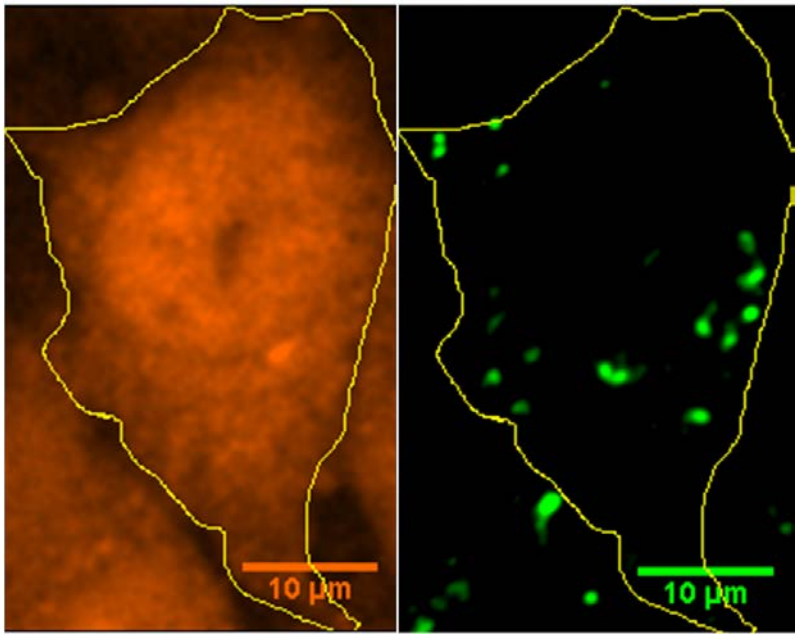

Figure 1.11: Example of the manual analysis of reflectance intensity The CTO cytoplasmic stain can be segmented manual by drawing around the plasma membrane, this can then be overlaid onto the NP channel to obtain intensity measurements.

split into different types of signal. The signal of interest (normally high intensity, low frequency signal), unavoidable background signal (mid to low intensity signal corresponding to cellular reflectance) and noise (low intensity, high frequency signal: predominantly shot noise in confocal microscopy images). Sheppard *et al* have summarized the main types of noise in confocal microscopes [227]. Image filtering can be used to remove the effects of noise prior to segmentation where necessary. Noise removal is often used in fluorescent image analysis. This is partly due to the low laser powers used and short acquisition times in an attempt to reduce photobleaching. Morphological filters can be used prior to segmenting cellular regions. Image convolution, or filtering, is a popular method for removing noise effects within fluorescent images. There are a large variety of filters available and often a simple Gaussian filter or mean / median filter on a fluorescent cell stain is sufficient to smooth the noise components allowing subsequent segmentation of cells due to the high intensity signal offered by the CTO stain (Figure 4.17A). That being said, noise from photons can be modeled by a Poisson distribution, whereas noise from the equipment can be modeled by a Gaussian distribution. For this reason there are

a number of sophisticated noise reduction algorithms that accommodate for both types of noise [272].

One of the most important processing stage involves the successful detection and segmentation of objects of interest from the background, which can be thought of as assigning or grouping the pixels based on specific characteristics (more often than not, the pixel intensity). Efficient segmentation ultimately determines the eventual success of any automated analysis procedure. As such there are a number of available options depending upon the intended purpose and image type. Comparisons of the main methods used for detection in fluorescence images are available [273, 274]. Although many routines exist for fluorescent images, reflectant image analysis protocols are not so readily available. The development of analysis procedures is therefore discussed further in later Chapters (Chapter 4 and 6).

1.4 Thesis Structure

Following the discussion of the relevant literature regarding man-made NPs, in terms of their impact, uses and detection, a brief outline of the remainder of the thesis is presented. The main aims of this thesis are to: 1) Develop existing and new label free methods to visualize NPs using inherent properties, rather than using modifying labels, such as fluorescent tags; 2) Develop computational tools to increase the throughput of investigations using these methodologies including computational image processing and analysis and 3) Apply these techniques in combination with existing tools, such as fluorescence labeling, to investigate the cellular uptake and processing of NPs, particularly the clinically relevant, SPIONs.

Chapter 2: Materials and methods section

A complete list of all reagents and description of the experimental protocols used within

this thesis.

Chapter 3: Nanoparticle characterizations

NP characterization is an often overlooked but important predecessor to investigation of the cellular effects of NPs. Therefore this chapter aims to characterize different properties of the NP, including the core size, dispersity, hydrodynamic diameter and surface charge, with and without the presence of serum proteins. This chapter also aimed to characterize the proteins that bind to the NP surface.

Chapter 4: Development of label free microscopy methods and analysis routines for the detection and quantification of intracellular NPs

Most imaging methodologies rely on the use of additional fluorescent probes tagged to NP surfaces for visualization inside cells. This chapter aims to optimize existing label-free imaging methodologies (RCM) and develop new label-free imaging tools (R-SIM and CREM) to increase the information attainable from cell samples labeled with NPs. Use of the same sample for each technique can minimize the effects of inconsistencies in sample preparation. Reflectance image analysis work-flows have also been developed and validated within this chapter, that aid the consistency, reliability and throughput while decreasing the effect of human bias during result generation. Comparisons between the techniques applied will also be enabled by the investigation of computational cell realignment strategies.

Chapter 5: Determining the cellular uptake of SPIONs

Cellular uptake of clinically relevant SPIONs by non-macrophage cell lines is not well established. Studies previously done have generally relied on labeling methodologies that alter the surface properties of NPs. We will apply label-free methods, along with analysis work-flows, to determine the extent of cellular SPION accumulation in a variety of cancer cell models. SiRNA inhibition studies, in combination with pharmacological inhibitors,

will be used to indicate pathways that are instrumental in the accumulation of SPIONs within specific tumor cell models. Extension of these methods into 3D multicellular studies is a key step in the assessment of the potential for NP-therapies in subsequent animal and clinical trials. Therefore we aim to demonstrate the use of RCM for investigating NP uptake in multicellular spheroid assays, to provide a starting point for further development and continuation of cellular assays in a 3D environment.

Chapter 6: What happens next?

Following uptake there are classical models of the cellular processing of NP. These intracellular trafficking and degradative pathways can be visualized using correlative fluorescence and reflectance imaging of labeled compartments and NP respectively. Using this methodology, the trafficking and fate of NP was determined in HeLa cancer cells. Subsequently the degradation of NP in a solution that mimics that of the respective intra-endosomal / lysosomal fluid was partially determined, in preliminary experiments that indicate subsequent areas for experimental optimization.

Chapter 7: Final conclusions and future work

This section summarizes the key findings within the thesis, contextualizing this within the field of nanoresearch and nanomedicine. This includes a discussion of future directions that arise as a result of the work done within this thesis.

CHAPTER 2

MATERIALS AND METHODS

Routinely used experimental methods are detailed here. Other methods are included in Appendices, including bacterial transformation, western blotting protocol in detail with buffers and solutions and in depth correlative workflow summary and analysis MATLAB routine.

2.1 Nanoparticle characterization

2.1.1 Nanoparticle Suspensions

Sienna$^+$ SPIONs (Endomagnetics, Sysmex UK) and cerium dioxide (synthesized and characterized as previously described [275]) were employed within this thesis. Nominal sizes of the NPs were 60 nm and 70 nm (core and coatings), respectively. NP stock solutions were sonicated (XUB18; Grant Instruments, Shepreth, UK) for 15 minutes prior to use and dispersed in SCM at the specified concentrations in the relevant experiment. Particles were vortexed and applied to cells immediately upon preparation. The main physicochemical characteristics are summarized in Table 2.1.

	Sienna+ SPIONs	Cerium dioxide
Core size (TEM - nm)	4.49 +/- 2.7	8 +/- 2 nm
Nominal size	60 nm	70 nm
Size in PBS (DLS - nm)	58.8 /- 3.9	65.0 +/- 24.19 nm
Zeta potential in dH20	-11 +/- 4.4	47 mV

Table 2.1: Summary of the physical properties of Sienna$^+$ SPIONs and cerium dioxide. The measured size (TEM and DLS), manufacturer (nominal) given size and the zeta potential of the Sienna$^+$ SPIONs and cerium dioxide NPs are given in the table.

2.1.2 Dynamic light scattering

Average sienna$_+$ SPION size (hydrodynamic diameter) measurements were performed using a Zetasizer Nano ZS ZEN 3600 (Malvern Instruments Ltd, Malvern United Kingdom). SPION stock solutions of 28 mg/mL (Sienna$^+$ Endomagnetics, Sysmex, UK) were prepared as previously in Section 2.1.1, diluted in Serum Containing Media (SCM) (10% Fetal Bovine Serum (FBS) 1% Penicillin (P) and Streptomycin (S)), SCM is also known as complete SCM, or Phosphate Buffered Saline (PBS). SPIONs were diluted to the required concentrations in PBS or culture media that replicate those used for cellular experiments that aligned with the large EU-FP7 NanoMile project (280 µg/mL, 112 µg/mL, 56 µg/mL). Solutions were vortexed, and 800 µL of solution was pipetted into a disposable DLS glass cuvette. Diameter was measured using an Standard Operating Procedure (SOP) for iron oxide: Refractive Index (RI) 2.42, absorption 0.5, 37 °C and water stated as a dispersant. Measurements were taken a minimum of three times.

2.1.3 Zeta potential

Surface charge measurements were acquired with a Zetasizer Nano ZS ZEN 3600 (Malvern Instruments Ltd, Malvern, U.K.). SPION solutions (Sienna$^+$, Endomagnetics, Sysmex, UK), were prepared as previously in Section 2.1.1 at the required concentrations (280 µg/mL, 112 µg/mL, 56 µg/mL) diluted in SCM (10% FBS 1%P/S) or PBS prior to measurements. The prepared solution (1 mL) was injected into a disposable folded capillary

cell and the zeta potential was measured using an SOP for iron oxide; RI 2.42; Absorption 0.5; 37 °C with water stated as the dispersant. Cells were first run with a zeta potential transfer standard at -42 mV +/- 4.2 mV in aqueous buffer (pH 9) prior to first use for quality control. Measurements were taken a minimum of 3 times.

2.2 Dissolution studies

Test tube dissolution studies were performed for up to 144 hours in dH_2O and Artificial Lysosomal Fluid (ALF). The full composition of ALF is listed in Appendices B.1.2. At time 0, solutions (200 mL) containing different concentrations of SPIONS (70 - 7000 ppb) SPIONs were aliquotted into glass bottles and incubated at 37°C. At each time point, T=0, 1 hr, 6 hrs, 24 hrs, 48 hrs, 72 hrs, 96 hrs, 120 hrs and 144 hrs different measurements of the properties were acquired. The DLS and Zeta potential were taken as previously described in Section 2.1.2 and 2.1.3 and the pH of solution noted. An additional 10 mL was retained and subject to sample preparation for subsequent ICP-OES elemental analysis as detailed below.

2.2.1 Inductively coupled plasma - optical emission spectrometry

Samples were prepared at each time point (from 24 hrs) during dissolution studies for subsequent elemental analysis with ICP-OES to detect the level of Fe ions present within the sample. At each time point 10 mL of solution was transferred into 3kda Millipore centrifuge tubes (Satorious, UK) and subjected to centrifugal ultrafiltration at 5000 g for 50 minutes. These samples were then acid digested by the addition of (HNO_3 to a concentration of 0.2 %) (5 mL) as detailed below, and stored at 4°C for analysis.

Upon completion of the dissolution study, the samples were analysed with ICP-OES in bulk. Prior to analysis, in order to construct a calibration curve, iron standard solutions

were prepared using a serial dilution of 1000 ppm in 2% nitric acid. The final concentrations used were as follows: 1000 ppb, 500 ppb, 100 ppb, 50 ppb, 25 ppb and 12.5 ppb. Samples were analysed using a Perkin Elmer ICP-OES Optima 8000 platform. Prior to acquisition, the instrument torch was aligned (radially and axially) using the Mn wavelength. Four wavelengths for iron detection (238.204 nm, 239.562 nm, 259.939 nm and 302.107 nm) were assessed for peak intensity. The wavelength with the highest peak intensity, and therefore sensitivity, Fe 259.939 nm, was selected for sample analyses. A delay time of 60 seconds was implemented before each sample infusion and samples were analysed in triplicate; read outs were given as a mean of the three triplicates. Initially the calibration standards were analysed followed by a blank prior to samples. A flow rate of 1 mL/min was implemented with flush time of 10 seconds. In between samples a 30 second wash of 2% nitric acid was applied to eliminate any carry over.

2.3 Cell culture and maintenance

All cell culture techniques were performed under a sterile tissue culture hood (Gelaire BSB 4a laminar flow hood; Gelaire Pty Ltd, Australia or SterilGard, The Baker Company, Sanford, Maine). Cancer cell lines were cultured at 37℃ in a humidified CO_2 incubator (MCO-17AIC; SANYO, Osaka, Japan (UK) or Nuaire NU-5100 E/G Air Jacketed Automatic CO_2 Incubator; Minnesota (USA)) at 5% CO_2. All solutions and equipment were bought sterile or sterilized by autoclave when required.

A549 alveolar cells, HeLa carcinoma cells (PHE), MDA-MB231 breast cancer cells (Purchased from Public Health England Culture Collections (PHECC), London UK) and THP-1 leukemia cells (Health Protection Agency Culture Collections (HPACC),UK) were cultured at 37℃ in 5% (v/v) CO_2 atmosphere in T_{75} culture flasks (Invitrogen, UK) containing Dulbeccos Modified Eagles Medium (DMEM, Lonza) or Roswell Park Memorial Institute (RPMI) 1640 media (Lonza) supplemented with 10% Fetal Bovine Serum (FBS)

(v/v) (BioSera Ltd., Boussens, France) (FBS) and 1% P/S (100 µg/mL, Invitrogen, UK). Adherent cells were grown to confluence and passaged using a standard trypsin-EDTA (0.25%:0.2%) protocol (Invitrogen, UK). Briefly, the trypsin-EDTA protocol consists of removal of the cell culture media by aspiration, washing of the cell monolayer with PBS, removal of PBS and the addition of 1-2 mL trypsin into the container. The culture is then incubated for 2-5 mins at 37℃ in 5% (v/v) CO_2 until cells are rounded and in suspension. The trypsin reaction was halted by the addition of fresh media and cells were diluted as necessary for experiments and maintenance - generally a 1:5 split ratio. Suspension cells were maintained at $2x10^5$ cells/mL and passaged by media splitting.

2.4 THP1 differentiation

Cells, 4 x 10^4 were plated per well of a 24-well glass bottom MatTek plate (MatTek Corp, Maryland, USA) or 24 well plastic dishes containing 13 mm coverslips in complete RPMI containing 200 nM phorbol 12-myristate 13-acetate (PMA) (Sigma-Aldrich, UK) for 72 hours. Following PMA treatment, differentiation of THP-1 cells was enhanced by replacement of PMA containing media with normal SCM without PMA; this is known as the PMA rest phase (PMA^r); and incubated for a further 48 hours in this PMA^r phase [276].

2.5 Transfection

2.5.1 DNA transfection

For cDNA transfection, $1x10^5$ cells were plated in each well of a glass bottom 24-well MatTek plate (MatTek), or 24 well plastic bottom dishes containing 13 mm coverslips, 24 hours prior to transfection to give approximately 70-80% confluence. Per well, one tube containing 0.5 µg cDNA with 50 µL of Opti-MEM media (Thermofisher, UK) solution and

a second tube containing 1.5 µL lipofectamine 2000 (LF2000; Invitrogen) with 50 µL Opti-MEM media were prepared. Following a 5 minute Room Temperature (RT) incubation, the tubes were combined and incubated for a further 15 minutes at RT. The mixture was then added drop-wise to the cells. Cells were then incubated for 3 hours before the media was replaced with fresh SCM. A second round of transfection was carried out 24 hours post initial transfection to increase transfection efficiency. Assays were performed 48 hours post initial transfection.

2.5.2 SiRNA transfection

Prior to siRNA inhibition studies, a test transfection and inhibition experiment was performed using Lipofectamine 2000, lipofectamine RNAiMAX and Dharmafect to determine which reagent offered superior knockdown ability (Appendix Figure B.20). RNAiMAX showed highest transfection efficiency and was therefore used in subsequent experiments. For siRNA transfection 2 x 10^5 cells were plated per well of a 6-well plate 24 hours prior to transfection. Culture media was replaced with Opti-MEM media just prior to transfection treatment. Per well, one tube containing 7.5 µL Lipofectamine RNAiMAX with 150 µL OptiMEM medium and a second tube containing 3.75 µL (or 25 pmol) of siRNA with 150 µL Opti-MEM medium were prepared. Following 5 minutes RT incubation, the tubes were combined and incubated for a further 15 minutes at RT. The mixture was then added drop-wise to the cells. Media was replaced with fresh SCM 24 hours post transfection to maximize efficiency and cell viability. A second round of transfection is often necessary to increase transfection efficiency of stable proteins such as AP2, we ascertained that double transfection led to better knockdown efficiency (Appendix Figure B.19) [277]. 24 hours post transfection cells were detached and re-plated into 24 well plates using a standard trypsin EDTA protocol. A second round of transfection was then carried out 48 hours post initial transfection. Assays were then performed 72 hours post transfection.

2.6 DNA constructs

The Rab5-mRFP construct was a gift from Ari Helenius (Institute of Biochemistry, ETH, Zurich). The Rab11-mRFP construct was a gift from Prof. Thomas Kirchausen (Harvard Medical School, Boston, USA).

2.7 siRNA constructs

A non-silencing control (NSC) siRNA (ON-TARGETplus NON-targeting siRNA; Dharmacon) designed for use with rat, mouse or human cell lines was employed as a negative control. The α-adaptin (AP2 inhibition) siRNA was custom made with target sequence: 5-AAGAGCAUGUGCACGCUGGCCA-3 as used in previous studies [278]. The caveolin-1 siRNA was a SMARTpool of 4 siRNAs (ON-TARGETplus Human Cav1 siRNA; Dharmacon) targeted to caveolin-1. The P21-protein activated kinase (PAK-1) siRNA was custom made with target sequence: 5-UGAAUGUCUAGGCCGUUAU-3. The Wiskott-Aldrich syndrome protein family member-2 (wave2) siRNA was a SMARTpool of 4 siRNAs (ON-TARGETplus Human Wave-2 siRNA; Dharmacon) targeting to wave-2.

2.8 General NP uptake experiment procedure

HeLa, A549, MDA or THP-1 cells were cultured in appropriate dishes (35 mm MatTek dishes; 24-well MatTek cell culture imaging plates; gridded MatTeks for correlative studies) and incubated overnight. Cells were treated with Sienna$^+$ SPIONS prepared as previously described (Section 2.1.1) to final concentrations of 280 µg/mL, 112 µg/mL or 56 µg/mL in SCM (detailed in the relevant experiments) for either 1 hour, 15 mins and 5 minutes (detailed in the relevant experiments). Nanoceria (stock 10 mg/mL) prepared as previously described in Section 2.1.1 were diluted to a final concentration of 500 µg/mL. Following completion of incubation, cells were washed with PBS (x3) and then treated with CellTracker Orange (CTO) diluted 1:1000 using the standard protocol (Invitrogen,

UK) for 30 minutes. CTO passes freely through cell membranes into the cytoplasm, where it is thought that the chloro- groups react with thiols (mediated by Glutathione-S-Transferase (GST)) giving a cell-impermeant fluorescent dye-thioether adduct reaction product, thereby staining the cytoplasm. Although CTO reacts mildly with thiol groups, it is reported by the manufacturer to not effect cell viability or function. However the CTO concentration is kept as low as possible to minimize overloading effects. The effect that CTO has on ROS levels in the cells could be investigated in future experiments. Cells were then washed twice with PBS followed by SCM incubation for 30 min. Cells were washed twice with PBS and then fixed as described in Section 2.9.1.

2.9 Chemical fixation

2.9.1 Fixation for routine cell culture experiments

Following treatment, cells were washed with 3 x PBS, and fixed with a 4% Para-formaldehyde (PFA) (Electron Microscopy Sciences, Hatfield, PA) solution for 15 minutes. Cells were then washed with 3 x PBS. Experiments performed in MatTek dishes were then stored at 4ºC in a refrigerator. Prior to imaging, PBS was replaced with Vectashield (VS) mounting media containing 4',6-Diamidino-2-Phenylindole, Dihydrochloride (DAPI) (Vector Laboratories Ltd, Peterborough, United Kingdom). Coverslips were removed from wells using tweezers and mounted cell side down with VS containing DAPI, with excess mountant removed, Coverslips were held in place with nail varnish. Slides were stored at 4°C in a refrigerator prior to imaging.

2.9.2 Correlative fixation

Fixation for correlative experiments differed to that used for general cell culture fixation; this is discussed further in Section 4.2.6. Immediately following NP exposure and fluores-

cent labeling with CTO, cells were washed with 3 x 0.1 M Cacodylate Buffer (CB) and then subsequently fixed with either 4% PFA alone or 2% Gluteraldeyhyde (GA)/ 4% PFA (EMS, Hatfield, Pennsylvania) in 0.1 M CB for 60 minutes, followed by 0.1 M CB wash (X3). CB was then replaced with VS containing DAPI prior to imaging. Following Light Microscopy (LM) cells were post-fixed with 2% GA / 4% PFA in 0.1 M CB for 60 mins overnight, and subsequently processed for TEM as described in Section 2.14.

2.10 Cell growth assay

HeLa cells were grown in a 24-well plastic cell culture dish for 24 hours in 1 mL of SCM. Cells were then incubated in SCM containing 1% NP solution, made as described in Section 2.1.1, for 60 minutes at 37°C, washed with PBS and counted at T = 0 or re-incubated in SCM for a further 24 hrs or 48 hrs and then counted. For counting, cells were then rinsed twice with 1 mL PBS and incubated in 50 µL trypsin for 5 mins. SCM (500 µL) was added to stop the digestion and 10 µL of the solution was put into a Hawksley counting chamber (AS1000 Improved Neubauer Double Cell Standard; Hawksley, Sussex, UK). Cell number was counted directly after treatment and at 24 and 48 hours post incubation in all adherent cell lines used in subsequent experiments, to indicate the growth rate of the cells over 48 hours.

2.11 SYTOX green viability assay

HeLa cells were cultured on 22 mm coverslips in 6 well plates and incubated overnight. Cells were treated with SCM containing 1% NPs, or SCM alone (treatment media) for 60 mins. Particle solutions were made as previously described in Section 2.1.1. Following the 1 hr treatment, media was replaced with fresh SCM (2 mL) and incubated for a further 24 hrs. All wells were then treated with SYTOX Green (0.01%) (Invitrogen, Grand Island, NY) for 15 minutes prior to fixation, except the positive control groups. Positive controls

were treated with SYTOX green, saponin (0.05%) and FBS (2%) in PBS post-fixation. An NP treated well was also used as a second positive control to test the potential NP interference with saponin and the effect this has on the SYTOX green intensity, post-fix treated as per other positive controls. Sytox green is a membrane impermeant dye. Where membrane damage has occurred, SYTOX can pass freely into the cell, and binds to DNA with high affinity. Sytox binds DNA by intercalating cooperatively with a 3.5 bp binding site [279].

2.12 Endocytosis assays

2.12.1 Pinocytosis control experiments

Endocytosis assays were conducted in HeLa, MDA, A549 and THP-1 cells to confirm the effects of AP2 knockdown, caveolin-1 (Cav1) knockdown, protein-activated-kinase-1 (Pak1) knockdown and Wave2 knockdown. Prior (96 hrs) before the assay, 2 x 10^5 cells were plated per well of a 6-well plastic culture dish and then transfected with siRNA as detailed in Section 2.5.2. A pre-assay incubation with Serum Free Media (SFM) was carried out for 30 mins. After which cells were incubated for a further 30 mins with Transferrin (TF; Alexa Fluor 488 conjugate; Tf-AF488; Invitrogen) at 10 µg/mL in 2 mL SFM, Cholera Toxin Subunit B (CTxB; Alexa fluor 488 conjugate; CTx-AF488; Invitrogen) at 1 µg/mL in 2 mL SFM or FITC-Dextran 500,000 kda at 1 mg/mL (Invitrogen, UK). After incubation cells were washed twice with SFM followed by a PBS wash. Cells were fixed with PFA as detailed in Section 2.9.

2.12.2 Phagocytosis control experiments

THP-1 macrophages were first differentiated as previously described in Section 2.4, then pre-incubated with SFM for 30 minutes. Phagocytosis was inhibited in THP-1 derived macrophages using Cytochalasin-D (CytD) at a concentration of 10 µg/mL for 30 mins.

Cells were then treated with 1.2 µm fluorescent polystyrene NP (stock concentration 10 mg/mL; Sigma-Aldrich, UK) at a concentration of 100 µg/mL in SCM for 30 mins and then washed with SFM (X2) and PBS (X2) then fixed as detailed in Section 2.9.

2.12.3 Route of NP uptake experiments

Endocytosis assays were conducted to assess the route of NP uptake in A549, HeLa, MDA and THP-1 cells. Inhibition was as follows: AP2 siRNA for the inhibition of CME, Cav1 siRNA for inhibition of caveolae mediated endocytosis and Pak1/Wave2 siRNA for the inhibition of macropinocytosis; all used at a concentration of 25 pmol. Following the 72 hrs siRNA transfection treatment performed as described in Section 2.5.2, cells were treated for 1 hour with 280 µg/mL SPIONs prepared as previously described in Section 2.1.1, followed by a further 30 min incubation with CTO. Cells were then washed with PBS (X3) and fixed as previously described in Section 2.9 and stored at 4°C for imaging. Cyt-D was used to assess the contribution of phagocytosis for NP uptake in THP-1 derived macrophages. Cyt-D was used as previously described in Section 2.12.2, following this THP-1 derived macrophages were treated with 280 µg/mL SPIONs followed by 30 min CTO incubation. Cells were then washed with PBS (X3) and fixed as detailed in Section 2.9.

2.13 NP trafficking experiments

Cells ($1x10^5$) were plated into 24-well MatTek, or 24-well plastic cell culture dishes containing 13 mm coverslips and incubated overnight. Cells were then either transfected with cDNA for Rab5a, Rab7 or Rab11a as described in Section 2.5.1 or left untransfected for treatment with Lysotracker DND-99 (Invitrogen, UK). Following 48 hr transfection, cells were treated with NPs diluted in SCM, made as previously described in Section 2.1.1, for one hour. For the lysosomal colocalization studies, 15 minutes before the end of the incubation cells were treated with Lysotracker to stain acidic lysosomal compartments.

Following treatment cells were washed with PBS (X3) and fixed as described in Section 2.9.

2.14 TEM processing

TEM processing was performed after LM for correlative experiments. The protocol of which is discussed in more detail in Section 4.2.5 and Appendix B.1.4. The brief protocol for TEM processing was performed as follows.

Following the post LM imaging fixation with 2.5% gluteraldehyde / 2% paraformaldehyde (EMS, Hatfield, Pennsylvania) in 0.1 M CB then washed with 0.1 M CB buffer (X3). Cells were then stained with 2% Osmium Tetroxide (OsO_4; EMS, Hatfield, Pennsylvania) for 1 hr followed with 3 x dH2O washes. Cells were then fixed with Uranyl Acetate (UA) for 1 hr, followed by washing with dH_2O (X3). Cells were then dehydrated with a series of ethanol washes (each X2) (50%, 60%, 70%, 80%, 90% and 100%) before infiltration with 50:50 % absolute alcohol:EmBed 812 for 1 hr. EmBed 812 was made up as per the standard protocol for hard resin (EMS, Hatfield, Pennsylvania). Two subsequent infiltrations were performed for 45 min each with EmBed 812 alone, before inverting and mounting the MatTek dishes on resin-filled embedding BEEM capsules (EMS, Hatfield, Pennsylvania) with care taken to remove all bubbles from within the capsule. Samples were then baked overnight at 60°C in an oven (Thelco Laboratory Apparatus by Precision Scientific Co., India). Coverslips were separated from BEEM capsules by plunging into liquid nitrogen, and samples were then allowed to re-equilibrate with room temperature. The area of interest (0.5 mm^2) was visualized, marked, trimmed and isolated with a sharp single edge razor blade (EMS, Hatfield, Pennsylvania) under a light microscope (Leica UltraCut UCT, Leica Microsystems Inc., IL, USA). Following trimming, 70 nm or 150 nm serial sections were cut using a Diatome diamond knife (EMS, Hatfield, Pennsylvania). Sections were then collected onto 200 mesh copper (Cu) grids or slotted grids (EMS, Hatfield,

Pennsylvania) that had been pre-treated with alcohol. Samples were then stored for staining. Grids containing sections were stained by inverting on top of small blobs of 2% UA for 10 mins (EMS, Hatfield, Pennsylvania) inside petri dishes; grids were then washed with dH_2O and air dried before repeating this step with Reynolds lead citrate. Calcium Carbonate ($CaCO_3$) crystals were used to remove moisture from the air within the chamber/petri dish). Grids were washed with dH_2O and air dried before storing for TEM imaging.

2.15 Polyacrylamide gel electrophoresis and western blotting

Western blotting was used to quantify relative protein levels following specific treatments;knockdown following siRNA transfection and identification of proteins present in the protein corona following isolation from SCM. All solutions and reagents used for western blotting are listed in the appendices. Following the specific treatment described where necessary, cells were lysed in 1% Triton X-100 (Sigma, UK) in PBS containing protease inhibitor cocktail (Roche, UK). Laemlli buffer (3X) was added in a 2:1 ratio to the lysate. Western blots were performed using the Mini-Protean Tetra Electrophoresis System (Bio-Rad). All acrylamide gel details, running, transfer and Tris-Buffered Saline with Tween (TBST) buffer recipes are as listed in Appendices Section B.1.3. Briefly proteins were separated by Sodium Dodecyl Sulfate (SDS) Polyacrylamide Gel Electrophoresis (PAGE) on a 12.5% acrylamide resolving gel with a 4% acrylamide stacking gel at 100 mV.

2.15.1 Protein corona isolation

Following protein separation with PAGE, coomassie and silver stain were employed to identification of protein corona constituents. Gels were first washed with dH_20. Gels were then stained coomassie brilliant blue R-250 (Thermo Fisher Scientific) at RT for one hour as per manufacturers protocol. Gels were then de-stained overnight at RT to visualize

bands, again as per standard manufacturers protocol. Following coomassie staining, silver staining was performed using Proteosilver Staining Kit (Sigma-Aldrich, UK) as per the manufacturers protocol to identify proteins of low concentration (sensitivity 0.1 ng/mm^2). Briefly, gels are washed with ethanol, sensitized with silver stain sensitizer, washed with dH_2O, then developed with developer solution. The reaction is stopped when bands become visible.

2.15.2 Western blotting to assess protein knockdown

Following electrophoresis separation, gels for western blotting were transferred onto Immobilon FL membrane at 350 mA. The membrane was then blocked in 5% milk solution for 1 hr at RT and subsequently probed with the relevant primary antibody in 5% milk over night at 4°C. The next day the membranes were washed and probed with the relevant secondary antibody for 2 hours at RT. Primary antibodies used were polyclonal anti-AP2 (Santa Cruz Biotechnology), polyclonal rabbit anti-Cav1 (Abcam), polyclonal anti-Pak1 (Abcam), polyclonal anti-Wave2 (Santa Cruz Biotechnology) and monoclonal mouse anti-Tubulin (Tub) (Sigma). Secondary antibodies used were goat anti-rabbit IRDye 800 and goat anti-mouse IRDye 680 (Li-Cor) for use with an Odyssey detection system. Quantification of knockdowns was done relative to Tub and Non-Silencing Control (NSC) using ImageJ/FIJI software.

2.16 Microscopy

Microscopy images were acquired at two facilities, The Birmingham Advanced Light Microscopy (BALM) facility at the University of Birmingham, UK, and The Centre for Advanced Microscopy (CAM) and Nikon Imaging Centre (NIC) at Northwestern University, Feinberg School of Medicine in Chicago, IL, USA.

The instruments and objectives used are listed:

BALM: Nikon A1R inverted confocal microscope (Nikon Corp, Japan), 10X 0.3 NA, 40X 1.3 NA, 60X 1.4 NA, 100X 1.4 NA.

CAM/NIC: Nikon A1R inverted confocal microscope (Nikon Corp, Japan), 10X 0.3 NA, 40X 1.3 NA, 60X 1.4 NA, 100X 1.4 NA 100X 1.49 NA. Nikon N-SIM (Nikon Corp, Japan) 100X 1.49 NA. FEI Tecnai G2 Spirit at 80 KeV (FEI, USA)

The general imaging procedures are described below, the detailed acquisition instrumentation, parameters and settings are described in detail in the relevant sections in Chapter 4, 5 and 6.

2.16.1 Confocal Microscopy

Cells immersed in Vectashield or PBS were imaged using a Nikon A1R inverted confocal microscope (Nikon Corp, Japan). To set up the reflectance optical configuration in NIS Elements, the first dichroic mirror was set to B520/80 to facilitate light transmission and reflectance, the fourth channel was set up for reflectance imaging using the 488 nm laser, and all channel light paths were set to through. The CTO stain was excited using the 561 nm laser, DAPI nuclear stain was excited using the 405 nm laser. Red fluorescent protein (RFP) and lysosomal stain were also excited using the 561 nm laser. CellTrace FarRed (CTR) was excited using the 636 nm laser.

2.16.1.1 Structured Illumination Microscopy

Cells mounted on slides or immersed in PBS or Vectashield in MatTek dishes were imaged using reflectance Structured Illumination Microscopy (R-SIM) (Nikon Corp., Japan) with an EM-CCD camera iXon3 DU-897E (Andor Technology Ltd.). For correlative studies reflectance SIM followed RCM imaging in the developed workflow (supplementary methods). To facilitate reflectance SIM image acquisition a half mirror (50% transmitted /

50% reflected) filter cube was placed into the light path. The 488 nm or 405 nm laser was used to illuminate the sample using 2D-SIM imaging. The 561 nm laser was used to excite cytoplasmic CTO stain in wide-field mode. The 561 nm laser was also used to excite RFP and lysosomal stain in 3D-SIM acquisitions.

2.16.1.2 Transmission Electron Microscopy

TEM was employed in the characterization of SPIONs (Sienna$^+$ or Sigma Aldrich). SPIONs (8 µL) were dropped onto 200 mesh Formvar film copper grids (Agar Scientific, UK). Following blotting, grids were left to dry for 24 hours prior to imaging with TEM. TEM images were recorded on a LaB 6 filament JEOL1200 TEM operating at an accelerating voltage of 80 keV at a 50,000X magnification. Images were recorded by a Gatan wide-angle CCD camera.

Correlative TEM imaging was carried out on an FEI Tecnai G2 Spirit operating at 80 keV (FEI, Center for Advanced Microscopy, Northwestern University, Chicago, IL). Images were taking with a Gatan imaging camera. 200 mesh Formvar coated copper TEM grids were loaded into the TEM and cells of interest, that were previously imaged during RCM and R-SIM experiments, were located on low (690X) magnification, and then imaged at higher magnification (up to 49,000X) to visualize individual and clusters of NPs.

2.17 Image processing and analysis

Image processing and analysis was conducted with FIJI (ImageJ) or MATLAB 2011b or 2016a. For all cell experiments, cells were segmented manually or automatically using either platform as detailed in the relevant experiments and described and validated in Chapter 4. Results were calculated as an average over the specified number of cells. For NP uptake experiments, NP regions were also segmented (MATLAB). This is detailed and discussed further in Chapter 4, Section 4.2.9.

2.17.1 Uptake Assays

2.17.1.1 NP uptake and endocytosis assays

Images were acquired using Nikon A1R (BALM, UK) with a 40X objective and employing optical zoom. For all uptake experiments, cell segmentation was achieved using MATLAB 2016a, using the workflow described in Section 4.2.9. All NP segmentation was achieved using the workflow described in Section 4.2.9. Quantification of various parameters was performed using MATLAB on a per-cell basis. Automated quantification was validated against manual methods as shown in Section 4.2.9.

2.17.1.2 Endocytosis control assays

Images were acquired using BALM Nikon A1R (BALM, UK) with a 60X objective and employing optical zoom. For all fluorescence uptake experiments, cell segmentation was achieved using ImageJ manual delineation of each cell region. Total mean fluorescence intensity was measured. In the case of FITC-dextran control experiments, a background subtraction was performed prior to quantification.

2.17.2 Colocalization analysis

2.17.2.1 Colocalization with fluorescent markers

Images were acquired using BALM Nikon A1R with a 60X objective with Nyquist sampling. Colocalization between fluorescently labeled cellular compartments and NP reflectance signal was assessed using manual and automated methods in FIJI and MATLAB. Maximum intensity Z-projections of 3 adjacent planes (totaling 600 nm) were created using ImageJ or MATLAB. Prior to colocalization analysis, image misalignment was characterized using reference images taken with beads that are both fluorescent and reflectant, as described in more detail in Chapter 6. Transformation was then applied to the images using MATLAB "imtranslate" function to facilitate alignment. In the manual analysis,

cell segmentation was achieved using manual delineation in FIJI. Fluorescent signal was isolated using smoothing, background subtraction and wavelet transform spot detection (courtesy of Dr. William Pitkeathly) in FIJI. NP signal was isolated by smoothing, background subtraction and thresholding in FIJI. The Coloc2 plugin can then give different parameters of colocalization between the processed images. Number of segmented regions were ascertained by counting. In the automated MATLAB analysis, cells were segmented using cellular autofluorescence. The image was first denoised by smoothing with a Gaussian filter kernal, and setting all pixel values above the mean equal to the mean. K-means was then used to segment intracellular and extracellular regions, followed by a watershed segmentation (described in finer detail in Section 6.2.2). Fluorescent endosome signal was segmented by convolution with a Gaussian kernal, and background subtraction that involved morphological image dilation and subtraction of the resultant dilated image from the original. This was followed by segmentation using the image mean intensity (described in detail in Section 6.2.2)) [280]. Reflectance signal was detected using methods described in detail in Section 4.2.9. The following parameters were then calculated to determine the most representative measure of colocalization: Pearsons correlation coefficient and Manders signal overlap coefficients, The M1 and M2 coefficients. This is described in more detail in Chapter 6, Section 5.

2.17.2.2 Colocalization and comparisons between RCM and R-SIM

Correlation existing between RCM and R-SIM images of the same cells were performed using MATLAB. Maximum intensity Z-projections were created with MATLAB from Z-stack multi-plane acquisitions from both systems. Cell segmentation was achieved using Gaussian smoothing followed by K-means clustering (nClusters=2) of CTO stain. NP segmentation was achieved as described using smoothing, background subtraction and K-means clustering as detailed in Section 4.2.9. Comparisons were then made between matching cells, in terms of the number of spots detected and the resolution (in terms of the FWHM), the information was then visualized graphically using MATLAB.

The resultant segmented binary images created from SIM and RCM NP segmentations were analyzed The binary image gave the total number of connected components; using the "bwconncomp" function in each image. The images were then multiplied together and the number of connected components that appear in both images was computed, and subsequently the percentage of the total detected (number in multiplied image divided by number in the initial binary image) that correlate was calculated.

2.17.3 Line intensity profiles: Colocalization and FWHM

Line intensity profiles to determine colocalization between signal, in reflectance modalities, and between reflectance and fluorescence signals, were created using ImageJ/FIJI. The FWHM of different modalities (RCM and R-SIM) was also measured using the same line plotting tool in ImageJ/FIJI. A line was drawn on images (single or overlaid; FWHM and colocalization experiments respectively), and the intensity originating from both channels was plotted.

2.17.4 Image registration

2.17.4.1 Image registration of RCM and R-SIM images

For the reflectance image co-alignment (R-SIM and RCM maximum intensity Z-projections), between 3 and 6 points pairs were selected on corresponding images. Following user selection of points, MATLAB calculates the transformation matrix that best aligns the pairs, using rigid registration. Alternatively, MATLAB has a built in function called imregister. This can be initialized using the multimodal configuration setup. imregister can automate the alignment of RCM and R-SIM images using an intensity based method. However, in order to be successful, images must first be smoothed and background subtracted, to negate the contribution of background reflectance to the intensity registration. Overlays were created using MATLAB, however pseudocolour was created in ImageJ.

2.17.4.2 Image registration of adjacent TEM sections

TEM image scales were equalized using the 'imscale' function and subsequent co alignment of adjacent TEM slices was achieved using the intensity based registration function 'imregister'. The parameters were initialized with 'multi-modal' configuration, and iteration was increased to facilitate alignment. Transformation was a rigid alignment to prevent deformation.

2.17.4.3 Image registration of reflectance and TEM images

Co-alignment of TEM and reflectance images was performed in MATLAB. Co-alignment was achieved using the "cpselect" function with between 3 and 10 matching points. The transformation matrix was then calculated that re-aligns the selected points. This could then be applied as an affine transformation, to cope with cell shrinkage. The Coherent Point Drift (CPD) algorithm was explored for the fully automated realignment of matching slices based on nuclear segmentation from light and electron microscopy.

2.17.5 Statistical analysis

Statistical analysis was done wherever possible. In each case the significance levels were: ***=p=<0.001; **=p=<0.01; *=p=<0.05. Statistical methods implemented throughout the thesis are students T-Tests unless otherwise stated in the relevant sections and figures.

CHAPTER 3

NANOPARTICLE CHARACTERIZATION

Parts of this chapters are published as part of a multi-author mini-review paper (Guggenheim *et al.* Int. J. Biochem. Cell Biol. 83. pg 65-70.).

3.1 Chapter summary and introduction

A large number of studies investigate the biological impacts of NP exposure, however important physicochemical characterizations are often not considered [281]. This can significantly reduce the impact of these studies and undermine conclusions. It is well established that the physico-chemical properties of NPs in solution, including the surface area, surface functionalisations, charge, size, size distribution and agglomeration state may lead to different cellular interactions and effects *in vitro* and *in vivo* as discussed in Section 1.2.1 [282, 283]. It is also established that preparations are rarely homogeneous suspensions of mono-disperse NPs. As previously discussed in Section 1.2.1, upon exposure to biological media, proteins interact and bind to the NPs surface leading to alterations of the surface properties and therefore the biological 'identity' and effects of these NPs [284]. This effect is partly driven by the physicochemical properties of the NPs themselves and partly driven by the environment and composition of the exposure medium [116, 119]. Therefore, during exposure, it is highly unlikely that the NPs will encounter the cell in its native, or synthesized form. It is critically important that the

characterization of these NPs encompasses both the intrinsic properties of the NPs itself (including size, composition, coatings at synthesis) and the extrinsic properties that are acquired following exposure to biological media containing serum proteins (protein adsorption, increases in diameter) in order to relate specific observations back to particular properties.

The aim of this chapter was therefore to characterize the physical properties of Sienna$^+$ SPIONs, used in subsequent studies within this thesis. Characterizations were performed in PBS and protein containing cell culture media. v, were first developed for use as an MRI contrast agent, but the current clinical use is as a tracer for the magnetic detection of Sentinel Lymph Nodes (SLN) in SLN-biopsy procedures. SLN biopsy is a procedure used to determine if cancer has spread beyond a primary tumor into the lymphatic system [285]. Sienna$^+$ consist of an iron oxide core containing magnetite (Fe_3O_4) and maghemite (γ-Fe_2O_3), coated in carboxydextran. The iron and carboxydextran exists in a 1:1 ratio. The carboxydextran aids biocompatibility and is designed to prevent and reduce agglomeration of the NPs, which can occur naturally on bare un-coated NPs due to attractive forces (mainly van de Waals) between NPs [286, 20]. The coating increases the stability of the NPs preparation. It is critically important that NPs for applications in biomedicine, such as these SPIONs, are stable against agglomeration both in biological fluid and, for magnetic particles, within a magnetic field [131]. Although it is not specifically stated, Sienna$^+$ resemble Ferucarbotran (Resovist TM) based upon characterizations of both SPIONs displayed in the literature [287]. Characterizations that were carried out within this chapter include visualization of the metal-oxide core using TEM (JEOL 1200), quantification of NP diameter, the hydrodynamic size / diameter (HDS), surface charge and dispersity of preparations measured using the Zetasizer ZS Nano (Malvern Instruments). These characterizations were done in the presence of 10% serum, or in PBS, over a 2 hour time course. The proteins directly attached to the SPION's surface following exposure to protein containing media were isolated using standard protocols, and then identified using

MS [288, 289]. Further characterizations in intracellular mimic fluid (Artificial Lysosomal Fluid (ALF)) media were also conducted as part of a dissolution study; presented in Section 6.

3.2 Results and discussion

3.2.1 NP core size

TEM was used to examine the Sienna$^+$ stock solution. TEM is thought of as the gold standard for NP visualization and characterization, as individual NP can be resolved and their shape, core size and agglomeration state determined [290]. TEM requires that samples are imaged under vacuum on a metallic grid. Sienna$^+$ in aqueous solution (280 µg/mL) were dropped onto Formvar coated copper mesh grids, left to dry and then imaged using a JEOL 1200 TEM as detailed in the methods section (Figure 3.1A). Another SPION from Sigma-Aldrich was also imaged in the same manner as a standard, non specialized SPION for comparison (Figure 3.1B). Sienna$^+$ SPIONs appeared to have a diameter of around 4 nm (Figure 3.1).

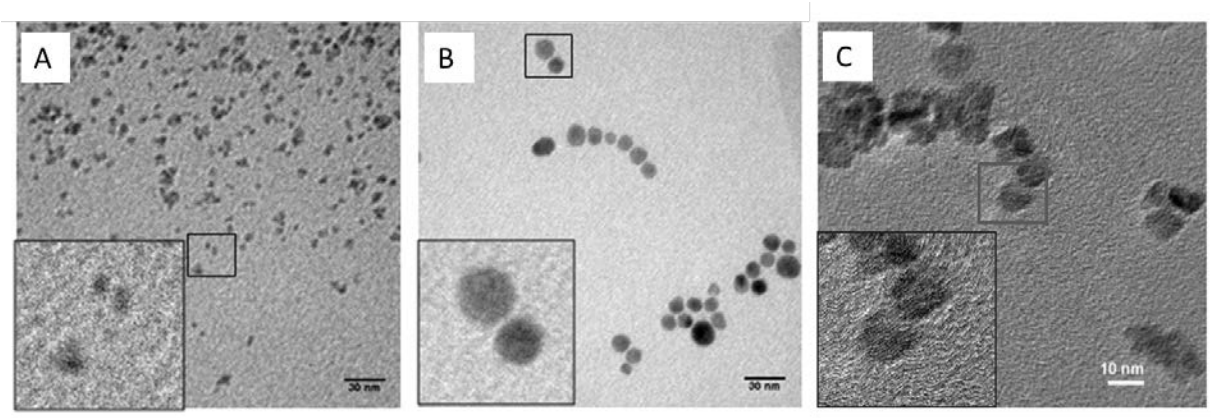

Figure 3.1: TEM of Sienna+ and Sigma SPIONs and nanoceria dropped onto grids. NP suspensions were dropped onto TEM grids and imaged at high resolution. A) Carboxyl-coated Sienna$^+$ SPIONs in saline solution, B) Dextran coated SPIONs (Sigma-Aldrich) in dH2O and C) Uncoated nanoceria in dH2O [275]. Inserts show an enlarged region from the main image.

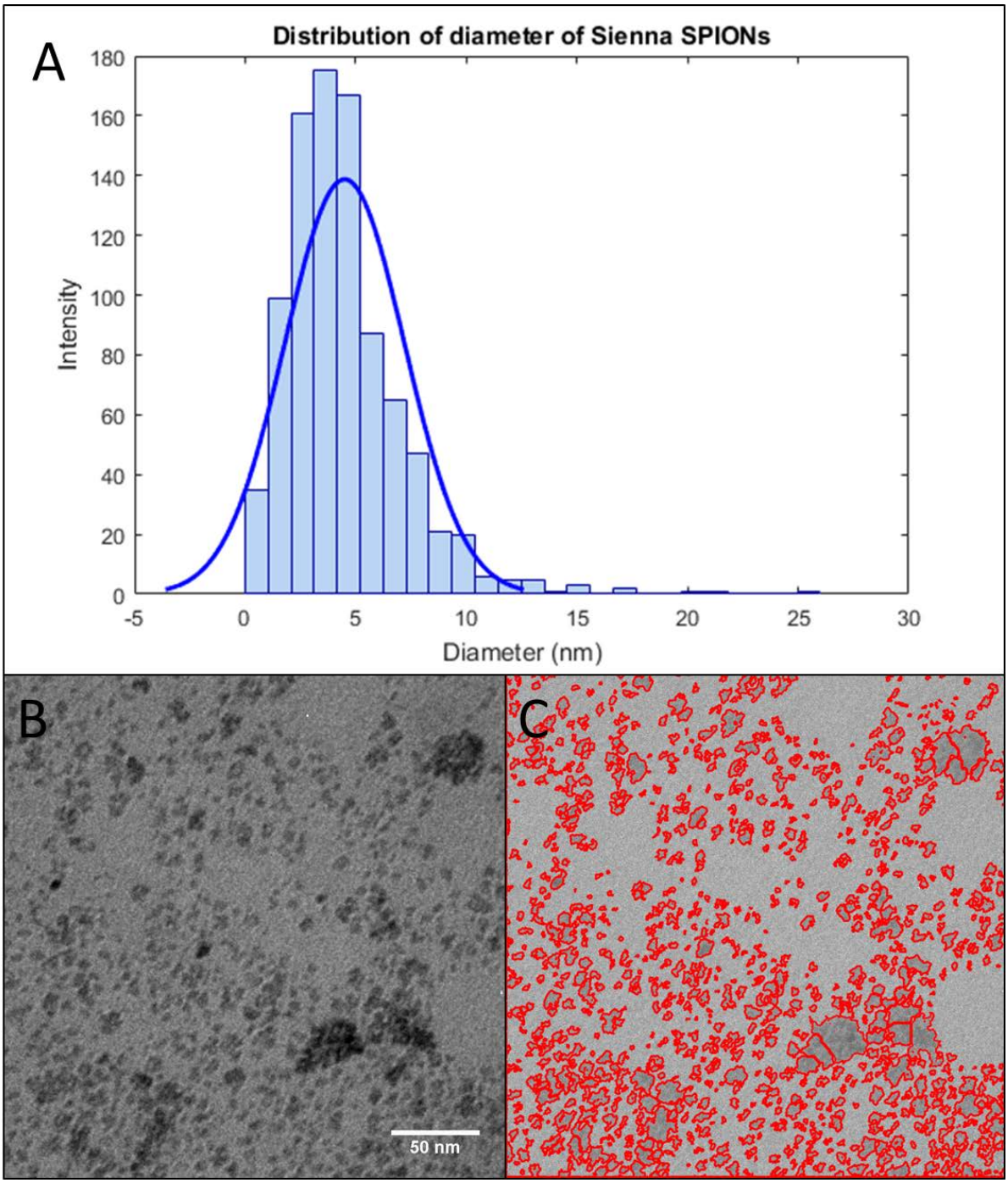

Figure 3.2: Distribution of the Sienna$^+$ core diameter measured from TEM. MATLAB was used to segment TEM images, the area of each connected component was then calculated. Each area was converted from pixels to nm, and the histogram of 902 detected NPs is displayed on the distribution histogram. A mean of 4.49 nm +/- 2.7 is determined, and a median of 4.06 nm.

Their morphology strongly resembled that of Resovist, which has been previously determined to have a core of 4.2 nm (Supplementary Figure B1) [291, 287]. An estimation of the core size diameter in nm was determined by automated detection of NP from the TEM image and plotted as a distribution histogram (Figure 3.2A). This was done using MATLAB. Briefly, image filtering was performed (filter size 4; sigma 2), and objects were detected using thresholding. The boundaries of the regions detected in the original image, Figure 3.2B, are shown in red in Figure 3.2C. Once the objects were detected, the area of each object was computed as a pixel area, and then be converted into a diameter (in nm) by using πr^2 and pixel size. This calculation was based on the assumption that NP cores are circular, which is not the case, however it gives an approximation.

The mean of the 902 detected regions or NP cores was 4.49 nm +/- 2.69; the median value is 4.06 nm. This is very close to the stated core size of 4.2 nm. However, slight variations may well be caused by the spherical assumption of the detected regions. The core size is important as it, in part, dictates the magnetic properties of SPIONs; NP with core sizes below 15 nm will exhibit super-paramagnetism, previously discussed in Section 1.1.3). Sienna$^+$ and Resovist look to be slightly agglomerated in some areas (Figure 3.1A, 3.2B) and Supplementary Figure B1). This was evidenced in the distribution plot in Figure 3.2, where a small percentage of NP agglomerates are observed with a diameter of >10 nm, the maximum diameter observed it 25.99 nm. In comparison, the Sigma-Aldrich SPIONs in aqueous solution have a spherical core of 10 nm stated by the manufacturer. The actual measured diameter was averaged at 8.2 measured by detection software courtesy of previous PSIBS student Lyndsey Van Gameren. Cerium NP, previously synthesized and described by Chen *et al* are also shown (Figure 3.1C), as they were used in subsequent experiments as a positive control due to their ability to efficiently reflect light in microscopy experiments [275]. Subsequent characterizations presented in this chapter were performed only on Sienna$^+$ SPIONs, as these are the main focus of this work.

3.2.2 Measuring NP hydrodynamic size using Zetasizer ZS Nano

The size distribution, dispersity and surface charge of SPION suspensions was determined using the Zetasizer ZS Nano, which has DLS and zeta potential capabilities, to guide experimental conditions for subsequent investigations. DLS is often employed for assessing NP size distributions. The z-average size or z-average mean peak intensity represents the cumulative mean and provides the most stable parameter produced by this technique, providing only one peak is present in the sample [292]. However if one or more peaks are present, the largest peak (peak-1) gives a more representative measure. DLS detects the light scattered by dispersed particles undergoing Brownian motion over time. The random changes in the intensity of the scattered light is used to determine the diffusion coefficient of the NPs in solution. The diffusion coefficient depends upon the size of the NPs, the viscosity of the solution and temperature. The Stokes-Einstein equation links the diffusion coefficient to NP diameter and applies for non-interacting spherically shaped particles. For this reason the reported value is an estimation based upon an equivalent sphere. Therefore, DLS cannot always provide absolute values for NP diameters [293]. The ZS Nano instrument also provides a measure of the breadth of the size distribution within the colloidal solution, termed the Polydispersity Index (PDI) [293]. This PDI gives an indication on the range of sizes present within the solution. A low PDI is indicative of a mono-dispersed solution. A high PDI indicates a large size distribution or polydispersed sample. If sample sizes are non-uniform it is likely that the NPs will elicit a range of confounding effects. Size is known to play a role in the cellular effects of NP [294]. Larger agglomerates can elicit a less toxic response *in vitro*, partly due to reduced cellular uptake [294].

3.2.3 Method of SPION dilution

When NPs are dispersed in an aqueous solution over time they have a tendency to form interactions with their surroundings. This can lead to agglomeration into larger structures

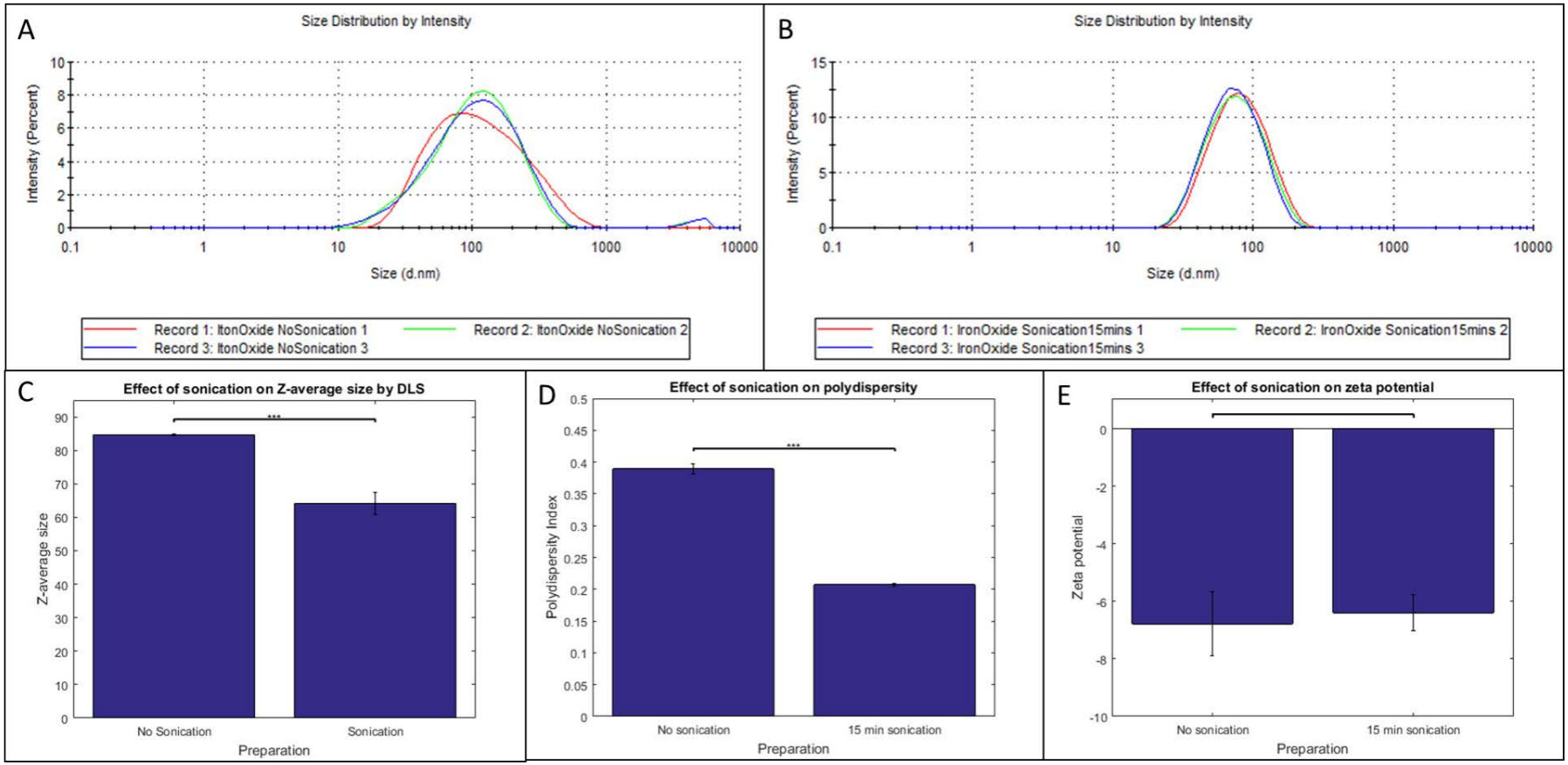

Figure 3.3: Size, Zeta and PDI of Sienna$^+$ NP preparations (280 µg/mL) with and without 15 minutes sonication prior to dilution in SCM Sonication of NP preparations for 15 minutes leads to a significant decrease in NP diameter and PDI. A slight but insignificant decrease in zeta potential is also observed.

which will exhibit different characteristics and biological effects to their smaller counterparts [295]. Although these agglomeration interactions are relatively weak and reversible, Brownian motion does not have sufficient energy to separate them. Sonication is therefore often employed to disperse these agglomerates as it provides enough energy to break the van der Waals forces between NPs [296]. Before characterizations for subsequent experimental conditions were performed, the effects of performing a sonication prior to SPION dilution were assessed using DLS measurements. Aqueous SPION suspensions were either subjected to a 15 minute sonication immediately prior to dilution in biological 10% SCM, or the SPIONs were diluted directly to the SCM, to the final concentration of 280 µg/mL, followed by vortexing. The size, surface charge and dispersity of both preparations was then assessed to determine the best protocol for SPION dilution in future experiments and characterizations. The size distribution by intensity curves indicate that sonication increases the reproducibility between measurements, as qualitatively there seems to be less variation between replicates (Figure 3.3A and 3.3B). The peak-1 average diameter was significantly larger in the non-sonicated preparation, with an average diameter of 133.7 nm +/- 9.9 nm compared to the sonicated solution with an average of 78.6 nm +/- 4.3 (p= 0.0012), (Figure 3.3C). The standard deviation is also higher in the non-sonicated sample (Figure 3.3A, Figure 3.3B and Figure 3.3C). The z-average significantly decreased from an average of 84.6 +/- 0.2021 nm in the non-sonicated solution to 64 nm +/- 3.22 in the sonicated solution (p<0.001). The peak-1 diameter is more representative in this case due to the appearance of a larger peak in the non-sonicated preparation, most likely arising due to NP agglomerates. The PDI decreased significantly from an average of 0.389 +/- 0.0076 to an average of 0.207 +/- 0.002 (p <0.001), (Figure 3.3D). There was a slight but insignificant change in zeta potential, the non-sonicated solution had a surface charge of -6.8 +/- 1.12 mV compared to the sonicated solution which was -6.4 mV +/- 0.6 mV (Figure 3.3E). The surface charge greatly depends on the DLS measurement, so this may lead to alterations in the measured potential. Nevertheless, these results clearly indicate that sonication leads to alterations of the physical properties of NPs in solution, including

a reduction in the polydispersity and a reduction in the peak-1 and z-average diameter of NP in the preparation. It is necessary to ensure that the solution is as uniform as possible to maximize the accuracy of nanoscale investigations. Therefore sample sonication should be implemented prior to dilution in the relevant media for NP exposure and cellular uptake experiments (shown in Section 5 and 6). A similar conclusion was reached for the preparation of other NP suspensions for biological experiments [296]. However, sonication can have negative effects on NP suspensions. These negative effects can include heat induced agglomeration, therefore the effects of sonication should always be quantified prior to conducting NP exposure experiments.

3.2.4 Characterization in PBS and biological media

Aqueous Sienna$^+$ SPIONs (280 µg/mL) were diluted in PBS and DMEM-SCM to different final concentrations: 56 µg/mL, 112 µg/mL, 280 µg/mL and 520 µg/mL. Subsequent measurements were taken for the size, surface charge and dispersity of the different suspensions. Resovist has previously been reported to have an average hydrodynamic size of 59-62 nm in aqueous solution [297]. According to the manufacturer, the average size of Sienna$^+$ SPIONs is 60 nm, this appears to be in agreement with our results obtained in PBS solution; where no proteins were present to bind to the NP (Figure 3.4A). Only one peak was obtained in the DLS data, therefore the z-average provided a stable measurement. A z-average diameter of 57 +/- 0.4 nm was observed when the NP solution in PBS was measured at the lowest concentration tested (56 µg/mL). This average size remained roughly the same (up to 59 +/- 0.4 nm) until a concentration of 280 µg/mL. Above this concentration, the z-average diameter appeared to increase significantly (p<0.001) (Figure 3.4B). The peak-1 intensity also remained stable between 56 µg/mL (70.16 nm +/- 0.25 nm) and 280 µg/mL (74.16 nm +/- 3.9), however above this concentration the measured diameter increased significantly (p<0.001). The PDI was consistent (0.18 +/- 0.005 to 0.22 +/- 0.006) increasing insignificantly as concentration increased up to 280 µg/mL. The PDI then increased significantly (P<0.001) when the concentration increased

above 280 µg/mL indicating an increase in the polydispersity of the solution (Figure 3.4C).

Despite NPs displaying certain size characteristics at synthesis, following exposure to fluids of different compositions, NP size, HDS, and other properties may be altered due to agglomeration or protein corona formation. This can alter cellular responses. Therefore it is important to monitor NPs physicochemical changes due to this protein adsorption to facilitate accurate predictions of the subsequent 'biological' properties the NPs will have. If the HDS of the NPs were to change following immersion in biological media, then the results would be irrelevant to the characterizations performed in water or PBS. DLS was therefore employed to determine the HDS of the NPs in solution following protein adsorption in SCM (DMEM + 10% FCS) at different concentrations. DLS data for the suspension media alone, shown in Figure 3.4D, gives rise to two peaks at ∼10 nm and ∼70 nm of similar magnitude, which likely correspond to protein and lipid aggregates from the serum. The results presented demonstrate that upon exposure to biological SCM the HDS of the NPs increased (Figures 3.4A and B). This indicates protein adsorption to the surface of the NPs. This is in agreement with other studies that have demonstrated an increase in the HDS of NP when exposed to biological media [298, 125]. Previously dextran coated SPIONs, after exposure to serum proteins, increased in measured diameter from 82 nm to 111 nm [298, 125]. The PDI of the NP preparation also increased (Figure 3.4C). This may be expected, as protein adsorption to the NP surface can lead to changes in the HDS. This protein adsorption may or may not be homogeneous [125]. If it is not homogeneous then the PDI measurement will be expected to increase as there is a larger range of sizes as proteins begin to adsorb. The measured z-average diameter of the SPION solution at a concentration of 56 µg/mL was 63.85 nm +/- 1.63 nm and the measured peak-1 diameter was 89.14 nm +/- 4.7 nm. Increasing the concentration of SPIONs led to a slight increase in the measured diameter, seen as a shift of peak-1 to the right in the DLS graph in Figure 3.4C. This coincided with an increased peak intensity and contribution to the total signal. There was also a relative decrease in the

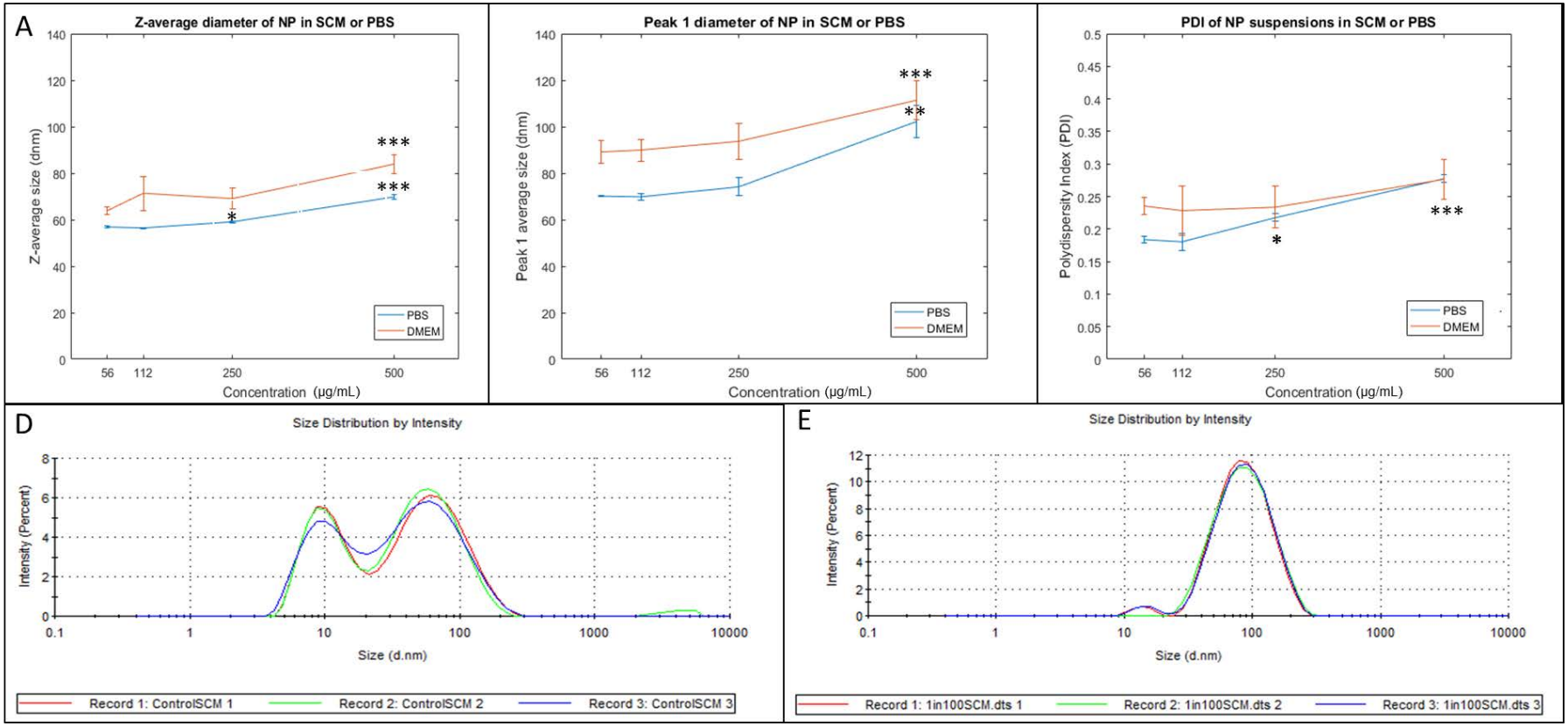

Figure 3.4: DLS characterization of Sienna $^{+}$ SPION suspensions diluted to different concentrations in PBS and SCM. A) z-average size of different concentrations of Sienna $^{+}$ SPION suspensions diluted in PBS and SCM; as concentration increased the measured diameter increased. B) Peak-1 diameter (given as two peaks present in some samples) of Sienna $^{+}$ SPIONs diluted in SCM and PBS; as concentration increased the measured diameter increased. C) PDI of different concentrations of Sienna $^{+}$ SPION suspensions diluted in PBS and SCM; as concentration increased the measured PDI increased. D) Overlay of the DLS peak measurements of 3 repeats for SCM alone and E) Overlay of the DLS peak measurements of 3 repeats of 280 µg/mL Sienna $^{+}$ SPIONs diluted in SCM.

observed 10 nm peak intensity indicating a decrease in the contribution of free protein in the media. Although the assumption is made here that the decrease in the 10 nm peak is due to protein binding, if larger particles are forming due to protein binding and / or agglomeration, relatively smaller peaks, such as the 10 nm peak, could become masked due to the nature of the sizing measurement technique by DLS. Similarly to the PBS-NP characterizations, above 280 µg/mL the z-average diameter of the DMEM-SCM NP preparation increased significantly to 83.92 nm +/- 4 nm and the peak-1 diameter increased to 111.4 nm +/- 8 nm. This peak is where >95% of the intensity arises and an HDS above 100 nm is observed. Although it seems likely that protein adsorption is responsible, at least in part, to the increase in size observed, there are other properties that can lead to size increases such as agglomeration, discussed further in the next section. Size is one of the vital properties that determine the success of NPs for cellular internalization within biomedical applications, be it MRI contrast enhancement or therapeutic targeting, for this reason 280 µg / mL was determined as the maximum permitted concentration for subsequent experiments. A summary table is included of SPIONs diluted in PBS, two types of SCM (DMEM-SCM; RPMI-SCM) at this maximum concentration (280 ppb; 280 µg / mL).

Solution	DLS	Zeta	PDI	pH
PBS	58.8 +/-3.9	-11+/-4.4	0.204 +/- 0.04	7.4 +/- 0.04
DMEM-SCM	65.05 +/- 5.0	-8+/-0.77	0.222 +/- 0.004	8.4 +/- 0.035
RPMI-SCM	65.7 +/- 3.6	-8+/-0.59	0.236 +/- 0.03	8.3 +/- 0.12

Table 3.1: Summary of characterization of Sienna $^{+}$ SPION suspensions at T=0 in PBS and SCM and ALF. Summary of characterizations of Sienna $^{+}$ SPIONs in different types of media. All suspensions are concentration of 280 ppb / 280 µg / mL at T = 0).

3.2.5 Characterization in biological media over time

Properties of NP suspensions can also change over time. Therefore NP suspensions diluted to the established maximum concentration of 280 µg/mL, were measured using the

Zetasizer ZS Nano. These were measured over a 2 hour exposure time-course at 60 minute intervals (T=0, 60 and 120 mins) to determine time courses to be used in later experiments (i.e. Chapter 5). The SPIONs properties were characterized in both DMEM + 10% FCS (DMEM-SCM) and RPMI + 10% FCS (RPMI-SCM). This is because different cell lines require different growth media. Both types of SCM, RPMI and DMEM were used in subsequent experiments. The FCS used to make the SCM was consistent between the two different media, however the differing composition of amino acids and nutrients in the media may lead to slightly different observations. Figure 3.5 shows the results in RPMI-SCM and DMEM-SCM. The HDS does not increase significantly during the 2-hour exposure in both types of media tested. In DMEM-SCM the z-average diameter was initially measured as 65 nm +/- 5 nm, and increased to 74.3 nm +/- 7.2 nm. In RPMI-SCM the z-average diameter was initially measured as 65.8 nm +/- 3.6 nm and increased to 69.1 nm +/- 2.4 nm. These changes in the Z-average size were not calculated to be significant using MATLAB ANOVA1 function followed by multiple comparisons using the MULTCOMPARE function. This change in diameter is unlikely to be a result of NP agglomeration or interaction between the SPIONs in solution as the increase is marginal (between 5 and 10 nm). This is supported by the PDI measurements which do not change significantly in either DMEM-SCM or RPMI-SCM, over the 2 hour time course. Therefore the slight increase in HDS may represent changes in the protein layer surrounding the NPs. Changes in the surface-adsorbed proteins can occur due to the previously mentioned 'Vroman Effect' whereby higher affinity proteins replace those that adsorbed initially but with a lower affinity. The result of this is constant dynamic changes occurring between proteins and the NP surface [112]. Proteins may also undergo conformational changes over time following adsorption which can contribute to the observed changes in the SPIONs diameter. This alteration in protein conformation has been suggested for NPs of various core and 'at synthesis' size [299, 300]. These physicochemical alterations can lead to modulation of biological effects, such as mechanism of cellular uptake and sub-cellular processing of the NPs [**?**, 5, 301].

The pH did not alter significantly over the time course. This is important as pH can alter the charge of the NPs if it drops below or increases above the isoelectric point due to acidic or basic side groups present on the surface coatings (e.g. COOH). Even so, it is important to monitor the surface charge of SPIONs in the solution over time, as this can influence the cellular interactions. Zeta potential provides a measure of the magnitude of surface charge or attraction between NPs in solution. It describes the electric potential of the NP's surface at the slipping plane (interface between the solution and diffuse surface later) as discussed previously in 1.2.1 [121]. It can be used to determine the colloidal stability of the NP preparations and provide insight into potential interactions that occur following NP exposure [302, 303]. Differing charges can lead to different cellular interactions following cellular NP exposure [302, 303]. For example, cationic (positively charged) NPs have been seen to internalize more efficiently then anionic (negatively charged) particles, but distribute poorly through tumors; mathematical modeling also supports this theory [158, 303, 120]. Negatively charged SPIONs appear to show a less efficient rate of uptake when compared to cationic NPs, as in the case of 2,3-Dimercaptosuccinnic Acid (DMSA) coated SPIONs [303]. Interestingly, the internalization rate of negatively charged SPIONs increased when co-incubated with positively charged SPIONs [158]. However, it has been suggested that in most biological scenarios that the protein corona will consist of a net negative charge [113].

The observed zeta potential underwent different changes upon dilution in the different SCM medias over the time period measured. SPIONs diluted in DMEM-SCM led to an observed zeta potential of -8 mV +/- 0.15 mV initially, decreasing to -9 mV +/- 0.7 over the two hour period. SPIONs diluted in RPMI-SCM gave rise to a similar initial charge of -8.2 mV +/- 0.65 mV, however the potential did not change significantly over the 2 hour time course. The zeta potential of the solution, regardless of conditions was not large enough to indicate electrostatic stabilization (observed at >+30mV or <-30 mV).

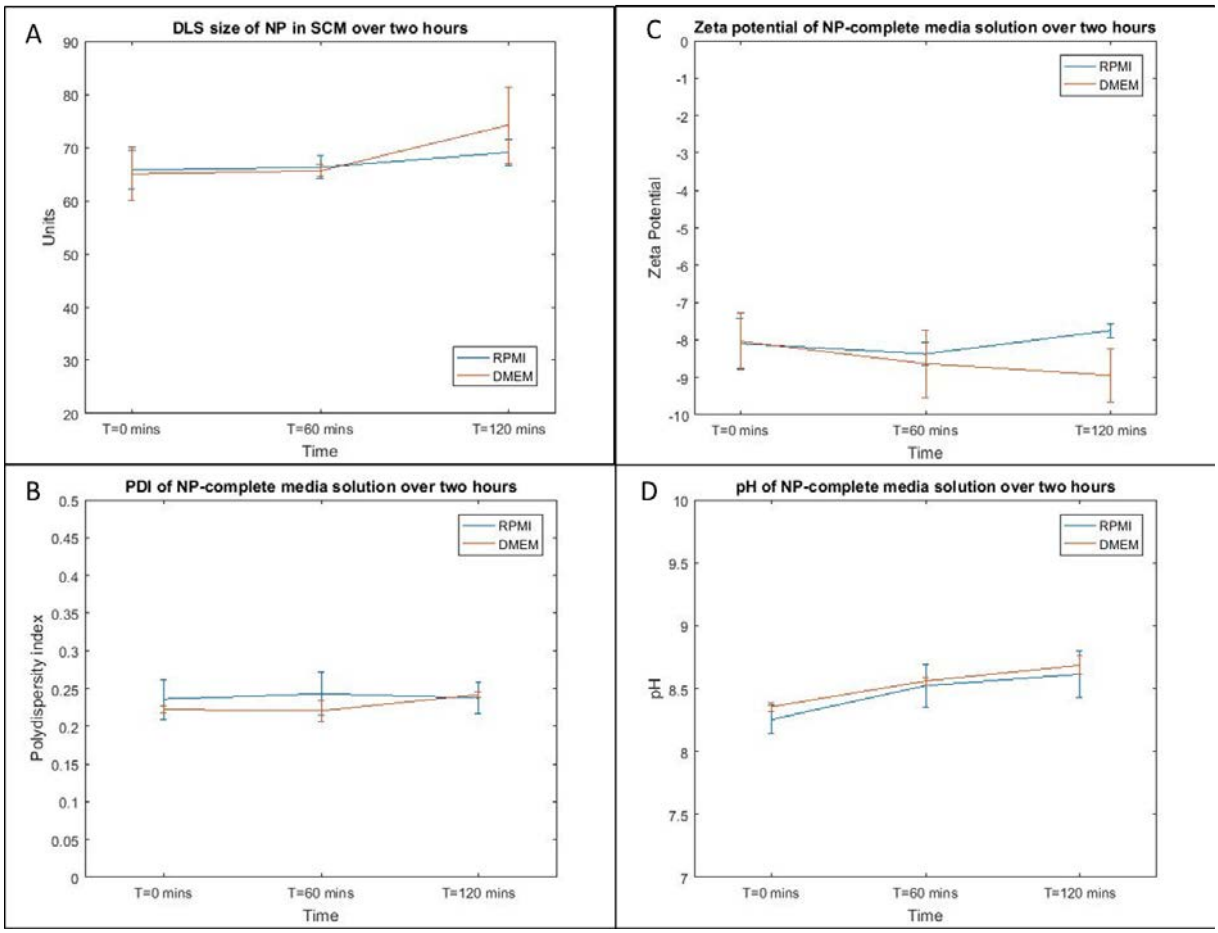

Figure 3.5: Comparison of size, surface charge, pH and PDI of 280 µg/mL Sienna$^+$ SPION solution over a 2 hour incubation time in different media (SCM-DMEM and SCM-RPMI). A) The diameter increases by 5-10 nm over the two hours, presumably due to protein binding. The zeta decreases slightly in SCM-DMEM and remains the same in SCM-RPMI. The PDI (C) and pH (D) do not alter significantly in either media during the two hour time course.

The determined zeta potential is similar to those reported for other SPIONS (silica and dextran coated) in other studies (-11.24 mV +/- 0.86 mV and -9.79 mV +/- 0.4 mV respectively) [125]. Given that the Sienna$^+$ SPIONs are coated in carboxydextran, it is likely that steric effects are the main initial stabilising forces within these NP suspensions, a conclusion also made by Sonvico *et al* based upon the observed stability of dextran-coated SPIONs in solution [304]. As previously stated it is important that NPs for use within biomedicine are stable against agglomeration both in biological fluid and, for magnetic particles, within a magnetic field [131]. These results indicate that, due to the steric stabilization by dextran, these NP preparations can avoid agglomeration at these exposure conditions and times. It has been reported that coating with hydrophilic, biocompatible surface coatings such as dextran facilitates the evasion of opsonization and therefore clearance by macrophages allowing increased circulation and increased potential for cellular uptake [305, 91, 306, 307]. This is promising for the application of NPs to the delivery of drugs as it may facilitate their escape of the RES, improving circulation time of these NPs and therefore increasing the potential for accumulation at a target site [304]. One potential issue arises due to the suggestion that dextran is not very firmly attached at the SPIONs surface and therefore prone to detachment. This could potentially facilitate agglomeration of the iron cores and similar toxicities associated with uncoated SPIONs [305]. The results presented indicate that the Sienna$^+$ SPION suspensions are stable at the concentration of 280 µg/mL for the duration of 2 hour time course. However zeta potential measurements rely on the accuracy of DLS measurements, and therefore in some cases where the preparation is polydispersed, the measurement of surface potential may not be accurate thus limiting the technique.

3.2.6 Characterization of protein corona constituents

The aforementioned properties of NPs are postulated to modulate aspects of the protein corona that is formed following immersion in biological media [119, 116]. This biological corona, as previously discussed in section 1.2.1 can lead to different subsequent cellular

interactions, dependant upon composition. Protocols such as magnetic separation can be used with NPs, such as SPIONs [117]. Sakulkhu *et al* used this technique to compare the isolated coronas of SPIONs with different surface coatings and charge. Composition and quantity of proteins isolated from the coronas is strongly dependant on size, charge and coating material [117]. Unfortunately, the corona of the Sienna$^+$ SPIONs could not be isolated through magnetic separation This may be a result of the small Sienna$^+$ SPION core size. Although magnetic separation of small, 4 and 12 nm, SPIONs has been documented, the actual separation of very small SPIONs is debated [308, 309]. Brownian forces have been shown to be far stronger than the force exerted by a magnet, which prevents magnetic separation of SPIONs <50 nm in diameter [309]. Therefore standard centrifugation was used to separate the SPIONs and subsequently isolated the corona using centrifugal seperation [289]. The protocol involved the sequential washing and centrifugation of pelleted SPIONs to remove unbound proteins. However, the protocol was modified so as not to include the sucrose cushion, as this led to the isolation of proteins in the absence of NP. The proteins present in the supernatant following each wash were visualized by PAGE (Figure 3.6). The number of washes necessary to remove visible unbound proteins was found to be 4 (Figure 3.6).

SPIONs were incubated with DMEM-SCM, with or without previous exposure to cells in a step known as media 'conditioning' (C-SCM)), SFM or in PBS (Figure 3.6 and 3.7). Proteins isolated from the NP surface were visualized and separated using PAGE (Figure 3.7). Following separation no protein bands would be expected in PBS columns, regardless of the inclusion of NPs in the solution. Although there does appear two faint bands in these lanes (50-70 kda) (seen in Figure 3.6), this is likely the result of keratin contamination of the sample buffer / running buffer, or from contaminants in the reducing agent, 2-mercaptoethanol. Both are common reasons for this band artifact between 55 kDa and 65 kDa [310, 311, 312]. Replacement of 2-mercaptoethanol with DTT has been suggested to alleviate some artifact problems when using silver stain. Aside from this apparent band, there appears to be no other detected protein in the PBS samples as expected. In

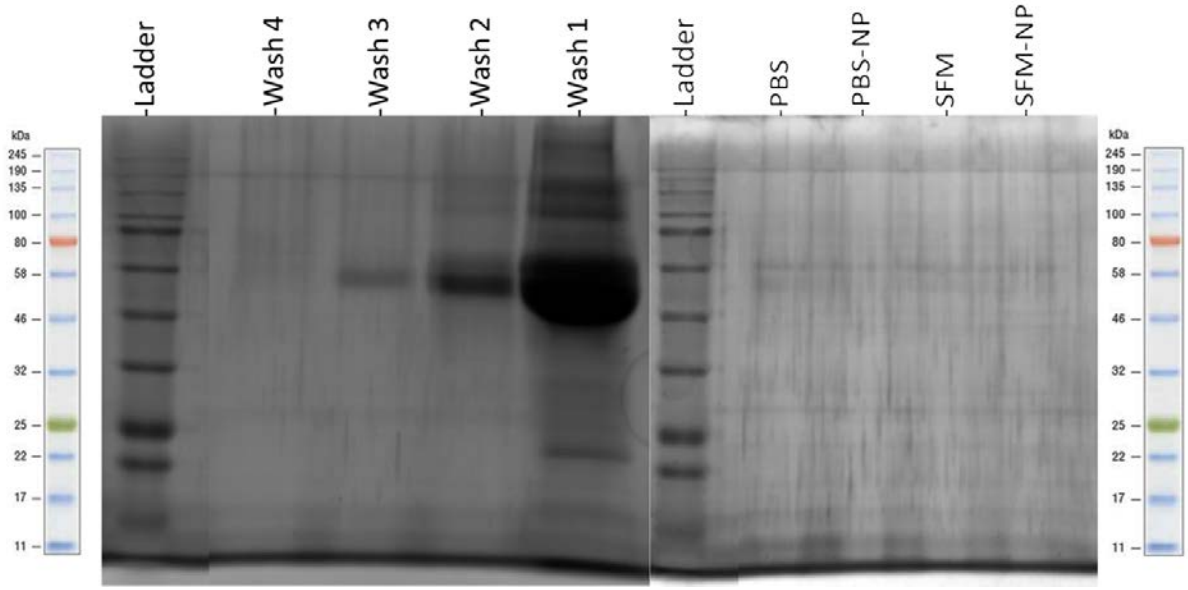

Figure 3.6: Silver staining of PAGE gels to detect the presence of protein in the hard corona isolation protocol. The lanes marked 'wash' correspond to the supernatant taken during the PBS washing phase of the corona isolation. After the first wash (Wash 1), maybe proteins are recovered, indicating that the first wash removed a significant portion of unbound protein within the solution. Subsequent washes (2,3 and 4) show less protein recovery, and therefore indicated that the washing steps are successful in removing a large amount of the unbound protein. After four washes, protein present in the supernatant appears undetectable. The gel on the right shows control samples whereby NP were incubated in PBS and the 'corona' isolated to indicate the lack of proteins binding when no proteins are present. However, in these samples, some bands are present, these may in fact belong to components of the SDS buffer, or keratin contamination (58 kDa) from human skin.

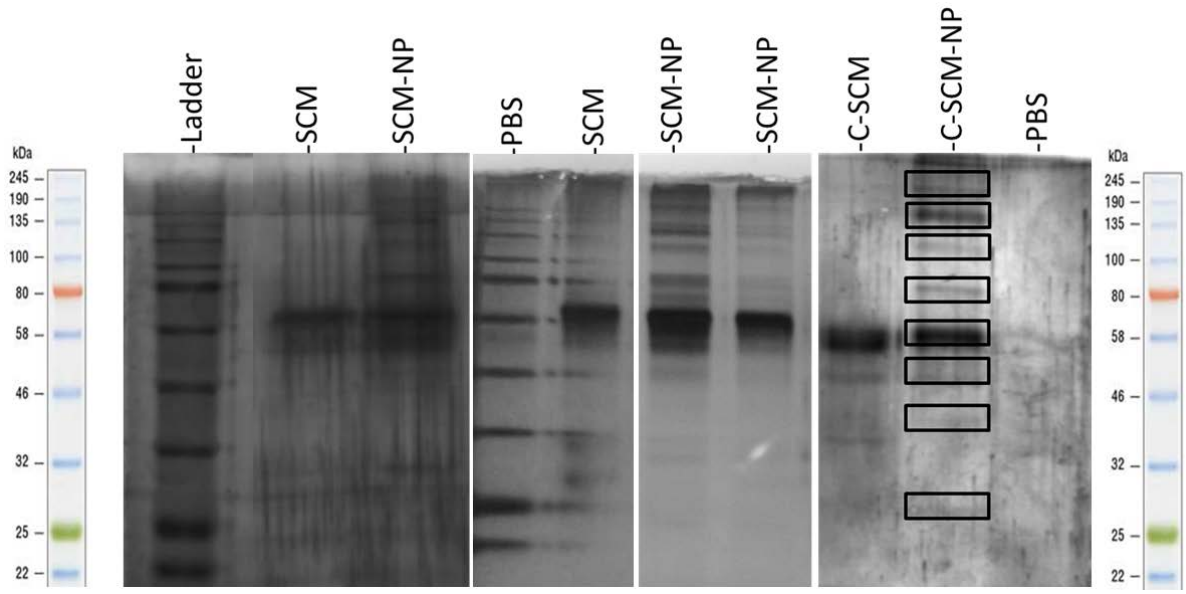

Figure 3.7: Silver staining to detect proteins present following corona isolation under different conditions. Silver staining highlights proteins present in each solution following isolation procedure. Proteins visualized in SCM and C-SCM appear consistent between repeats. Unfortunately on occasion the ladder runs through into the nearby lanes and confounds results. The bands in the C-SCM-NP lane show the bands sent for MS-analysis from this group.

DMEM-SCM and C-SCM alone, a band is observed just above the 58 kDa marker protein. This likely indicates a small portion of albumin was being pelleted during the isolation procedure, as no NPs were present in this condition. This highlights that the method needs more optimization to ensure that no proteins are mis-identified as being part of the NP corona. A variety of other MW proteins appear to be separated in the NP containing lanes, mostly in the upper end of the marker size range (>58 kDa). However after multiple repeats, the proteins isolated and separated with PAGE in the SPION containing lanes were fairly consistent across samples, therefore proteins were quantified MS. All visible bands in one sample (C-SCM + NPs) were quantified, and then a portion of corresponding bands from other samples. The other two groups analyzed were coronas isolated 24 hours post cell-treatment and SCM + NPs). The percent of proteins identified in each sample (Figure 3.8A) and the percent of proteins that overlap between different groups (Figure 3.8B and C) are presented. A large proportion of proteins identified in the coronas of SCM-NP group were also identified in the coronas from the C-SCM-NP group and the coronas isolated from treated cells. The identified proteins that are found across the differ-

ent groups in at least two MS-analysed samples are presented (Figure 3.8D) (Figure 3.8). The full list of identified proteins from each group is listed (Appendix Tables B.2 and B.3).

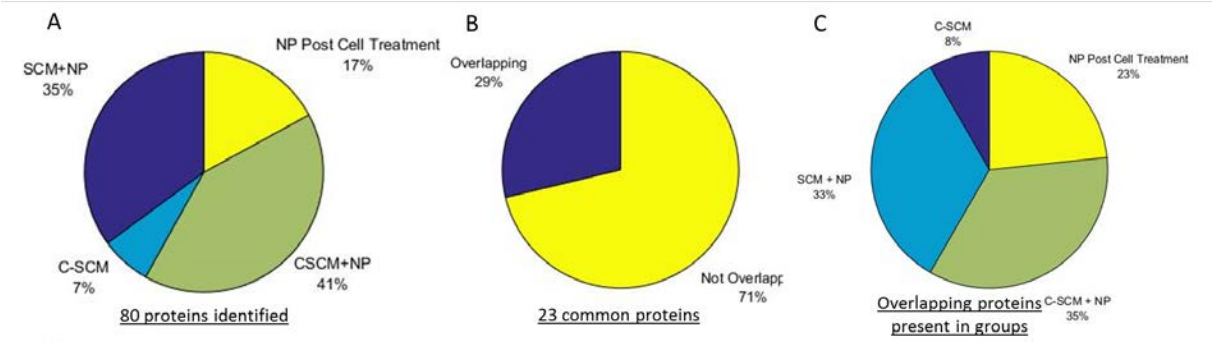

D

C.SCM	SCM + NP	C.SCM+NP	Treated from cells
Alpha-2-HS-glycoprotein Serum Albumin	Alpha 2HS Glycoprotein Serum Albumin	Alpha 2HS Glycoprotein Serum Albumin	Alpha 2HS Glycoprotein Serum Albumin
Serotransferrin	Serotransferrin Beta Casein Alpha S1 casein Keratin (I and II) Lyzozyme C Alpha S2 ceasin Lactotransferrin Kappa Casein Actin Trypsin	Serotransferrin Beta Casein Alpha S1 casein Keratin (I and II) Lyzozyme C Alpha S2 ceasin Lactotransferrin Kappa Casein Actin Trypsin	Beta Casein Alpha S1 casein Keratin (I and II) Lyzozyme C Alpha S2 ceasin Lactotransferrin Kappa Casein Actin Trypsin
		Elongation Factor 1 GTPase IMAP family member Beta-Lactoglobulin	Elongation Factor 1 GTPase IMAP family member Beta-Lactoglobulin
Fetuin-B Hemoglobin Subunit Alpha	Fetuin-B Hemoglobin Subunit Alpha		
	Gelsolin Fibronectin Alpha-1 Antiproteinase Factor XIIa Inhibitor Beta-Lactoglobulin Plasma Serine Protease Inhibitor	Gelsolin Fibronectin Alpha-1 Antiproteinase Factor XIIa Inhibitor Beta-Lactoglobulin Plasma Serine Protease Inhibitor	

Figure 3.8: Identification of proteins isolated in the coronas of SPIONs incubated under different conditions (SCM, C-SCM, and recovered from cells). The number of proteins found in each group is shown in a pie chart (A), 23 of these identified proteins were found in more than one sample (B) and the percentage of the proteins that overlap with other groups is shown in pie chart (C). D) Shows the identified common proteins, and where the overlap between groups exists.

Previously, MS has been combined with bioinformatics to identify the corona composition of dextran and silica coated SPIONs of roughly equivalent size [125]. Dextran and silica coated SPIONs were found to have different corona compositions indicating that

surface coating is a determinant of corona identity [125]. This is further supported by another study where modulation of the size and coatings of polystyrene NP's were found to modify protein adsorption patterns [116]. Two particular proteins were identified in all samples analyzed; alpha-2HS glycoprotein (fetuin a) and serum albumin (Figure 3.8), that have previously been reported present in the corona of a variety of NPs [313, 138]. Serum albumin and fetuin a are known to enter cells via caveolae mediated endocytosis and micropinocytosis respectively, and their presence in the NP corona could be investigated as a means of cellular entry for these NPs [138]. Serum albumin may be present due to insufficient washing identified in the PAGE silver stain (Figure 3.7) and it has been suggested some charged and neutral SPIONs need up to 8 washing steps, which could be incorporated into an optimized washing protocol [117]. However, Sakulkhu *et al* found that a subset of proteins present in high abundance in the exposure media, including serum albumin and transferrin, were present in the corona of all SPIONs they tested (Dextran and PVA coated, positive, neutral and negative charged) [117]. Indeed multiple NPs have been found to contain serum albumin in their corona following serum exposure [116, 117, 314, 113, 313]. Under high ionic strength washing solution, serum albumin was the only protein still isolated in all the SPIONs tested [117]. This indicates that serum albumin may also be found in the corona of these dextran coated, Sienna$^+$ SPIONs; however those used in the study by Sakulkhu *et al* are smaller than the Sienna$^+$. Serotransferrin was also found in each sample, except for that isolated post cellular uptake, indicating that this protein may be lost during the uptake process, or following internalization. Serotransferrin has also been found in the protein corona of multiple different NPs including cerium dioxide, SPIONs, polystyrene and silver NPs [138, 117, 313]. Serotransferrin is internalized via CME and may provide a mechanism of entry in specific cell types which should be investigated further. Previously it has been shown that the binding of transferrin and serum albumin to SPIONs leads to changes in the protein conformation. In the case of transferrin this was found to be an irreversible change from a compact, to an open structure, thought to be related to the release of iron from the transferrin [315, 316].

Changes in the secondary and tertiary structures of serum albumin were also observed following binding to gold NPs. The effect that this has on these proteins, and others, in relation to their function should be investigated [316].

Functionally diverse proteins are found in the NP corona, including proteins from complement activation, coagulation, lipoproteins and many others. Future studies that identify which proteins are bound at the hard corona, and which are dynamic and loosely bound in the soft corona will aid the interpretation of uptake and effect data. Attempts have been made to classify the various proteins that are found in NP coronas, and to determine their singular contribution to the fate of the NPs in a protein fingerprinting methodology [317]. Certain proteins that were previously classified as promoters of cellular association by using computational modeling were found only in the corona of NPs exposed to C-SCM in these studies, such as inter-alpha trypsin inhibitor heavy chain 1 [317]. Although the studies in this chapter give an indication of proteins that are present in the isolated corona in this particular media, it is necessary to perform corona assessment studies with other types of biological media, such as human in the presence of human serum, for different lengths of time to determine the dynamics of protein corona evolution over time. NP surface coating and functional chemistry have been suggested as influential in determining the protein adsorption patterns of NPs [125, 314, 113, 317]. Charged particles appear to form more protein associations than neutral NPs, presumably due to electrostatic interactions. Smaller NPs have also been found to adsorb a higher density of proteins due to increased surface curvature and therefore less steric hinderence [317]. However protein density has not been found to enhance the capacity of NPs to associate with cells [317]. It seems likely that this is conferred more so by the identities and abundance of key receptor-binding proteins present in the corona [317]. Elucidating the links between different NPs, surface properties and protein adsorption will be instrumental in predicting the corona formation and constituents of different NPs *in silico*, whether this is in terms of the protein identities, or the protein functionality [125]. This in turn can

then be used to model the subsequent cellular interactions and effects before *in vitro* and *in vivo* studies are performed. Understanding the interplay between these factors in different conditions in a corona fingerprinting strategy will help to predict critical proteins that shape certain cellular interactions. This type of framework has been established for a library of functionalised gold NPs and has been shown to more accurately predict the cellular association of these gold NPs when compared to using other physicochemical characteristics combined [317]. However, this same determined model did not work when applied to NPs with a different core composition [317]. Different NP core materials, despite having the same surface ligands, are suggested to lead to substantial differences in the fingerprint of the protein corona. The core properties will modulate the arrangement, conformation, density and other properties of the attached surface ligands, which therefore can confer different protein binding fingerprints, implying tailored models would be required. Clearly the interplay between physicochemical characteristics and corona formation is very complex. Therefore it would be beneficial to use NP libraries to modify single parameters, such as same core different coating, or same coating different core, to determine the relative contributions of each physical property to overall corona formation. Ideally creating libraries and models of different properties, protein binding and effects will allow better predictions of clinical outcomes and aid the rational design of future NPs for specific applications.

Protein corona studies require several rounds of identification from multiple samples, therefore more repetitions would be beneficial to determine proteins that are consistently isolated with a high level of certainty to determine the NPs protein corona constituents. Furthermore, the proteins that are detected likely depends on the degree and success of the corona isolation and separation (and which part of the corona is intended to be isolated: i.e. hard or soft corona). The soft corona is particularly challenging as it is lost during most purification processes [318, 289]. There are a variety of methods that can be used to isolate the proteins within the hard corona, including that used within

this thesis. Other methods include equilibrium dialysis, size-exclusion chromatography and microfiltration, however each different method has its own advantages and limitations [319]. It is likely that variations will be detected using different methods and therefore it would be interesting to investigate these thoroughly by comparing the identified proteins using these different isolation procedures.

3.3 Conclusion

The characterization of NPs before and throughout experimental procedures is critical in nanoscience, as the properties of NPs are dynamic and constantly evolving dependant upon their surrounding environment. Factors that can effect the properties of NPs include concentration, the exposure time, and composition of the exposure media. Indeed it has been suggested that NP studies do not provide reliable conclusions regarding the 'biological NP' if adequate characterizations are not performed in the correct exposure conditions [320]. Therefore NPs must be characterized fully both in their synthesized form and in the media in which they will be exposed to (cells for e.g.). Critical parameters of Sienna$^+$ NP suspensions that were assessed include the size, surface charge (zeta potential) and dispersity of the solution over the maximum exposure duration to determine experimental parameters for future investigations. This included the the effect of sonication during the preparation of suspensions. Immersion in biological SCM led to the adsorption of proteins to the NPs surface, and sonication prior to dilution in this SCM was shown to lead to more uniform NP suspensions with more consistent properties. The NP's diameter was seen to increase upon exposure to SCM (DMEM and RPMI), the expected result given the current understanding of NP-protein adsorption. Above 280 µg/mL the properties of the NP preparation begin to alter significantly in terms of the z-average size, largest peak size and PDI. A similar conclusion that was true for exposure times approaching 2 hours. These results indicate that these NP preparations are likely to be stable at the highest concentration of 280 µg/mL and for one hour incubations. These provide the conditions

employed in subsequent chapters in the exposure experiments. The corona constituents were also identified, to indicate potential points of interaction in future cell studies as further investigated in Chapter 5. It would be interesting to identify and quantify proteins present at different stages of cellular uptake, and over different time courses in biological media, and relate this back to the observed properties of NPs.

3.4 Key findings

1. Sienna SPIONs have a core diameter of 4.5 nm as measured from TEM images, and a HDS of 60 nm, however this increases upon protein adsorption in complete media containing proteins.

2. Above 280 µg/mL SPIONs start to increase in diameter and polydispersity. Therefore subsequent experiments will not employ NP concentrations higher than this.

3. Sonication decreases the z-average size and PDI of the sample significantly, therefore NP stock suspensions will be sonicated before every experiment for 15 minutes prior to dispersion in SCM.

4. Over the time course of the experiments the properties measured (size, pH, PDI, Zeta potential) appear to be stable.

5. Corona constituents are different in conditioned and unconditioned media. More experiments are necessary to determine relationships between physicochemical properties, adsorbed proteins, and cellular effects.

CHAPTER 4

DEVELOPMENT OF LABEL FREE MICROSCOPY METHODS AND ANALYSIS ROUTINES FOR THE DETECTION AND QUANTIFICATION OF INTRACELLULAR NP

Parts of this chapters have been published in a multi-author paper (Guggenheim *et al.* PLoS One. 2016.11(10)).

4.1 Chapter introduction and summary

Detection and quantification of intracellular NPs is a challenge associated with investigations into the toxicity and efficacy of NPs, such as those with biomedical applications. No single method is, as of yet, capable of delivering adequate spatial and temporal resolution of intracellular NPs with satisfactory throughput to combat the challenges associated with increasing NP use. As discussed in section 1.3.6, TEM is often considered the gold standard for NP visualization due to the ultrahigh resolution it can offer. However TEM imaging is restricted to ultra-thin, fixed samples that must be imaged under high vacuum [321, 181]. Fluorescent tagging in conjunction with fluorescence microscopy is also regularly employed. Fluorophore conjugation, however, is difficult and often alters the NP's surface properties [223, 222]. Fluorophores have also been seen to dissociate following uptake and photobleaching limits lifetime studies [224]. The method of NP visualization

should, where possible, not alter the surface properties and potential interactions that occur between the NPs and their surroundings.

Reflectance imaging methods, such as RCM, that offer label-free visualization are available in several different illumination and light collection techniques that have been developed and discussed over the years [322]. Despite this, reflectance imaging is often underutilized when compared to its fluorescent counterpart. This leads to a lack of discussion in the literature regarding sample preparation and image acquisition. Therefore within this chapter the sample preparation protocols and image acquisition routines used have been carefully optimized and discussed. Current reflectance methods are generally restricted to diffraction limited investigations. Increases in the spatial resolution of available techniques is necessary within nanoscience, due to the small size of the NPs in question. Therefore within this chapter the collection of reflected light on a commercially available superresolution instrument, the Nikon N-SIM platform, has been demonstrated. The methods were validated and compared in terms of resolution and detection, for application to Sienna$^+$ investigations.

Investigative research using these tools can still be limited by a lack of analytical power to quantify NP uptake with sufficient throughput. Image quantification regularly involves manual delineation of regions which can be error prone, time consuming and subject to human bias. Reflectance images also suffer high levels of background intensity that can confound results. Therefore extensive efforts have been made to facilitate automated processing and quantification to enable high throughput analyses. This is particularly true within fluorescence microscopy analysis, however these methods are rarely tailored to the analysis of NP reflectance images. Therefore this chapter also introduces an analysis work-flow for the processing and quantification of reflectance images, both RCM and R-SIM. This facilitates the detection and segmentation of NP signal which can be used for fast, accurate, bias-free quantification within subsequent imaging experiments.

The automatically isolated signal, either reflectance or fluorescence signal components, can also be used to facilitate realignment of images taken of the same cells acquired using different imaging modalities. The combinatorial use of multiple modalities that offer different advantages in such a way is a current focus area within nanoresearch. This type of methodology maximizes the information that can be gleaned from a single prepared sample limiting unavoidable experimental fluctuations but also reducing sample number. Combinations of reflectance microscopy with other modalities, such as electron microscopy, is documented rarely [323]. For this reason, a procedural work-flow based on existing CLEM methodologies was developed, to allow cells that were imaged with reflectance modalities to be subsequently imaged with TEM. This chapter therefore also includes methodological detail of this process and a discussion that compares the information available with TEM, RCM and R-SIM of metal oxide NPs including indications of the strengths and limitations of each.

4.2 Results

4.2.1 Transmission electron microscopy

Initially TEM images were acquired of HeLa cells treated with two medically relevant metallic NPs: cerium dioxide, and the Sienna$^+$ SPIONs that were previously characterized in Section 3. Figure 4.1 shows images of these intracellular NPs imaged with TEM. Traditionally, ultra-thin (70 nm sections) are imaged, to achieve the highest possible definition and contrast at the boundaries of organelles present in the cell cytosol (Figure 4.1 top panel). Thick sections (150 nm) can also be obtained and imaged with high power TEMs (Figure 4.1 bottom panel), leading to an effective decrease in Z-resolution. This leads to acquisition of a TEM slice with increased density of particles in a particular location, but additionally increased density of cellular constituents. Electro-dense NPs,

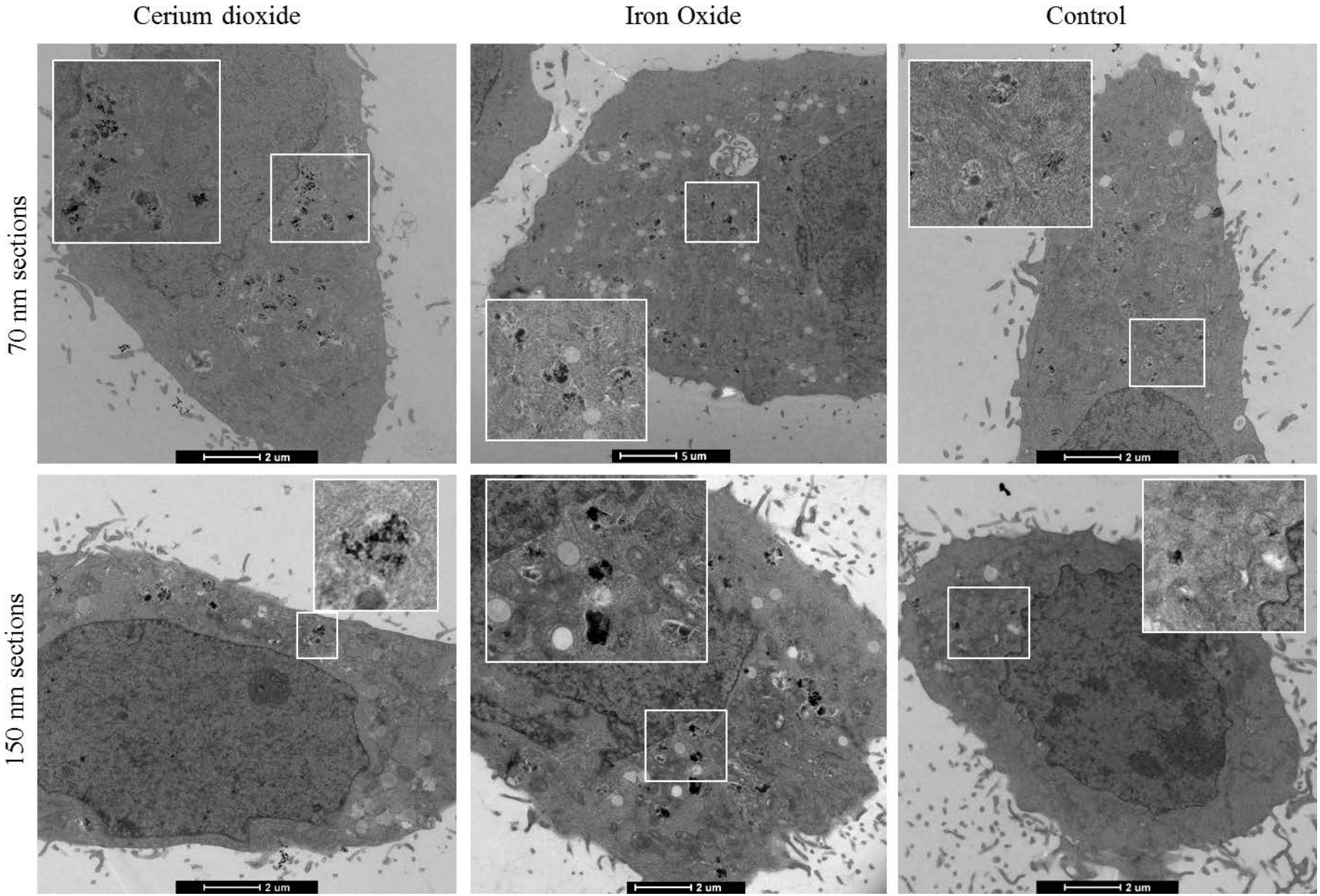

Figure 4.1: Electron micrographs of A) cerium dioxide NPs, B) SPIONs, and C) Non-treated cells.
The top panel depicts 70 nm ultrathin sections, the standard TEM mode, while the bottom panel uses 150 nm sections. Ultrathin and semi-thick sections can thus be successfully imaged. Thin sections give rise to a crisper image, with increased contrast visible at organelle boundaries. Thick sections have slightly less contrast due to the denser area being imaged but allow alignment with confocal slices (see below).

such as SPIONs and cerium dioxide give rise to contrast within the electron micrograph, alone or inside cells on both thick and thin sections (Figures 3.1 and 4.1). This can then be used to benchmark reflectance methods against, in order to validate the suitability of each technique for the detection and quantification of NP internalization in future studies.

Despite the ultrahigh resolution that TEM provides, there are significant disadvantages associated with this imaging approach as mentioned in Section 1.3.6. The nature of the transmission of electrons through a sample under high vacuum restricts TEM to specific sample types. Samples must be ultra-thin / thin, and must be stable within the vacuum itself. This means extensive sample preparation either through dehydration and resin embedding, or cryo-freezing. Clearly this removes the possibility for dynamic imaging, unless multiple sections and multiple time points are imaged sequentially. Imaging at such high magnifications is a laborious process even after the sample preparation has been performed. The field of view in TEM is also restricted, especially at ultra-high magnifications (such as 30,000X) where only small regions of the cell can be observed. While it is true that TEM can provide absolute quantification of NPs inside cells, provided the NPs have sufficient electron-density, the restricted field of view limits the number of cells that can be quantified. This renders the technique unsuitable for high throughput investigations. Sampling only small amounts areas leads to inaccurate measurements of the entire cell population, and complicates conclusions regarding different experimental conditions. There is also significant potential for the incorporation of artifact, through the processing steps, particularly heavy metal staining, and the loss of NPs from the sample through diamond knife sectioning.

4.2.2 Reflectance confocal microscopy

Due to the limitations that exist with TEM, research is often focused toward the development of alternative imaging strategies. RCM is one such tool that exploits the inherent Refractive Index (RI) changes within samples to allow the visualization of intracellular

NPs such as cerium dioxide and SPIONs. The basics of RCM have been previously introduced in Sections 1.3.8 and 1.3.11. Reflectance background intensity is inherent to images as these techniques do not selectively capture reflectance originating from NPs. Therefore, the acquisition settings that maximize this signal to noise ratio (SNR) and minimize unwanted background effects must be established. This is particularly important due to the small amount of signal of interest generated, 10^{-8} - 10^{-6}, relative to the incident light, in reflectance images. When imaging the Sienna^{+} SPIONs in particular, a low level of signal was detected, when compared to other NPs, such as the slightly larger sigma SPIONs (Appendix Figure B.2).The SNR between optical systems with different objectives will vary and a detailed discussion of the SNR effects in confocal microscopy can be found here [227]. The SNR of images acquired of medically relevant Sienna^{+} SPIONs, on both Zeiss LSM 710 and Nikon A1R microscopes using high magnification objectives, were assessed. Qualitatively the image quality and SNR appeared better on the Nikon A1R than the Zeiss LSM 710 as shown in Figure 4.2A and B and in Appendix Figure B.3.

When quantified this translated into a higher SNR in the Nikon microscope for each objective tested. Interestingly, the highest SNR is seen with the 40X objective, likely due to the lower contribution of background effects that appear to increase in severity with increasing magnification (Figure 4.2A and B). The 40X also offers the advantages of a reduced artifact presence and larger field of view. When compared using ANOVA the p=value is 1.05 x 10^{-8}, indicating significant differences within the groups. When compared using "MULTCOMPARE" function in MATLAB, no significance is determined between the Zeiss 63X and the Nikon 100X, and the Nikon 60X and Nikon 40X. All other comparisons between objectives were found to be significant (p<0.001). Increasing magnification and numerical aperture gave increased optical resolution and in turn facilitate higher detection rate of NP signal as seen in Figure 4.3 and Appendix Figure B.5. This was assessed across the same sample area (depicted as an insert in Figure 4.3C). When the zoom approaches that of the Nyquist sampling rate, maximum reflective objects are detected. However,

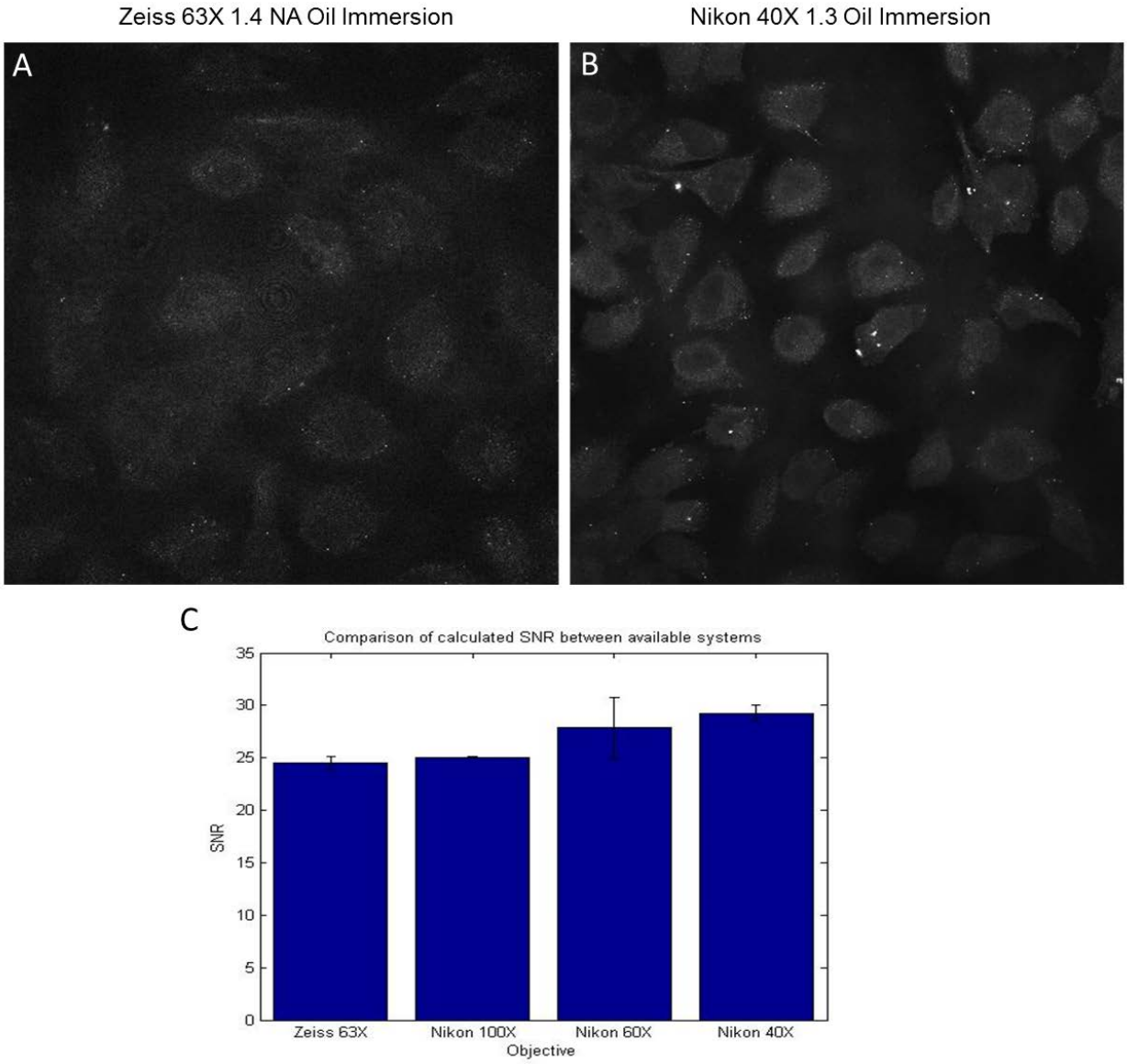

Figure 4.2: SNR across different available microscope systems and objectives. Signal to noise ratio (SNR) will depend on the imaging system and the sample itself. The Nikon A1R (A) led to increased SNR when qualitatively compared to the Zeiss LSM 710 (B). C) Quantifying SNR from multiple microscope images (N=3) the SNR appeared highest on the Nikon A1R using a 40X objective. No significance is determined between the Zeiss 63X and the Nikon 100X, all other results were significant $p<0.001$ (***).

increasing magnification decreases imaging throughput due to the decreased field of view.

The Nikon A1R suffers from ring artifacts within reflectance images caused by optical elements within the microscope, depicted in Figure 4.3. This artifact effect is well documented [324]. The intensity and severity of the observed artifacts increase with objective magnification, and different imaging configurations can lead to deterioration of image quality due to this artifact [324]. For example, when image tiling is performed with optical zoom on the 40X, the artifact is particularly obvious (Figure 4.3A) [325, 326]. Therefore imaging configuration must minimize this problem, such as reducing magnification or increasing field of view. The artifact has a relatively high intensity compared to the background signal (seen in 4.3A). Therefore false signal detection could occur when imaging NP containing samples if the artifact was present.

To investigate this, the same NP treated sample was imaged multiple times at the exact same location using different sized fields of view (using the zoom magnification control) on the 40X. This was to determine the impact of the artifact intensity on NP detection using these acquisition settings. These were performed using the full field view, upto the Nyquist sampling rate for acquisition with this objective (Figure 4.3). For Nyquist sampling, the pixel should be at least two times smaller than the smallest feature expected in a sample (200 nm in confocal) to ensure maximum information is recorded. Using Nyquist sampling rate, the image quality will be as high as possible in the resultant digital image, however the field of view will be extremely small (2-3 cells per view on the 40X objective). Following acquisition, the detection rate of NP was compared across all the acquired images. Manual assessment of each of the images (counting) determined that 65 regions of signal were present within the image. Then, MATLAB was used to detect regions of intensity using methods discussed later on in Section 4.2.9. This determined the number of isolated regions detected within each of images. As optical zoom increases, there is an increase in the number of detected regions 4.3C. However, as the optical zoom

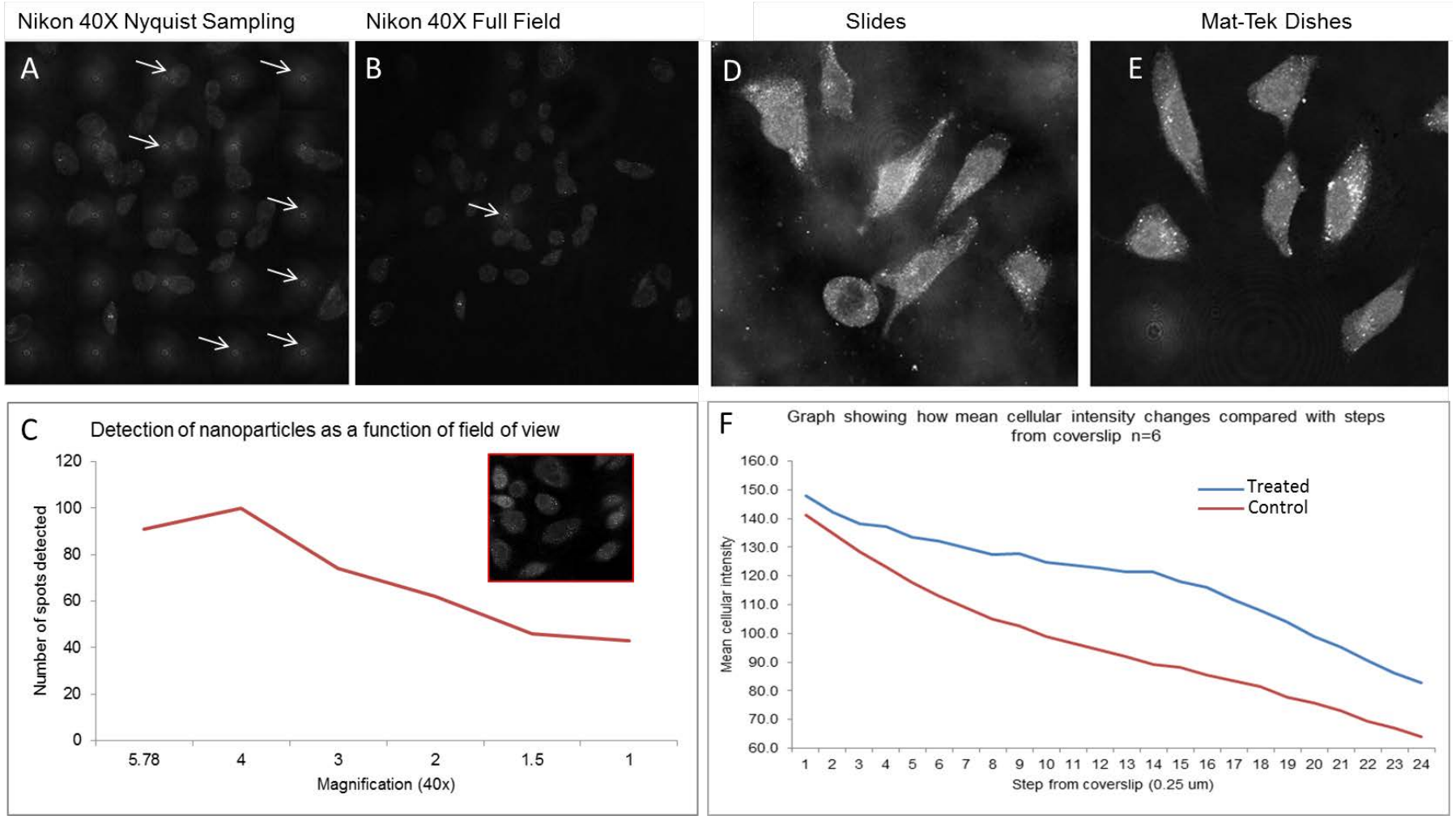

Figure 4.3: Field of view effects the detection of NP signal and imaging in MatTek dishes which improves the image quality. A) Optical elements within the objectives can lead to artifact within the acquired images, which is particularly noticeable when using high magnification for large tiled fields of view (white arrows indicate ring artefacts). B) The artifact is not as much of an issue with lower magnification objectives, and the artifact can be removed from the field of view by changing the image field electronically on the microscope software. C) Increasing optical zoom increases the detection of NPs, therefore there is a trade-off between increased background and increased detection. D) Uneven background intensity effects are seen when imaging with coverslips probably arising due to uneven liquid volume present. E) The use of glass bottom petri dishes for imaging enhances the image quality. F) Background intensity is greatest at the coverslip; for optimal imaging of reflectant objects acquisition must take place at sufficient distance from the coverslip. Imaging in the window between 8 and 14 (2 and 3.5 µm) steps from the coverslip leads to maximum SNR measurements.

increases, more than 65 (up to 40 more) regions were detected, indicating that the increase in artifact may be leading to an increase in detected signal due to its intensity. Because of this, it was concluded that the Nikon 40X objective with a 2X optical zoom and artifact removed from the field of view gave a good compromise between accurate detection and throughput. Therefore these settings will be employed for future experiments. However, the 60X and 100X objectives provide increased resolution and therefore are advantageous for use in colocalization experiments (Section 6.2.1). These analyses indicate the worth of employing the 60X objective to maximize SNR trade-off with magnification within future colocalization studies.

The laser line used can also effect the detected reflectance signal, and the amount of artifacts present within a sample. This is due to the relationship between incident light and reflected light. Reflected light depends on the loss of incident light through specimen absorption. Shorter wavelengths are more easily absorbed into specimens, therefore are paralleled by a loss of reflected light. However, when the specimen was visualized with laser powers higher than 488 nm, there was a visible deterioration of image quality due to the increase in ring artifacts from the optical elements within (Appendix Figure B.4). Therefore the 488 nm laser line was employed for RCM imaging.

Imaging coverslips mounted onto slides in VS leads to varied background reflectance across the image seen in Figure 4.3D. Uneven background illumination or high intensity background signals complicate analysis and lead to the false positive identification of signal. Glass bottom petri dishes are advantageous for microscopy as they can be placed directly onto an inverted microscope. These dishes, when imaging in reflectance mode, offer the advantage of maintaining a flat surface and consequently providing a more even background signal (Figure 4.3E). The dishes also provide a useful platform if multiple imaging methodologies are required, such as processing and imaging with TEM or SIM [322]. Therefore MatTek dishes were used whenever possible for reflectance imaging within this

thesis. High intensity reflectance signal is evident when imaging at or close to the coverslip, a fact taken advantage of during the imaging of cell surface contacts [238]. However, for the purpose of imaging inside cells, it is not advantageous to collect a high level of light scattered from the coverslip as this would obscure the NP signal of interest. The reflectance signal collected by the detector appears to decrease with increasing depth from the coverslip (Figure 4.4). This loss of intensity with increased depth can be explained due to the increased scatter of incident and reflected light through the sample, and therefore decreased backscattered light will reach the detector at increased sample depth [327]. Imaging within a region around 2.5 µm from the coverslip led to increased image quality, and maximum separation distance between control signal level and NP treated signal in Z-stack images (Figure 4.4F).

Imaging with VS, which has an RI of 1.44, rather than aqueous imaging medium such as PBS, RI 1.33, within Mat-Tek dishes appears to decrease the cellular background signal compared to imaging in dishes containing PBS (Figure 4.4). VS may lead to a weaker backscattered signal at the media/cell boundaries and by intracellular organelles, due to a slight change in RI between the imaging media and the cellular constituents [328]. Indeed when looking at control cells and treated cells under both PBS and VS imaging conditions, the level of background signal from cellular components qualitatively appears lower in VS (Figure 4.4A:D). Regions of bright intensity visualized in control cells appear to decrease upon the addition of VS. Some regions of mid-intensity in treated cells also appears to decrease (Figure 4.4A:D). This presumably indicates that some cellular constituents reflect light more strongly than others and that the use of VS reduces this effect and subsequently lowers their contribution to the final image. When visualizing intracellular NPs whose size is below that of the diffraction limit of light, the detected signal is visualized as a blurred unresolved object. This effect, described by the diffraction-limited Point Spread Function (PSF) of the system, always occurs when imaging point sources, such as small NPs. The PSF is modeled by a Gaussian distribution and is the response of

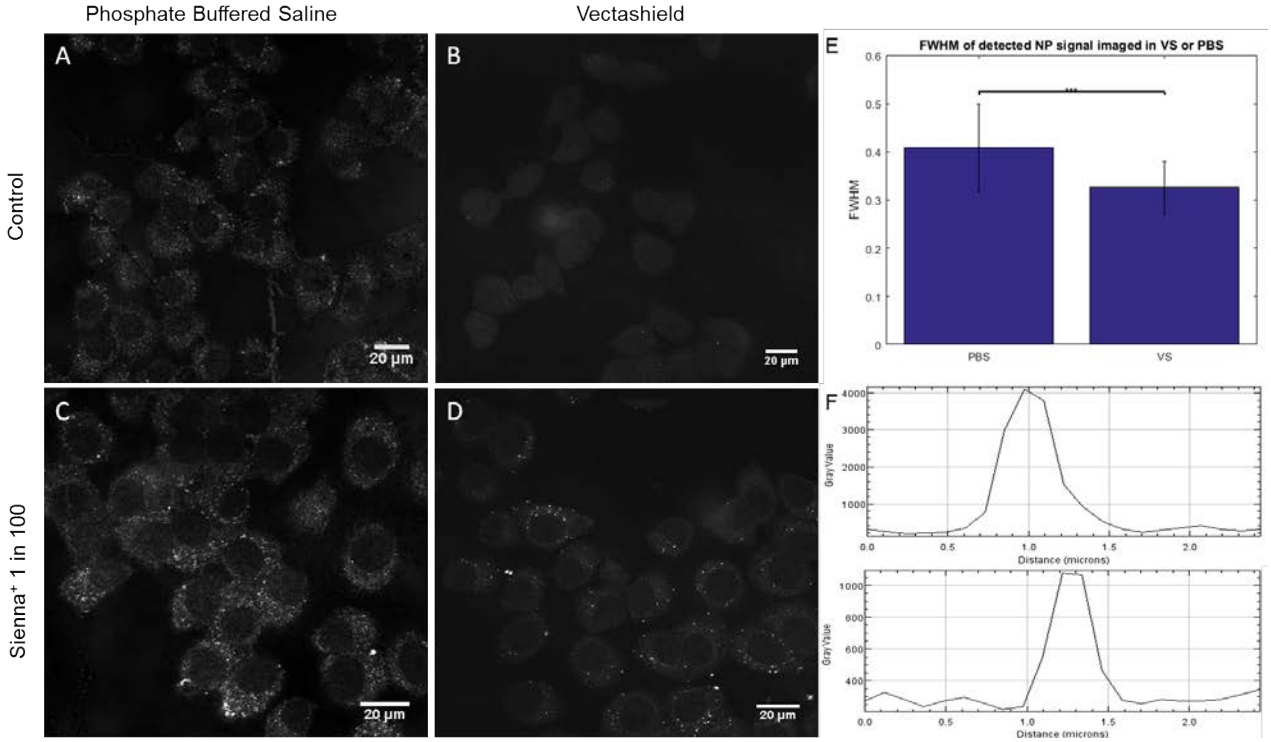

Figure 4.4: Imaging in VS increases image quality compared to imaging in PBS in MatTek dishes. Reflectance imaging of cells submerged in PBS within MatTek dishes (A and C) leads to an increase in non-specific background signal and increased blurring of the NP signal (C). This is particularly evident in the control cells where no amount of high level reflectant intensity would be expected, as no NP are present. When performing reflectance imaging of cells submerged in VS (in MatTeks), the use of VS leads to an apparent reduction in non-specific background and cellular signal (B and D). In PBS control images (top) and treated images (bottom) show increased level of background intensity, compared to VS imaged samples. E) shows the quantification of the FWHM of NP signal in treated cells imaged in VS and PBS; A decrease is observed in the FWHM when imaging in VS compared to PBS indicating an increase in image quality. The line intensity scans show an example of signal in PBS (F) and VS (G).

the optical imaging system to the point source. Properties of this Gaussian can be used to determine the effective resolution of microscopy techniques (i.e. FWHM), to determine the minimum separation difference of objects that can be resolved. The use of VS appears to increase signal contrast and decrease the FWHM, leading to an 'apparent' increase in resolution (Figure 4.4E and F). Quantification was therefore performed to measure the FWHM from line intensity scans in ImageJ. The FWHM of signal arising in PBS samples is 405 nm +/- 95 nm, whereas with VS the FWHM is significantly decreased at 325 nm +/- 50 nm. This indicates that VS does increase image quality and resolution.

Appropriate acquisition settings are crucial for obtaining meaningful and quantitative data. Therefore numerous extensive reviews exist in terms of FCM settings [329, 330]. Similar principles apply for RCM. Briefly, when laser power settings are determined from an untreated control sample (i.e. laser power is set so that no signal is observed in the control) valuable signal may in fact be lost in the case of subsequent samples. Although this technique removes unwanted contributions from noise, the dynamic range of the sample is effectively clipped to a minimum and signal will be lost. Likewise, if laser power and gain are too high the detector will be saturated. The intensity values are then restricted to the detector maximum i.e. 4096 for a 12 bit detector. Settings should instead lead to acquisition of images that utilize the entire detector dynamic range to maximize the SNR, image contrast and signal detection. Therefore settings should be determined by using an NP treated positive control. The laser power should facilitate the detection of signal nearly up to the maximum attainable value, using the entire dynamic range. It is crucial to retain the same laser power and gain settings across experiments that are to be compared or quantified relative to one another, and to facilitate automated detection of signal in subsequent processing stages.

4.2.3 Reflectance structured illumination microscopy

As introduced in Section 1.3.12, conventional diffraction limited microscopy is restricted to resolution capabilities of approximately 250 nm. An increasing number of superresolution techniques are available and under continued development to improve the spatial resolution of LM, however these almost always are paralleled by the sacrifice of temporal resolution [257, 259, 331]. SIM, introduced briefly in section 1.3.12, is one such established method that provides more than two-fold increase in resolution relative to conventional light microscopes such as confocal [233, 257]. SIM requires no special sample preparation and therefore is an ideal complement to other microscopical investigations [331]. SIM sacrifices less temporal resolution than techniques such as Stochastic Optical Reconstruction Microscopy (STORM) / Photo-Activated Localization Microscopy (PALM) rendering it particularly advantageous for live cell applications in terms of low laser power and short imaging time.

Despite the widespread use of Fluorescence SIM (F-SIM), SIM in reflectance mode (R-SIM) has only previously been documented on custom built microscopes [233]. In an F-SIM acquisition, a filter cube is present within the light path consisting of an excitation filter, emission or barrier filter and a dichroic mirror. This filter cube allows fluorescent light emitted from the specimen to pass through and reach the detector, and blocks the light used to excite the specimen. When collecting reflected light, this type of spectral separation is not employed. In order to collect light reflected back from the sample in a SIM acquisition, a filter cube that contains a half-mirror (partially silvered) in the place of the dichroic, can replace the standard filter cube. This half mirror permits the passage of reflected light (same wavelength as incident light) to the detector, rather than filtering specific wavelengths. The sample is illuminated in the same manner as F-SIM using a grating (grid) to structure the light incident to the sample to acquire multiple (9 or 15 in 2D or 3D respectively) Moiré fringe images due to interference. Superresolution image reconstruction is performed in the Fourier (frequency) domain [331]. The Fast Fourier

Transform (FFT) is a discrete Fourier Transform (FT) algorithm that mathematically converts the observed signal in its acquired spatial or time domain into the Fourier frequency domain [331, 332]. In the Fourier domain, the frequency content is restricted by the Optical Transform Function (OTF), which is the FT of the PSF [331]. The Moiré fringes contain higher frequency information than would otherwise have been possible to capture, outside of the OFT of the objective. The effect of combining these different Moiré fringes can be visualized on the FFT image, where the signal space is significantly extended when compared to the central sphere that represents the OTF (Figure 4.5) [331].

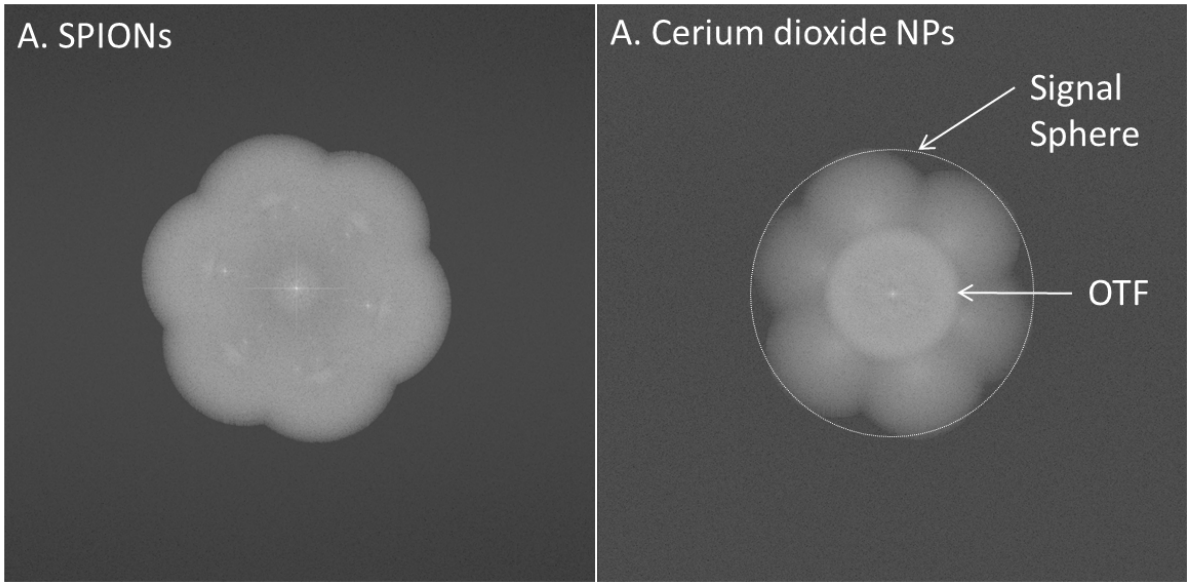

Figure 4.5: Example FFT of R-SIM of Sienna$^+$ SPIONs and cerium dioxide NPs. The FFT indicates that the reconstruction was successful due to the 6-lobed flower structure evident in the images.

The inverse of the reconstructed frequency space image (iFFT) then produces the final SR-image in the spatial domain. Therefore the FFT image also gives an indication of the success or failure to acquire SR image data in the spatial domain. Figure 4.5 shows the FFT of 2D R-SIM images acquired of Sienna$^+$ SPIONs and cerium dioxide NPs: the characteristic 6 lobed petal structure indicates that the reconstruction was a success. Four different NPs were successfully visualized using R-SIM (Figure 4.6A-F). This provides the first example of a commercial SIM microscope being used for super-resolution imaging of

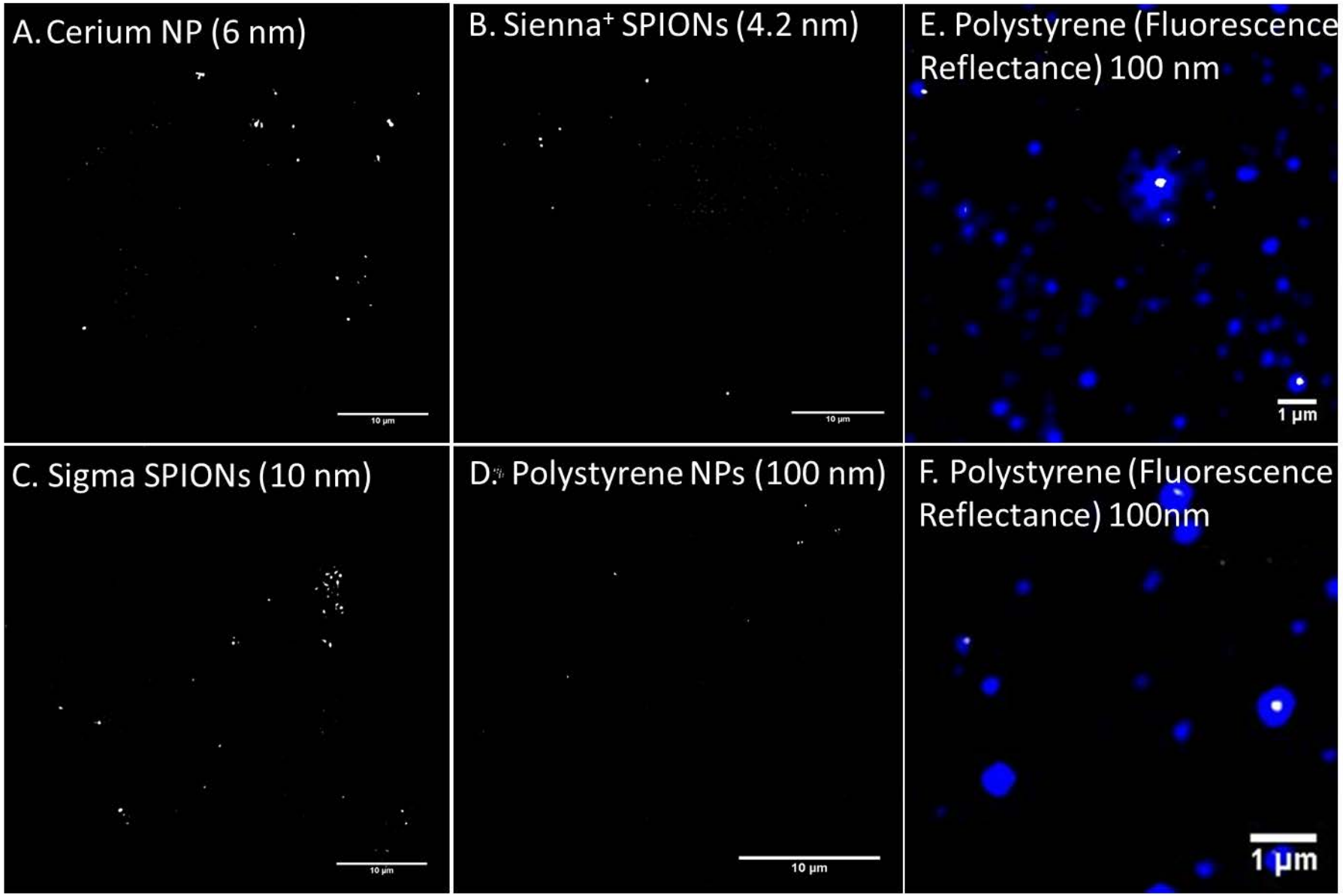

Figure 4.6: Reflectance SIM images of NPs with different compositions. A) shows an example R-SIM image of 6 nm core cerium dioxide NPs, B) and C) show R-SIM images of different types of SPIONs and D) shows reflectance of polystyrene NPs. E) and F) show the fluorescence (blue) and reflectance (grey) SIM images of the same fluorescent/reflectance polystyrene NPs to confirm that the reflectance signal is originating from NPs.

intracellular reflectant (NP) structures, utilizing the half-mirror filter cube. This is advantageous particularly for the imaging of non-fluorescent NPs, such as SPIONs and cerium dioxide NPs, which would otherwise be undetectable using F-SIM. This therefore negates the need for fluorescent modification and labeling. Two types of SPIONs, polystyrene and cerium dioxide were imaged (Figure 4.6A-F), indicating the breadth of application for this technique. The fluorescent polystyrene NPs provided the opportunity to visualize NPs in both R- and F-SIM mode near-simultaneously. This determined that there was not any major offset between the reflectance and fluorescence signal (Figure 4.6E and 4.6F). The fluorescent overlay also provided evidence that the detected reflectance signal arises due to NPs in the sample and are not an artifact. The brightest fluorescent NPs are visible with reflectance at the same location. Interestingly, the resolution in R-SIM appears higher than that of F-SIM. This has also been noted between RCM and FCM, where the resolution in RCM is roughly 50 nm higher [247]. The detection capacity, particularly for polystyrene, appears lower in R-SIM compared to F-SIM (Figure 4.6E and 4.6F). This is likely to be a product of the low reflectance, or RI, of polystyrene and the high background inherent to reflectance images. This background is enhanced during epi-illumination acquisition, such as in SIM, and can mask signal during Fourier reconstruction.

The use of VS imaging media led to a superior image quality when compared to images taken in PBS, this is evident in Figure 4.7. The addition of VS, as with RCM, led to a decrease in background signal, again presumably due to the increase in refractive index. Thus, R-SIM can be performed with the same sample preparation conditions as RCM, which is advantageous as samples can be imaged sequentially by both techniques. This renders SIM a complimentary technique for high resolution investigations of specific samples. Different laser lines can also effect the reflected signal. This is assumed to follow the rule that as laser wavelength decreases, absorption increases, and therefore reflectivity will decrease. It can therefore be expected that longer wavelengths of light will lead to

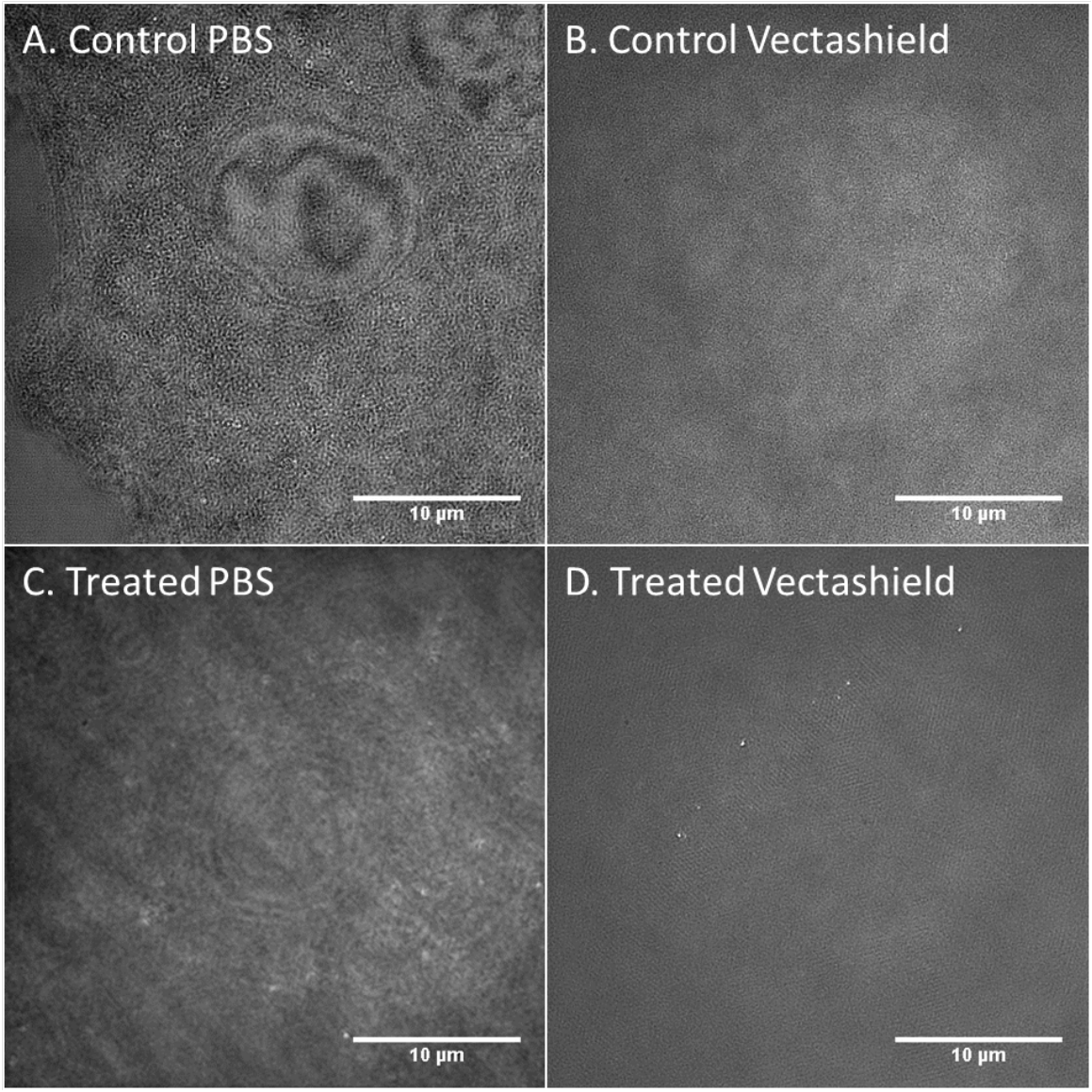

Figure 4.7: Imaging in VS appears to increase image quality in R-SIM images. Comparison of the signal detected when imaging in PBS (left hand images) and VS (right hand images). VS decreases background signal and increases R-SIM image quality.

increased reflectivity. A superior SNR was obtained with 488 nm incident light, seen in Figure 4.8, as expected. The 488 nm laser led to an increase in the reflected signal, therefore the 488 nm laser was used for R-SIM imaging.

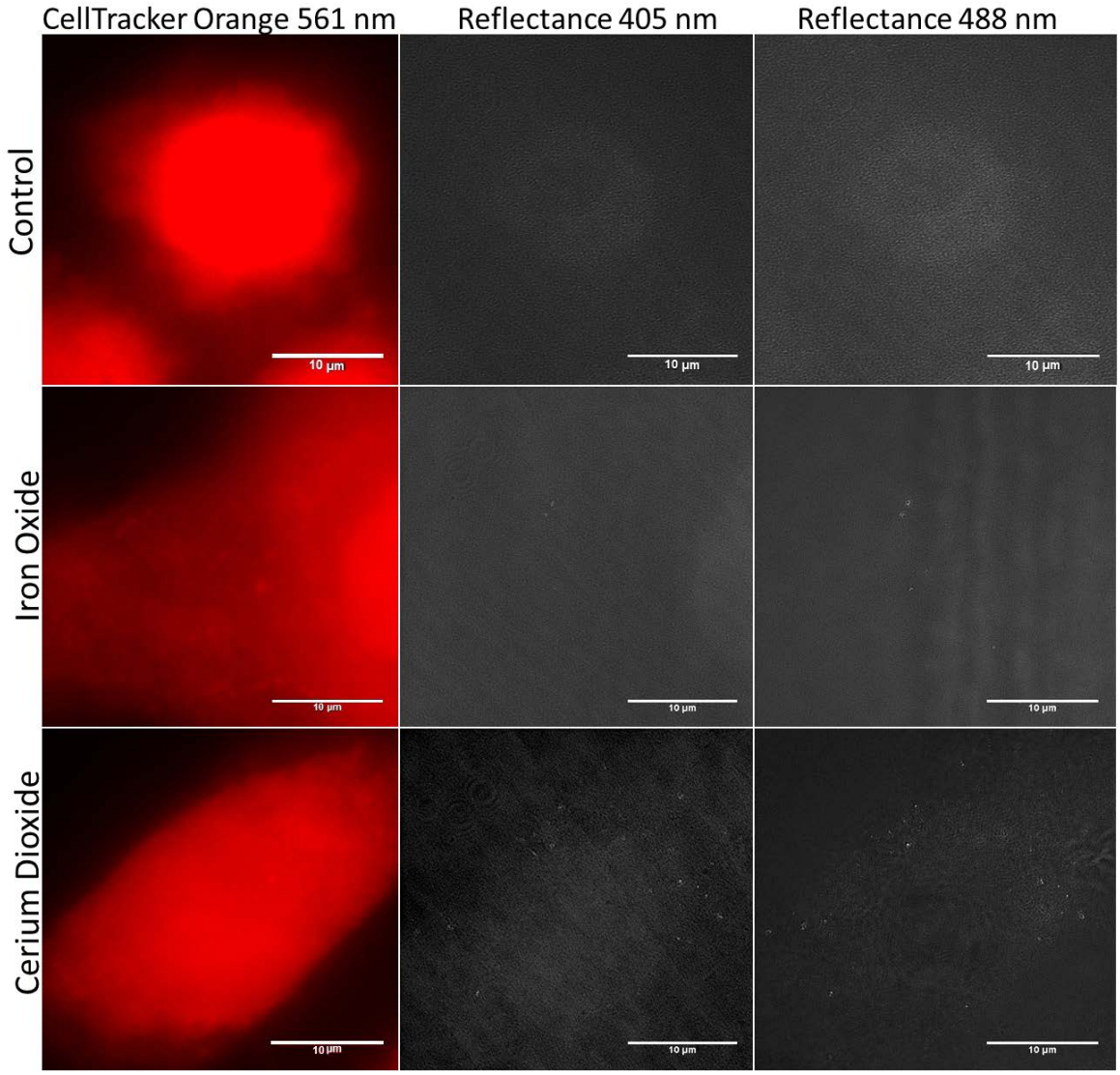

Figure 4.8: R-SIM with the 488 nm laser appears to lead to increased signal detection. Comparison of the signal obtained when cells with or without NPs are imaged with 405 nm laser (middle panel) and a 488 nm laser (right panel). CellTracker Orange stain is used to visualize the cell cytoplasm. Use of the 488nm laser appears to lead to an increase in reflection signal.

4.2.4 Comparison between R-SIM and RCM of NPs inside cells

Figure 4.9 shows the CLSM reflectance (NPs) and fluorescence (CTO and DAPI stain) images of SPIONs and cerium dioxide NPs when using a 100X objective with Nyquist sampling rates for maximal resolution. Both NPs provide a substantial RI difference compared to the surrounding media and therefore provide excellent contrast. This allows detection in cancer cell models indicating their applicability to subsequent studies (Figure 4.9). Figure 4.10 shows the R-SIM images of the NPs inside HeLa cells, using the same 100X objective. Raw images acquired from both RCM and R-SIM show evidence of background signal, which can be removed later using the post processing methods described in Section 4.2.9.

Figure 4.10, middle and bottom panels, show the results of post processing of R-SIM images. The method uses image filtering followed by intensity clustering to segment signal. This allows quantification of NP uptake relative to control cells. This procedure is described in detail in Section 4.2.9 [322]. In order to make qualitative conclusions regarding the advantages offered by R-SIM and RCM, cells were incubated with NPs and imaged sequentially first with RCM, and then R-SIM. This process is detailed in the first part of Appendix B.1.4. The increased resolving power of the R-SIM technique is evidenced by the appearance of multiple smaller structures on the R-SIM image where RCM shows single correspondingly larger structures at the same locations when using both the 60X (Appendix Figure B.6) and the 100X (Figure 4.11) objectives for RCM. Thus, the higher resolution allows separation of regions that would otherwise be non-resolvable using RCM alone. This is also evidenced in the line intensity profile of the selected region on the raw intensity image (Figure 4.11). The RCM line scan shows a single broad peak, where the R-SIM line scan displays two peaks at the same location (Figure 4.11). The decrease in the width of the detected R-SIM peaks indicates a decrease in the FWHM. The FWHM for regions detected by RCM using the 100X 1.49 NA objective with Nyquist sampling is 345 nm +/- 83 nm averaged over 100 regions. The average FWHM for regions detected

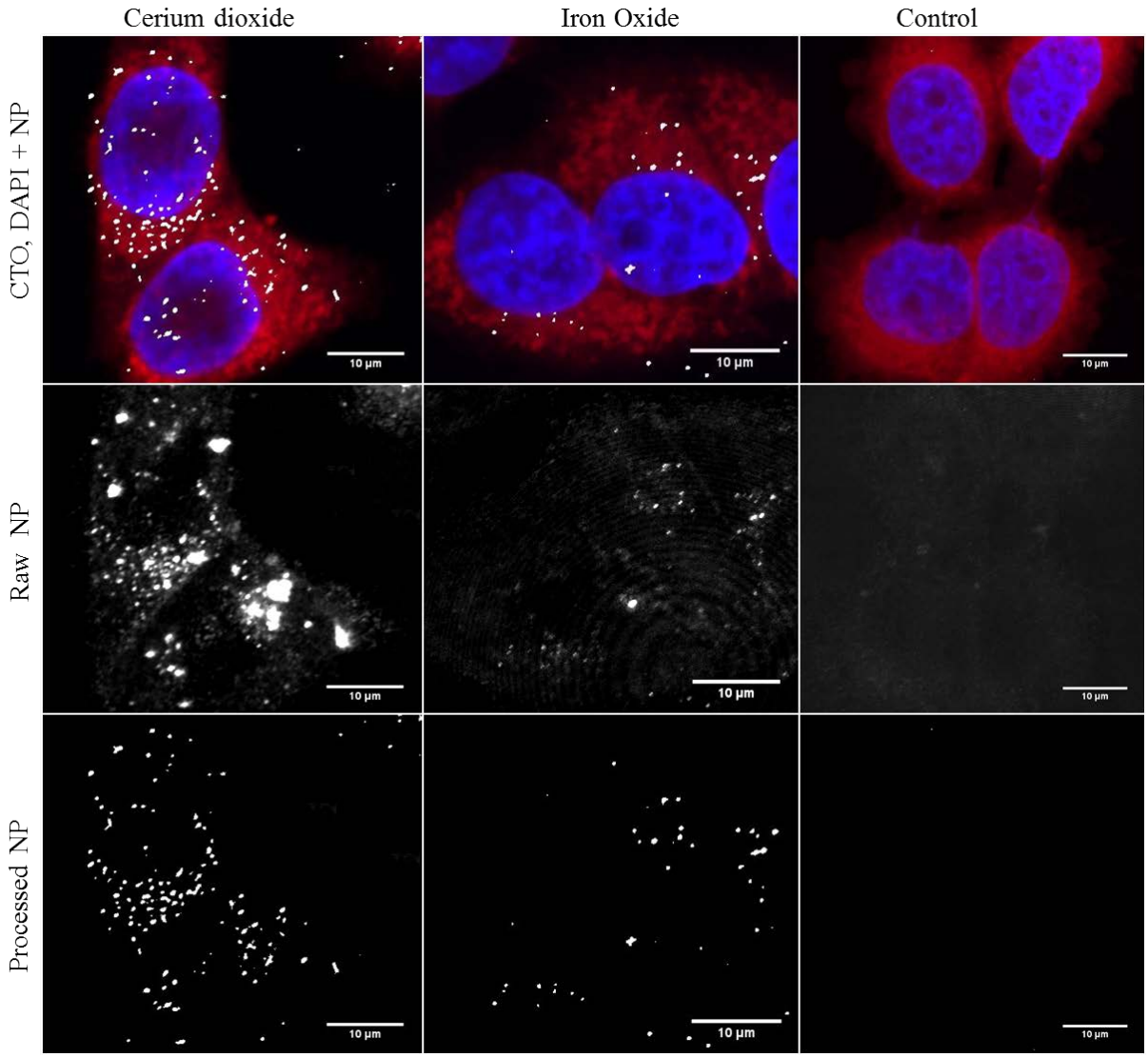

Figure 4.9: RCM images of SPIONs and cerium dioxide NPs inside HeLa cells. NP uptake can be visualized in HeLa cells treated with cerium dioxide NPs or SPIONs compared to untreated control cells. Images show maximum intensity Z-projections of cells stained with Cell Tracker Deep Red (CTDR) (red), 4,6-diamdino-2-phenylindeo (DAPI) nuclear stain (blue) and NP reflectance signal (grey). Control cells show no high intensity reflective spots. The raw intensity reflectance images show background reflectance in both control and treated cells (top and middle panel). Following post processing, regions of high intensity signal are segmented from background signal (bottom panel). Overlay of fluorescence stains and segmented reflectance NP signal (grey) are also included (top panel).

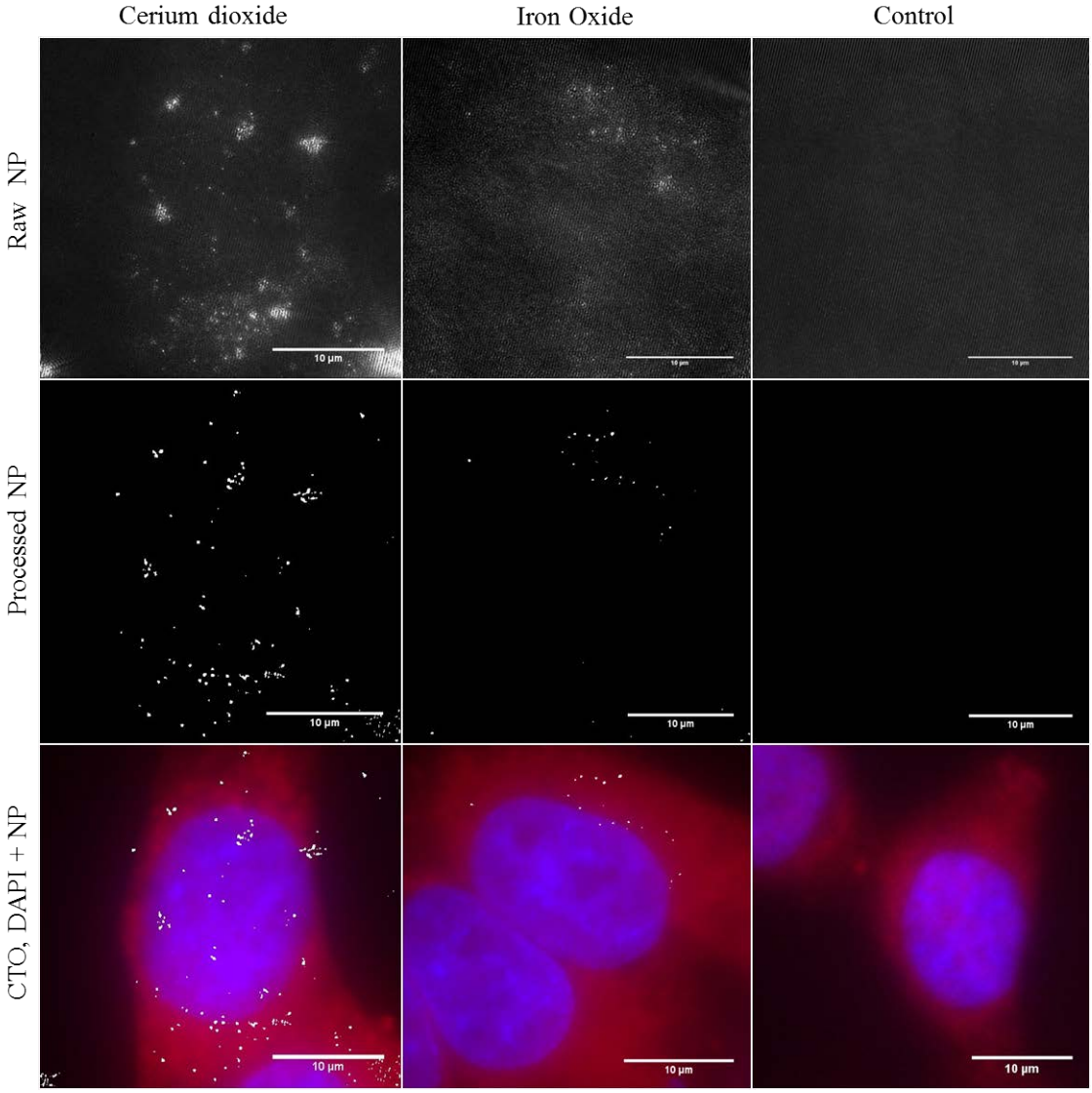

Figure 4.10: R-SIM allows visualization of NP uptake at increased resolution. NP uptake can be visualized in HeLa cells treated with cerium dioxide NPs (86 cells), SPIONs (32 cells) or untreated (25 cells). Images show maximum intensity Z-projections. Fluorescence images show conventional wide-field epi-fluorescence of cells stained with CTDR (red) and DAPI nuclear stain (blue). Reflectance images show 2D SIM acquisition of reflectance NP signal (grey). Control cells show no high intensity reflective spots. The raw intensity reflectance images (top panel) show background reflectance in control and treated cells. Post processing and segmentation can isolate regions of high intensity reflectance (NPs) from background signal (middle panel). Overlay of cells stained with Cell Tracker Deep Red (CTDR) (red), DAPI nuclear stain (blue), and segmented reflectance NP signal (grey) (bottom panel).

by SIM reflectance is 115 nm +/- 21 nm averaged over 125 regions. This is substantially better than the theoretical maximal X-Y resolution offered by confocal systems: 200-250 nm.

When comparing images obtained with RCM using the 100X objective to those taken with RCM using the 60X, the 100X performs substantially better. Regions detected using the 100X objective with RCM align to those detected by R-SIM with little to no offset (Figure 4.11 and Appendix Figure B.6). This indicates the advantage of utilizing the same objective. R-SIM did not appear to reveal as many isolated regions as RCM. This is evident in the image shown where the majority of regions detected with R-SIM correspond to a region detected by RCM (Figure 4.11C and D). This can be quantified as a percentage of total objects detected (Figure 4.11H). Pixel based methods are not appropriate for this type of analyses due to the difference in resolution. Objects that are detected within R-SIM images are also observed with RCM with an average of 74% across 27 analysed cells (Figure 4.11H). Conversely, 54% of regions detected on RCM correlate to regions detected with R-SIM (Figure 4.11). Although volumes of approximately the same regions were acquired with corresponding Z-step size, the identical volumes cannot be directly compared which could lead to discrepancies. These variations occur due to variations in the start or end points within the stack, number of Z-planes within the stack and Z-resolution / optical section thickness of the modality. The perceived center of the detected region is not perfectly aligned in all cases seen in Appendix Figure B.6 and Figure 4.11. This may, in part, relate to the different reflected rays that are collected from irregular shaped NPs and agglomerates under the different illumination patterns. Agglomerate shape, size and orientation with respect to the optical axis are all known factors that contribute to the angle of reflectance, and therefore the perceived center of detection [333, 334, 335]. Problems with centroid alignment may also arise from the dish not sitting completely flat during acquisitions. Taken as a whole, the analyses suggest that although SIM provides better resolution, RCM permits identification of more iso-

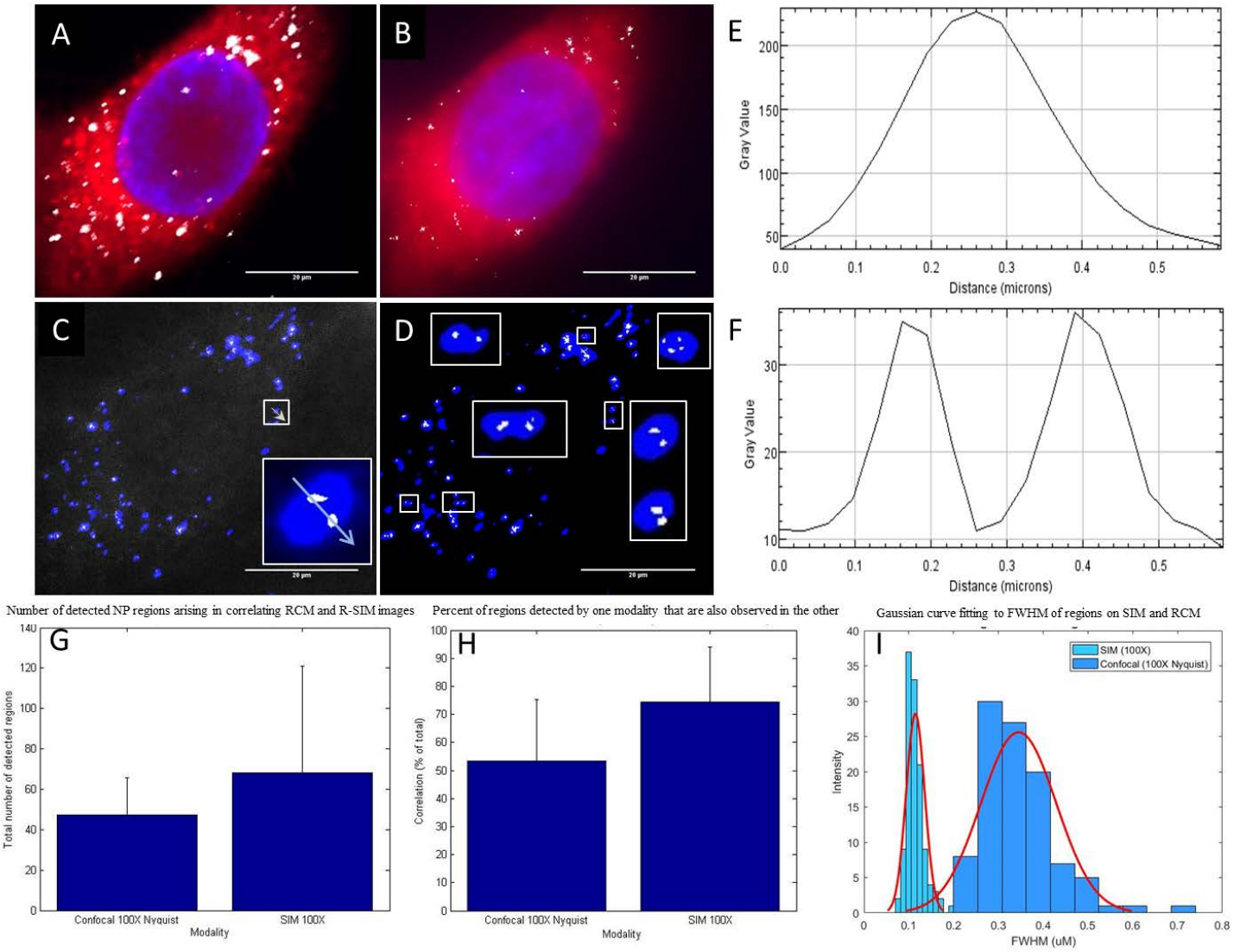

Figure 4.11: Comparison of data obtained from RCM and SIM reflectance. Maximum intensity Z-projection images of a HeLa cells treated with cerium dioxide NPs, acquired with RCM and R-SIM using identical 100X, 1.49 NA objective. RCM imaging volume is 3.6 µm and SIM is 4 µm. Images A) (RCM) and B) (R-SIM) show CTDR (red) cytoplasmic stain, DAPI (blue) nuclear stain and NP signal (grey). Overlay of the cerium dioxide NP regions show particles detected in RCM (blue) and SIM (grey) in both the raw (C) and processed (D) images. White boxes display a sample of regions where RCM detects one spot and SIM detects multiple spots, illustrating the enhanced resolution of SIM. Intensity line scans of RCM (E) and R-SIM (F) show the decrease in peak width in SIM and the detection of two peaks where RCM detects one. The average total number of regions detected via each technique was computed (47 and 68 for RCM and R-SIM, respectively) (G). The percentage of regions or connected components visualized with each modality, RCM and R-SIM, that are also seen in the other modality (54% and 74%, respectively), were computed automatically using MATLAB as detailed in the methods section using 27 cells from multiple experiments performed on separate days (H). The means and STD are plotted. Comparison of the size distribution of the FWHM of 100 / 125 regions for RCM and R-SIM respectively are shown (I), with a fitted probability density function.

lated NP positive structures. The total signal detected (isolated regions) when imaging cerium dioxide NPs is increased in total number when analyzing R-SIM images when compared to RCM 4.11. Despite the higher detection of 'isolated singular regions' with RCM, the perceived increase with R-SIM is expected due to the increase in resolution due to the resolving of smaller structures previously detected as one with RCM. Interestingly, the detection of SPIONs remains roughly the same, therefore it may be that R-SIM is inferior to RCM for the investigation of particular types of NPs, such as SPIONs. It is likely that the low intensity reflectance signal generation associated with these particular SPIONs, possibly relating to the low density dextran coating, is being masked by the increased background signal associated with SIM due to epi-illumination. The core size of the SPIONs used in this study is small (4 nm) and irregularly shaped, as seen in the TEM micrograph (Figure 3.1). These results indicate that particle material, size and homogeneity, in part, determine their detection capacity with R-SIM and, therefore, may dictate the imaging system preferred for NP visualization and quantification.

Intensity profiles of signal from Z-stacks were used to determine the Z-PSF in both RCM and SIM (Figures 4.12A, B, D and E). The observed FWHM in the Z direction of RCM is 1077 nm (Figure 4.12). The optical slice for SIM is approximated by the measured Z-PSF, and is larger than the theoretical optical slice thickness of RCM. However, the SIM reconstruction algorithm will only successfully reconstruct high contrast (in-focus) signal near the center of the plane, leading to a Z-FWHM that is smaller than the Z-FWHM of RCM (685 nm and 1077 nm respectively) when measured over 20 regions (Figure 4.12C). The effect this has on particle inclusion within the imaged plane was concluded by comparing the number of consecutive planes that particles are present within on matching R-SIM and RCM images. Particles appeared for an average of 7 consecutive optical slices with 0.2 micron increments in RCM, and an average of 4 consecutive optical slices with 0.2 micron increments in R-SIM (Figure 4.12F). This is logical given the FWHM measurements, and indicates that the Z-PSF is smaller in SIM than RCM, leading to an increase

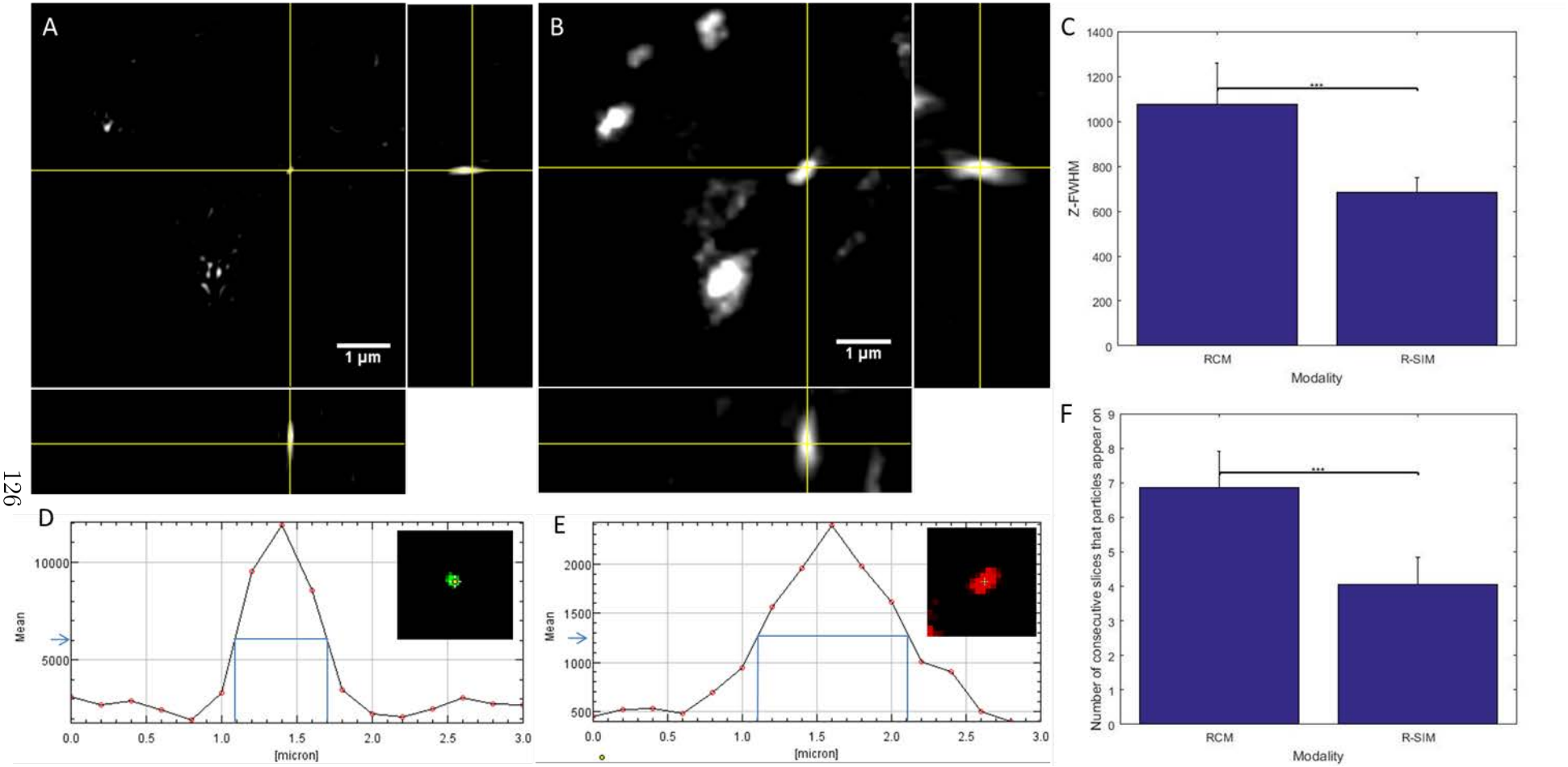

Figure 4.12: FWHM and Z-PSF of intracellular cerium dioxide NPs. Z-Y and Z views of R-SIM Z-stacks (A) and RCM Z-stacks (B) showing the Z-PSF of the same NP signal using each technique. R-SIM has a narrower Z-PSF despite the larger optical slice thickness. Identification of multiple regions on images from both RCM and R-SIM indicated the effect this has on particle inclusion across imaged Z-planes. Intensity line scans were plotted along the Z axis at these regions and the FWHM measured. (C) represents 20 regions with the STD plotted. Students T-Test gave P-Value of 5.210^{-12} indicating the groups are significantly different to one another. The FWHM of line intensity scans can be used to measure Z-PSF on R-SIM (D) and RCM (E).

in Z resolution.

RCM allows acquisition of large amounts of 3D data with apparent increased detection sensitivity when compared to R-SIM. RCM can also be performed with live cells. R-SIM, however, provides a substantial increase in resolving capabilities compared to RCM and distinguishes between NP clusters with an average FWHM of 115 nm compared to 354 nm with RCM. This distinguishes clusters previously unresolvable by other reflected light techniques, such as RCM, affording more accurate investigations and conclusions regarding the presence and location of NP clusters within cells, and permits the superresolution imaging of unlabeled NPs that would not be possible with current fluorescent SIM acquisitions. The relatively long effective exposure time of SIM, 3 seconds, makes it less compatible with living samples, however it is possible. Together, the combination of RCM and R-SIM techniques can highlight important information regarding the cellular uptake and localization of NPs, with no additional sample preparation needed to transition between the two modalities.

NPs with varied compositions appear to be detected with different efficiency using R-SIM. SPIONs, for example, appear to be better detected by RCM than R-SIM. It would be of interest to synthesize NPs of varying material, size, shape and homogeneity to subsequently systematically compare the detection of these with RCM and R-SIM. This could be used to infer conclusions regarding the limitations of R-SIM in terms of NP physical properties. The difference in detection can somewhat be explained by the different scattered light collection methods used in each optical sectioning technique. In RCM, out-of-focus light is filtered by the conjugate pinhole system, resulting in an increase in image quality, greater depth of field and increased particle detection. SIM, however, utilizes wide-field illumination at multiple angles and phases, and therefore suffers from the detection of outof-focus blur; only high contrast in focus signal will be successfully reconstructed, leading to a narrower plane of particle inclusion [247]. The algorithm used for

performing the reconstruction is part of proprietary Nikon software designed primarily for fluorescence imaging, which cannot readily be replaced or modified by the user. Reflected light images can include high levels of background scattering from cellular components, which the reconstruction software is not designed to deal with. Thus, it is likely that this background scatter leads to obscuring of signal, especially in the case of the smaller, irregularly shaped SPIONs. This can limit particle identification. Potential future changes to the image processing and reconstruction algorithm may lead to increased image quality and increased detection. Despite this limitation, these analyses indicate the increased detection power of RCM, relative to the significantly improved resolution of SIM, suggesting that their combined application can provide maximal information in the investigation of certain suitable NPs (such as cerium dioxide).

4.2.5 Correlative reflectance electron microscopy

Reflectance signal arises from a variety of cellular constituents in addition to signal from NPs. Therefore it is beneficial to include comparisons to ensure that signal detected is arising from NPs. As previously shown metallic NPs give rise to contrast with TEM, allowing the visualization of NPs and NP clusters localized within the cell, thus confirming that NP uptake has occurred. TEM images of HeLa cancer cells treated with cerium dioxide NPs and SPIONs were acquired following reflectance imaging, allowing visualization of the preserved ultra-structural detail within the cell and intracellular NPs (Figure 4.15). This is a methodology termed Correlative Reflectance and Electron Microscopy (CREM), which falls into a sub-category of CLEM experiments. Different protocols were tried to obtain the best possible quality and correlation and the main findings are summarized below.

4.2.6 Gluteraldehyde fixative provides ultra-structural preservation

Generally for light microscopy investigations PFA provides sufficient fixation. However, when cells must withstand the dehydration and infiltration steps of TEM processing, Gluteraldehyde (GA) fixation is often necessary. The use of a short PFA fixation alone can lead to coagulation of the cytoplasmic and nuclear constituents, also known as the induction of cell death. For this reason, in CREM experiments, an initial fixation with PFA was used, followed by a longer fixation in 4% PFA / 2% GA. This mixture of both takes advantage of the fast penetrating PFA monomers, and the slower penetrating but fast fixing GA monomers. This is advantageous as the speed and degree of cross-linking are two important factors in adequate fixation. Initially, before reflectance imaging, cells were fixed with standard 4% PFA. Following LM imaging, the cells were post-fixed for one hour in 4% PFA / 2% GA. TEM imaging of these cells indicated that coagulation of the cytoplasm had occurred in the majority of samples imaged (Figure 4.13A). This suggests that the fixation was not adequate, or the imaging was too intensive. Therefore the use of GA in the initial fixative was assessed at a concentration of 2%, and again, following LM imaging, the cells were post-fixed for one hour in 4% PFA / 2% GA. This led to a well preserved ultrastructure (Figure 4.13B). This indicated that in these CREM experiments the first initial fixative should be carried out with 4% PFA and 2% GA, in addition to the post LM fix, to facilitate the optimal ultra-structural preservation to allow accurate conclusions regarding the investigations.

4.2.7 CREM protocol

Figure 4.14 shows a schematic of the protocol for acquisition of reflectance images and subsequent TEM processing. The protocol is described in more detail in Appendix Figure B.1.4. Briefly, cells were seeded on gridded MatTek dishes to facilitate relocation of specific cells across modalities. RCM was performed following the initial hour long 4% PFA / 2% GA fixation. RCM should normally be performed prior to R-SIM imaging to minimize

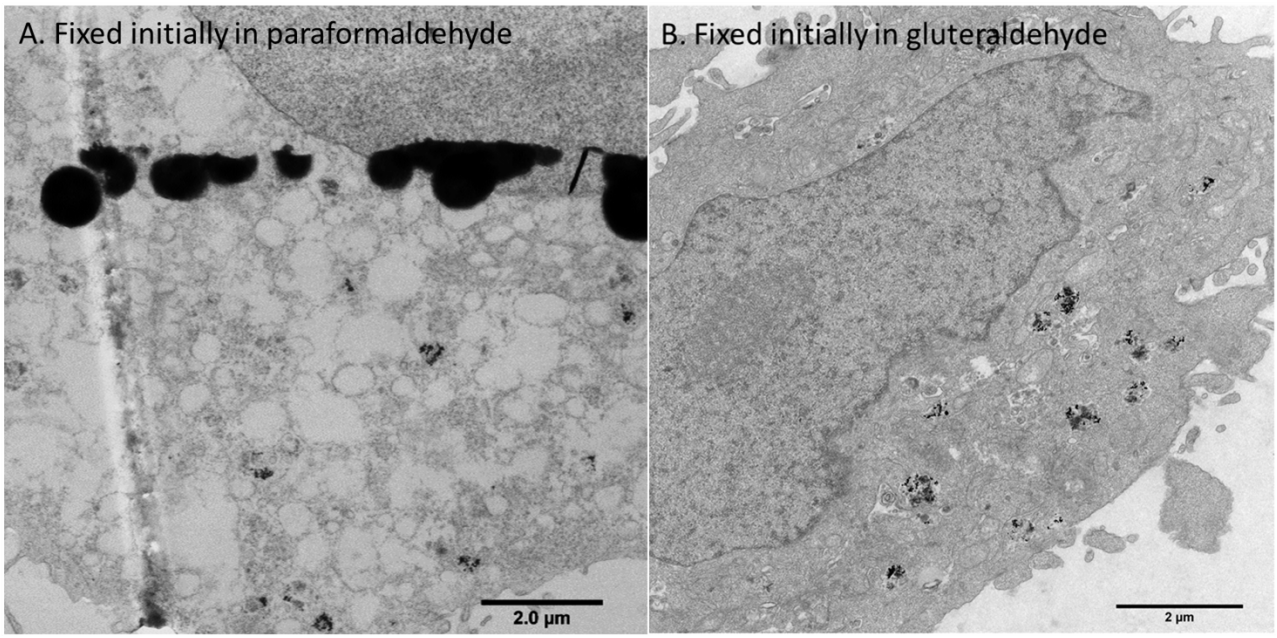

Figure 4.13: Fixation with PFA or PFA/GA for LM followed by TEM. Initial fixation prior to LM was in 4% PFA. A) Shows the resultant TEM images of cells fixed in PFA prior to LM; coagulation of the cytoplasmic components is evident. B) Shows the preservation following an initial fixation in 4% PFA / 2% GA. Ultra-structural preservation is clearly better when the initial fixative includes GA. The effect of staining artifact is also visible in A.

photobleaching of fluorescent stains used to mark the cytoplasm, nucleus and lysosomes. RCM Z-stacks of an entire grid square using the 100X objective at Nyquist sampling rate should be performed. This procedure allows acquisition of maximal information. Following RCM imaging, individual cells were identified using the RCM grid square / map, and R-SIM Z-stacks were acquired. Cells were then post-fixed with 4% PFA / 2% GA for 1 hour and subjected to standard TEM processing (fixation, dehydration, infiltration, sectioning and staining) as detailed in Appendix Figure B.1.4.

Acquiring data with different sample processing steps and using several modalities poses significant problems in terms of cell identification and image registration, limiting the widespread use of CLEM. Strategies have been developed and employed to circumvent these problems. The approaches include the use of completely integrated imaging and alignment systems, the use of fiducial / navigation markers to aid realignment and automated computational work-flows to realign post acquisition [265, 264, 336, 266]. The

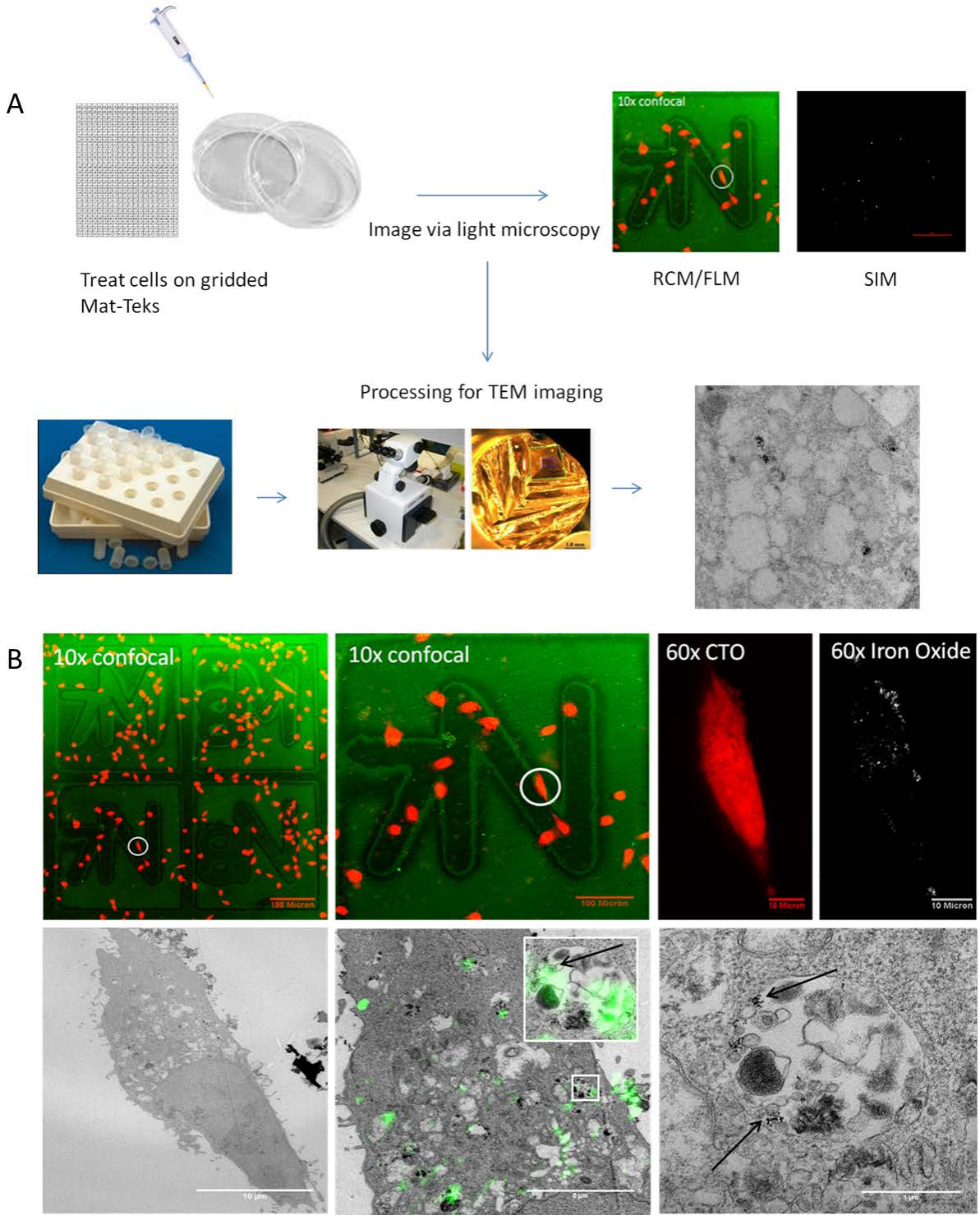

Figure 4.14: Depiction of the CREM protocol stages to obtain correlative images of NP treated cells. A) Cells were seeded onto a gridded MatTek, 24 hrs later they were treated with NPs for 1 hour and labeled with fluorescent dyes (CTO or CTR for cytoplasm stain, and lysotracker for lysosomes). Cells were fixed in 4% PFA / 2% GA and imaged by RCM and R-SIM. Following a second post-fix cells were processed for TEM. Cells were relocated using the RCM grid map. B) Example of the process. Confocal and TEM of fixed A549 cells treated with SPIONs. Cell outlines are highly preserved facilitating identification of the same cell. The ultastructure of the cell is well preserved and the sub-cellular localization of NPs within vesicles is evident. Individual NPs can be visualized distinctively at high magnification up to 30,000X.

limiting factor in many of these procedures is cost, therefore computational realignment post image acquisition was performed in this case. To maximize the accuracy of realignments, roughly equivalent areas should be registered from the different modalities. Table 4.1 summarizes the specifications that were determined for each technique. Different modalities will include different amounts of Z- information. Adjacent TEM serial sections can be registered automatically using the MATLAB imregister function in 'multimodal' configuration using optimized parameters. MATLAB automatically calculates the intensity-determined rigid transformation between given sections. Following registration, a minimum intensity (min) projection combines information from each image plane. This resulting min-projection TEM image can be co-aligned with correlating RCM and SIM optical slices. It is beneficial to include multiple optical sections from SIM, due to the narrower Z-FWHM when compared to RCM, to ensure that information is consistent between modalities.

	Max observed X-Y Resolution	Max observed Z Resolution	Theoretical Optical thickness	Live	Large Image	3D volume
RCM	>340 nm	1077 nm	~480 nm	Yes	Yes (~ 1 hr)	Z-Stacks
R-SIM	>115 nm	685 nm	~685 nm*	Yes	Yes (~24 hrs)	Z-Stacks
TEM	>4 nm	NA	~70-150 nm	No	No	Serial Sections / Tomography

*Approximated by the Z-PFS as this greatly depends on the RI of the sample and the extent of out of focus light.

Table 4.1: Comparison Table of the Achievable Specifications from each modality

The rigid ICP-algorithm can be used to aid identification of matching planes between TEM and LM. Non-rigid registration would be unsuccessful in determining the co-aligning planes because it would deform features in every plane to such an extent that the error would be minimal and consistent. This would prevent distinction between the actual matching slice, and other deformed slices. Segmentation of TEM and RCM cell outlines

(in manners discussed in Section 4.2.9, with examples for TEM shown in Appendix Figure B.8, and transformation of the RCM image by the ICP- algorithm determines planes that align, i.e. the Z-stack plane with the minimum Least Squares Error (LSE). The accuracy of the ICP algorithm is dependant upon the number of iterations; as the number of iterations increase so does the computational cost (Appendix Figure B.10.). Accurate registration in CLEM protocols is hindered by alterations in cellular morphology, such as shrinkage, that arise due to the sample preparation methods in TEM processing, such as dehydration steps and sectioning. This imposes constraints on the resultant correlation. Cells with irregular shapes or large sizes have areas that may experience shrinkage at different rates compared to the bulk of the cell. Semi-automated methods, such as user input of defined points on the images, such as on the cell cytoplasm or nuclear regions, can facilitate accurate realignment using MATLAB built in functions, such as CPSelect and imwarp, or ImageJ plug-ins such as TurboReg. MATLAB can compute the transformation matrix using these matching points. This however is open to bias, as it requires user input of point pairs, and is therefore also time consuming. Alternative fully automated methods can also be employed that rely on the nuclear segmentation in reflectance and TEM images to increase accuracy, and decrease realignment time and errors. Figures illustrating some of these segmentation and registration methods are displayed in Appendix Figures B.9 and B.10.

The Coherent Point Drift (CPD) algorithm offers a promising solution. Appendix Figure B.10 (bottom right) shows how the DAPI nuclear regions, segmented using fluorescent stain, and TEM image can be compared and registered automatically. The DAPI region on the TEM will shrink the most extensively, due to its intracellular location, and therefore provides a landmark for registration. Appendix Figure B.10 (bottom left) shows the result of the transformation calculated from the DAPI CPD realignment subsequently applied to the NP channel. In this instance the automated transformation works well. However this method is currently limited to images that contain distinct features (such as multi

nuclear cells) Appendix Figure B.10 (bottom left) [337]. Realignment methods should be explored further to increase the efficiency and accuracy of fully automated realignment between modalities.

4.2.8 Correlation of reflectance image data to TEM

Following alignment, correlation between reflectance signal, both RCM and R-SIM, and TEM signal can be visualized in HeLa cancer cells treated with NPs (Figure 4.15). The signal detected with R-SIM appears to correlate with the TEM signal with increased accuracy, in part due to the increase in resolution that allows the separation of nearby clusters (Figure 4.15). The signal detected across all three modalities co-occurs with signal from fluorescent lysosomal stain, indicating the localization of the NPs within the cell (Figure 4.15). The intracellular localization of NPs inside vesicular structures provides additional information regarding the sub-cellular trafficking of these NPs within the endocytotic transport system (Figure 4.14). It is also clear that signal detected from the reflectance modalities corresponds to multiple NP clusters (possibly agglomerates) rather than single NP structures. In some cases reflectance signal does not co-occur with signal on the TEM image, this likely corresponds to TEM signal from neighboring sections. This occurs because, despite the increase in TEM section thickness used in this study, the volume is not exactly the same and particles from up to 7 optical slices may be included into one RCM slice. Therefore, for further quantifiable correlative studies, imaging of multiple serial sections in TEM would be beneficial to create an imaged volume. It would be of interest, in such an experiment, to utilize 3D CREM to systematically evaluate the number of NPs per reflectance spot, in order to evaluate the sensitivity of each technique.

Signal from cellular matter often resembles NP signal when assessing TEM images at 1900X magnification. However when magnification is increased to 30,000 it becomes much more apparent which of these are signal from NPs and which are signal from cellular matter (Appendix B.11). This could be confused for discrepancy between TEM and

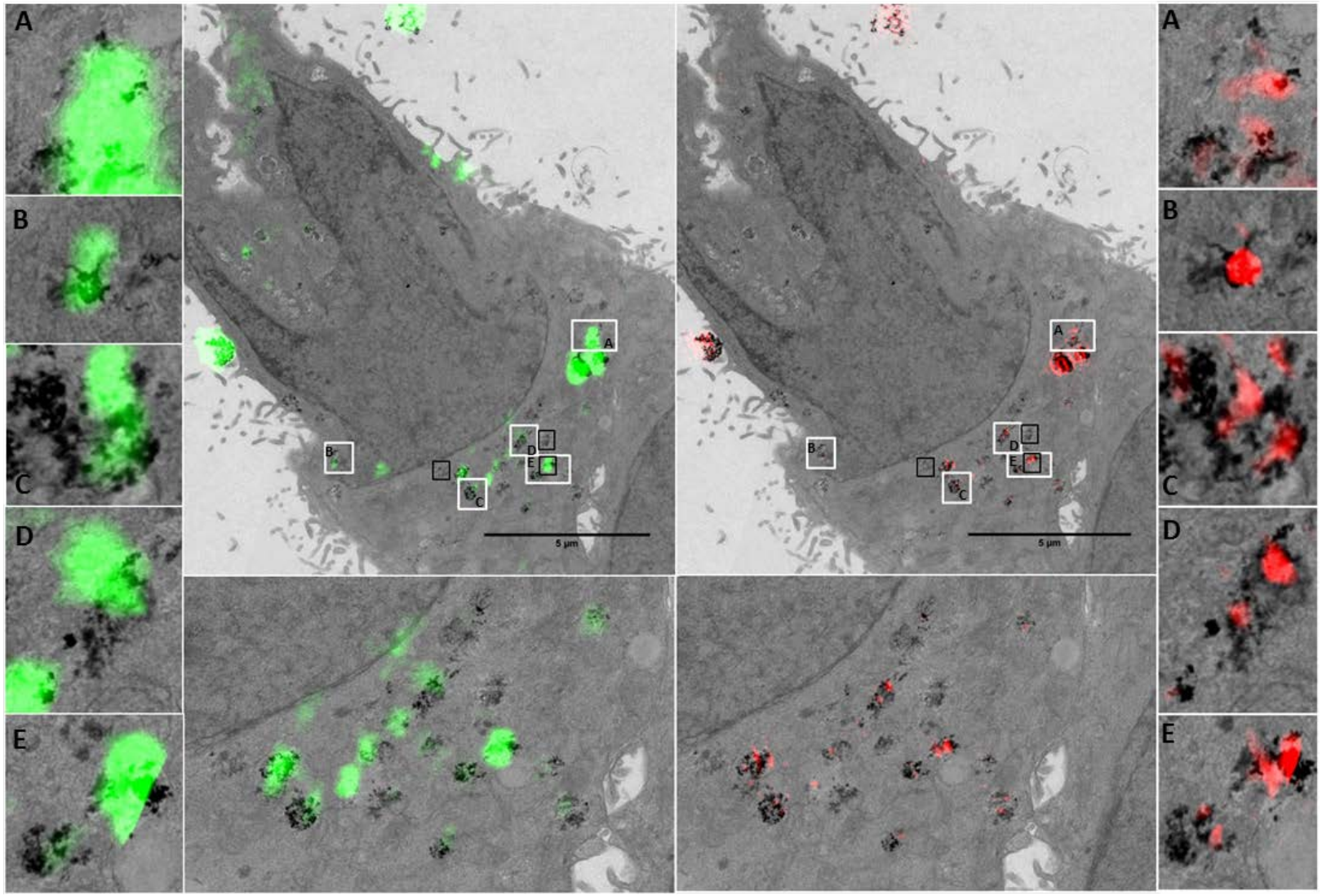

Figure 4.15: Cellular uptake and localization of cerium dioxide NPs visualized by RCM, SIM and TEM. Reflectance and TEM overlays of HeLa cells treated with cerium dioxide NPs. The cell outline in both TEM and reflectance microscopy is highly preserved, facilitating identification of the same cell. The ultrastructure of the cell is preserved and the sub-cellular vesicular localization of NPs is evident. Individual NPs can be visualized at high magnification with TEM. RCM has a theoretical optical thickness of 480 nm. R-SIM has optical thickness approximated by the FWHM-axial, calculated to be 685 nm. Adjacent image sections were combined so that the thickness across modalities was as consistent as possible. Reflectance intensity arising in both RCM (green) and SIM (red) correspond to regions detected by TEM. White boxes show regions of correlation between all three modalities with increased magnification. Black boxes show regions that are presented in Appendix Figure B.11.

reflectance images, if only low magnification was evaluated. In other cases, small NP clusters may be masked by larger nearby clusters. The light scattered by an object within a sample is dependent upon physical properties such as size and density [334, 335]. It is therefore possible that regions not detected on SIM or RCM, but detected on TEM are not sufficiently agglomerated or aggregated and therefore do not give rise to a detectable signal in the reflectance techniques. It would be beneficial to combine the study with TEM-EDX to determine if NP are present at specific locations within the sample. The presence of cellular structures with increased inherent reflectance above or below NPs may effectively mask the signal, in particular with SIM imaging. This effect could be examined further by comparing reflectance and TEM images of cells treated with NPs coated in a dispersing, non-toxic surfactant, thereby decreasing agglomeration, in order to identify a potential decrease in correlation between the reflectance techniques and TEM. It would be important to determine the extent of this masking effect, if it is indeed occurring, as it could prove to be a limitation of this technique for translation to other samples, such as within highly scattering tissue environments.

The combination of reflectance image acquisition and subsequent correlation to ultrahigh resolution TEM imaging can increase the confidence that the signal detected by each modality is originating from NP internalization within cells, and not an artifact from processing and imaging. The combination of techniques also offers maximal information regarding a single sample as each technique offers different advantages and disadvantages in terms of the imaging specifications (resolution, optical thickness, live and 3D capabilities), summarized in Table 4.1. TEM provides the superior NP detection capabilities and remains uniquely able to resolve NPs and NP clusters. Whereas the use of reflectance methods provides a relatively cheap, alternative technique, that is compatible with fixed and live cell imaging through 3D samples with, in the case of R-SIM, super-resolution. However, resolution of individual NP and absolute quantification of individual NPs inside cells requires time consuming, ultrahigh magnification imaging with TEM and data inter-

pretation is complicated with some materials due to low contrast [218]. New correlative methodologies that combine spatial elemental analysis, such as ICP-MS at small intervals using techniques such as laser ablation / desorption could provide a means of integrating absolute quantifications into different imaging protocols [182, 183]. This could prove extremely beneficial for developing algorithms and models that can accurately determine the relationships between microscopically observed signal and elemental NP concentrations. Once determined, this could then be applied to enable the extraction of absolute concentrations from either reflectance data, or TEM image data: this is discussed further in subsequent sections (Chapter 6).

4.2.9 Image analysis protocol

Reflectance background intensity is inherent to images as these techniques do not selectively capture reflectance originating from NPs. A high level of unwanted background signal can occur particularly within the highly scattering environments such as cells. This is due to the large number of interfaces of differing RIs that exist within most biological samples. This high level of background can reduce the detection of NPs and lead to associated problems when attempting to quantify relative signal intensities, which, compared to noise components, is a relatively small portion of the total signal [227]. Figure 4.16 illustrates the issues with background scatter in RCM. Both images contain reflectance signal from the cell itself, whereas the treated cell also contains regions of high intensity. These regions presumably arise due to the NP treatment. However, when quantified, the NP treated cell appears to have lower mean intensity (57.4) than the control cell (58). This was a recurrent problem. Therefore preprocessing of images to remove this sort of cellular auto-reflectance, along with any other artifact / noise is necessary. Unwanted background noise (intensity) in reflectance images arise due to intrinsic photon noise (shot noise), detector electronics (Gaussian noise), auto reflectance and artifact (Poisson noise) [327, 227].

The following image acquisition protocol was therefore developed for reflectance images

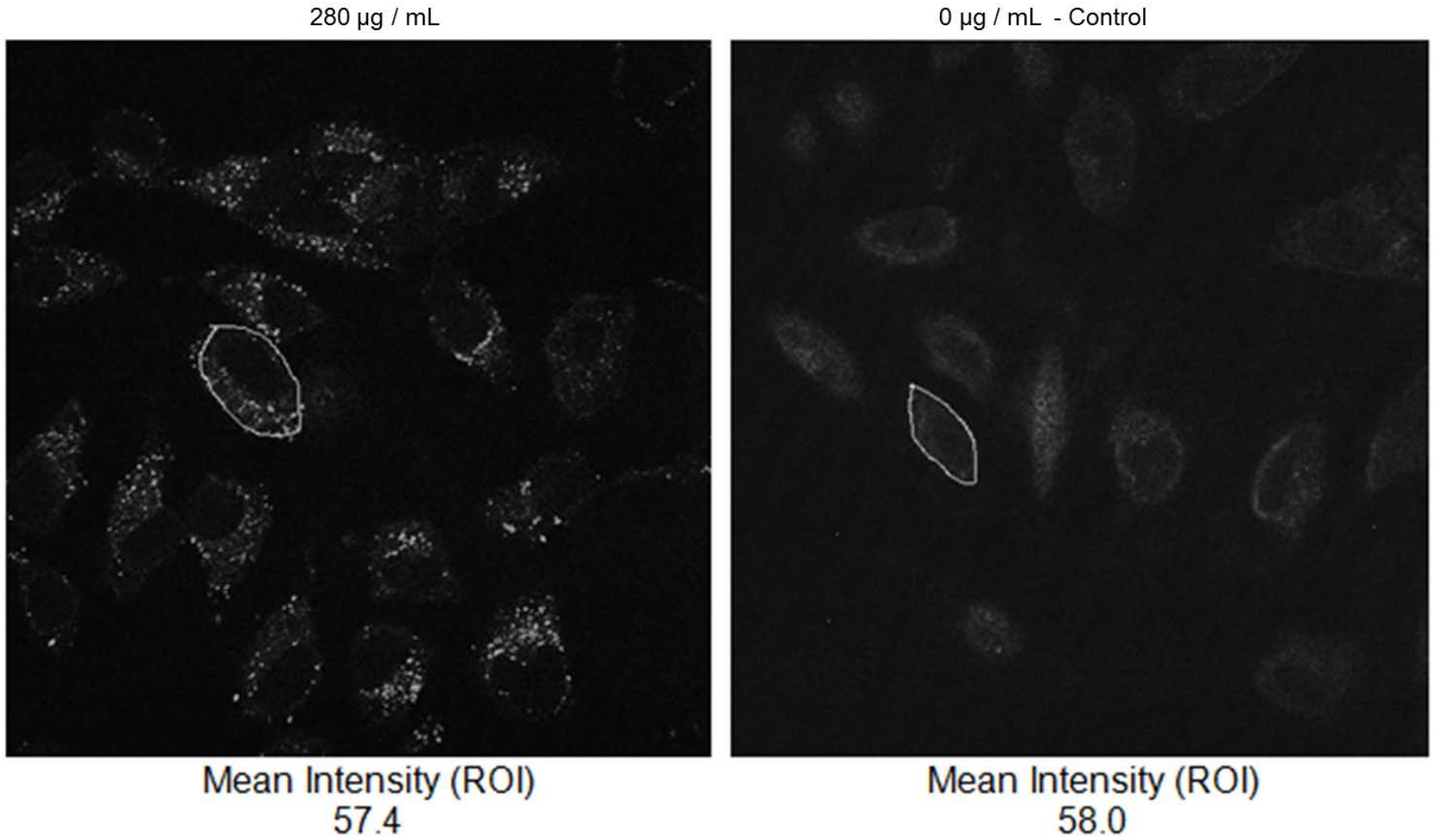

Figure 4.16: The result of suboptimal imaging and quantification of reflectance images. The images acquired with RCM contain background intensity that can skew the results of an experiment (seen as white haze across the cell cytoplasm in both treated and control cells). This example highlights the necessity for optimization of the imaging procedure and appropriate analysis methods. The mean intensity of the cell highlighted in the image is written below each image; the mean intensity of the treated cell is actually lower (57.4) then the control cell (58), despite clearly displaying high intensity signal.

involving computational post processing for the sequential segmentation of cells and intracellular regions of interest (NP). Although the work-flow here is designed for RCM images, the same techniques can be applied to SIM images, and to an extent, TEM images. Similar methods have been recently applied for the analysis of fluorescent, images indicating the scope of the workflow [338]. These detected regions can then be analysed for a host of parameters such as number, size or intensity values which can easily be applied in 2D or 3D for specific studies. This method significantly reduces the time associated with image processing and analysis providing an unbiased means of attaining consistent results. The processing steps involve noise removal, signal segmentation and numerical extraction of relevant values. Each of these will be described in the subsequent section for both the fluorescent cell stain and the reflectance NP signal and then the workflow summarized. The main stages include: 1) the automated cell-segmentation facilitated by CTO staining, through a process of denoising (Gaussian smoothing) and intensity clustering (K-means) and 2) NP segmentation, consisting of denoising (Gaussian smoothing), background subtraction and intensity clustering (K-means). Different parameters, such as detected spot area, detected spot size, number of spots present and cell intensity, of the resultant segmented cell regions can then be collated to give a thorough picture of the NPs behavior following cellular internalization.

4.2.10 Cell segmentation

Cytoplasmic dyes aid image segmentation, providing strong contrast at intracellular locations. Therefore CTO was used to stain the cellular cytoplasm. A variety of segmentation algorithms exist, as introduced previously in Section 1.3.15.1 [274, 273]. A combination of K-means clustering and watershed segmentation was performed to identify and separate touching cells (Figure 4.17A). First, the image was smoothed by convolution with a Gaussian kernal (radius of 4, sigma of 2) and normalized (to scale the values between 0 and 1). Then K-means clustering was performed to assign pixel values to clusters. K-means clustering, also known as Lloyds Algorithm, is a simple unsupervised clustering method,

originally proposed by Lloyd in 1957, and first used by MacQueen in 1967 [339, 340]. K-means partitions 'n' observations into 'k' clusters, based on pixel intensity and distance from the mean of the assigned clusters based on the Euclidean distance. This process is then iteratively refined until the cluster means do not change [339]. Cluster means can be initiated prior to segmentation to facilitate consistent segmentation groups. Other methods are available that permit segmentation (Appendix Figure B.12). However, as the CTO cytoplasmic stain is intense, K-means clustering is sufficient (Appendix Figure B.12). The number of clusters that K-means will search for can be input into the algorithm manually, and normally represent the number of different types of signal that would be present, i.e. cell background, noise and signal (3 clusters). When assessed, using 3 and 4 clusters resulted in segmentation of the boundary, indicating the robust nature of the technique. Despite this, some differences were seen between using 2 and 4 clusters (Appendix Figure B.12) therefore 3 clusters were used. This effectively segments foreground objects from background, however, cells that are touching will segment as one object (Figure 4.17). Therefore a watershed transform was applied. The watershed transform is a region based segmentation originally proposed by Digabel and Lantujoul. The underlying principle is that of a gradient landscape being flooded by water, where the watershed barriers are placed at partitions where regions would meet. This results in barriers that constitute the watershed segmentation [341]. For this to be successful constraints need to be placed on the energy minima. This can be done automatically or by manually picking a threshold. In order to do this, the built in MATLAB function 'IMHMIN' was performed, which suppresses minima to a value below a certain user set threshold (in this case 2). When applied, touching cells were effectively separated, seen in Figure 4.17.

4.2.11 NP segmentation

Before segmentation the inherent background reflectance originating from cellular constituents must be removed. There are multiple ways of dealing with background effects.

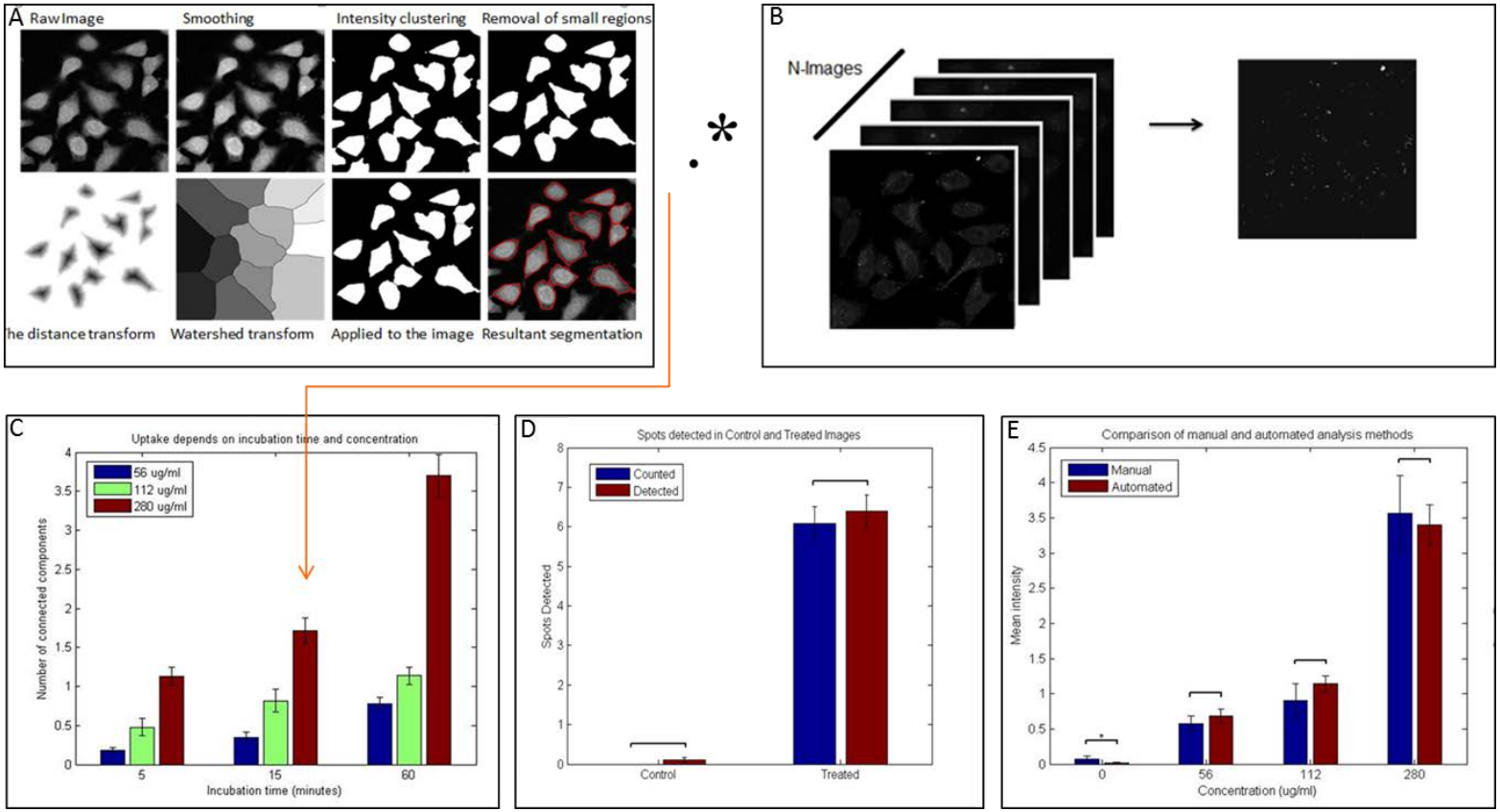

Figure 4.17: Example of the analysis work-flow that can be applied to reflectance images A) Shows the various stages for cell segmentation. B) shows the method of segmentation of NP images. C) Example of results that can be expected following the example imaging protocol and analysis method. The elapsed time for analysis of 122 images with roughly 10-20 cells per image is 124 seconds (following data loading). D) and E) Verification of the technique was performed using as a measurement of connected components and as a comparison of intensity values obtained using the algorithm compared to the gold standard of manual delineation. Intensity values obtained for NP time and concentration incubations via both methods show no statistical difference. Control groups showed significantly less signal when analysed by the automated system, this is likely due to the large number of samples that can be analysed when using automated software (control =294; low=238; mid=206; high = 371) compared to the manual analysis (control =25; low=56; mid=47; high = 109). When comparing spots detected by eye to those detected by the software, good agreement is seen across a large number of cells (Control: 88 cells and Treated: 76 cells). No statistical difference was seen between the groups. More spots are detected in control cells by the software.

Control images provide a reference background intensity, however, laser fluctuations with temperature and time can lead to changes in the intensity incident to the cells and this can alter the actual effects on an image to image basis. Therefore the image itself can be used to calculate the background in a method known as background subtraction. First the image was normalized to scale values between 0 and 1, then morphological opening of the image was performed to increase the size of elements within the image, using a level radius value of 4 (which is assumed to be the size of the smallest element of interest within the image - roughly equivalent to the PSF). This creates a background image that can then be subtracted (Figure 4.17B). This dilation is performed with a radius of 4 pixels. Following removal of the cellular background, K-means clustering is performed with a cluster number of 3. The cluster number represents the different groups of pixel intensities that one might observe. In this case, for a treated cell, the expected pixel intensities arise from image background, auto-reflectance and NP signal. K means clustering classifies these pixels into three groups. However, if K-means clustering is to be performed on treated and control cells, then the cluster means of the different signal groups would differ between image types - and the expected number of clusters in control cells would be 2. This would cause inconsistencies in the analysis and segmentation of information that is not comparable across images groups. Therefore, prior to segmentation, the images were placed into a n-(3)D matrix or stack. In this way, control and treated samples are segmented relative to one another, simultaneously. In this way, segmentation is always occurring relative to control cells within the group, increasing accuracy. An example of the segmentation is shown in Appendix Figure B.14. This combination of background processing method and segmentation of NP signal was determined to preserve the most signal when compared to alternative processing routines (Appendix Figure B.13). An overview of the entire cell and NP segmentation and analysis process is given in Appendix Figure B.16.

4.2.12 Process of analysis in MATLAB

Once the segmentation routines were verified, the processing methods can be applied to entire data sets sequentially using MATLAB for loops, to automate the procedure.Firstly the images are loaded into a data struct into MATLAB using bfopen (from loci tools). Each image is separated into its channels (CTO, DAPI, NP and Tranmitted light for separate processing). First the CTO stain in the fluorescent 561 channel is used to segment all the cell outlines in the entire data set, giving a binary image of segmented cells. Then the reflectant image channel from each sample is combined into the 3D-stack, the stack is normalized, background subtracted and segmented using K-means to give binary NP images. Segmented cells and segmented NP are then multiplied together, this removes any binary NP signal that is not intracellular. Then each image is looped through sequentially, and each cell is assessed. Parameters can be automatically determined from binary images in this way, including the number of isolated regions and the size of these isolated regions. Additionally, the segmented cell and NP image can be multiplied by the original image to get a segmented image that contains intensity values. This segmented intensity image is used to generate the 'mean intensity value'. The mean intensity value across the whole cell is measured for each and every cell that is detected across the image data set. These results are linked using the number of the iteration (i) to the exposure concentration and exposure time. Once the entire routine is performed on the data set, MATLAB can generate graphs of the acquired data. This entire process is presented in Appendix Figure B.16. The method of writing this process into MATLAB is also detailed in the Appendix following Figure B.16.

4.2.13 Verification

The automated technique can be validated by comparing the results generated to those obtained via manual methods for different parameters. In order to compare the number of detected NP spots, the number of spots can be assessed by eye across a range of treated and

control cells. This can then be compared to the number of connected components detected using the developed work-flow (Figure 4.17D). This indicated that similar numbers of regions are identified using either approach, with no statistical difference. To further verify and assess the accuracy and success of the automated method, the outcome of the mean intensity analysis of multiple sample groups can be compared to manual measurements. Manual measurements were obtained using hand drawn ROIs of background subtracted images using ImageJ. This was performed for a variety of concentrations in two cell lines, HeLa and A549 cells, (HeLa shown - Figure 4.17). These results were then compared to those generated by the automated method (Figure 4.17E). The same conclusions can be drawn from both methods for the different data groups, with no statistical difference between the numbers obtained (Figure 4.17E). Additionally both methods show similar performance when analysed via Receiver Operator Characteristics (ROC) curves using GraphPad Prism, which compares the sensitivity and specificity of different techniques by analyzing the values of treated and control groups (Appendix Figure B.15). The area under the curve, which is a measure of accuracy was slightly better in the automated method (0.89 compared to 0.88) and the standard deviation was lower (0.013 compared to 0.027). More spots are detected in control cells by the software when compared to the manual method, this is likely due to random high intensity artifact or protein aggregates within cells, which would not be counted during manual detection, but whose intensity would allow inclusion into the detection software. Verification was also performed on A549 cells however the data is not shown as conclusions reached were consistent with the HeLa cell analysis. Speed of analysis is a limiting factor in some investigations. The speed of analysis is much faster with the automated software, roughly 1200 cells can be analysed in 120 seconds, whereas manually this would take several hours. The automation of graph generation following information extraction is also very convenient for assessing the results in a time efficient manner. A box explaining the stages in MATLAB is shown in the Appendix Figure B.16. All code is available on the UoB data archive.

4.3 Conclusions

Reflectance imaging is shown to provide a label free method for visualizing NP uptake. Metal oxide NPs, such as cerium dioxide and SPIONs, introduce significant contrast into reflected light images, providing opportunity to elucidate the cellular interactions that occur during NP uptake [138, 322]. Reflectance imaging is a time effective investigative method that requires little sample preparation and can readily be used in conjunction with fluorescence imaging, offering significant advantages over TEM alone. The utilization of a commercial N-SIM module to acquire reflectance imaging data offers a 2-fold increase in resolution compared to RCM [322]. This allows clusters of NP separated by ∼115 nm to be detected and resolved. This is a necessary pre-requisite for subsequent accurate colocalization studies to determine the precise localization and trafficking route of NPs within cells, the elucidation of which is critical to the future success of NPs for therapy vehicles in biomedicine. R-SIM as a method is validated by the comparison to RCM and TEM, confirming cellular entry of electro-dense NPs and their sub-cellular localization. Together the combination of imaging techniques maximizes the information that can be gained from a sample regarding NP uptake route, uptake form (single NPs or NP clusters) and sub-cellular localization. In this chapter two different metallic NPs of significant environmental and biomedical interest, SPIONs and cerium dioxide NPs, were used. Cerium dioxide NPs are advantageous as they are slightly larger in core size than Sienna$^+$ SPIONs, as shown in section 3.2.1, and scatter light very efficiently. Both NPs have been visualized through all three means, revealing information about the cellular uptake of these NPs in addition to insights into the relative merits of these different imaging techniques.

While it is true that reflectance lacks specific labeling, when controls and TEM imaging have been performed alongside the diffraction limited objects visualized in treated cells and not control cells can be determined to be NPs. This is evidenced when comparing TEM and RCM images of the same samples. Correlative techniques provide the

maximum amount of data within experiments, but the choice of imaging method or combinations of imaging methods used for each experiment will depend upon the nature of the sample and type of investigation. For example where high resolution is not absolutely necessary, such as determining if NPs are or are not inside cells, then RCM would be the most advantageous as it can be done quickly across a large sample size. Likewise if the composition of the NPs leads to a better detection with RCM, then RCM would be employed. R-SIM can provide additional information. If R-SIM detects the NPs efficiently, and high resolution co-localization studies are required, then R-SIM will offer increased precision and accuracy for the investigation. TEM will exhibit unrivaled resolution in NP investigations provided that the NPs introduce contrast with TEM. However, due to the limited throughput it cannot be employed in larger investigations with many samples. Likewise correlative methods can be extended to the use of analytical techniques which are rapidly being developed to facilitate spatial sampling of elemental or spectral information. This could be employed when absolute quantifications are required and to establish relationships between signal detected microscopically, and NP / elemental concentrations.

The reflectance image analysis work-flow that was developed and employed in this thesis offers significant benefits for NP investigations. It provides an HTS, automated, consistent, time efficient and robust solution for determining reflectance signal within treated cells compared to control cells, crucial for the identification of specific factors involved in NP uptake. The method would be applicable to a host of experiments that involve the internalization of reflectant substrate, such as toxicity, endocytosis and mechanism of uptake studies. The software can be extended to co-occurrence or colocalization analysis. This can involve images from two modalities (as shown here with RCM and R-SIM) or can include fluorescent compartment segmentation, including a quantification of co-occurrence step for the NPs within labeled cellular compartments (Pearson correlation values, M1 and M2 coefficients, object-based), as exemplified later in Chapter 5. The image analysis work-flow is applicable to other types of reflectance images. The same pre-processing and

segmentation techniques can be carried out on R-SIM images (see Figure) 4.10 for quantifying NP uptake. Correlative approaches that utilize both SIM and confocal reflectance can therefore be overlaid and compared following automated analysis. These comparisons can give insights into the differing detection and resolution capabilities of the instruments.

The examples presented so far demonstrate the method analysis for 2D images. However due to the potential multi-dimensionality of the analysis methods, the procedures could easily be extended for the 3D analysis of reflectance images (Appendix Figure B.17). The method presented here will form the basis for automated assessment of nanoparticle uptake, localization and impacts, both toxicological and therapeutic, and could become an established part of regulatory decision making in due course, both for nanomedicines and NPs in consumer products.

4.4 Key Findings

1. Metallic NPs, in this case CeO2 and SPIONs, give rise to significant contrast with RCM, providing a cheap and quick method for visualizing NPs with a theoretical X-Y resolution of 200 nm, but measured FWHM of 340 nm.

2. Metallic NPs, in this case CeO2 and SPIONs, and some non-metallic NPs, polystyrene, give rise to signal with R-SIM, this provides an increase in resolution in X-Y up to 110 nm, which can be advantageous for specific studies.

3. The detection capabilities of R-SIM appear inferior to that of RCM in this case of CeO2 and SPIONs.

4. Correlation of reflectance and TEM images indicates that reflectance modalities can detect a large portion of NPs within cells and therefore can be used in subsequent studies

to assess the uptake and effects of these NPs relative to control / untreated cells.

5. Automated processing of reflectance images facilitates removal of the strong reflectant background that arises due to the highly scattering intracellular environment allowing quantitation of signal.

6. Automated work-flows greatly reduce processing and analysis times from several hours to just a few minutes, and can be designed to be applicable to a variety of different experimental work-flows and image types. Verification of these methods to manual analyses provides assurance on the results obtained.

CHAPTER 5

DETERMINING THE CELLULAR UPTAKE OF SPIONS

5.1 Chapter introduction and summary

The increased exposure to NPs and their accumulation potential gives rise to an urgent need for characterization of the NP-cell interactions that occur during exposure. NP with different physicochemical properties can induce different cellular outcomes. Understanding how specific properties lead to particular cellular internalization patterns of NPs is necessary in order to tailor the design of NPs for specific purposes, such as localization within target cells and reduction of off-target effects. The degree of internalization will depend largely upon the properties of the NPs in the exposure medium, such as size and agglomeration potential, and the previously discussed and characterized 'Protein Corona' (Section 1.2.1 and Section 3). Another important consideration is the cell population itself. Different cell types are designed to carry out very different specific functions *in vivo* and therefore have varied needs, including capacity for division and requirements for nutrients leading to modifications of internalization potential. This leads to varied cell surface protein / receptor expression, internalization mechanisms and detoxification processes. Therefore the results obtained in studies using one particular cell type may not hold true for all cell types. The specific uptake of SPIONs into macrophage cells is well studied, due to their involvement in SPION clearance following *in vivo* administration [168, 163, 164].

However, uptake of SPIONs into other cell lines is less well studied. Additionally, following exposure, the uptake processes, clearance and trancytosis potential are unclear. Studies have suggested a variety of mechanisms for the internalization of carboxydextran coated SPIONs, including caveolar endocytosis, CME and macropinocytosis in different cell types [157, 173, 152]. Gu *et al* found that CME, caveolin and macropinocytosis were all involved in the internalization of SPIONs in RAW267.4 cells [157]. Calero *et al* saw that, in MCF7 cells, DMSA-SPIONs were internalized through both macropinocytosis and CME dependant upon size [173]. Bohmer *et al* found that Caveolin, rather than CME or macropinocytosis, was responsible for the uptake of sillica coated NP in HeLa cells [152]. The clarification of NP uptake route in non-macrophage cells is vital if these NPs are to be targeted specifically to cell populations to elicit therapeutic or diagnostic aid. Understanding the internalization and trafficking pathways may also facilitate better, more accurate predictions of the NP toxic potential following administration, which may depend on the uptake pathways used. It is particularly important to study SPION uptake in cancer cells due to their potential application within chemotherapeutics.

Investigation into the uptake of cargo within cell types often include the use of specific inhibitors of internalization pathways or machinery using siRNA or drugs [249, 342, 164]. For example, Kuhn *et al* and Dos Santos *et al* used specific pharmacological inhibitors to determine the differential route of uptake of polystyrene NPs in cancer cells and macrophages [342, 160, 159]. In previous studies, SPIONs, including Resovist, were shown to enter macrophages and neural progenitor cells through CME [343, 164]. Fewer studies have focused on non-phagocytosing cells, and of those performed, some had apparent flaws. For example, SPIONs were often combined with uptake enhancing agents, such as transfection medium or modified with peptides [344, 345]. Soenen *et al* used SPIONs in conjunction with transfection agents, and the conclusions regarding uptake mechanism were ascertained by colocalization studies with TF, a cargo for the CME pathway [164]. Two issues exist with this method. Firstly, it is possible that the route of uptake is

influenced by the use of a transfection reagent, which is internalized through dynamin dependent endocytosis and has been shown to escape lysosomal degradation [346]. Secondly, NP uptake mechanisms were deduced through subjective red/green image overlays of NP signal with TF signal. These types of overlays are only truly representative when the channel histograms are roughly equal, a scenario that is unlikely when different fluorophores are used [164, 347, 348]. Alternative measures of colocalization can be performed such as object or statistically based methods, which offer increased accuracy [348]. Moreover, although colocalization studies can be indicative of NP and labeled cargo residing within a common membrane bound organelle, this does not necessarily implicate a common mechanism of internalization. Determining the method of internalization solely by signal colocalization with a labeled pathway cargo is particularly confounding as different endocytotic routes can converge into a common early sorting compartment. SiRNA based approaches such as those used within this thesis circumvent some of these problems by specifically inhibiting the internalization proteins, leading to knockdown of pathways, rather than inferring the mechanism through association with cargo.

Uptake studies often involve the use of fluorescent NPs, which, as previously discussed, can lead to an alteration in the NP surface properties. This can therefore lead to changes in the uptake route and subsequent effects [164]. In this chapter, the aforementioned label free methods (RCM and R-SIM) were used to visualize NPs without the use of fluorescent tags. This allows us to visualize the Sienna$^+$ SPIONs in the administered form. The previously described analysis procedure was employed to limit bias in result generation and interpretation, and to increase sample size and therefore confidence in the results generated. A concentration and time dependent uptake of SPIONs in different cell types is established, benchmarked against the well studied macrophage model. A variety of cells were exposed, including HeLa cells, a well-established cancer cell model often used for *in vitro* studies; A549 cells, often used to model the human lung, particularly well studied in nanoscience to mimic airborne exposure; and MDA-MD-231 cells, a breast cancer cell

line. A variety of studies were performed, including the potential membrane penetration of SPIONs, which also serves as a marker for toxicity and the effect of SPIONs on cell growth. Various uptake pathways were inhibited using siRNA and in some cases pharmacological inhibitors (inhibition of phagocytosis) to determine the differential route of uptake in different cell lines. Preliminary studies, that aim to overcome some known limitations of 2D cell culture, were also included that involve 3D spheroid models, providing the starting point for continuation of uptake studies in a more physiologically relevant environment [349].

5.2 Results

5.2.1 Effect of SPIONs on cell growth

Counting the number of cells over multiple days can give an indication of the effect of NP treatment on cellular viability. Cell number is a measure of the ratio of cell proliferation compared to cell death. Cell number can therefore give indications of cytotoxicity associated with NP exposure and of effects on the cell cycle that may occur. However, this is only a measurement of the ratio and therefore if cells both proliferate and die faster then effects can be missed [350]. For these studies, cells were plated in 6-well dishes and incubated with NPs or left as controls. Cells were counted 0 h, 24 hr and 48 hr post incubation to assess any changes in the cell number. Cells treated with SPIONs appeared to show a slight but insignificant increase in number by 48 hr in both MDA and HeLA cells (Figure 5.1). Although this indicates that SPIONs do not increase cell growth, it has previously been reported that SPIONs can enhance the G2/M phase of the cell cycle and increase proliferation in human mesenchymal stem cells [45, 351].

Various groups have reported a lack of significant cytotoxicity of SPIONs below 200 µg/mL, however viability has been shown to reduce as concentration and exposure time

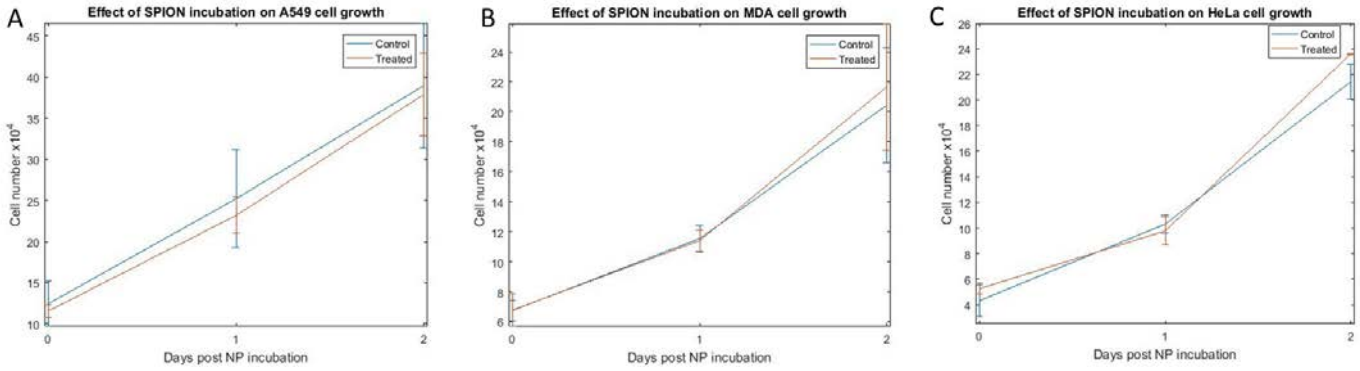

Figure 5.1: Growth of cells over 48 hours following NP treatment. The growth of cells was measured at time 0, 24 and 48 hours post NP incubation in treated cells, and at the same time points in untreated control cells. A) Growth of A549 cells, B) Growth in MDA cells and C) Growth in HeLa cells. No significant difference was observed between the treated and untreated groups in any cell line.

increase, highlighting a possible concentration-dependency of SPION-induced toxicity [62, 352, 353]. Mueller *et al*, Wu *et al*, and Berry *et al* reported toxicity due to SPIONs, including varied levels of cell death, cytoskeletal disruptions and vacuole formation [354, 164, 91, 355, 356]. It has been suggested that assessing the cytotoxic potential of such NPs requires incubation times of longer than 24 hrs post treatment and that short duration studies may miss delayed effects [174]. This could relate to delayed changes in protein expression, time scale for beginning of NP degradation, or cell doubling for example. Lunov *et al* noticed no cytotoxic effects earlier than 24 hrs post SPION treatment, but ROS induction occurred at later time points (+24 hrs) leading to delayed apoptosis and loss of cell viability [174]. This ROS induction was similar to that seen with uncoated NPs, therefore is likely related to the degradation of the carboxydextran coating. In line with this theory, SPIONs with a thinner dextran coat (therefore more easily removed) led to faster ROS induction and stronger cytotoxicity than those with thicker coats (significance at 24 hrs compared to 48 hrs) [174]. The level of ROS production within cells has been seen to correlate with NP exposure concentrations [353]. SPIONs, and therefore excess iron, accumulation is a particular problem in cells such as macrophages, due to their limited division potential, and therefore limited means of redistribution of the excess iron [174].

Cytotoxicity can lead to cell death. There are three types of cell death, including necrosis, apoptosis and autophagy [357]. These modes differ in the cellular response, for example, in necrosis, cell membrane integrity is lost, whereas in apoptosis the cell membrane integrity is preserved. The toxicity of NPs, assessed on the basis of membrane integrity, or necrosis, can be assessed using membrane impermeant dyes such as SYTOX green [358]. Dyes such as this will not cross intact membranes in live cells, however if the membrane becomes compromised it will enter the cell and bind tightly to DNA, emitting a green fluorescent signal. Cells were exposed to SPIONs at a concentration of 280 µg/mL for 1 hr. SYTOX green was applied to the cells 24 hrs post incubation and cells were fixed and mounted in Vectashield containing DAPI. In order to properly assess damage caused by NPs, a membrane permeabilization agent was included. A positive control for membrane damage (saponin) was therefore included. Saponins are steroid or triterpene glyocisdes, and they selectively interact with membrane cholesterol, removing it and forming membrane pores allowing SYTOX uptake within the cell [359]. Following treatment with Sienna$^+$ SPIONs, the characteristic yellow/green nuclei of permeabilized cells, seen in cells treated with saponin, were not evident. NP treatment at this concentration of 280 µg/mL therefore does not appear to have caused cellular damage or death (Figures 5.2 and 5.3). There has been previous evidence suggesting that some NPs can bind to, or react with, certain dyes and analytes of toxicity assays, limiting the results of this assay unless an appropriate control is performed alongside, therefore a saponin + SPION treated control was included [360]. Figure 5.2 shows example confocal images from HeLa cells depicting the SYTOX green staining and cell cytoplasm stain. It is clear that no SYTOX intensity is visualized in the negative control or SPION treated samples. These same trends were seen in all other cell lines tested (MDA, A549 and THP-1 derived macrophages). The toxicity, implied by the intensity of the SYTOX stain, can be quantified by measuring the intensity of the 488 channel (SYTOX excitation), and plotted graphically (Figure 5.3). No statistically significant difference was seen between the negative control cells and the

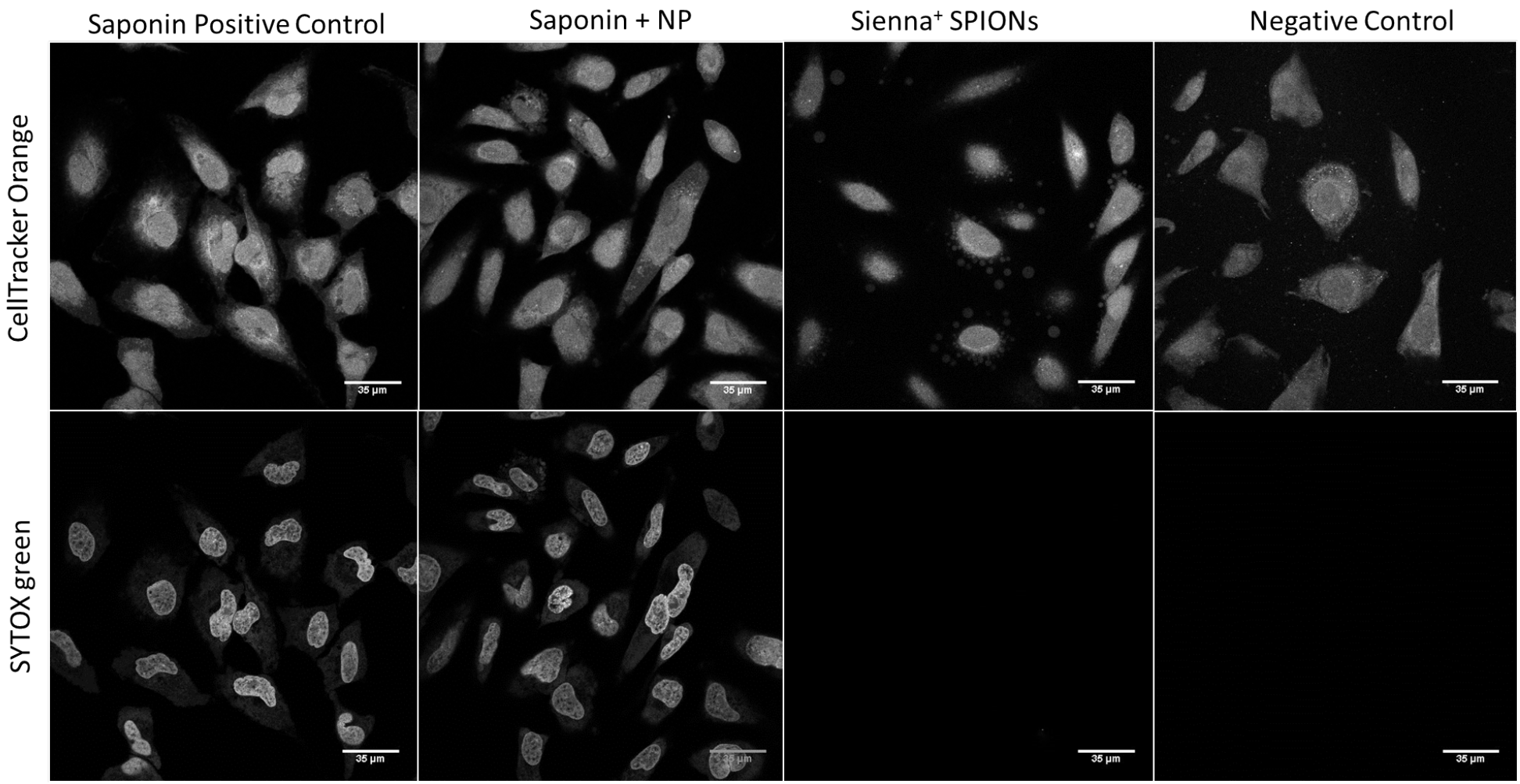

Figure 5.2: SYTOX green assay for membrane permeabilisation. The fluorescence of SYTOX dye (bottom panel) and the cytoplasmic stain (top panel) 24 hrs following incubations with saponin (positive control), SPIONs + saponin, NPs (280 µg/mL) and no NPs or saponin (negative control). SYTOX fluorescence is evident in the both samples treated with saponin, and not in the negative control or NP treated samples.

Sienna$^+$ treated cells in any cell line tested. Additionally, no significant difference was seen between saponin treated cells and NP + saponin treated cells. There was however a significant difference between the NP treated group / negative control and the cells that included saponin in the treatment (Figure 5.3).

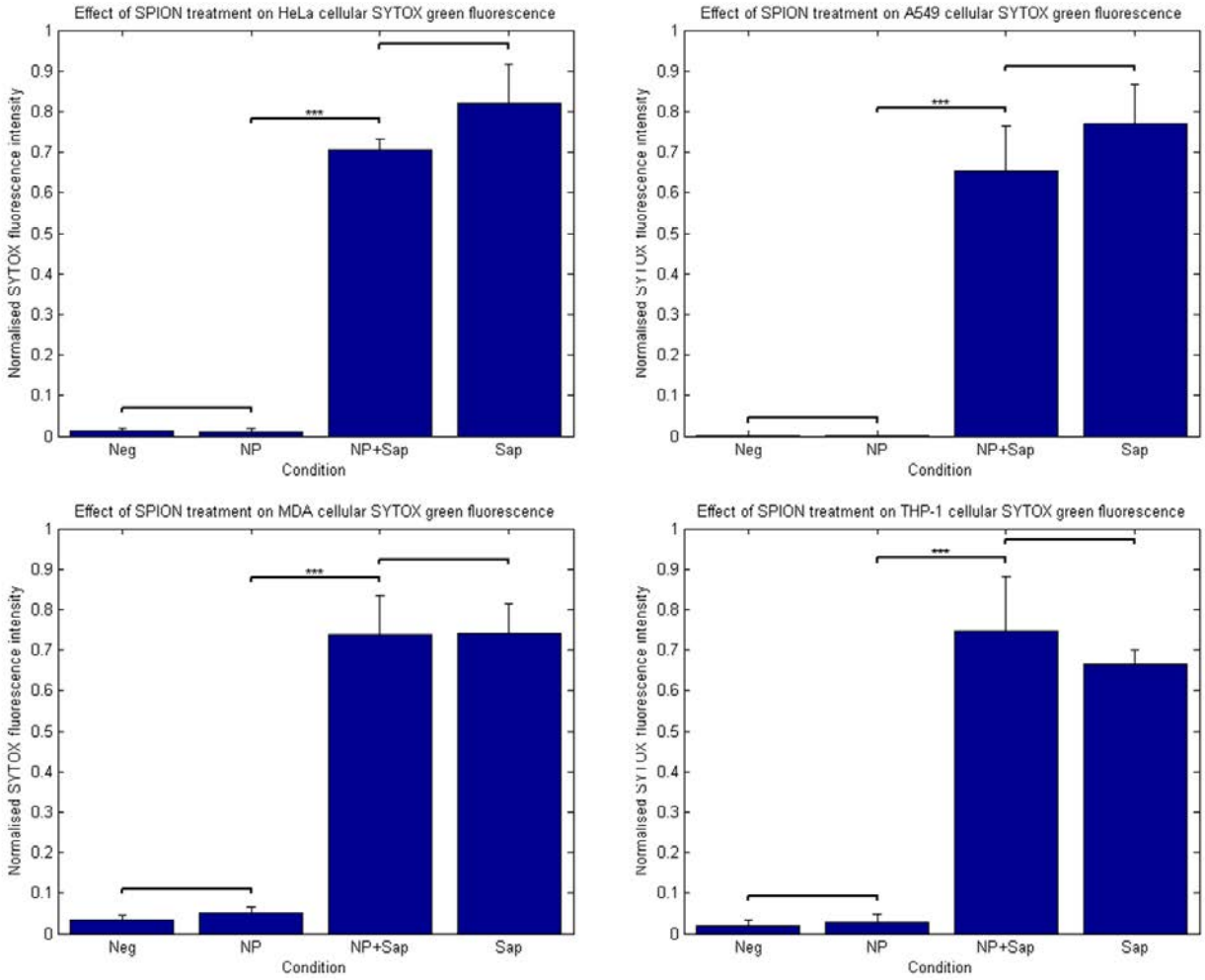

Figure 5.3: Quantification of SYTOX green fluorescence 24 hrs following NP treatment in different cell lines. Graphs showing the quantification of SYTOX green fluorescence in experiments performed in different cell lines. No statistically significant difference was seen between NP treated (280 µg/mL) and control cells in any cell line. Likewise no significant difference was seen between positive controls and NP + saponin treated groups. Mean + STD is plotted. Students T-Test gave significance of $p<0.001$ between saponin treated and non-saponin treated samples in each cell line.

The addition of the positive control (saponin) plus NPs indicated that, although NPs do appear to provide a small amount of protection from saponin induced toxicity in some

cases (HeLa and A549 cells), that there is still a significant difference between the saponin with NPs and the negative control/NP alone groups. However, Ong *et al* discussed the fact that NPs may bind to certain dyes or components of assays, effecting the result. As saponin is a surfactant known to disperse NPs it was important to test if saponin binds SPIONs reducing its availability for cell permeabilization. However, as the SYTOX signal in cells treated with saponin was not significantly different regardless of whether NPs were present, this is not a great concern. Nevertheless, the size distribution of NP preparations of the same concentration (280 µg/mL) with and without the addition of saponin was measured by DLS. Following SPION incubation with saponin, the size distribution is narrower, as seen by the size by intensity graph (Figure 5.4). Saponin containing solutions have a significantly decreased diameter (nm) ($p<0.05$) and a significantly decreased PDI ($p<0.001$). This supports the idea that saponin dispersed the SPIONs in suspension and acts as a surfactant.

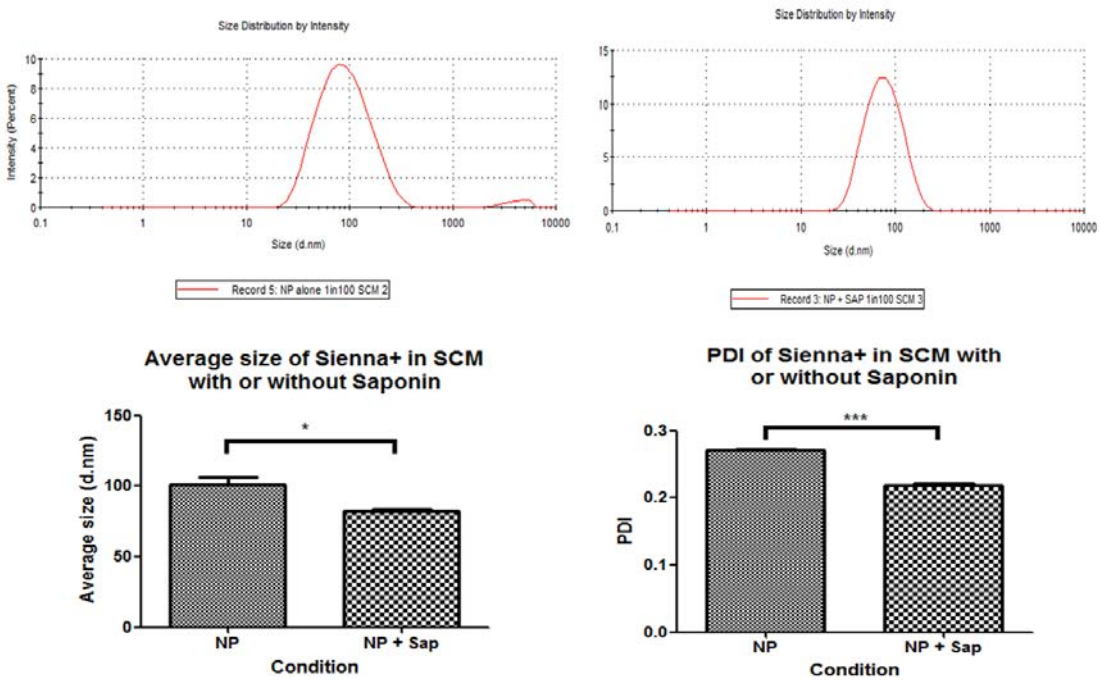

Figure 5.4: DLS size distribution data of SPION samples with or without saponin. The size distribution of NP preparations is decreased following the addition of saponin. The peak indicates a slight decrease in the calculated diameter ($P<0.05$), and the PDI indicates a significant decrease in the polydispersity of the sample ($P<0.001$)

5.2.2 Cellular uptake of SPIONs

The internalization of SPIONs into different cell lines was assessed using the conditions previously ascertained in Chapter 3. Therefore the maximum concentration of 280 µg/mL and maximum incubation time of one hour were used. Incubations were performed immediately following sonication of the NP solution for 15 minutes and subsequent dispersion in media, as detailed in the methods section (Section 2.1.1). As the uptake of SPIONs by macrophages is the most well studied, a macrophage model is necessary against which to benchmark findings. THP-1 cells are a monocytic cell line derived from an acute leukaemia. Phorbal-12-myristate-13-acetate (PMA) and 1,25-dihydroxyvitamin D3 (VD_3) are often used to stimulate the differentiation of THP-1 monocytes into a macrophage-like phenotype [276]. There are a variety of different protocols that exist regarding the conditions for this differentiation; Daigneault *et al* compared the phenotype of differentiated macrophages under various conditions [276]. They established that a modified PMA differentiation protocol that consists of two phases, a PMA treatment phase, followed by a PMA^r (rest) phase led to enhanced differentiation and increased similarity to Monocyte Derived Macrophages (MDM)s, both in their cytokine profiles and cellular characteristics [276]. Following THP-1 differentiation using Daigneault's established protocol, the morphology of the THP-1 derived macrophages was assessed using confocal microscopy and Fluorescence Activated Cell Sorting (FACS) (Figure 5.5). FACS utilizes laser light to count and characterize single cells within a fluid based on fluorescence emission and light scattered (forward and sideways) by the cells. FACS can be used to assess the changes in the side and forward scatter of the cells pre and post differentiation.

Macrophage differentiation is characterized phenotypically by an increase in the cytoplasmic to nuclear ratio. The confocal images in Figure 5.5 clearly show an increase in the cytoplasmic volume in the differentiated cells when compared to an image of pre-differentiation monocytes, as previously seen [361, 276]. Adherence of the differentiated cells to the bottom of the dish was also observed. The forward and side scatter can also

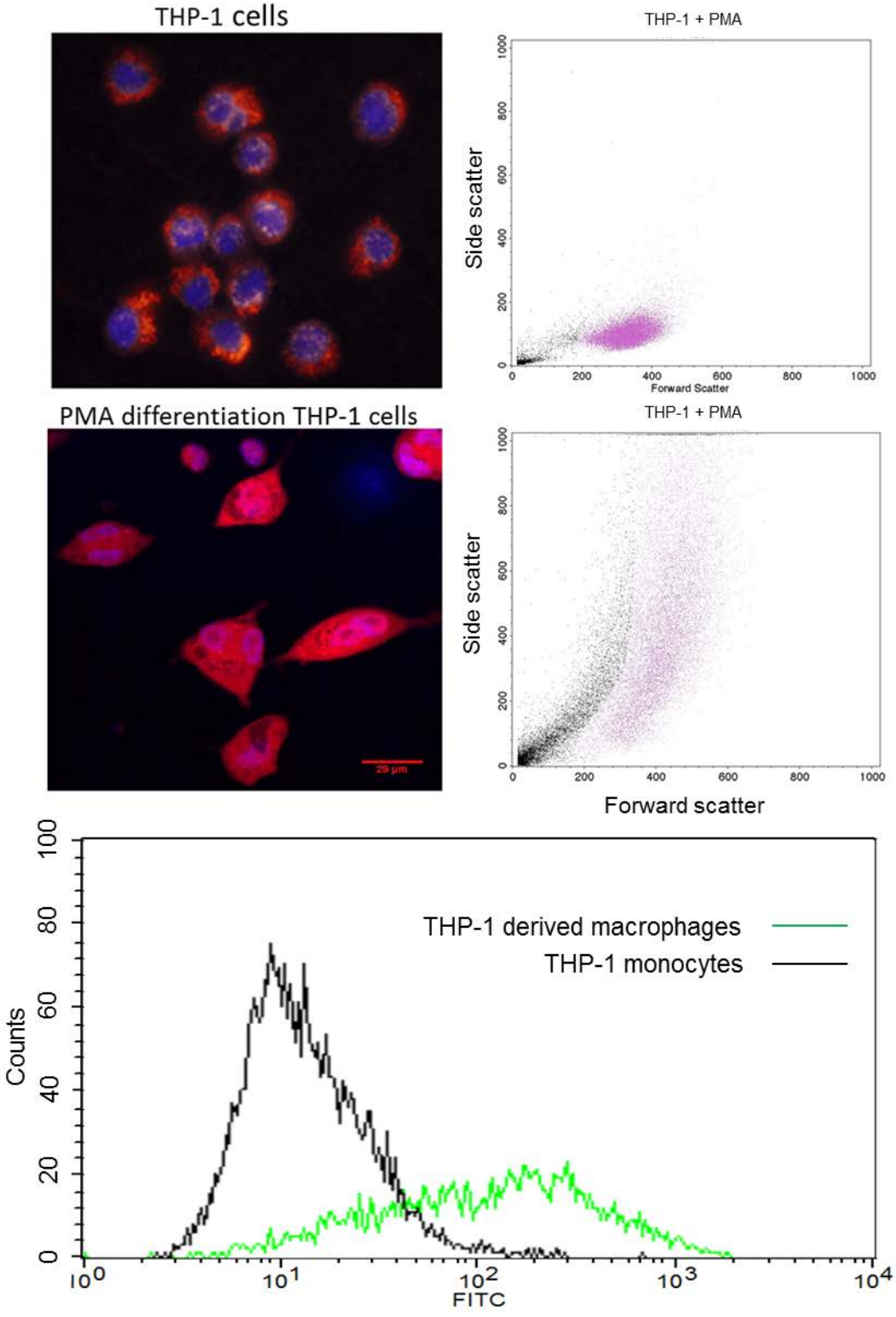

Figure 5.5: Differentiation of THP-1 cells to macrophages. The images on the left show THP-1 cells before (top) from [361] and after PMA differentiation (bottom). The increase in cytoplasmic to nuclear ratio is evident following PMA-induced differentiation, visualized by the red CTO stain and blue DAPI stain. Cells also become adherent and spread. FACS shows an increase in the forward and side scatter of the cells as evident on the images on the right. The expression of CDC36 also increases, seen on the FACS graph as an increase in FITC intensity in differentiated cells

be used to indicate the extent of differentiation [276]. An increase in the side scatter is evident in Figure 5.5 (bottom right) when compared to the monocytes (top right). This indicates an increase in granularity, which originates from the increase in the number of membrane bound organelles in the differentiated cells. An increase in the forward scatter is also observed, this indicates an increase in cell size compared to the monocytes. The increase in the expression of CD36, a known macrophage marker used to assess differentiation, is also indicative of the successful differentiation of the cells into macrophages. Therefore FACS was employed to identify the expression of the macrophage marker CD36 (Figure 5.5). Taken together these results demonstrate that the protocol suggested by Daigneault *et al* can be used to successfully differentiate THP-1 monocytic cells into macrophages that resemble MDM cells; this is consistent with previous studies [276].

5.2.3 Quantification of uptake in cancer cell lines

Cell lines exposed in these experiments include THP-1 derived macrophages, A549, HeLa and MDA cells. Cells were plated onto glass-bottom 24-well MatTek plates. The cells were subsequently treated with SPION suspensions of 56 µg/mL, 112 µg/mL or 280 µg/mL for 5 mins, 15 mins or 1 hr, 24 hrs post initial plating. Cells were then stained with CTO, 30 mins prior to fixation, and counter-stained with DAPI present in the mounting medium. Figure 5.6 shows an example of cells treated with 280 µg/mL SPION solution for one hour. It is apparent from Figure 5.6 that SPIONs are efficiently internalized into all cell lines tested at this exposure condition. Although qualitatively uptake is clearly seen when comparing treated (Figre 5.6: top panel) and control cells (Figure 5.6: bottom panel), it is very difficult to ascertain differences between the cell lines themselves. The uptake of SPIONs into these different types of cells can be quantified using the previously described analysis work-flow, whereby the cell outlines can be identified and then the NP regions can be segmented. Different parameters can be assessed such as the number of connected components and the intensity across the cell lines. Any number of parameters can be assessed leading to collection of large amounts of data. However, this thesis mainly

focuses on, and discusses, the intensity measurements (as this is a regular measurement when using standard manual analysis) of NP uptake within the cell lines.

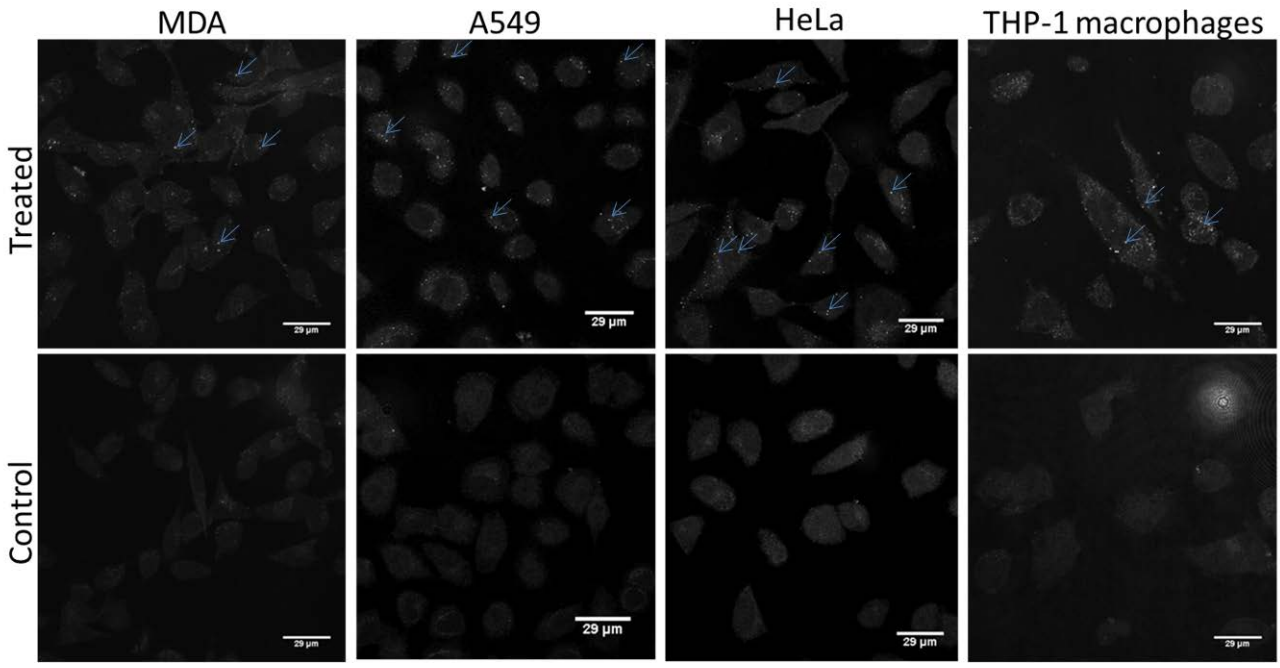

Figure 5.6: Example reflectance images showing SPION internalization into different cell lines. The uptake of NPs can be visualized in different cell lines using RCM. Uptake is evident in all cell lines. The images show cells treated with 280 µg/mL SPIONs for one hour and shows only the reflectance channel, indicating NPs (examples highlighted with blue arrows) in the SPION-treated case and nothing reflectant present in the untreated controls.

Another factor to consider in experiments such as these is the method for conducting statistical analysis. The determination of such methods often relies on the underlying distribution of the collected data and the model that best describes the data. The distribution of data acquired using RCM was plotted and the data appears to follow a Poisson distribution (Figure 5.7). A one-sample Kolmogorov-Smirnov test, when applied to the data using MATLAB, also indicated the lack of normality. Regularly used non-parametric tests include the Mann Whitney U test, which compares two independent samples, and is therefore not relevant (9 samples in for each cell line: 3 time points x 3 concentrations). Another is the sign test and the Wilcoxon Rank Test, which again compares two samples: matched or paired. The Kruskal-Wallis test is the non-parametric equivalent of

the ANOVA, and is ideal for the comparison of a continuous outcome in more than two samples when conditions for an ANOVA are not met (such as the data being modeled by something other than a normal distribution). An ANOVA can be considered conceptually similar to a multiple two sample T-Test but has a reduced type 1 error rate (false positive). Despite the observed data distribution, the Central Limit Theorem (CLT) states that when sample size is increased, the distribution tends towards the normal. Therefore if the sample size is large enough (generally classed as above 50 events) the data can be approximated by a normal distribution, and can therefore be assumed to fulfill the criteria for parametric testing. This is because, although the raw data does not follow a normal distribution, the underlying distribution of the means of randomly sampled data tends toward normal. This can be proven by examining the distribution of the means of randomly sampled data; the histogram of which can be seen to be modeled by the normal distribution (Figure 5.7). Therefore, for the purpose of the analyses a multiple comparisons ANOVA was used to assess the significance of observed differences to ascertain conclusions regarding the NP uptake by different cell lines.

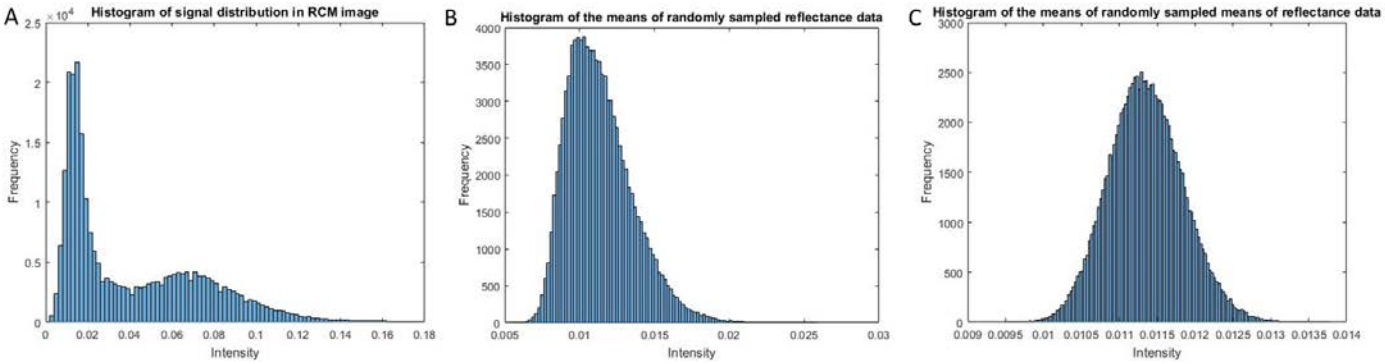

Figure 5.7: The distribution of reflectance image data and the central limit theroem for the assumption of normality. A shows the non-normal distribution of the histogram of the raw reflectance data. B shows the distribution of the randomly sampled means of reflectance image data, and C shows the means of randomly sampled data (2000 samples averaged) iteratively 1000 times. Clearly the randomly sampled mean data follows a normal distribution, as predicted by the central limit theorem

The analysis was performed and plotted to compare the mean cellular intensity post processing and segmentation of the different treatment groups as indicated on the graphs

(Figures 5.8 and 5.9). For each cell line, graphs present the data in concentration groups and time point groups, as indicated in the legends. This was to indicate the significance between different groups. The graphs indicate that increased SPION exposure time and exposure concentration leads to increased cellular intensity in all cell lines tested (Figures 5.8 and 5.9) as expected, and indicating no evidence of saturation. Cells that exhibit a higher intensity can be assumed to have internalized more NPs. Time and concentration dependant uptake has previously been established for a variety of NPs / cell lines. The time and concentration dependence of uptake has been previously described for NPs including polystyrene and gold [5, 362, 363].

In this case (SPIONs in this thesis), the effect of increased exposure time appears to be significant in most of the groups tested across the different cell lines. However, although an increase in uptake is still observed that coincides with increasing SPION concentration, more often than not this is insignificant, potentially implying that the uptake is limited by the number and availability of receptors. This is seen to be true for A549, THP-1 and HeLa cell lines, aside from at the highest concentrations at the longest time points. MDA cells however show significantly different uptake at the different concentrations tested, which may indicate an increased sensitivity to NP uptake. This could indicate an increased amount of receptor availability at the surface, or could indicate that MDA cells experience a certain level of membrane damage, leading to increased internalization. There appears to be a slight increase in the intensity of SYTOX green staining in MDA cells upon the addition of NPs, although this cannot be used to make conclusions as the different is insignificant (Figure 5.3). The significance levels between time and concentration increases indicate that uptake may be more dependant upon exposure time than the exposure concentration in THP-1, HeLa and A549 cells, which implies that a receptor mediated interaction may be responsible for the SPION uptake. The uptake kinetics of various SPIONs (DMSA-coated, PEGylated, pullulan (PN-) coated, Dextran coated) have previously been demonstrated to show time and concentration dependence in

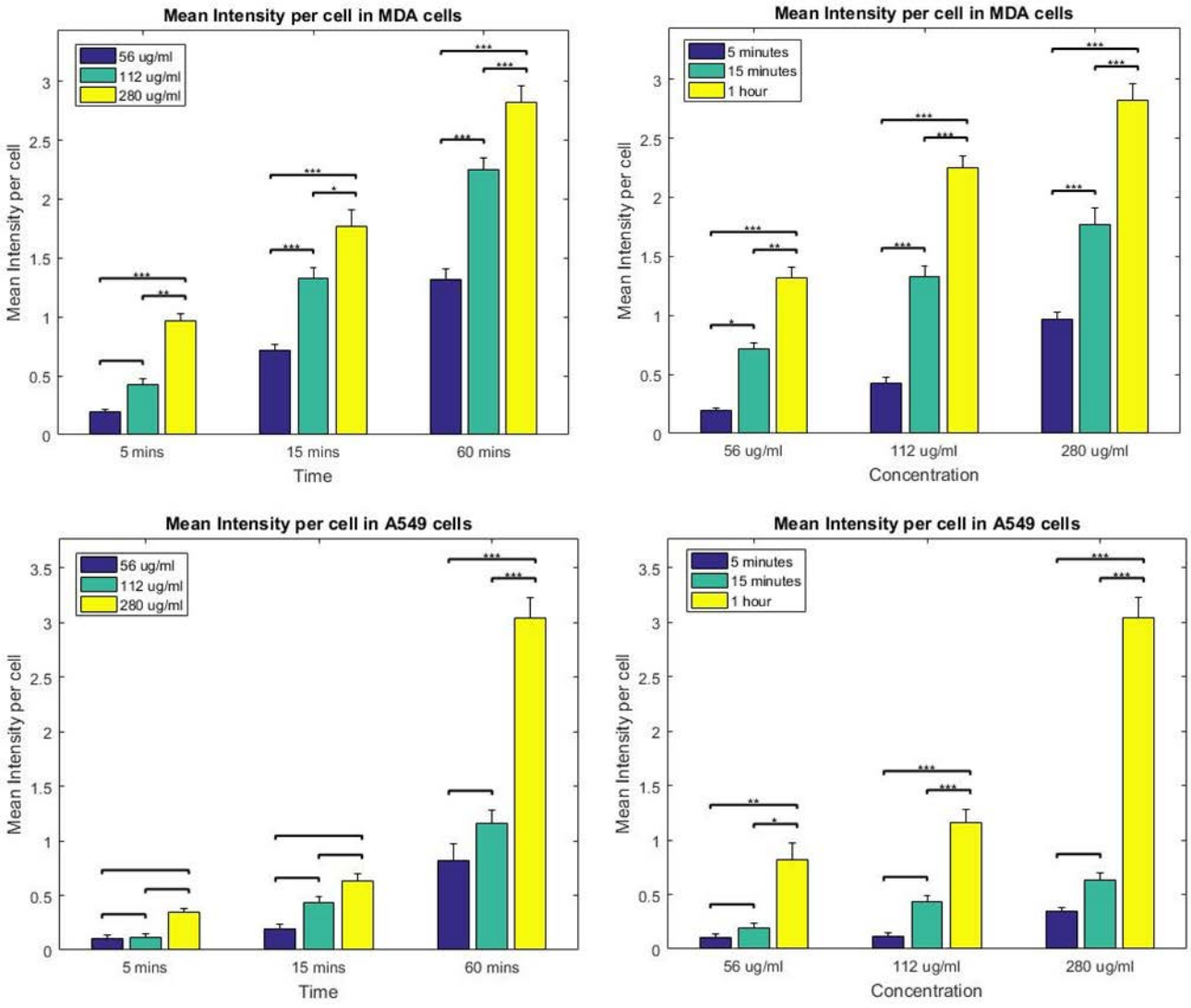

Figure 5.8: Analysis of SPION uptake in MDA and A549 cells using MATLAB. SPION uptake in MDA and A549 cells shows a time and concentration dependence. Differences between the different SPION concentration groups incubated for the same length of time are more significant (A549). MDA cells display increased significance between all groups compared to other cell lines. Significance *** = $p<0.001$.

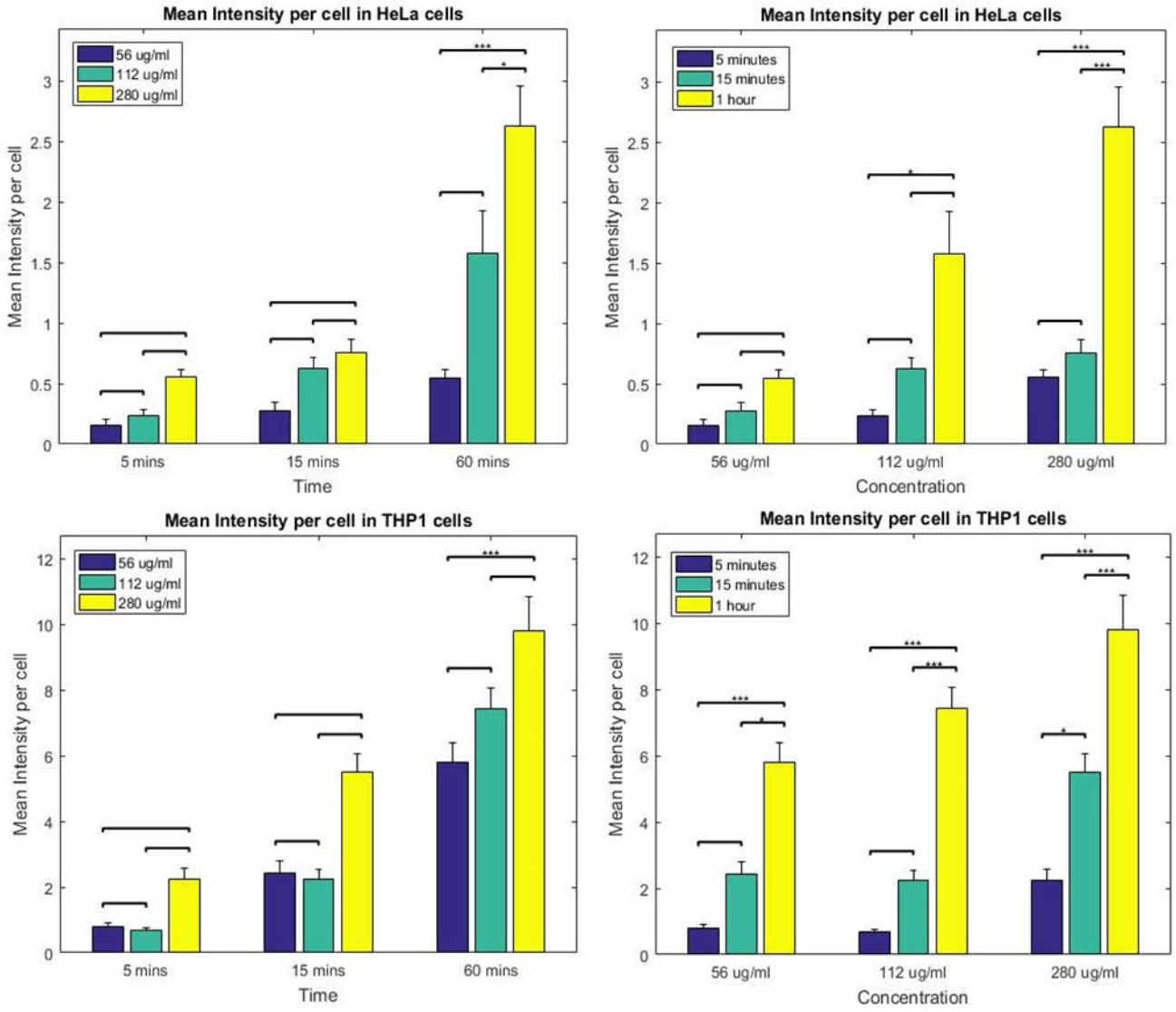

Figure 5.9: Analysis of SPION uptake in HeLa and THP-1 derived macrophage cells using MATLAB. SPION uptake in HeLa and THP-1 cells shows a time and concentration dependence. Differences between the different SPION concentration groups incubated for the same length of time are more significant than differences between different incubation times at the same SPION concentration (THP-1). HeLa cells display less significance between all groups compared to other cell lines. Significance *** = $p<0.001$.

different cell lines (MCF-7, MDCK, NIH-3 T3,CHO-K1, Brain Capillary Endothelial Cells (BCEC), human Blood Outgrowth Endothelial Cells (hBOEC)), measured through a host of methods including magnetization measurements, Prussian blue staining, AFM, TEM and fluorescence imaging ([364, 134, 173, 365, 164]). However previous studies do not appear to have yet made use of label-free imaging to visualize the unmodified core; rather, for light microscopic studies, fluorescent imaging was performed ([365, 364, 173, 164]). Although the literature does not specifically state that Sienna$^+$ SPIONs have been investigated, Resovist (Ferucarbotran) also displayed time and concentration dependence of uptake in hBOECs and human Aortic Endothelial Cells (HAoECs), visualized by immunofluorescence and colorimetry [164]. However, the label-free visualization of SPIONs, particularly Sienna$^+$, has not been previously demonstrated. Therefore our studies minimize problems associated with indirect measurements and labeling, providing a means of quantifying observed signal generated directly from the SPION cores.

Although all the cell lines assessed exhibited a time and concentration dependent uptake, there was little difference at the lowest concentrations and time points. Therefore the results obtained for each cell line at 280 µg/mL, and for one hour incubation was compared (Figure 5.10). At all concentrations and time points compared, the THP-1 macrophages internalize a significantly greater proportion of NPs when compared to other cell lines (except at the lowest time point where no significant difference was seen). This is likely due to the specialized function of macrophages to engulf foreign material; macrophages have previously been established to internalize NPs at a faster rate than other cell types [159]. The extent of uptake has previously been established to depend on the NP's size, a factor known to influence the employed internalization route [366]. It is possible that the route of uptake within macrophages differs to that of other cell types, which has previously been suggested [59]. When comparing the MDA, HeLa and A549 cells, similar levels of uptake are observed, and no statistical difference between groups is seen, as measured by an ANOVA and multiple comparisons (Figure 5.10). This may imply a similar

route of uptake in these cell lines, that may differ to that of macrophages. Not only does it indicate promising results regarding the similarity of the NP uptake in these different cell lines, it also indicates that the analysis method used can offer consistent results.

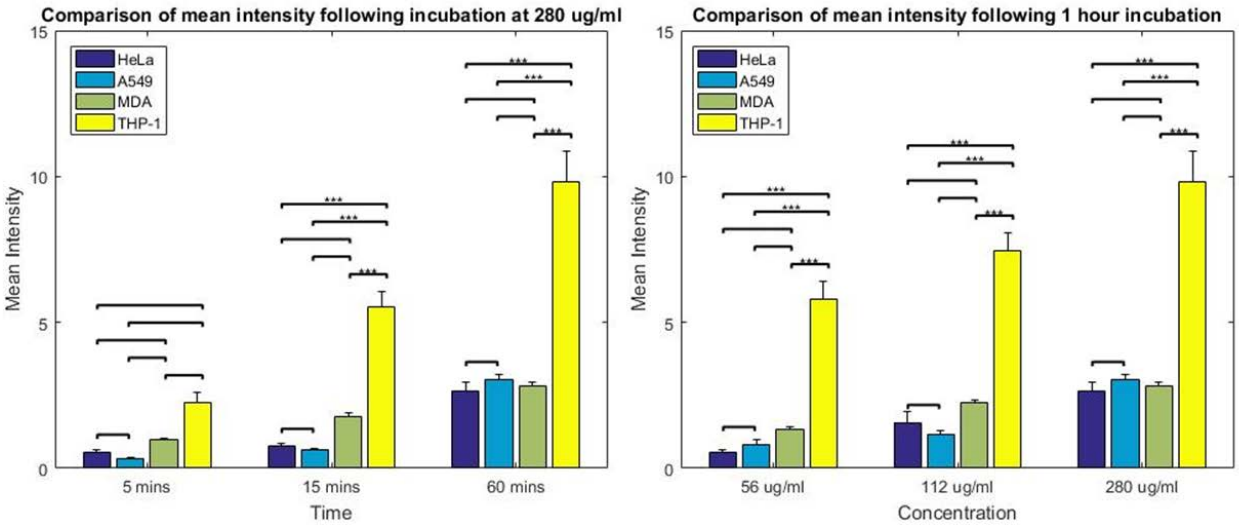

Figure 5.10: Comparison of SPION uptake in HeLa, A549, MDA and THP-1 derived macrophage cells at 280 µg/mL and incubated for one hour. The graphs show comparisons between cell lines incubated with 280 µg/mL for different time points (left) and incubated for 1 hr at different concentrations (right). Statistical significance was calculated using MATLAB ANOVA and *multcompare* functions. Values between cancer cell lines did not appear to be significantly different, however the THP-1 cells appeared to internalize NP significantly more then the cancer cells. Significance *** = $p<0.001$

5.2.3.1 Value binning for data analysis

Analyses that assess the response of cell populations post-treatment by use of metrics such as collective mean intensity of several cells are suggested to be somewhat inadequate for the assessment of subtle cellular changes, including the study of NP effects [350]. Neighboring cells have been seen to undergo different responses to NPs and cell averaging can mask subtle changes that occur in minority populations, an effect that is applicable across most fields of biology. Manshian *et al* showed the value of binning data to determine significant toxicity values in subsets of the population, rather than simply averaging cell values when estimating the safe concentrations of NPs [350]. They showed

that sub-populations of cells undergo different effects following NP treatments, including a portion that undergo cyto-protective effects and some that undergo cytotoxic effects. This was masked by a net-zero overall change in the cell population measured as a whole. This has similarities to the use of flow cytometry which measures single cell responses, rather than populations as a whole. Therefore the resultant data was further analyzed to reveal the percentage of cells within different groups that have a high or low intensity of signal. In this way the uptake can also be described in terms of the percentage of cells that have a total intensity above or below a particular threshold.

The thresholds introduced were the same across the different groups within each specific cell-line. For the high intensity threshold the mean of the highest concentration groups was used and for the low intensity threshold the mean of the lowest concentration groups was used. This allows the classification of the cells present in the specific treatment group based upon their intensities. This provides a profile of the quantities of high intensity, mid intensity and low intensity cells per group. This is shown for all cell lines tested (Figure 5.11). Indeed in these analyses it was observed that a portion of the cells internalize a large amount of NPs, and some internalize very little, regardless of concentration (Figure 5.11). These values can be directly compared between cell lines as the same thresholds used will differ according to the overall observed cellular intensities within the specific cell-line. There is a clear trend shown between higher concentrations and time points, and the increase in percentage of high intensity cells. This supports the idea that sub-populations of cells respond differently, i.e. some cells internalize a large amount of NPs, and some cells still do not internalize many NPs, regardless of the exposure conditions. This indicates that different measures of toxicity may give very different profiles of NP effects, and employing multiple analysis types may be necessary to make full conclusions regarding the effects of NPs. The differences observed within each treatment group is interesting, and highlights the heterogeneous nature of groups of cells from the same population. This effect could relate to a number of things, including the actual dose received by each cell

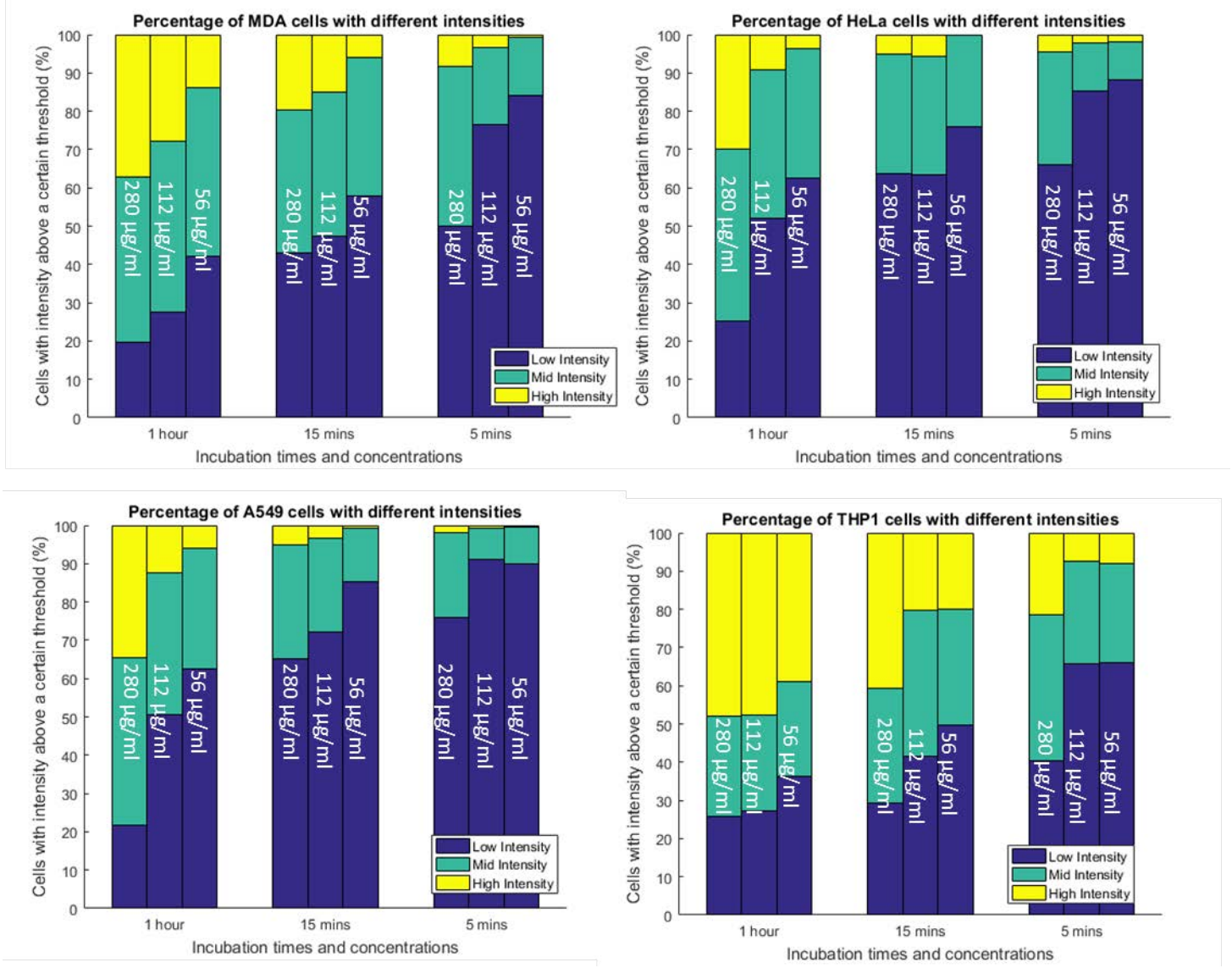

Figure 5.11: Intensity threshold analysis of SPION uptake in MDA, A549, HeLa and THP-1 derived macrophage cells. Within each treatment group tested, the quantity (%) of cells within that group that can be classified as 'high', 'mid' or 'low' intensity is shown. Within each group there exists populations of cells that internalize many, or few NPs. The proportions of these cells that internalize many increases with increasing incubation times and concentrations

which may not be homogeneous across the population, or subtle differences across the cell population due to their local environment. NP accumulation has also been shown to depend upon cell cycle stage; cells can reduce their internal NP load using asymmetric division and therefore the observed dose can depend upon the stage the cell is in during exposure [367]). SPIONs themselves have previously been shown to alter the balance of cell cycle regulatory proteins, favoring cell cycle progression and increased cell growth and proliferation [107]. Flow cytometry could be performed, to collect fluorescent signal from toxicity markers (i.e. SYTOX or ROS assay) in addition to light scatter (indicating NP uptake) collected per single cell could be compared to imaging data of SYTOX and reflectance intensity to indicate the similarities and differences across cells populations and the two techniques.

5.2.4 Mechanism of uptake in different cells

5.2.5 Specificity of siRNA used in endocytosis assays

Endocytosis pathways are often characterized by their sensitivity to different pharmacological inhibitors. These inhibitors can be used to inhibit particular pathways in order to ascertain the cellular internalization mechanisms employed by different substrates. However, the non-specific nature of these drugs, and the consequent unwanted side-effects is often overlooked [368]. Silencing the expression of protein components within the endocytotic pathways using siRNA offers an alternative more specific approach to investigate the contributions of different pathways to the internalization of a substrate, such as NPs. Even so, issues arise when inhibiting specific pathways, as it is likely that pathway compensation occurs, leading to up-regulation of alternative internalization pathways [369]. SiRNA targeted to the most commonly used pathways that exist within cell lines were assessed in order to elucidate the main uptake pathway of SPIONs. SiRNA targeted toward AP2 was employed to inhibit the CME pathway. To inhibit caveolae, Cav1 is targeted, and for macropinocytosis a combination of Pak1 and Wave2 are used. However

following initial experiments, the knockdown of wave2 appeared to be irreproducible, and therefore was not taken further (See Appendix). RNAiMAX gave superior transfection efficiency when assessing Cav1 and AP2 knockdown (data not shown), therefore was used in subsequent studies. The use of different transfection protocols was assessed, and it was found that a 72 hour incubation and a double transfection (one 24 hours post plating, and one 48 hours post initial transfection) gave rise to the best knockdown results (data not shown).

To ascertain the specificity of protein silencing, control experiments were carried out using cargo known to be internalized through the specific pathway being inhibited. Transferrin is generally accepted as a ligand that is exclusively internalized via CME, and therefore can be used as a model for CME investigation. To investigate AP2 inhibition, Alexa488-tagged TF internalization was quantified, and to assess caveolae inhibition, Cholera Toxin subunit-B-488 (CTxB) was used. Fluorescently labeled Dextran has often been used to determine macropinocytosis in cell types. However there has been some confusion over the most appropriate molecular weight Dextran to use. Li *et al* determined that 70kda dextran was internalized specifically through macropinocytosis, whereas smaller (10 kda) is also internalized through micropinocytic pathways; therefore 70kda dextran was utilized for the macropinocytosis specificity assays [370]. Cells were treated as previously described in the siRNA transfection methods section. Following 72 hour double knockdown experiments cells were either lysed for WB analysis or imaged using FCM. Inhibition was observed in each case, as can be seen from the Western blot images (Figure 5.12).

Qualitatively, the inhibition of different components of the uptake machinery led to reductions in the internalization of specific cargo (Figure 5.12). Quantitatively, in all cell lines tested, transfection with Cav1 siRNA led to a decrease in the uptake of cholera toxin B. Conversely with transfection of AP2 directed siRNA, a decrease in transferrin uptake was seen (Figure 5.13). Interestingly in THP-1 cells, there was no detectable levels of

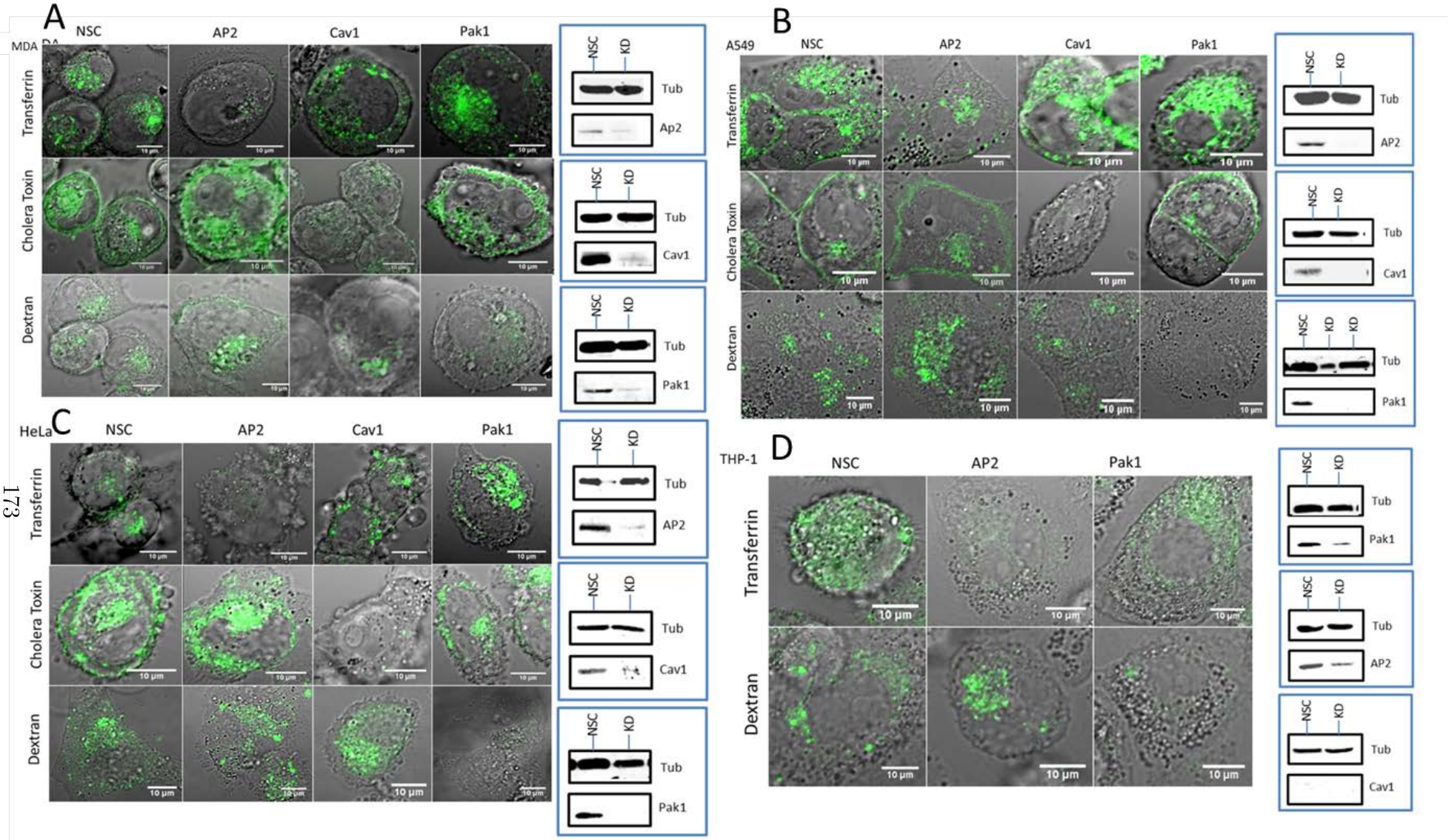

Figure 5.12: Representative images of control experiments used to determine the specificity of siRNA for endocytotic pathway inhibition Images show experiments performed in A) MDA, B) A549 C) HeLa and D) THP-1 cells. Each example shows a set of representative images of the effect of the siRNA (NSC, AP2, Cav1 and Pak1) protein inhibition on the internalization of different cargo, transferrin, cholera toxin and dextran. Each example (A-D) also shows accompanying Western blots that confirm the knockdown of each protein as compared to the housekeeping gene tubulin.

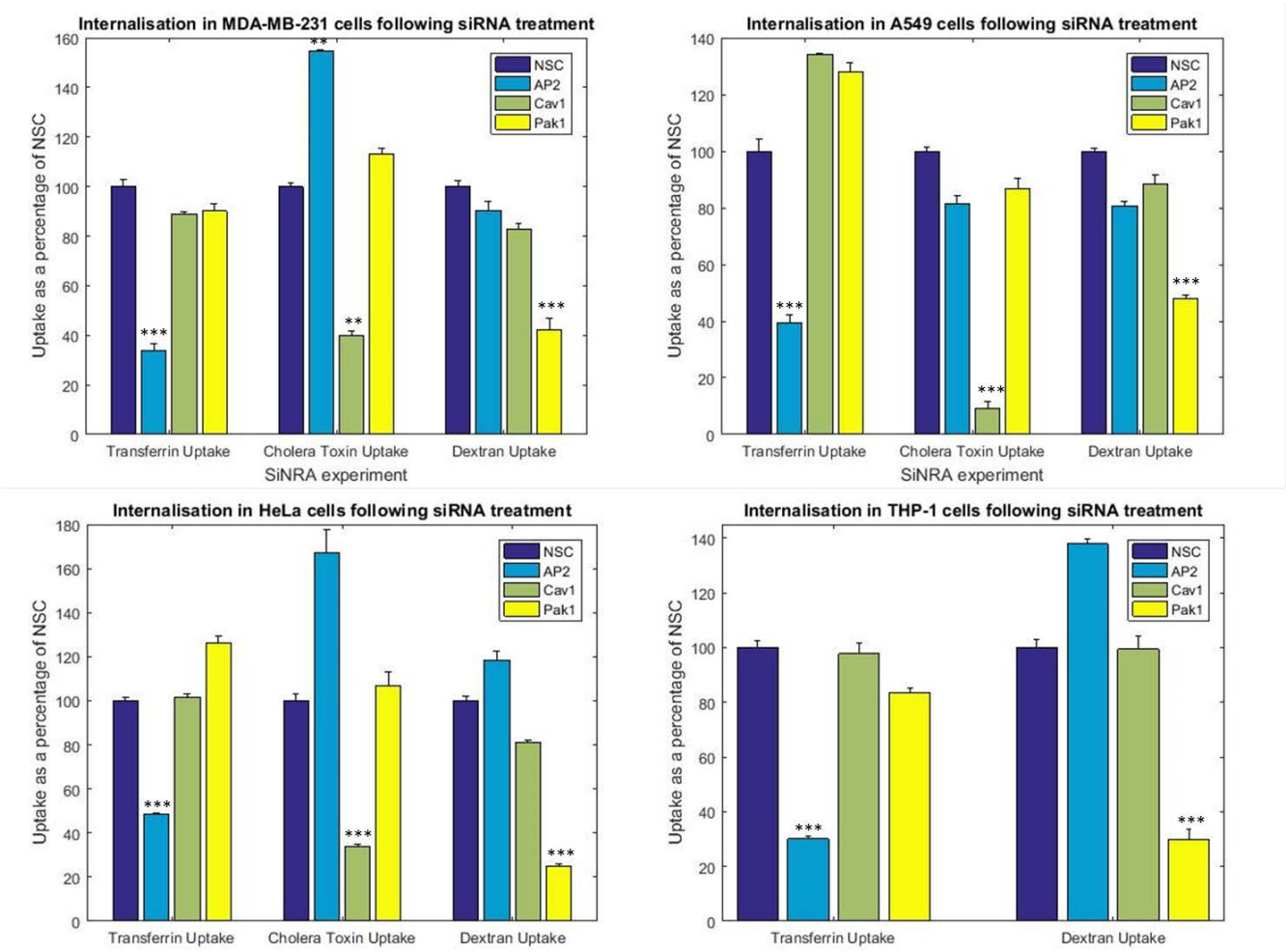

siRNA	Clathrin-mediated	Caveolin-mediated	Macropinocytosis
NSC	-	-	-
AP2	+	-	-
Cav1	-	+	-
Pak1	-	-	+

Figure 5.13: Quantification of siRNA specificity for specific pathways based on cargo internalized via that route. Quantifications are performed based on mean fluorescence intensity of cells under different treatment conditions compared to the Non-Silencing Control (NSC). The results indicate that siRNA to AP2 inhibits CME, siRNA to cav-1 inhibits caveolin endocytosis and that siRNA to Pak1 inhibits macropinocytosis. T-Tests were performed between treatment groups and NSC group. Bars with no stars indicate lack of significance. The table summarizes the results, with + signifying inhibition of the specific pathway.

caveolin-1. This led us to conclude that this protein was not expressed in THP-1 cells; therefore this condition was not assessed further (Figure 5.12). The expression of caveolin in monocytes and macrophage cell types is debated [371, 342]. Cav1 has previously been detected in THP-1 derived macrophage cells using Western blotting [372, 373, 374]. Inhibition of Pak1 led to a decrease in the internalization of 70 kda-dextran, indicative of the successful inhibition of macropinocytosis (Figure 5.13). These results demonstrate that the specific means of inhibition selected are suitable for use in subsequent experiments to determine the mechanism of internalization of SPIONs into different cancer cell lines.

5.2.6 SiRNA inhibition highlights a role for caveolin mediated endocytosis and macropinocytosis in NP internalization within cancer cell models

The uptake of SPIONs into different cell lines was investigated following siRNA knockdown of AP2, Cav1 and Pak1 to determine which pathway of internalization is being utilized by SPIONs to enter these cells (Figure 5.15). Cells were treated as described above and in Section 2.5. Cells were either lysed for WB analysis or treated with SPIONs and imaged using 40X with optical zoom on the Nikon A1R using reflectance and fluorescence configurations. The cell cytoplasm was stained with CTO and the nucleus was counter-stained with DAPI. Qualitatively there appears to be a distinct decrease in NPs present in A549, MDA and HeLa cells treated with Cav1 siRNA, indicating that this pathway may be involved in their internalization (Figure 5.15). There are ambiguous effects on the NP internalization when AP2 is inhibited; the internalization does not appear to have decreased visibly in MDA, HeLa and A549 cell lines (Figure 5.15). THP-1 cells however, appear to efficiently internalize NPs under all siRNA inhibition conditions except for when AP2 is inhibited, indicating a difference in the internalization mechanisms in these different types of cells.

Quantifications are necessary to ascertain the extent of inhibition of internalization under

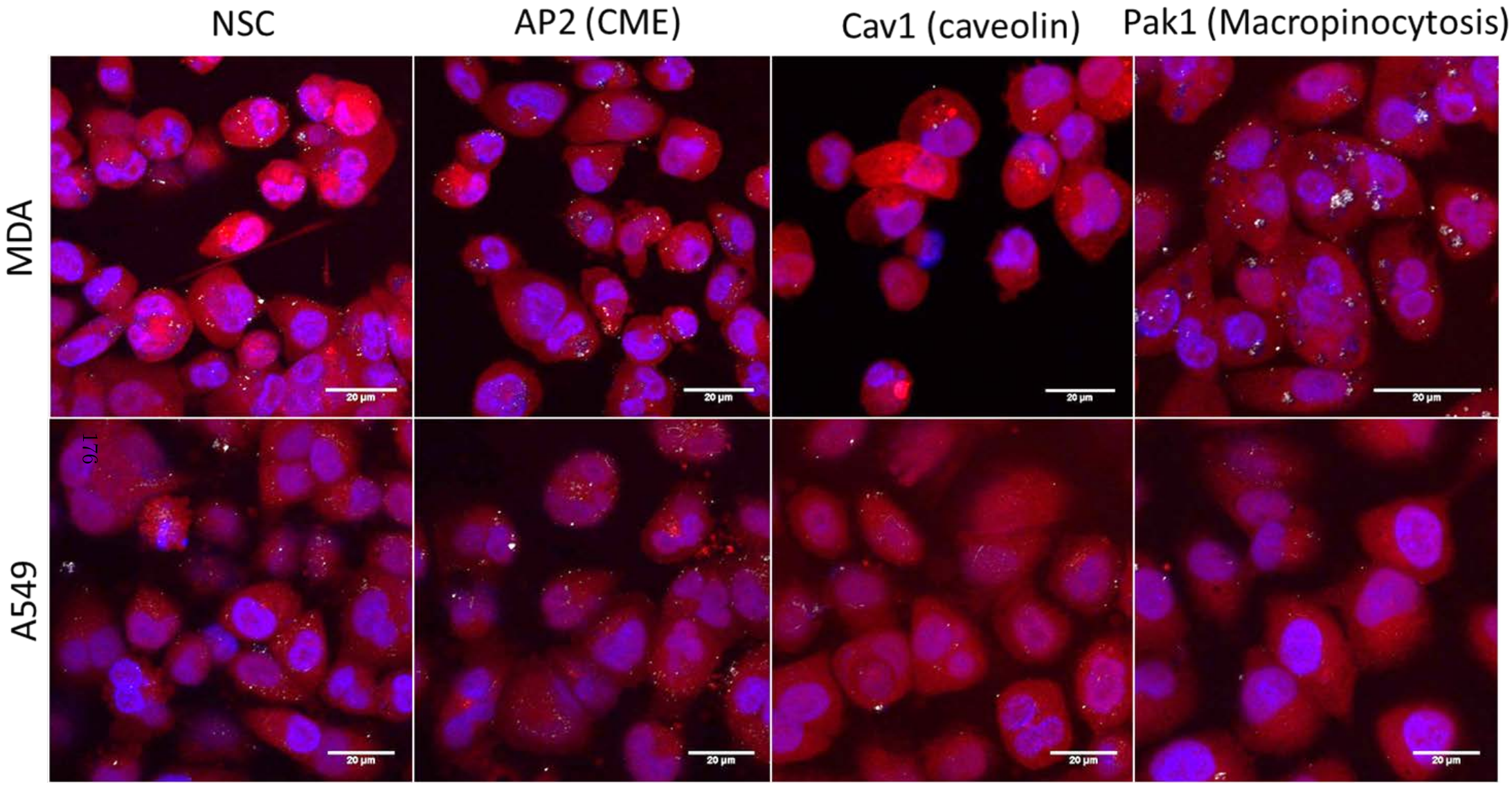

Figure 5.14: Results of siRNA experiments in cancer cell lines Images showing the uptake of SPIONs in different cell lines following treatment with siRNA (indicated along the left and top of the figures respectively). A decrease in SPION uptake is evident in MDA, A549 and HeLa following Cav-1 siRNA treatment. A decrease in SPION uptake is seen in A549 and HeLa following Pak1 siRNA treatment. A decrease in uptake is seen following AP2 siRNA treatment in THP-1 cells.

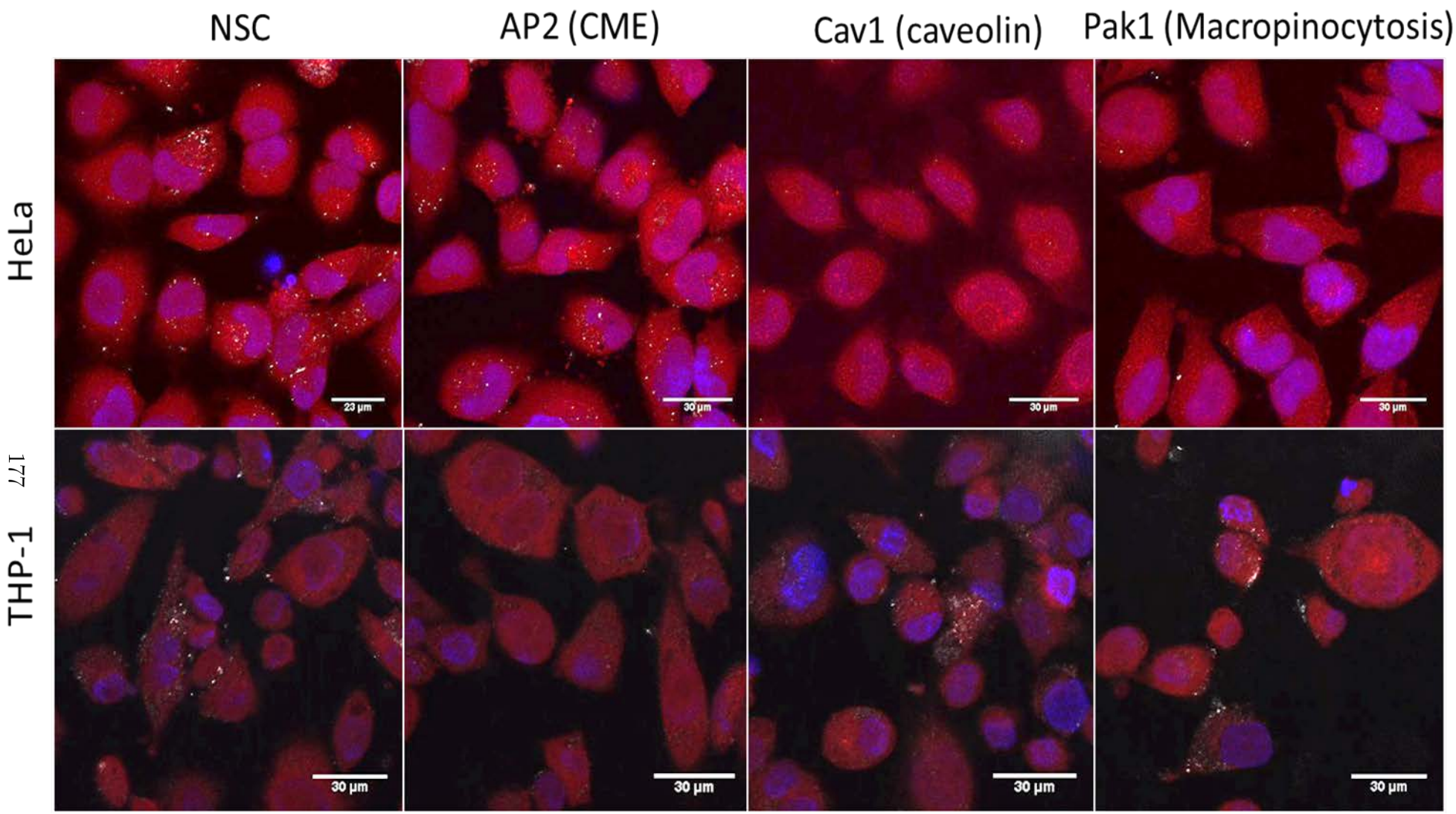

Figure 5.15: Results of siRNA experiments in cancer cell lines Images showing the uptake of SPIONs in different cell lines following treatment with siRNA (indicated along the left and top of the figures respectively). A decrease in SPION uptake is evident in MDA, A549 and HeLa following Cav-1 siRNA treatment. A decrease in SPION uptake is seen in A549 and HeLa following Pak1 siRNA treatment. A decrease in uptake is seen following AP2 siRNA treatment in THP-1 cells.

the different treatment conditions. Quantifications of the Western blot protein expression experiments were performed using ImageJ, protein expression levels were normalized to the expression of the house keeping gene Tub, as shown in Figure 5.16 and labeled as Tub in the WB images. Knockdown of the protein is then ascertained as a percentage of the expression when using NSC siRNA. Introduction of NSC introduces siRNA into the cell without specific targeting sequence, thereby ruling out effects that are irrelevant of the specific target siRNA sequence, and compensating for any effect that is due to the procedure or general siRNA introduction within cells. The WB results indicate that proteins were successfully knocked down to a suitable extent in each cell line tested as shown in Figures 5.16B and 5.17. Figure 5.17B shows the quantification of knockdowns from multiple experiments (shown in Figure 5.16) in each cell line. The mean inhibition of each pathway was >70% in each cell line and with each siRNA. Once again no expression of cav-1 protein was detected in THP-1 derived macrophages, as seen from the Western blot. Therefore no experiments were quantified to assess the effects of caveolin-1 inhibition in THP-1 cells. Quantifications must also be performed on imaging data. Likewise these quantifications were performed by normalizing the obtained mean pixel intensity values to the NSC cells (therefore NSC was converted to 100% and the samples were calculated as the percentage of 100%). This gives the percentage of SPION uptake compared to NSC which is 100%. Alternatively the data could be pooled tog

The internalization of SPIONs into macrophage models has been widely studied compared to non-macrophage cell types. In macrophage like RAW264.7 cells multiple endocytotic mechanisms were found responsible for the internalization of SPIONs, including CME, caveolae dependent mechanisms, and phagocytosis / macropinocytosis [157]. A study by Yang et al found that CME was responsible for the uptake of 45-60 nm SPIONs in two types of macrophage cells, so it appears entry mechanisms require more in depth investigation and one single mechanism is not responsible for the uptake of all SPIONs in all cell lines [157, 156]. However, the mechanism for SPION internalization within macrophage

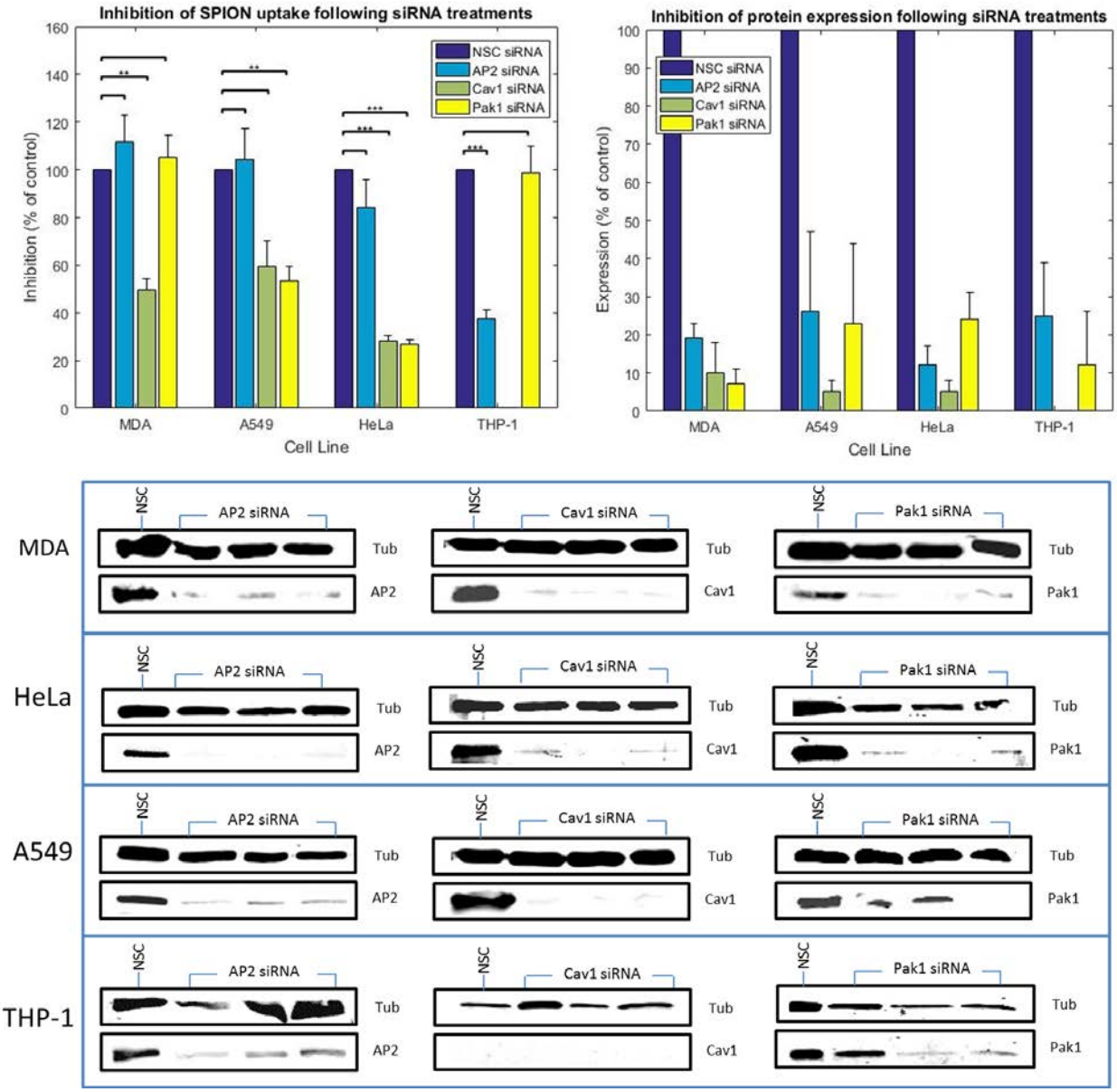

Figure 5.16: Quantification of SPION uptake following siRNA experiments in cancer cell lines. A) Quantification of the NP uptake (using MATLAB) indicating the inhibition of NP uptake when specific pathways are inhibited in different cell lines. The graph on the right shows quantification of average knockdown efficiency from WBs. A minimum of 238 cells were analyzed per group, from experiments run on 3 or more different days. Mean + SEM is plotted). B) Western blots showing the protein expression of the target proteins following siRNA treatments compared to the housekeeping gene Tubulin (indicated as Tub). NSC samples show the protein expression using control siRNA. NSC in this case does not have error bars due to the normalization that scales NSC to 100% in each case.

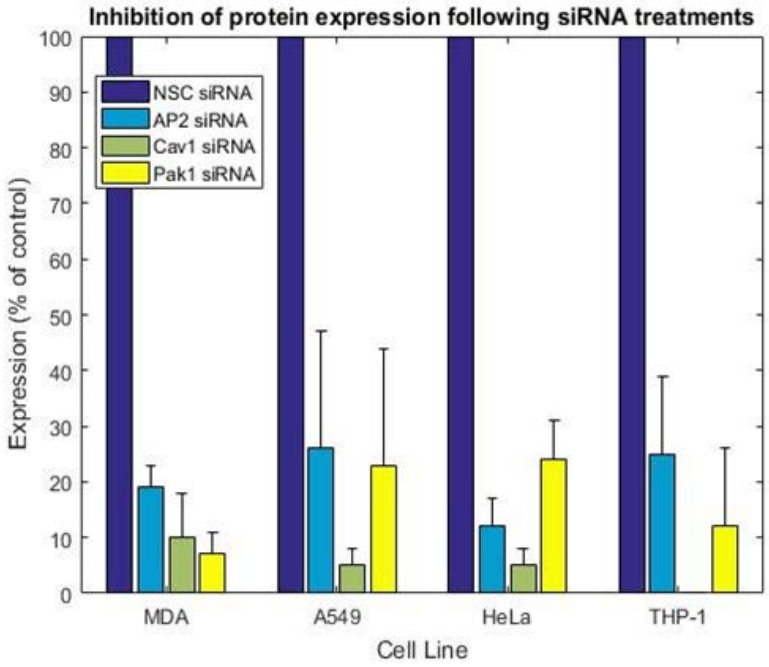

Figure 5.17: Quantification of protein expression using Western blot following siRNA experiments in cancer cell lines. Quantification of average knockdown efficiency from WBs (N=3 and STD is plotted in each case). Protein expression level was normalized to tubulin in each case, and then calculated as a percentage of NSC treated cells protein expression.

cell types is often reported to be predominantly through the CME route and phagocytosis, which is in agreement with our studies (Figure 5.16) [157, 343, 375, 376]. Similar studies performed in macrophage cell lines with two types of SPIONs (Resovist and Supravist) and polystyrene NPs, highlighted a role for CME and scavenger receptor A [366, 371]. TF has been reported as a common component of the corona of various NPs [117]. Transferrin was found to be present in the corona of the Sienna$^+$ NPs in our previous studies in Section 3.2.6. The transferrin receptor, along with its ligand transferrin, is internalized through CME and therefore may offer a mechanism of entry for corona coated SPIONs in these cell types, although the scavenger receptor has been implicated in other studies [366, 168].

SPION surface coatings such as silica have been shown to lead to cellular accumulation via caveolin mediated endocytosis in HeLa cells [152]. The quantitative analysis done here in non-macrophage cells also suggest the importance of caveolin mediated endocytosis, along with macropinocytosis in Sienna$^+$ NP internalization. In HeLa and MDA cells the inhibi-

tion of caveolin led to a significant decrease in the internalization of SPIONs ($P<0.05$). In A549 there was a similar decrease, however this was not determined to be significant ($P = 0.08$). There are limited identified cargo for caveolin mediated endocytosis, but other NPs/QDs of similar size (60 nm) have been found to preferentially accumulate in cells via caveolin mediated endocytosis [377, 152]. It has also been suggested that positively charged NPs favor CME, whereas negatively charged NPs prefer caveolin-mediated internalization [377]. Albumin was found to be present on the surface of the NPs (Chapter 3, Section 3.2.6). This is consistent with other studies of the corona composition of dextran coated SPIONs with neutral, or nearly neutral charge [117]. Albumin is known to bind to gp60 at the cell surface, which binds to Cav1 and forms vesicles, potentially providing a mechanism for the internalization of SPIONs, although this is speculative [378].

The inhibition of macropinocytosis using the siRNA directed toward Pak1, a kinase directly involved in macropinocytosis, led to significant decrease in SPION internalization in HeLa and A549 cells. Interestingly the inhibition of Pak1 in MDA cells did not lead to a decrease in the detected reflectance intensity. However, following Pak1 siRNA treatment, MDA cells appeared to have an increase in vacuole formation, that can be visualized in reflectance mode (Appendix Figure B.21). Therefore the contribution of SPIONs to the reflectance signal could not be deduced and the experiment was deemed inconclusive. More experiments would be necessary to determine the effect of Pak1 inhibition on SPION uptake in MDA cells. A second siRNA targeted towards components of the macropinocytic pathway, Wave2, was initially included in the assessment, as Pak1 inhibition altered the cellular morphology in MDA cells.However the use of wave2 siRNA appeared to lead to a decrease in cell viability, which can be seen in the WB Tub expression. Initially wave2 targeting appeared to lead to an efficient knockdown of wave2 protein expression (Figure B.18). However in subsequent experiments the knockdown that was first displayed appeared irreproducible, this is shown and discussed in the Appendix (Appendix Figure B.18).

Knockdowns experiments provide an indication of the mode of uptake employed by SPIONs in these studies however the conclusions are not definitive, partly because only a subset of cells experience a high level of inhibition. Therefore the pathways are still active in some cells, as displayed by the knockdown WB results (Figure 5.16). There has also been a suggestion that SPION treatment can lead to an inhibitory effect on the expression of the transferrin receptor, which, along with its ligand transferrin which can bind to NP surfaces, is a cargo for CME internalization [138, 107, 168]. CME is often suggested for its involvement in NP internalization. However controversy exists regarding the NP properties that determine the NP's route of uptake [139]. Size has been considered as an important determinant in uptake route [139]. Rejman et al, suggested that when NPs are above 200 nm, they become internalized by caveolar endocytosis, whereas those smaller than 200 nm are predominantly internalized by CME [139]. These SPIONs are determined to be 60-80 nm in cell culture media and do not appear to agglomerate under the exposure conditions, but it cannot be ruled out. It is often suggested that no single NP property can accurately determine the subsequent cellular effects, such as route of uptake utilized in different cell populations. CME is also reported to occur at a faster rate than caveolin mediated endocytosis [136]. This could, in part, explain the previous differences seen between macrophage and non-macrophage cell lines at the same exposure conditions, seen in Figure 5.10. It has also previously been demonstrated in this work that different cells internalize NPs with different efficiencies (Figure 5.8 and 5.9) regardless of pathway inactivation, and therefore cell to cell responses can vary considerably [350]. Therefore these factors will likely influence the measured phenotypes and responses. It is possible, or even likely, that there is a complex interplay of pathways and compensation occurring. Considering the variety of surface coatings and surface properties that are possible, and how the surface constituents modulate the NPs surface and therefore nano-cell interactions, it is likely that changing the identity of surface adhered molecules will cause different mechanisms to play a role in the internalization. Indeed, a variety of mechanisms

have been indicated in the literature for the pathway utilized by SPIONs to gain entry into cells, indicating the associated challenges with reaching definitive conclusions [157].

5.2.7 Effect of inhibition of phagocytosis in THP-1 cells

Macrophages are actively endocytosing cells, exhibiting fluid-phage pinocytosis, phagocytosis and receptor mediated endocytosis; other cell types do not exhibit phagocytosis. Therefore when assessing the mechanism of uptake, the contribution of phagocytosis in macrophage SPION internalization was also investigated. PMA treatment stimulates ruffling and macropinocytosis in macrophages, both of which require a functional actin cytoskeleton and therefore are sensitive to Cytochalasins [379]. Cytochalasin D is a potent actin-depolymerising agent and can therefore be used for the inhibition of phagocytosis [379, 380]. THP-1 derived macrophages differentiated as previously described were incubated with two different concentrations of Cytochalasin D (5 µM and 10 µM). First a control experiment was carried out using 1 µM fluorescent polystyrene NP, a cargo that can be internalized through phagocytosis, to determine the inhibitory effect of the Cytochalasin D. The results shown in Figure 5.18 indicate that, both qualitatively and quantitatively, internalization of 1.1 µm beads was inhibited by both concentrations of Cytochalasin D (5 µM and 10 µM). Therefore at the concentrations used a large proportion (˜90% based on mean cellular intensity) of phagocytosis is inhibited, validating the experiment for subsequent use to investigate the role of phagocytosis in SPION internalization in THP-1 derived macrophages.

Experiments indicate that the inhibition of phagocytosis in THP-1 derived macrophages leads to a decrease in the internalization of SPIONs through this route (Figure 5.19). This may be expected as macrophages are phagocytosing cells, specialized for the non-specific internalization of foreign material. There appears to be an apparent discrepancy between the dose and effects used with the two concentrations of Cytochalasin D in the control and SPION experiment. In Figure 5.18 it appears that even at the lower Cytochalasin

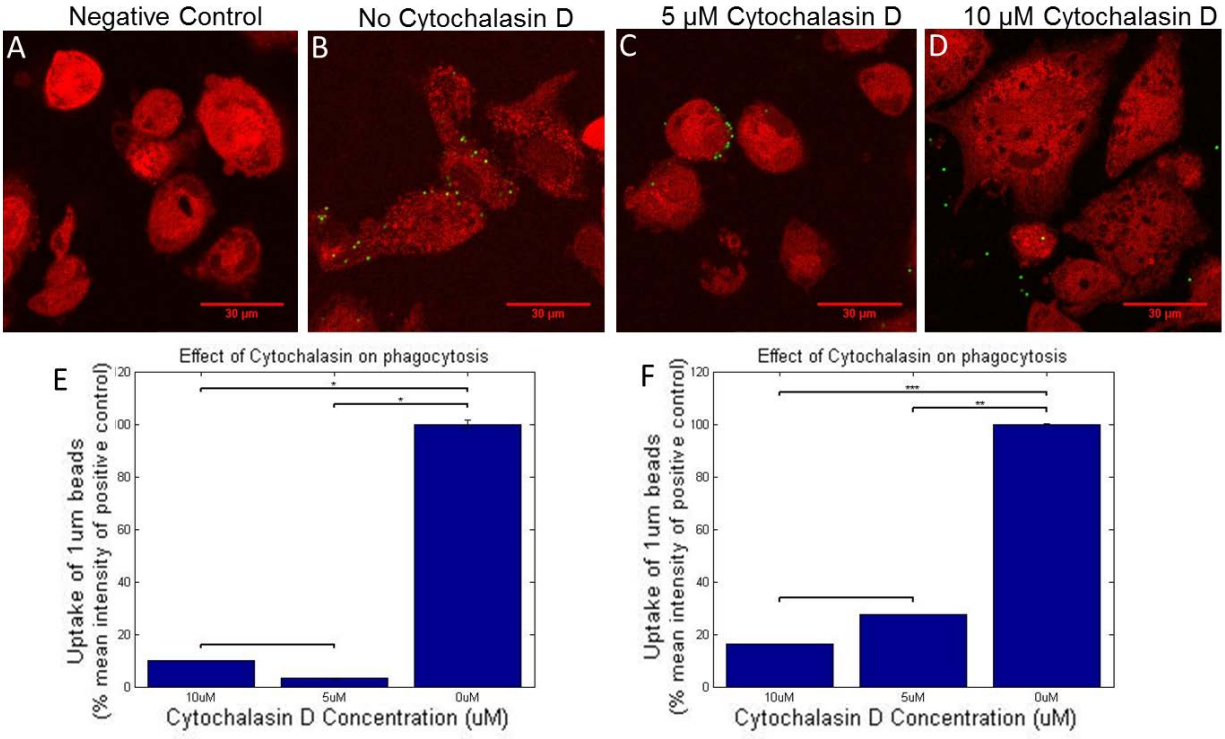

Figure 5.18: Cytochalasin D inhibits phagocytosis of 1.1 µm beads at concentrations 5 µM and 10 µM. Differentiated THP-1 cells alone (A), NP treated (B) or treated with Cytochalasin D + NP (5 µM (C) and 10 µM +NP (D) show a decrease in internalization qualitatively and quantitatively, in terms of the intensity measurements and detected spots (E and F) respectively. Means +/- SEM plotted. Red shows CTO, and Green shows the 1.1 µm polystyrene beads

D concentration, the uptake of 1.1 µM beads is inhibited to a high degree (Figure 5.18). By contrast, the internalization of SPIONs appears to be inhibited in a concentration dependent manner (Figure 5.19). The lower concentration of Cytochalasin does not appear to effect the internalization of SPIONs to the extent seen with the higher concentration. Cytochalasin D, like other pharmacological inhibitors or drugs, can cause various perturbations of cellular functions due to the cell wide disruption of actin. Actin is known to be involved in a host of cellular processes including internalization through CME. Therefore the effect of Cytochalasin D treatment on the internalization of transferrin was investigated, to see if perturbation of the CME route was effected.

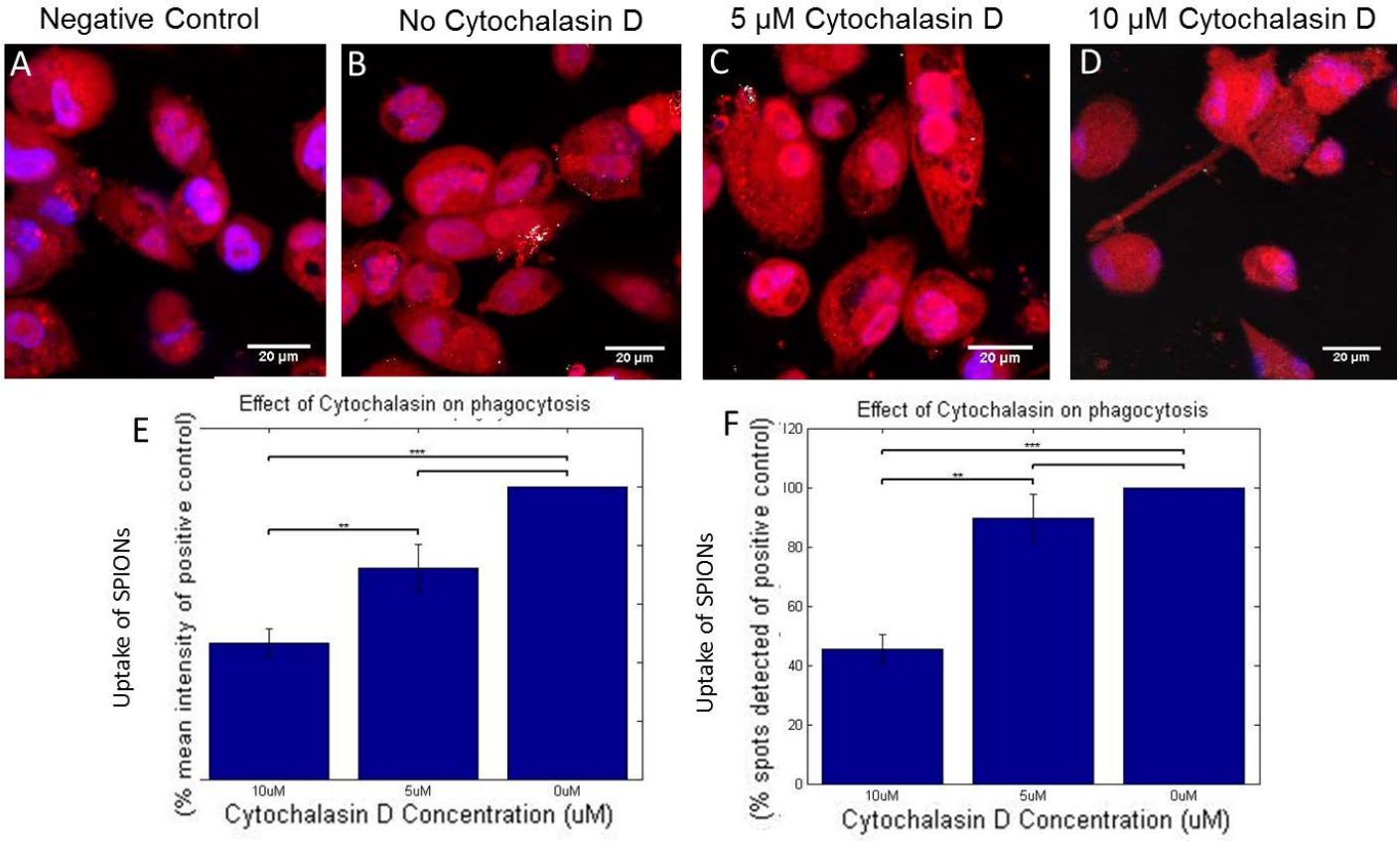

Figure 5.19: Cytochalasin D decreases the internalization of SPIONs through the inhibition of phagocytosis. Differentiated THP-1 cells alone (A), NP treated (B) or treated with Cytochalasin D + NP (5 µM (C) and 10 µM +NP (D) show a decrease in internalization qualitatively and quantitatively, in terms of the intensity measurements and detected spots (E and F) respectively. Means +/- SEM plotted. Red shows CTO, and white shows Sienna $^{+}$ SPIONs. Increasing concentrations of Cytochalasin D increased the inhibition of SPION internalization

Cells treated with Cytochalasin D were exposed to fluorescent TF as in previous control experiments in Section 5.2.5. Cytochalasin inhibition appeared to cause no decrease in the internalization of TF (Figure 5.20). Only one concentration of Cytochalasin D was assessed in this experiment. This was due to the lack of SPION uptake inhibition observed at the lower Cytochalasin D concentration (Figure 5.19) and the potent inhibiting effect of Cytochalasin D that was observed in control experiments (Figure 5.18). However it could be beneficial to include more concentrations to assess the effects of this in a concentration dependent manner; such an approach may be more conclusive for elucidating the role Cytochalasin D plays in CME inhibition / TF internalization. Lamaze *et al* have previously discussed the effect of Cytochalasin D on actin de-polymerization and CME / TF internalization [380]. There has been some confusion because of the different effects that Cytochalasin D can have on different types of actin filaments [380]. Our studies are therefore not conclusive on the effect of Cytochalasin D on TF internalization, and reinforce one of the important limitations of using pharmacological inhibitors in inhibition experiments.

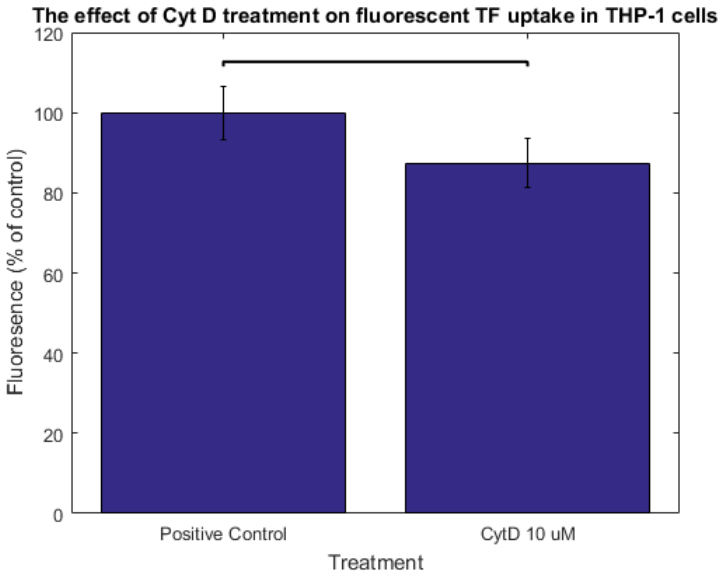

Figure 5.20: Cytochalasin D appears to decrease the internalization of TF in THP-1 cells. Cytochalasin D has a non-statistically significant effect on TF internalization at a concentration of 10 µM. Mean of n=3 experiments +/- STD is plotted. Statistical analysis was performed using students t-test (p>0.05).

5.2.8 Fluid-phase endocytosis

Some cell lines show evidence for the involvement of multiple mechanisms involved in the uptake of SPIONs. This has been previously documented for various NPs including hydrogel particles, polystyrene NPs and SPIONs [381, 157]. One possible reason for multiple pathways being involved in the uptake of NPs is fluid phase endocytosis. Some studies have suggested that SPION uptake is non-specific, as they observed non-saturable uptake, whereas others have assumed active processes due to the saturable nature of the observed uptake, leading to obvious discrepancies [382]. In each of the pathways utilized, NPs can form interactions with molecules on the cell surface, and be internalized specifically (receptor mediated in active processes), or they can be internalized non-specifically in the fluid encapsulated within these vesicles. Therefore it is important to determine which of these mechanisms is occurring. Equations can be used to quantitatively estimate the likelihood of NPs to enter cells through each pathway based upon their physical properties (Equation 5.1 and Figure 5.21). The number of NPs / mL of media can be calculated (Equation 5.1). The number of NPs / mL can then be substituted into the equations from Figure 5.21, to calculate the likelihood of fluid-phase and receptor mediated endocytosis occurring, as previously demonstrated by Smith *et al* [5].

$$N = \frac{(6x10^{12})}{(y\pi z^3)} \tag{5.1}$$

Equation 2: N = number of particles / mL; x = particle weight (g / mL); y = density; z = diameter.

The number of NPs present in 1 mL of the stock solution (N) of 280 mg / mL is $5x10^{13}$. As previously stated in the materials and methods (Section 2.1.1), the NP stock was diluted 1 in 100 for internalization experiments giving a final working concentration of 280 µg/mL. When substituted into equation 5.1 a total concentration of N = 5 x 10^{11} NPs/mL is determined. When this is substituted into the equations in Figure 5.21 the number of

- Vesicle diameter *(D)* = 150, 300, 500 nm
- Coat thickness – clathrin (*C*) = 22 nm
- Lipid bilayer thickness – (*L*) = 5 nm
- NP concentration (*c*) = 5 x 10^{11} NP/mL
- NP Radius (*P*) = 30 nm
- Inner lumen radius of vesicle

  $r = D/2 - C - L$
- Internal volume of vesicle

  $V=4\pi r^3/3$

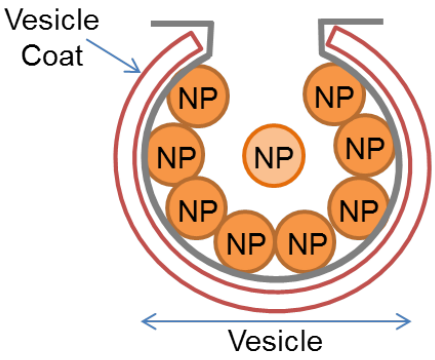

No of NP entering via each mechanism

- Fluid Phase: An average volume *V* of NP laden fluid contains:

  $N_1 = V^*c$
- Receptor Mediated: NPs pack on an inner radius: $p = r - P$
- No. of NP is calculated that can bind simultaneously to a flat region of equivalent surface area giving:

  $N_r = 0.91(4\pi p^2)/(\pi P^2)$ *

Figure 5.21: Calculations to obtain the number of particles that can enter a cell through fluid-phase endocytosis compared to receptor mediated endocytosis Figure and equations adapted from [5]. The equations can be substituted to determine the most likely means of NP cellular entry: fluid phase, or receptor mediated. The close circle packing density (where all NPs are touching and attached at a flat surface) is 0.91. The curvature of the membrane is neglected and therefore this will be an over estimation.

Table 5.1: Estimation of the number of particles that can enter a cell through different mechanisms based on calculations shown in Figure 5.21

Diameter (nm)	Inner radius (nm)	Lumen volume (nm^3)	Volume (ml)	NP in lumen	Packing radius of lumen (*p*) (nm)	NP on surface	Likelihood
Clathrin coat assumption							
150	48	463246	4.6×10^{-16}	2.3×10^{-4}	18	1.3	5652x
300	123	7794781	$7.8\ 10^{-15}$	3.9×10^{-3}	93	34.7	8897x
500	223	46451869	$4.6\ 10^{-14}$	2.3×10^{-2}	193	151	6565x
No clathrin coat assumption							
150	70	1436755	1.4×10^{-15}	7×10^{-4}	40	6.4	9142x
300	145	12770050	1.3×10^{-14}	6.5×10^{-3}	115	53.6	8246x
500	245	61600872	6.2×10^{-14}	3.2×10^{-2}	215	185.4	5794x

NPs that can internalize through specific routes is determined. The results are shown in Table 5.1. In each quantification based upon different vesicle diameters, the cellular entry of NPs via receptor mediated endocytosis or surface attachment is more likely rather than entry in the fluid phase within vesicle lumen. The diameters (nm) given are used to roughly estimate the NP numbers based on vesicle size, as this can vary. A limitation of the original equations used, which is based upon previously published work by Smith *et al*, is that they assume a Clathrin coat. If, as previous data has suggested (Figure 5.16), this process occurs through macropinocytosis / caveolin mediated endocytosis then the vesicle lumen will be larger (due to the lack of Clathrin coat), and therefore the number of NPs that can internalize via each route would increase. Calculations were performed whereby the radius was estimated without the inclusion of the 22 nm Clathrin coat (Table 5.1). Again similar trends were seen, although here the smallest vesicles exhibit the highest likelihood of internalization through receptor mediated route, a scenario which would be expected for smaller vesicles. However, in the case of the Clathrin vesicles, the very small internal vesicle size seems to reduce the likelihood of the surface attachment routes. Even so, internalization through NP receptor surface attachment still appears much more likely than luminal internalization. To confirm this, for vesicles of even bigger size (such as large macropinosomes which can be 0.2 - 5 µm in size), the equations were inputted into MATLAB and the graph of the likelihood of uptake through surface attachment compared to through luminal fluid internalization is plotted in Figure 5.22 for diameters between 0.15 µm and 5000 µm.

In each case presented, the calculation for NP attachment at the surface is likely to be an over-estimation, partly due to the neglection of the membrane surface curvature. The calculations are also based on the assumption that the entire membrane surface has the capacity to be coated in NPs. Despite this, the analyses indicate that NPs are likely to bind specifically to proteins or receptors at the cell surface and be carried into the cell in this manner, rather than being taken up within the vesicular fluid as evidenced

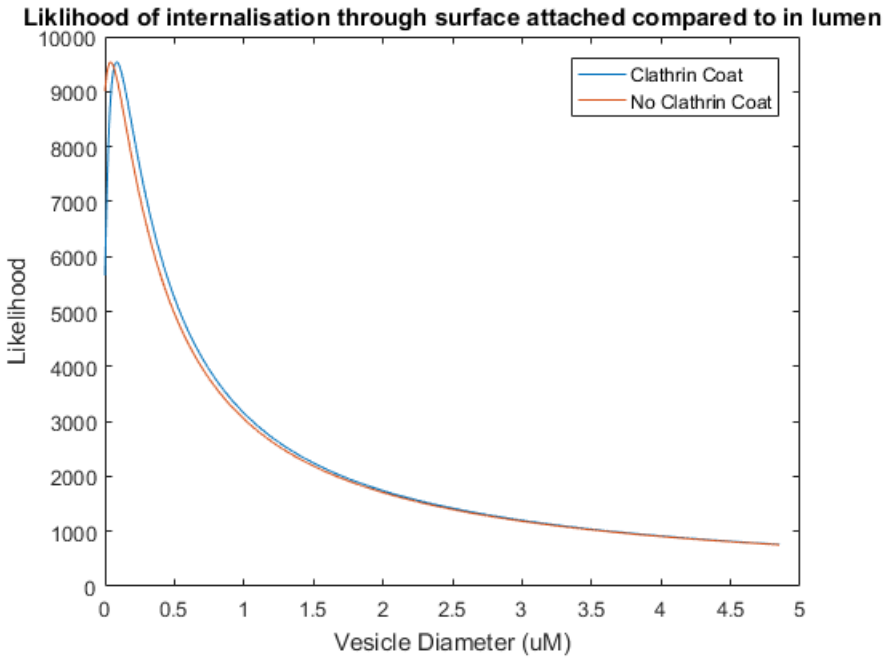

Figure 5.22: The relationship between likelihood of internalization through membrane attachment compared to presence within the luminal fluid, as a function of vesicle diameter. The graph clearly shows the it is much more likely that NPs will internalize through membrane attachment, rather than in the lumen of the vesicle. As the vesicle size increases, the likelihood decreases; however there is still a much higher chance of internalization through membrane attachment then within the fluid in the lumen.

in Table 5.1 and Figure 5.22. This is a favorable outcome for nanomedicine, which aims at the manipulation of the NP surface components in order to modulate specific cellular targeting and accumulation.

5.2.9 Translating studies into 3D cellular models

Flat, 2D cell culture techniques are regularly used in *in vitro* assays, however, there is a need for more representative cell culture models, given that most cells within the body reside in a 3D environment, critical for their growth and metabolism. Although 2D cell cultures offer a useful tool for the investigation of NP uptake and effects (amongst other things), it is generally recognized that they do not adequately represent this physiological environment *in vivo* [349]. Multicellular functions, and cellular interactions are lost when using simplified 2D culture systems. This leads to inaccuracies when assessing potential toxicities and poor translation of effects into clinical treatments and outcomes [349]. Often *in vivo* animal models are used, however with the increased pressure to reduce unnecessary animal studies, 3D cell culture models offer an attractive intermediate stage that allows screening of potential cancer therapies prior to animal studies and first studies in man. A multitude of methods exist for the creation of 3D cell spheroids, using either rigid scaffolds (e.g. micro-patterned surfaces) or non-scaffold based methods (e.g. hanging drop) to generate multicellular interacting environments. Traditionally these methods involve a plastic substrate with organic matrices such as collagen or matrigel [383]. The refractive properties of these organic matrix materials can lead to interference in microscopy studies challenging assessment of NP uptake. Methods such as SCIVEX NanoCulturePlate (NCP) avoid these organic matrices. Therefore these NCP offer a promising, reproducible method for spheroid generation that replicate *in vivo* conditions and overcome some of the limitations of traditional 2D cell cultures by the introduction of cell-cell interactions, oxygen and nutrient gradients, non uniform NP exposure conditions, altered enzyme expression profiles and drug reactivity [384]. The NCP plates have an inorganic micro-square (depicted in Figure 5.23) or micro-honeycomb (not shown) scaffold pattern printed onto

the synthetic resinous base of the plate [384]. This pattern enables reduced contacts between the cells and the surface of the well, therefore promoting uniform spheroid growth in routine 2D cell culturing conditions, greatly reducing the steps needed to create the multicellular spheroids [384]. The refractive index of the synthetic base closely matches that of glass, and therefore renders the dishes compatible with microscopy methods such as confocal; this is demonstrated with reflectance and transmitted light images at the plate base in Figure 5.23.

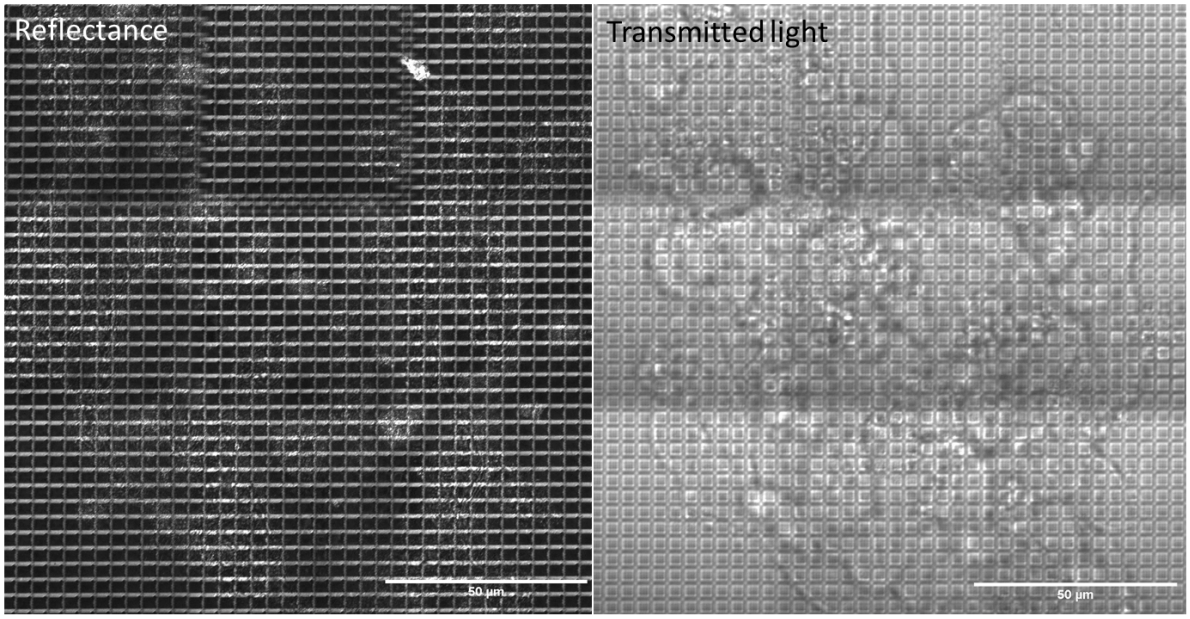

Figure 5.23: NCP plates have a thin film engineered with a micropattern to promote spheroid growth and can be visualized using microscopy. The pattern can be visualized using reflectance and transmission light microscopy when imaging at the base of the well.

Prior to spheroid studies, the best staining method for cell detection over long time periods had to be determined. Therefore cells were plated in standard dishes, 24 hrs later these cells were treated for 30 mins with a variety of cytoplasmic dyes to ascertain their stability and retention over experimental time courses. Following incubation for 72 hrs and 96 hrs post dye treatment, cells were fixed and imaged using confocal fluorescence, to determine which stain was successfully retained for the period of incubation. The CTV dye was not retained well in the cytoplasm. The CTV is also excited using the 405 nm laser which is regularly used for visualization of DAPI nuclear stains. Therefore this dye

reason was not used (Figure 5.24). CTR and CTO were both still retained within the cell at 120 hrs (Figure 5.24). Therefore CTO was used in subsequent experiments to increase experimental consistency between 2D and 3D studies.

Different cells have different spheroid forming capacities, and this can vary with scaffold micro-structure To determine the spheroid forming capacity of the different cell lines, A549, HeLa and MDA were all plated on square patterned micro-plates. Cells were detached, centrifuged and resuspended in 1 mL of media for CTO staining for 30 mins prior to plating. After this cells were centrifuged for 5 minutes at 150 g and washed with PBS (repeated 3 times). Cells were then plated onto pre-incubated (at 37°C) media containing NCP plates as detailed in the methods section. Care was taken to remove air bubbles present at the base of each well using a pipette tip. Air bubbles are known to inhibit spheroid growth. Different cell lines were plated onto the NCP plates at the recommended density ($6x10^4$) and monitored over 120 hours to observe spheroids formation, which can occur as little as 1 day post plating. Figure 5.25 shows images taken using an optical microscope on each day following plating. MDA and HeLa cells both appeared to form spheroids using the square patterned micro-plates. Spheroid generation was observed as soon as 24 hours post plating in MDA and HeLa cells; these spheroids continued to increase in size over the next 96 hours, however the size of the spheroids appeared fairly non-uniform, indicating that further method optimization may be necessary for future studies (Figure 5.25). A549 cells did not appear to form spheroids under these conditions, and continued to display a 2D mono-layer appearance. Upon media change, MDA cells seemed less stable; spheroids often detached from the base of the plate, despite the use of extreme care and careful pipetting, therefore experiments were continued with HeLa cells. Spheroid formation did not occur as effectively when using the honeycomb micro-pattern plates, therefore experiments were continued in the square plates only.

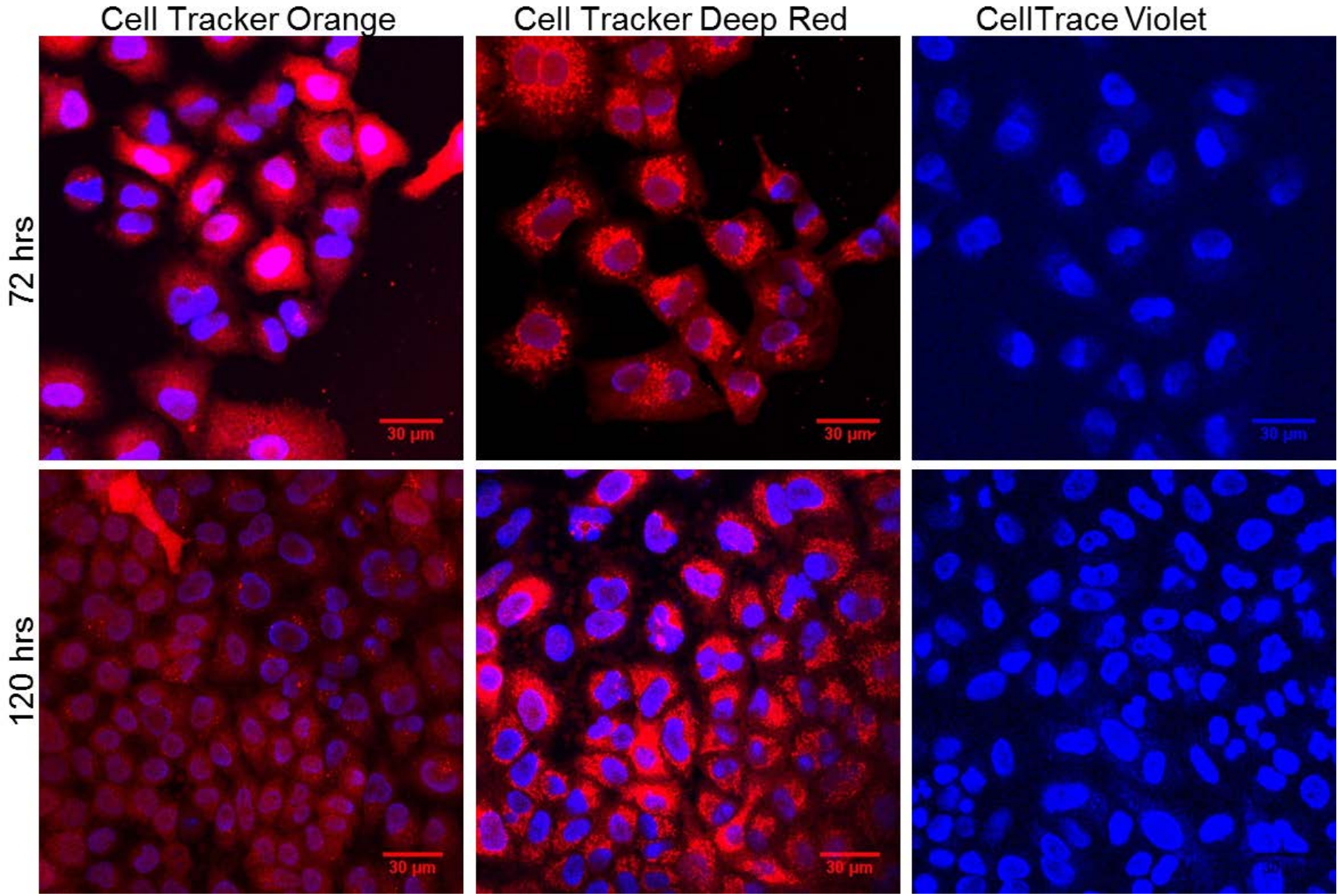

Figure 5.24: Fluorescent confocal images of the different possible cytoplasmic dyes for spheroid experiments. At 72 hours, CTR and CTO are both still visible using fluorescence confocal microscopy, CTV is no longer visible. At 120 hours CTO demonstrates even staining patterns across the cell cytoplasm, whereas CTR appears to be intense in some parts of the cell, and less intense in others.

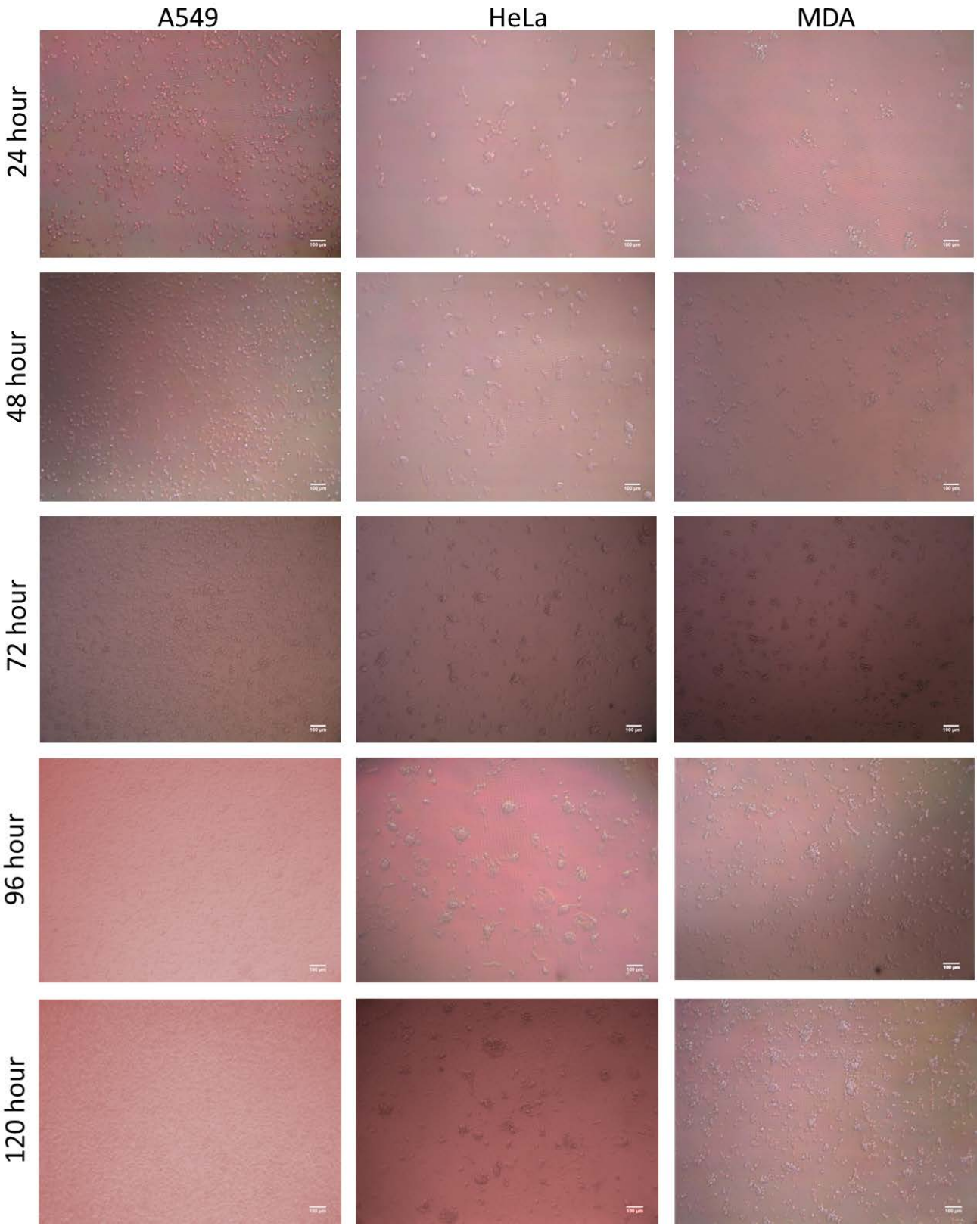

Figure 5.25: Spheroid growth in different cell lines over 120 hours. Spheroid growth was monitored over 120 hours. After 24 hours HeLa and MDA cells appeared to start forming small spheroids. Over the next 96 hours spheroids grew in size. A549 cells didn't appear to form spheroids for the duration of the incubations.

5.2.10 Uptake studies in spheroids

Previously, the uptake and translocation of NPs in cell spheroids has been found to depend greatly on the physical NP size. Gold NPs, for example, penetrate further into the spheroid when they are below 6 nm in size, whereas larger gold NPs, of 15 nm, penetrate less efficiently [385]. Small, sterically stabilized SPIONs have been shown by TEM to penetrate up to 100 µm into DLD-1 colon cancer spheroids, facilitating the diffusion of chemotherapeutic agents [386]. However the accumulation and localization was found to greatly depend upon the surface properties of the SPIONs, particularly the charge [386]. The SPIONs used in this experiment have a core of 4 nm, however their hydrodynamic size is 60 nm when coatings are taken into consideration, therefore the penetration into spheroids may be significantly decreased compared to that in cell mono-layers. The surface charge is also fairly close to neutral (slight negative charge), and cationic particles have been found to penetrate spheroids and tumors more efficiently and to a greater extent than neutral or negative NPs. To ascertain if these SPIONs can penetrate HeLa cell spheroids, cells were plated as described in the previous paragraph and in the methods section. A positive control was included due to the highly scattering intracellular environment which complicates the assessment of SPION internalization within these spheroids. Therefore, upon plating, additional wells that contained different concentrations of SPIONs were included (1 in 100; 1 in 200; 1 in 300 and 1 in 400 dilutions leading to concentrations of 280 µg/mL, 140 µg/mL, 105 µg/mL and 70 µg/mL respectively). Interestingly, the addition of SPIONs to the growth media led to the formation of larger and rounder spheroids when compared to the control cells (Figure 5.26).

It is possible that cells preferentially migrate together to reduce the exposure to the NPs surrounding them during growth. It is also possible that the SPIONs, over the 96 hr time course, lead to increases in proliferation or migration of these cells. An increase in free iron following partial SPION degradation, thought to occur as early as 24 hrs post internalization, could lead to the favorable formation of bigger spheroids over the

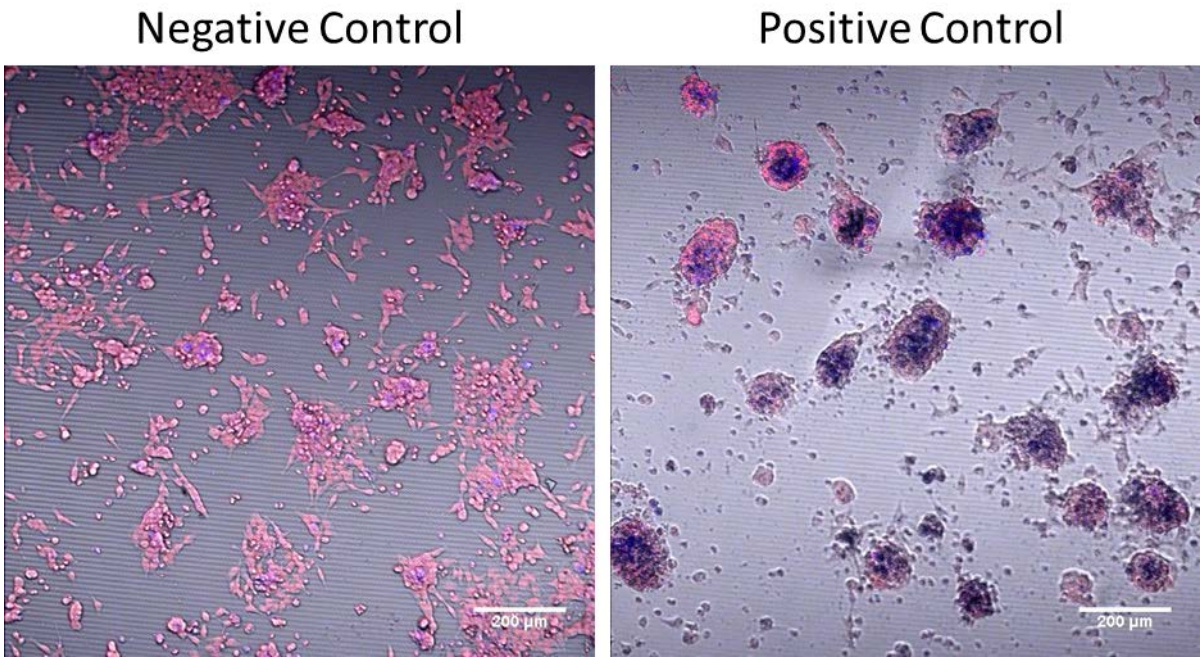

Figure 5.26: Spheroids form better in the presence of SPIONs. At 140 hours, spheroids appear to be larger and better formed in positive control samples that are grown in the presence of SPIONs (105 µg/mL) when compared to negative controls.

spheroid generation time-course [107]. Indeed, SPIONs have been shown to alter the balance of cell cycle regulatory proteins, favoring cell cycle progression and increased cell growth and proliferation [107]. However the mechanisms were not determined at this time. High concentrations (280 µg/mL, 140 µg/mL) in the positive control groups led to a large amount of cytotoxicity and cell death, and therefore these cell conditions were not imaged.

SPION penetration into the center of the spheroids was evident in some cases at longer incubation time points (6 hrs, 24 hrs and 48 hrs), indicating that SPIONs can accumulate within cells despite not being directly exposed (Figure 5.27). However the detection of signal is greatly hindered by the reflectant signal arising due to cell debris within or surrounding the spheroids (Figure 5.27). It is apparent that following an hour long incubation, SPIONs do not appear to penetrate the spheroids very deeply (Figure 5.27) an effect which has been noted previously, and is likely to accurately reflect the situation *in vivo*, where the inner tumor layers are protected from NP exposure [387]. With increasing lengths of time, SPIONs appear to penetrate the spheroids to a greater extent. However

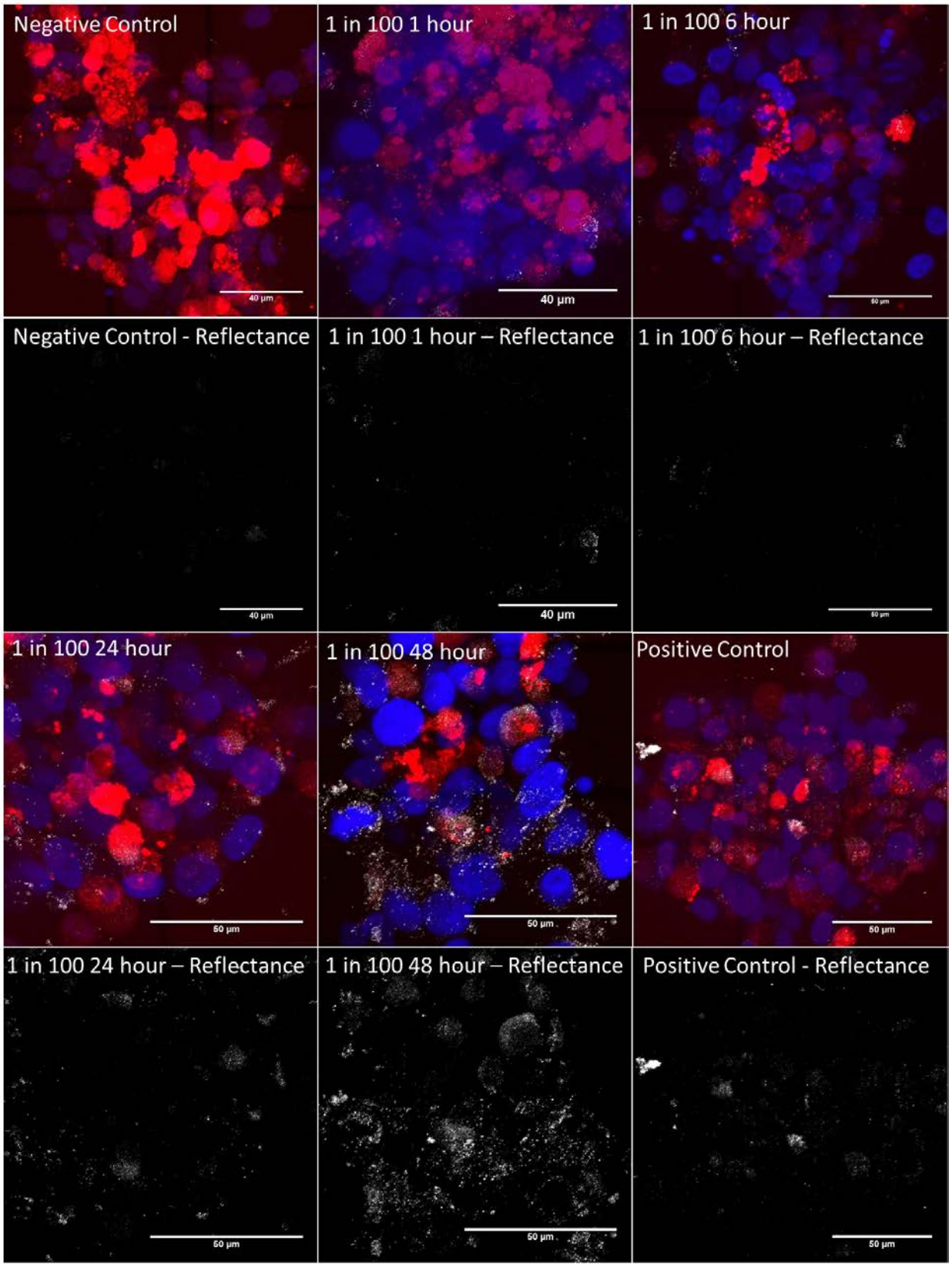

Figure 5.27: Confocal microscopy images of SPION uptake within HeLa cell spheroids. No reflectance from SPIONs is visualized in negative control cells, however some areas of cells do lead to reflectance intensity. Following one hour treatment (280 µg/mL) the intensity within the spheroid is clearly higher than in the control cells. When grown in the presence of SPIONs, reflectance signal can be clearly identified

uptake appears to be restricted largely to the peripheral cells. This indicates that the translocation of NPs may not occur, or may occur slowly or to a lesser extent. Either this or the detection of NPs is not sufficient in the spheroid samples, which is possible. Although the results indicate that SPIONs are able to penetrate into the spheroids, the extent of this could not be quantified at this time. The method has been demonstrated here as suitable for use with NP studies using reflectance imaging, paving the way for future experiments to determine the mechanisms, trafficking, translocation and toxicity of NPs, within the 3D multicellular environment. This would allow comparisons to be made between *in vitro* and replicated *in vivo* conditions. As the NCP plates allow spheroids to be formed under normal culture conditions it is possible that siRNA inhibition studies could be performed in a manner similar to those in 2D cultures. Careful optimization of the siRNA experimental parameters would be necessary to ensure efficient siRNA delivery to the center of the spheroids, and to ensure knockdown of the specific pathways. This could be performed prior to spheroid plating, or during spheroid formation, for example.

5.3 Conclusions

The efficient localization and internalization of SPIONs at a target site (and limited unwanted uptake at non-target sites) is key to their success or failure as therapeutic or diagnostic agents. The uptake potential of different cell lines can vary, and therefore the understanding of cellular factors involved is crucial for translation into intelligently designed nanocarrier systems. Accordingly the efficient internalization of SPIONs in phagocytosing cells cannot be assumed to represent the situation in other cell types *in vivo*, or even *in vitro* [343, 157]. In the studies presented here an accumulation of 60 nm, dextran coated Sienna$^+$ SPIONs was observed in macrophage and non-macrophage (A549, MDA, HeLa) cells. No statistically significant difference between the internalization of SPIONs by the different cancer cell lines tested was observed at the highest incubation concentration and exposure time. However, the macrophage cell line showed a significantly

increased internalization capacity compared to the cancer cell lines, determined due to the increase in observed reflectance signal at each concentration and time point. This may be expected due to the specialized functions of macrophages for engulfing foreign material. An 'intensity binning' analysis was also conducted, as it is suggested this gives a more representative overview of cellular activity, due to the heterogeneous responses a cell population can show [350]. Various parameters could be assessed in this way in future studies including cytotoxic responses and markers for various cellular effects (such as ROS production). This may provide a better insight into the toxicological effects of SPIONs post internalization, where other analyses that assess only global cell responses (mean averaging) may result in masking of sporadic local effects that are not population wide.

The results presented here have suggested the involvement of a variety of pathways in SPION internalization. It would be beneficial to confirm these findings using multiple target sequences where SMARTpool was not used, and extend the studies into knock-out models rather than knockdown (such as with CRISPR/Cas9). Non-macrophage cell lines appeared to use different mechanisms to internalize the SPIONs, depending upon cav-1 (caveolin mediated endocytosis) and Pak-1 (macropinocytosis) activity. This differs from the typical macrophage model of internalization, which is often suggested to occur predominantly through CME. Even so, regardless of mechanism, the likelihood of SPIONs entering cells through an active, receptor mediated process, is much higher then that of non-specific fluid phase uptake, as calculated. This is promising for the future targeting potential of SPIONs to specific cell populations, as active processes can be more easily manipulated than non-specific internalization events. Analysis and modification of the protein corona constituents could shed light on the importance of surface proteins in determining which pathway is preferentially utilized and could provide insights into pathway modulation. If conclusions regarding the relationship between cellular receptor expression, pathway activation and corona components could be established, this could

be incorporated into models along with NP properties to more accurately predict the internalization patterns of NPs in different cell lines. Such an approach is already under development for certain NP compositions, and data from within this chapter could feed into such models specific to SPIONs [317].

The studies shown here have provided mechanistic insight into the cellular internalization patterns in 2D cell culture. However the translation of results from *in vitro* tests to *in vivo* is often lacking. 3D models provide an intermediate between classical *in vitro*, animal *in vivo* and *in vivo* clinical studies, facilitating the elucidation of SPION interactions in a multicellular environment. Further development of the method for spheroid generation, and subsequent addition of properties that mimic *in vivo* conditions will better predict the clinical outcomes of engineered SPIONs vastly increasing the chances of successful therapy. Challenges still exist in the uniformity of spheroids generated using these methods, and therefore issues exist with reproducibility. Spheroid studies, despite providing a more representative model for *in vivo* studies, still often lack imitation of the leaky vasculature surrounding tumors, which is another added complexity in the successful delivery of nano-therapeutics to tumor sites. Spheroid culture models can be combined with an endothelial cell coating, such as that used by Ho *et al*, to mimic the endothelial of blood vessels surrounding the tumor, which can be used to model extravasion and penetration [388]. The method used by Ho *et al* allowed the generation of uniform spheroids due to the restriction by the endothelial cell layer, as well as providing a model system that more accurately represents the *in vivo* physiological environment. It is crucial, prior to translation of studies into animal models, that investigative studies of unlabeled NP are performed to provide mechanistic insight into how NPs, such as these SPIONs, interact with 3D tumor micro-environments This will, in theory, facilitate a better understanding of the ability of these SPIONs, and other modified forms, to fulfill their potential within the clinic.

5.4 Key Findings

1. All cell lines tested internalize SPIONs in a time and concentration dependent manner in 2D cultures.

2. Specialized cells such as macrophages internalize significantly more SPIONs under the same exposure conditions when compared to non-macrophage cells types.

3. SPIONs appear to enter cells through a variety of mechanisms; in macrophages CME appears to be the predominant mechanism, whereas in non-macrophage cell lines it appears that both caveolin mediated endocytosis and macropinocytosis played a role.

4. Internalization appears to be an active, not passive process based on calculations.

5. Spheroids can be generated using normal 2D culture conditions, and uptake of SPIONs into spheroids is evidenced in preliminary studies supporting future work into these 3D models.

6. Imaging of 3D spheroids using RCM and penetration of SPIONs into the outer layer of spheroids was demonstrated, as a basis for future uptake, efficacy and toxicity studies.

CHAPTER 6

WHAT HAPPENS NEXT?

Parts of this chapters are published as part of a multi-author mini-review paper (Guggenheim *et al.* Int. J. Biochem. Cell Biol. 83. pg 65-70.).

6.1 Chapter introduction and summary

When NPs enter cells via endocytosis they are encapsulated within vesicles that traffic through the endosomal network. Following budding at the plasma membrane, the resultant vesicles converge in the early sorting compartment (early endosome). Intracellular sorting and trafficking pathways can lead to a variety of fates within the cell, including the degradation of NPs, starting with the loss of protein corona and surface proteins. NP degradation can be evaded by endo-lysosomal escape, or by recycling pathways [389]. The trafficking route can be investigated by determining the colocalization of NPs, such as SPIONs, with particular compartment markers, as well as via the use of inhibitory strategies specific to individual trafficking pathways e.g. the Rab proteins.

Various types of SPIONs have been found to localize to endo-lysosomal compartments in *in vitro*. Most of these studies have been performed in macrophage models using fluorescently tagged NPs [168, 169, 163, 164, 164]. However, it is particularly important to examine cellular interactions of the unmodified Sienna$^+$ SPIONs (i.e. without fluorescent

tags) to better predict *in vivo* responses [181]. In the lysosome, the presence of chelates with a high affinity for Fe^{3+} and an acidic environment could cause SPIONs to dissolve in as little as 96 hours [168]. This could lead to the release of free iron into the cell cytoplasm [168]. The deleterious effects of free iron release and iron overload have been discussed previously in Section 1.2.3. It is therefore necessary to quantify free iron release following this degradation.

ICP-OES is a technique that is able to quantify the elemental composition of solutions and can be used to determine the concentration of iron ions in solution. This breakdown process can be simulated using solutions with a composition that mimics the internal lysosomal environment [390]. After incubation within this Artificial Lysosomal Fluid (ALF), free ions can be separated from the intact SPIONs by methods such as centrifugal ultrafiltration. Following acid digestion the amount of free iron can be analytically quantified [391]. This analysis can be combined with monitoring the physicochemical changes that occur to these SPIONs in the suspensions over the degradative time courses using DLS.

This section investigates the cellular trafficking of the clinically relevant Sienna$^+$ SPIONs within a HeLa cancer cell model. RCM and R-SIM NP imaging along with fluorescent compartment identification have been employed to determine the sub-cellular localization of SPIONs. Quantitative information can be obtained through automated processing and analysis to calculate signal overlap between reflectance (SPION) and fluorescent (compartment marker) channels. Microscopical studies performed within this chapter indicate that cancer cells process Sienna$^+$ SPIONs through the endo-lysosomal pathway, with a large portion accumulating within lysosomes. Therefore, the conditions of the lysosome were mimicked using ALF of pre-determined composition [390]. SPIONs were incubated in this mimic fluid for a maximum duration of 140 hours to model the breakdown of SPIONs in the lysosome over time. This dissolution was measured using multiple techniques including microscopy, quantitative ICP-OES, DLS, Zeta potential, pH and PDI.

6.2 Results

6.2.1 Trafficking of NPs following cellular uptake

The Rab family of proteins are highly conserved GTPases that are involved in the regulation of endosomal trafficking. Fluorescently tagged Rab proteins can therefore be used to identify specific compartments [147]. For example Rab5/5A regulates the kinetics of membrane trafficking through early endosomes [392]. Rab5 helps to recruit Rab7A, which is associated with maturation into the late endosomal compartment and the lysosome [392, 393, 147]. Rab11 is a marker for the recycling endosome which recycles cargo back to the cell surface [394]. In order to determine the trafficking route and fate of Sienna $^{+}$, HeLa cells were transfected with Rab5a, Rab7 or Rab11 DNA (detailed in the methods Section 2.5). The day after transfection, cells were fixed at various times following the addition of Sienna $^{+}$ SPIONs to ascertain their intracellular localization within the endo-lysosomal transport system.

While extremely informative when properly conducted, colocalization studies are notoriously difficult and time consuming to quantify due to the lack of standardized analysis procedures [348]. The use of reflectance and fluorescence optical configurations also gives rise to the possibility of misalignment between modalities. This effect is particularly pronounced at higher magnifications. Prior to colocalization analysis it is crucial to ensure that any misalignment is corrected. To facilitate this, red polystyrene fluospheres (100 nm) were imaged in reflectance and fluorescent confocal mode (Figure 6.1A) and any misalignment (Figure 6.1A) was corrected in MATLAB, post acquisition (Figure 6.1B). The rigid transformation that aligns the images was determined using intensity based registration (imregister function) with optimized parameters. This transformation was then applied sequentially and automatically to each image. This was performed for each experimental aquisition. The use of reflectance, rather than fluorescence, negates the contribution of fluorophore bleed-through and crosstalk.

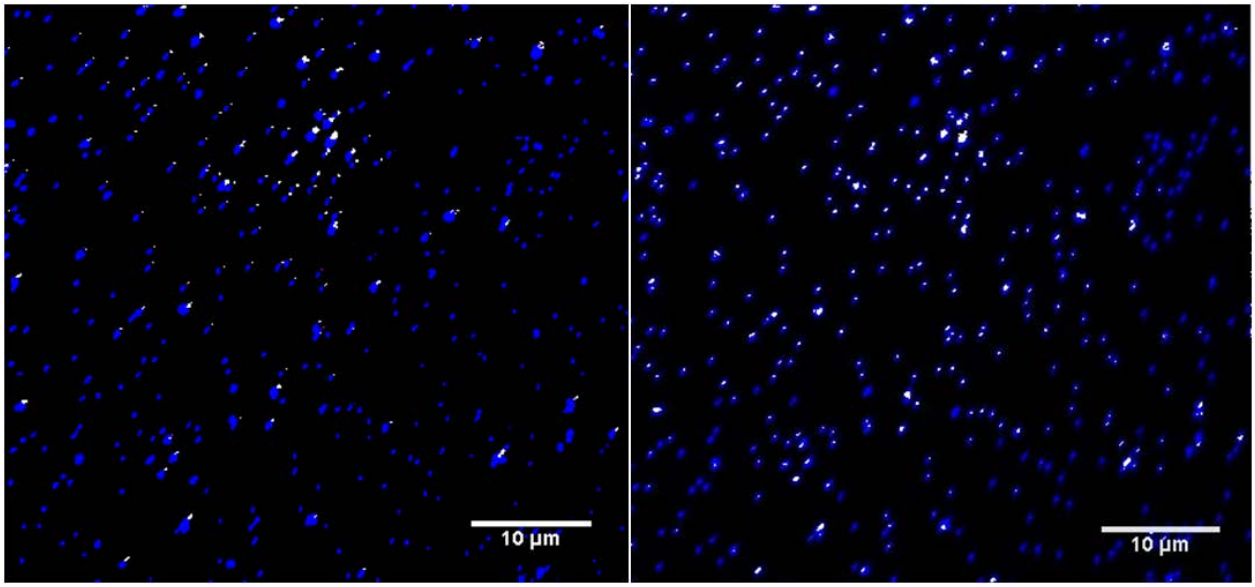

Figure 6.1: Example raw and realigned confocal reflectance and fluorescent images of polystyrene beads. A) Depicts the raw fluorescent (blue) and reflectance (grey) images of 100 nm red polystyrene beads showing considerable offset. B) Depicts the realignment results.

6.2.2 Analysis of colocalization

Despite the wide availability of quantitative alternatives, colocalization analysis often relies merely on overlaid color merges and human judgment [395]. This overlay or 'judgment' method is very ambiguous and can confound results. The image display itself, and the settings of the Look Up Tables (LUTs) can alter the perceived colocalization, in part due to the varied SNR across images (e.g. Figure 6.2).

Visualization in this way tends to assume both channels have nearly equal intensity values, which is an unlikely scenario in the case of reflectance and fluorescence images. Colocalization images are often combined with scatter plots. These are of limited value in most cases, unless significant processing is done to remove the high level of background reflectance signal that skews the observed correlation. Many different methods exists for quantification of the colocalization between different image channels. This includes Pearsons Correlation Coefficient (PCC), Manders (M1 and M2) coefficients, object based and statistical methods [395, 348, 396]. Each has its own significant advantages and disadvantages which are discussed and reviewed thoroughly [395, 396, 348]. PCC, for example,

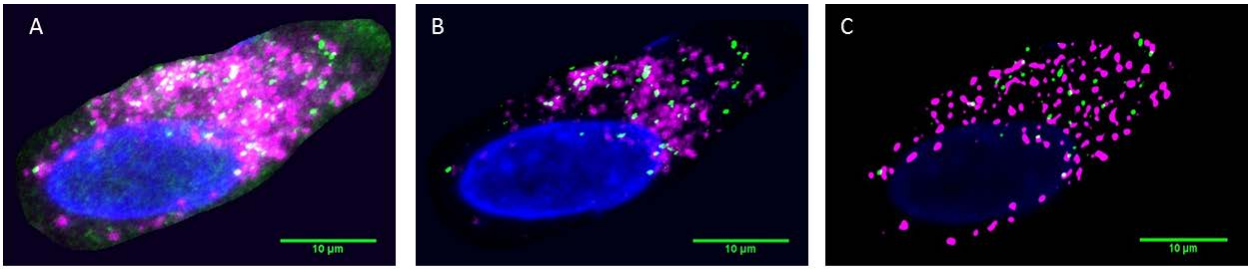

Figure 6.2: Example of the problems associated with overlaying unprocessed images for determination of colocalization in samples. A) Shows an overlay with the LUT's display increased, colocalization appears almost 100%. B) Example of the LUT's being decreased, and colocalization assessment is now a judgment call, and difficult to distinguish. C) Shows processed and segmented image where white represents colocalization of objects, giving a more definitive conclusion regarding colocalization

can be very difficult to interpret. However, in comparative studies, a change in PCC can indicate an increase or decrease in colocalization. Due to the large contribution of background reflectance (previously demonstrated in Section 4.2.9) processing of the images is highly desirable to achieve a quantification of the perceived colocalization. It is therefore advantageous to first isolate the signal of interest regardless of the colocalization analysis used.

6.2.3 Segmentation of cells and lysosomal regions

Lysotracker Red DND-99 comprises a conjugated multi-pyrrole ring linked to a weakly basic amine. It can pass freely through membranes at neutral pH and accumulates in acidic compartments where it becomes protonated. In these experiments, cellular autofluorescence was used to segment cellular regions (Figure 6.3A). Segmentation was obtained by image convolution with a Gaussian low-pass filter kernal with a radius of 5 pixels and sigma value of 3. The radius indicates kernal width in pixels and the sigma value determines the degree of smoothing. Image contrast was then increased using the built in 'imadjust' MATLAB function and pixel values that are above the mean of the image are set to the mean value. This gives an image that has signal intensity at intracellular locations and not in extracellular locations. The cells were then segmented using K-means

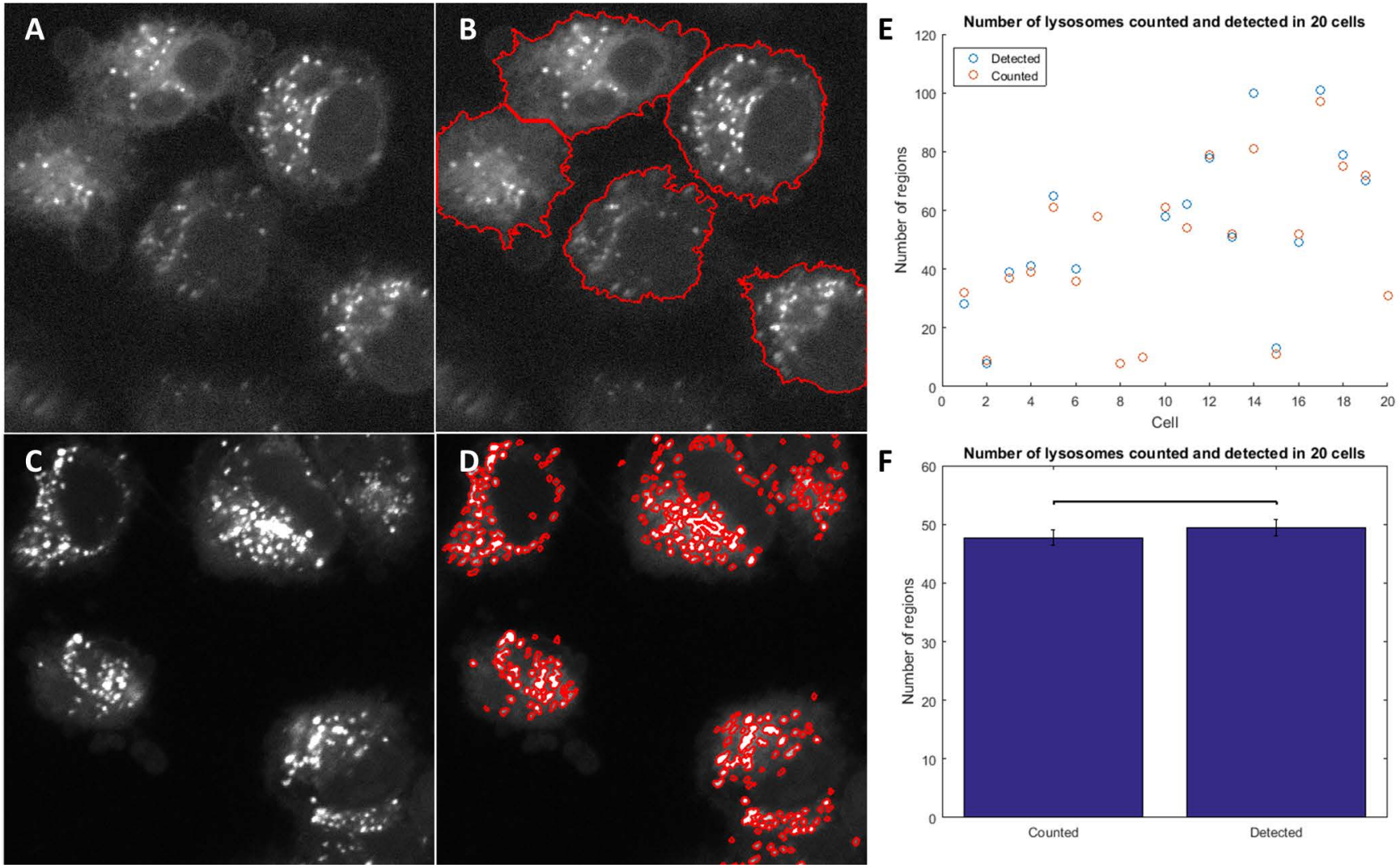

Figure 6.3: Segmentation of cellular and lysosomal regions with MATLAB. Cell segmentation is achieved using cell auto-fluorescence and lysosomal stain. A) Raw lysosome signal and autofluorescence, B) Corresponding outline resulting from the segmentation achieved using smoothing, clustering and watershed transform. C) Raw lysosome stain image D) Example lysosome segmentation using Gaussian denoising and La Trous wavelet transform segmentation. E) shows matching results from number of detected lysosomal regions per image (blue) and eye-counted regions per image (red). In columns that appear to only display a red dot and not a blue dot, the same number were observed using each method. F) indicates the lack of significance between the two groups (P=0.845).

clustering (nClusters= 2 or 3). The outcome of the segmentation is shown in red in Figure 6.3B, overlaid onto the cellular regions.

A variety of methods can be used to segment the endo-lysosomal regions. The lysosome stain displays a high SNR, therefore many methods would provide sufficient segmentation of this signal. Global thresholding can sometimes prove difficult to implement in an automated work-flow due to the variable nature of the fluorescence signal, and is often only successful in a subset of images, unless preceded by processing such as noise removal and background subtraction. The Difference of Gaussians (DoG) method is essentially similar to a 'Mexican hat' filter and simulates the Laplacien of the Gaussian (LoG) of the image. DoG and LoG methods exert local filtering and can therefore overcome natural variation that exists across images. Signal is detected if intensity is greater then a particular threshold. These methods generally require a manually set sigma radius value that restricts the size of detected spots [280]. Oliver-Marin introduced a method based on the Undecimated Wavelet Transform (UWT) [280]. UWT uses multi-resolution wavelet decompositions where each level represents a different resolution, allowing more robust detection of different sized signal areas. The use of the UWT transform led to a segmentation of lysosomal regions that closely matched manual counting methods (Figure 6.3). The lysosomal stain was first de-noised using a Gaussian filter kernal (radius of 2 pixels, sigma 1) and the La Trous wavelet transform segmentation was performed using iterative filtering. The result of the segmentation is displayed in red over the raw image (Figure 6.3C and D). The segmentation leads to the separation of a similar number of regions in each cell as a manual counting method. Different pairs of values for 20 cells are shown in the graph in Figure 6.3E. Blue spots represent detected lysosomes and red display counted lysosomes. The results correlate well and therefore this segmentation procedure was deemed suitable for the analysis of the lyosomal colocalization experiments.

6.2.3.1 Segmentation of endosomal regions

The signal detected using fluorescently tagged Rab5a, Rab7 and Rab11 DNA constructs often appeared less intense than the Lysotracker stains. The success of DNA transfections can often be very variable. For this reason, multiple methods were assessed to achieve the optimal segmentation of the signal. These methods included intensity thresholding, K-means, and UWT. Images were first preprocessed using a Gaussian filter and background subtraction. In contrast to the detection of lysosomal signal, the use of the La Trous wavelet transform appeared to lead to over segmentation of the image, likely due to the increased background signal and the decreased SNR of the images. As seen in Figure 6.4A, the wavelet transform detected many more endosomes than the manual method. K-means clustering (in a 3D stack) led to a slight over estimation in some cases. It is likely that the different intensities and different staining efficiencies across different sample areas (and therefore acquired images) lead to a larger variety of image intensities, therefore leading to over or under segmentation. The use of the image mean itself as a segmentation threshold appeared to lead to a segmentation that more accurately represented the signal distribution and the manually determined values. The image mean itself will be lower if the stain is less intense, and therefore allows the successful segmentation of endosomes in a variety of different image types (Figure 6.4A and B). The comparison of counted and detected endosomes using the intensity threshold is plotted in Figure 6.4B. Therefore for the segmentation of endosomes the mean thresholding approach was applied.

6.2.4 Colocalization with endo-lysosomal markers

6.2.4.1 Endosomal Colocalization

Colocalization is a general term that encompasses both co-occurrence and co-distribution. There is not necessarily any reason why NP signal would correlate directly or co-distribute proportionally to a compartment within which they reside, i.e. there is no reason why every endosome or lysosome would have the same amount of NPs inside. Therefore, when

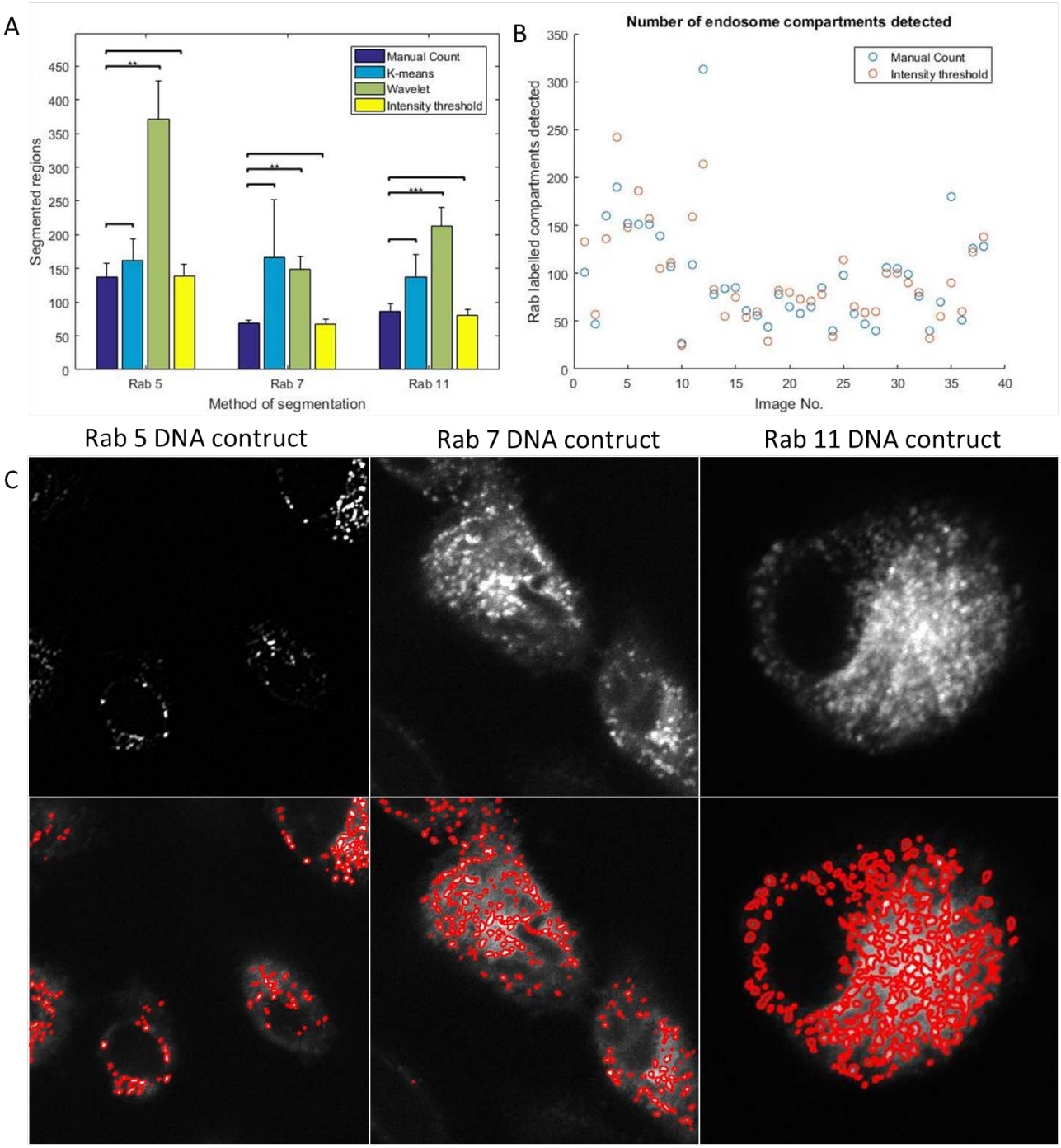

Figure 6.4: Segmentation of endosomal regions with MATLAB. A) Comparison of the different segmentation methods for different Rab DNA constructs. Mean +/- SEM is plotted, $p<0.01$ = **; $p<0.001$ = ***. B) Paired detected numbers of regions for different images using manual methods and intensity thresholding. C) Examples of the segmentation of each original image (top), red is the boundary of the segmented regions (bottom).

discussing colocalization in this thesis is it co-occurrence of the detected NP signal with signal from a labeled compartment that is referred to. Images were segmented to isolate the whole cell outline, the endosomal compartments, the NP signal, and DAPI nuclear regions. The DAPI region was subsequently removed from the colocalization analysis. The isolation of the endosomal signal can then be combined with isolated NP signal, using previously described methodologies for reflectance images (Section 4.2.9). The signal overlap of the detected NP objects with the detected endosomes effectively represents the Manders M1 coefficient. This was determined for SPIONs localizing to different compartments over the maximum duration of 48 hours (2880 minutes) (Figure 6.5). However, due to the diffraction limit and the limit in optical thickness of acquired planes, a certain degree of colocalization would be expected, regardless of true colocalization. This is so called random colocalization or false positives. Randomizations were performed at each time point with each marker to compensate for this. This randomization consisted of rotation of the SPION channel in 12° increments, this was repeated 10 times (10*12 °) for each cell, and subsequently the average of these randomizations was used as a measure of 'random' colocalization between the two channels. The mean of the random values at each time point was subtracted from the 'determined' value, to give a 'true' value. The PCC was also determined using the segmented intensity images, and again the random colocalization observed was subtracted from the original image.

SPIONs appear to colocalize with Rab5 positive compartments at early time points (0-6 hours) indicated by the analyses (Figure 6.5A, B and Appendix Figure B.22). Similar results have been described for other NPs, including polystyrene [249]. This colocalization increases up to 6 hours, thereafter it begins to plateau and decrease. This is expected as no new NPs would be internalized following removal of exposure media containing SPIONs at later time points. It is interesting that the colocalization is still increasing noticeably as much as 5 hours post-incubation. This could indicate that NPs attach at the cell surface and are internalized slowly. It could also be indicative of accumulation

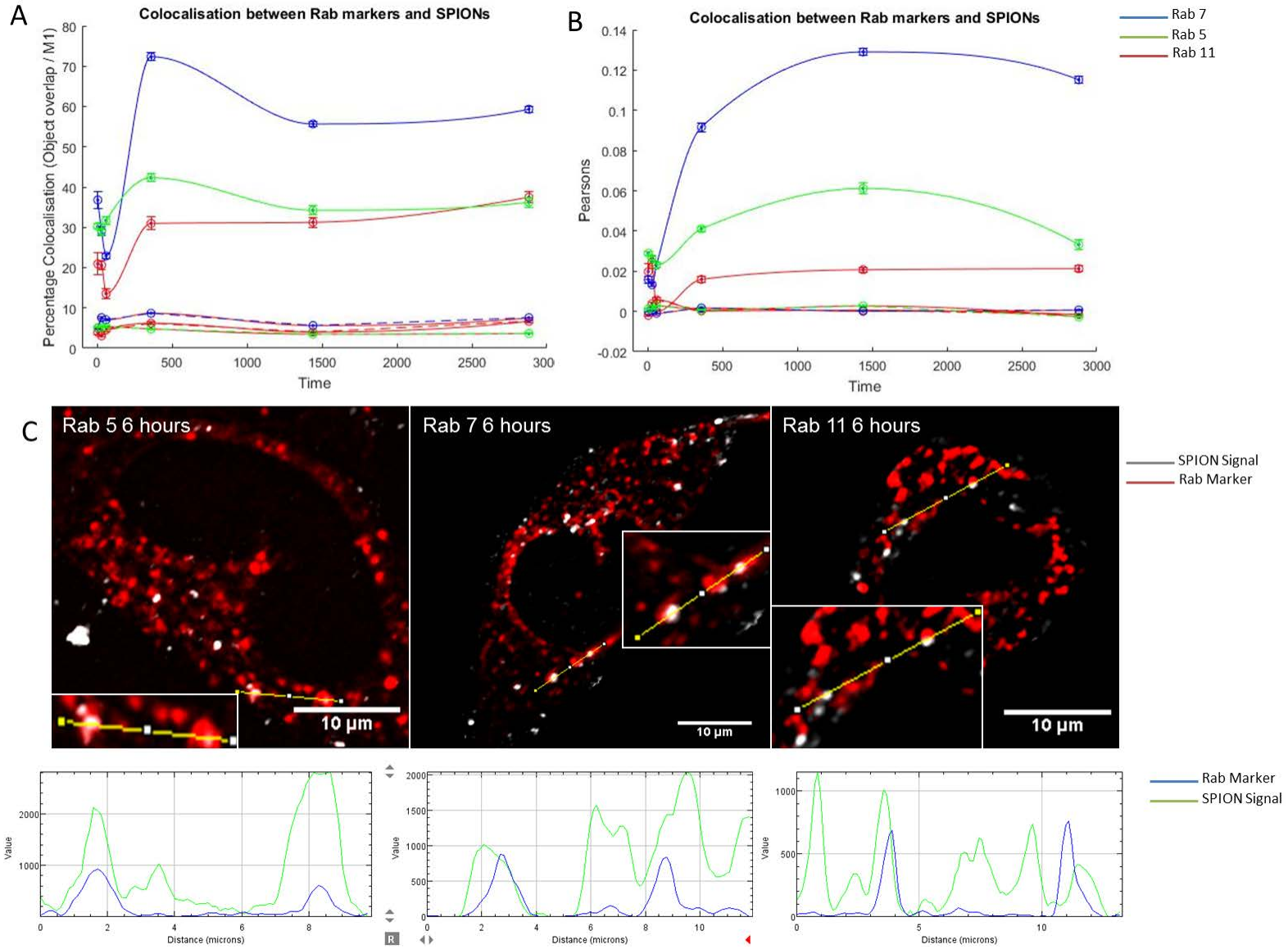

Figure 6.5: Colocalization between SPIONs and different Rab-positive endosomes between 0 and 24 hours (2880 minutes). A) The percentage of signal overlap of SPIONs to different Rab-positive endosomes. Increases in colocalization with Rab5 and Rab7 are seen initially, followed by an increase in colocalization with Rab11. The dashes lines show the values of the random colocalization and the solid lines show the calculations of colocalization in both graphs. B) Similar trends are seen with Pearsons analysis. C) Example images from the 6 hour time-point, the time point that displays the largest increase in colocalization between all channels. Corresponding line intensity plots are shown beneath the image which are plotted from the magnified region in each image.

and transfer of NPs between different Rab5 positive compartments. A 2-hour time point would be beneficial in future studies to determine the reason for this observation, and find where the curve plateaus. Interestingly, the increase in colocalization of SPIONs and Rab5 at early time points (such as 5 and 30 minutes) is fairly subtle, this reflects difficulties in analyzing colocalization between the very few detected NPs, particularly at 5 minute time point. It has been previously described that caveolar internalization takes longer than CME and therefore may explain, in part, the apparent delay in accumulation in different compartments [136]. It is also possible that SPIONs are not densely localized within these compartments until endosomal fusion occurs, which could lead to a decrease in detection of SPIONs present within compartments at earlier time points. Some early endosomes rapidly mature to late endosomes, however there is a subset that mature more slowly and are often occupied by recycling cargo [397]. Interestingly, colocalization between Rab11 and SPIONs appears to increase at the 6 hour time point (Figure 6.5). The degree of colocalization at this time point is shown in the overlay images and the line intensity scan, where a proportion of NPs can be seen to apparently overlay with the Rab11 stain. This may indicate that some of the SPIONs are destined to return to the plasma membrane following internalization. This could mark the ability of SPIONs to trancytose across the membrane to the external environment or neighboring cells. It has previously been reported that Ferucarbotran (Resovist) can be extruded from the cell. This was established by the identification of Rab11 associated Ferucarbotran and extracellular membrane bound Ferucarbotran [398]. If SPIONs are being recycled to the surface this could explain, in part, a continued level of association between Rab5 and SPIONs at later time points due to re-uptake. Rab11 labeling suffered a poor transfection efficiency compared to other DNA constructs. This restricted the sample size, therefore it would be beneficial to test alternative methods for labeling the recycling compartment and the results of studies involving this DNA construct should be interpreted with caution.

Colocalization of SPIONs with Rab7 positive compartments increases notably between 1

and 6 hours (144 mins). This represents the accumulation of SPIONs within the more acidic Rab7 late endosome compartments, which is a prerequisite for the degradation of SPIONs. This is in accordance with other studies that have suggested this pathway for SPION metabolism [163]. This colocalization remains high for the duration of the experiment, with only a slight drop occurring at 24 and 48 hours. Rab7 also marks lysosomal compartments. It is likely that during this time period Rab7 compartments fuse with lysosomal compartments and therefore may be coupled to the beginning of SPION degradation in the acidic lysosomal environment, which has been reported to occur as early as 24 hours post incubation [399]. Another study determined an increase in colocalization between various different SPIONs and late endosomes and lysosome markers at 6 and 24 hrs [158]. The data in Figure 6.5 appear to suggest that SPIONs are trafficked to the lysosome through the endosomal system, utilizing Rab5 and Rab7 positive compartments, with a small fraction being released extracellularly through Rab11 mediated recycling. However, both DNA transfections and colocalization studies are notoriously difficult to quantify and interpret. One problem is the potential effect that DNA transfection has on the cellular endocytosis and trafficking pathways. A decrease in SPION internalization seemed to occur following DNA transfection. This complicates analysis, especially at early time points (<60 minutes) - where patterns of colocalization between markers are less clear, as evidenced by the graphs in Figure 6.5. It would be beneficial to conduct these experiments using immunofluorescent staining, rather than DNA transfection, to try and reduce this apparent inhibitory effect on SPION uptake. Alternatively, the computational methodologies tested and described here could be further optimized and tested. For example, the Sienna$^+$ SPIONs were particularly difficult to detect successfully, when compared to reflectance NP such as the cerium dioxide or other types of SPIONs with a larger core size (Appendix Figure B.2)

6.2.4.2 Lysosomal Colocalization

Studies performed in macrophages, *in vitro* and *ex vivo*, indicate that the main fate of SPIONs within these cell types is degradation within the lysosome [163, 169]. In those studies colocalization was determined using fluorescence, TEM and EDX [163, 169]. In this experimental section, the colocalization of SPIONs with the lysosome compartment was investigated using label-free RCM and FCM. The lysosome compartment was visualized using Lysotracker Red DND-99. Little colocalization was observed at the earliest time points, however colocalization increased notably at 6 hrs, similar to the increase in colocalization observed between SPIONs and Rab7 (Figure 6.6). This is not surprising as lysotracker can also mark late endosomes, due to its pH sensitivity. Likewise, Rab7 has been determined necessary for fusion (in conjunction with other proteins such as SNARES) of late endocytotic structures and the lysosome [400, 401]. Rab7 can therefore also act as a marker for lysosomal compartments [400, 401].

Lysosomal accumulation of SPIONs reaches a maximum of 81%, but the curve appears to plateau. This could be indicative of lysosomal saturation, a phenomenon which would be interesting to investigate further by the concurrent exposure of cells to SPIONs for longer periods of time. This could identify if the lysosomes continue to accumulate more SPIONs, or if they reach a plateau or equilibrium. Similar studies were also performed with MDA, A549 and THP-1 cells at the 24 hr time point. Although the only compartment labeled was the lysosome in this case, each indicated a high degree of colocalization. These colocalization studies indicate that the lysosome is the predominant destination for SPIONs once internalized within these cells. This was confirmed in MDA, A549 and THP-1 cells with a 24 hour time point following SPION treatment (Appendix Figure B.13). This is in agreement with previous *ex vivo* studies that have indicated SPION accumulation in lysosomes following injection, identified by TEM and EDX. Interestingly, 7 days post injection, some NPs were still visible, but so are electron dense patterns that resemble endogenous iron storage proteins, characteristic of iron overload [169].

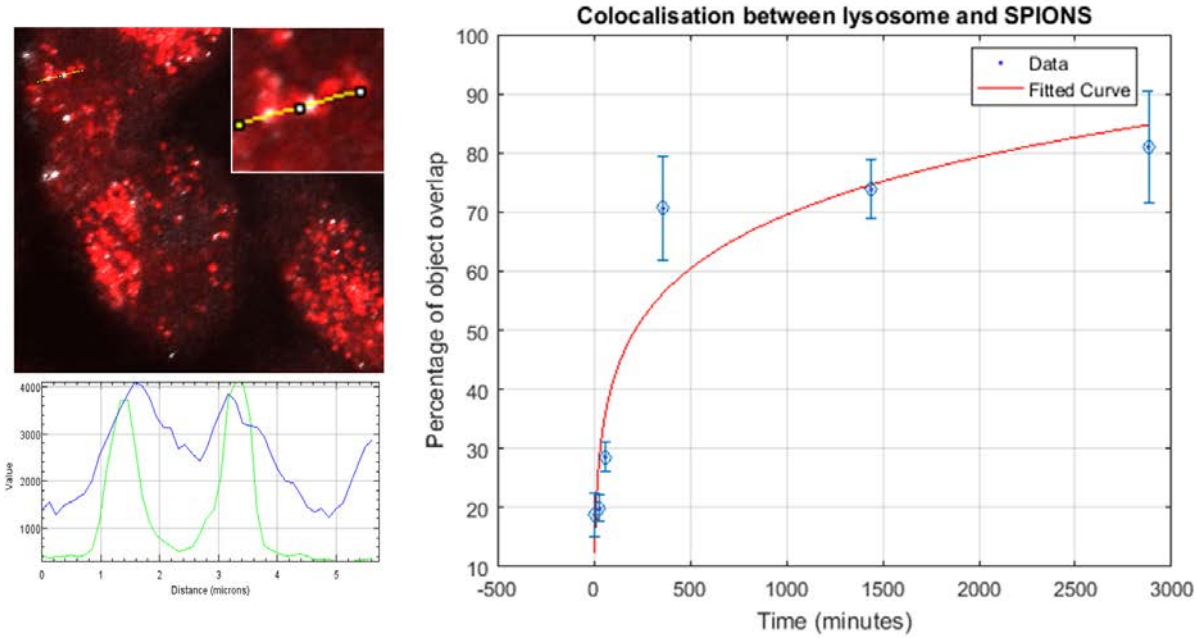

Figure 6.6: Colocalization seen between the lysosomes and SPIONs over time. A high degree of colocalization can be visualized at longer incubation time points (24 hours and 48 hours especially). This can be seen from the overlay (top left; SPIONs = grey, Lysosome = red) and the line intensity profile (lysosome = blue, SPION = green). These images can be computationally post processed and different parameters assessed (such as the degree of signal overlap) and used to make quantitative conclusions about particle trafficking and fate. Plotted points show the mean result for each time point, error bars show the standard error of the mean (SEM).

One problem with the previously applied quantification methods is the reliance of the quantification on the denoising method used and on the PSF size [396]. If the denoising is too harsh, colocalization will be missed. If denoising is not done to a great enough extent, colocalization will be over estimated. Other methods for the analysis of colocalization exist that do not count % of overlaps but rather work on a distance of detected region centroids based method. However these methods, such as Monte-Carlo based simulations, are computationally expensive and harder to implement. One method, the Ripley K-function, determines the distance between identified centroids that permits statistical quantification of colocalization [396]. Determination of statistical values using Ripleys K-function could offer more conclusive results in subsequent analyses.

6.2.4.3 Superresolution analysis of colocalization of NPs with the lysosome

As discussed, one of the drawbacks of conventional diffraction limited microscopy studies is the resolution limit [250, 255]. This limit is dictated by the finite wavelength of the incident light and is much larger than the size of the NPs used in this study. Although some lysosomes may reach up to, or even greater than, 1 µm in diameter, these too can be substantially smaller than the maximum resolution attainable in a diffraction limited system. Therefore two detected signals that appear to co-localize may actually be up to, theoretically, 200-250 nm apart, and practically even further [247]. R-SIM, shown previously in Chapter 4, offers a substantial (>2-fold) resolution increase compared to confocal microscopy. This can improve the likelihood of observing true colocalization between two detected signals. Figure 6.7 shows the lysosomal colocalization of two types of metallic NPs. Sienna$^+$ SPIONs (Figure 6.7A:F) and cerium dioxide NPs (Figure 6.7 G:L) were both imaged with RCM and R-SIM in conjunction with fluorescent imaging. The resolution increase is clearly demonstrated in (Figure 6.7 G:L). This supports the previous findings that a large proportion of the NPs do indeed colocalize with the lysosome

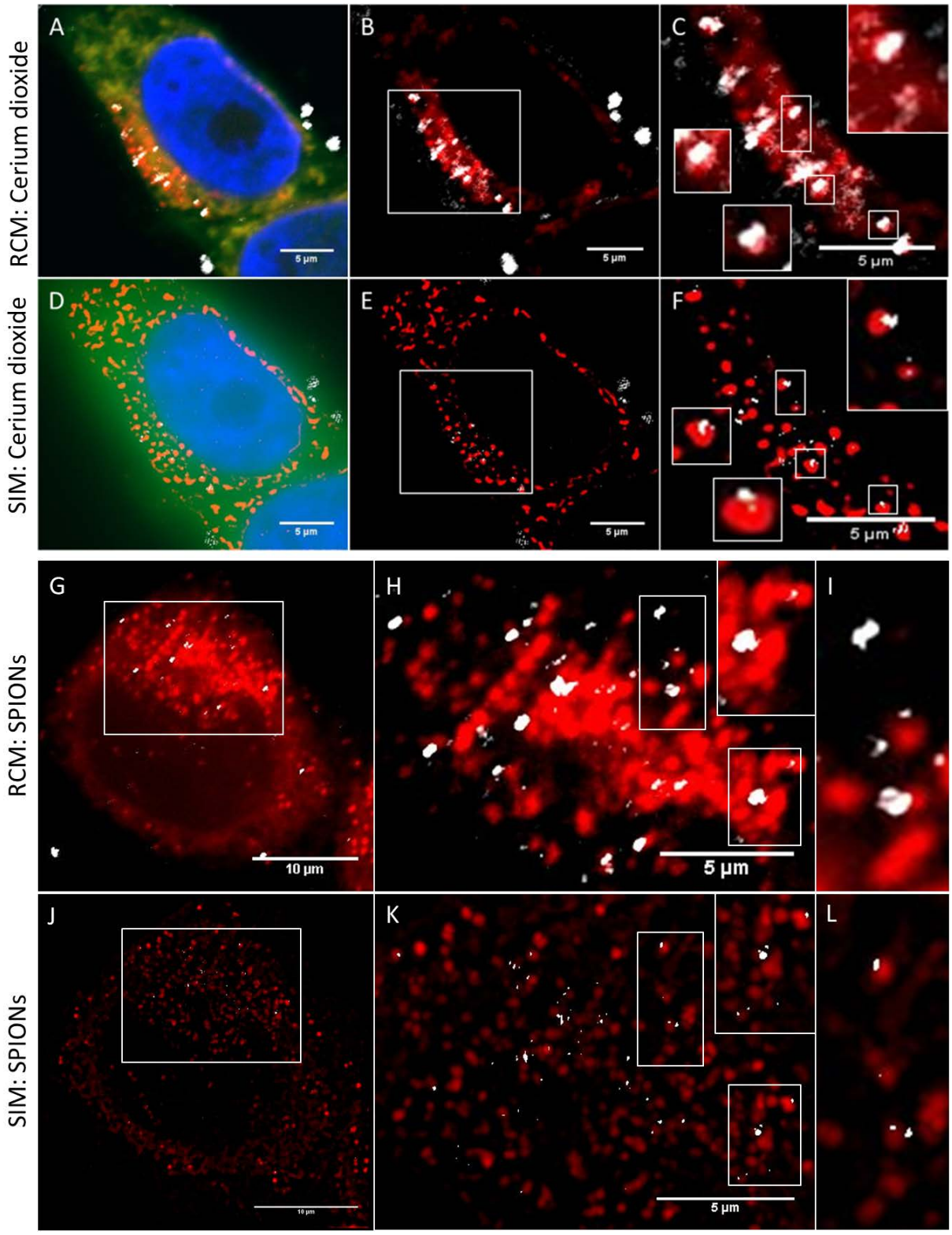

Figure 6.7: R-SIM provides increased resolution for colocalization studies of metallic (cerium dioxide and SPIONS) NPs with lysosomes in HeLa cells after an hour long incubation. Confocal images of cerium dioxide (A:C) and SPIONs (G:I) indicate colocalization with the lysosome. The same cells imaged with R-SIM (D:F and J:L), emphasizes the substantial resolution improvement, and confirms the findings that a large proportion of NPs colocalize to lysosomal compartments.

following cellular internalization and uptake. A thorough investigation using R-SIM to assess and quantify colocalization (with different markers and time points) would therefore be beneficial. This could be combined with analytical quantification, either following isolation or using elemental imaging techniques (i.e. MSI) [182]. Different compartments could be isolated (Rab5 positive, Rab7 positive, lysosome etc.) from treated cells. The presence of SPIONs (NPs and ions) could then be quantified by ICP-MS / ICP-OES or sp-ICP-MS to determine relative proportions of ions / NPs. One study, in the literature, took advantage of the magnetic nature of SPIONs, and their lysosomal localization to magnetically separate and purify the lysosome compartment [191]. Otherwise specific compartments can be isolated by centrifugation or Fluorescence Activated Cell Sorting (FACS) [402, 403].

6.2.5 Dissolution of NPs in different fluids

The dissolution or degradation of NPs is an important property that can alter the availability, toxicity, localization and function of the NPs. Dissolution depends upon the NPs properties and the properties of the surrounding media / solution. Surface properties can greatly influence the dissolution of NPs [391, 404]. Dextran functionalization is one of the most favored routes for the stabilization of SPIONs, however it is suggested that the dextran coat is not firmly attached at the SPIONs surface. Dextran coated SPIONs may not remain stable for long periods of time following lysosomal accumulation. The iron core and it's coatings are thought to be degraded by the acidic environment leading to the release of free iron into the cytoplasm [163, 174, 164, 168]. Test tube dissolution studies can be performed to measure the changes in SPIONs over time. Test tube dissolutions were performed in distilled water at pH 4 and pH 7, to ascertain if the SPIONs would dissolve over time or if they are stable in dH_2O, regardless of pH. The DLS, pH and Zeta potential were taken at 24 hour intervals following initial incubation of the SPIONs (Figure 6.8).

Some changes were observed in the SPION preparations (7000 ppm or 7 µg/mL) over the

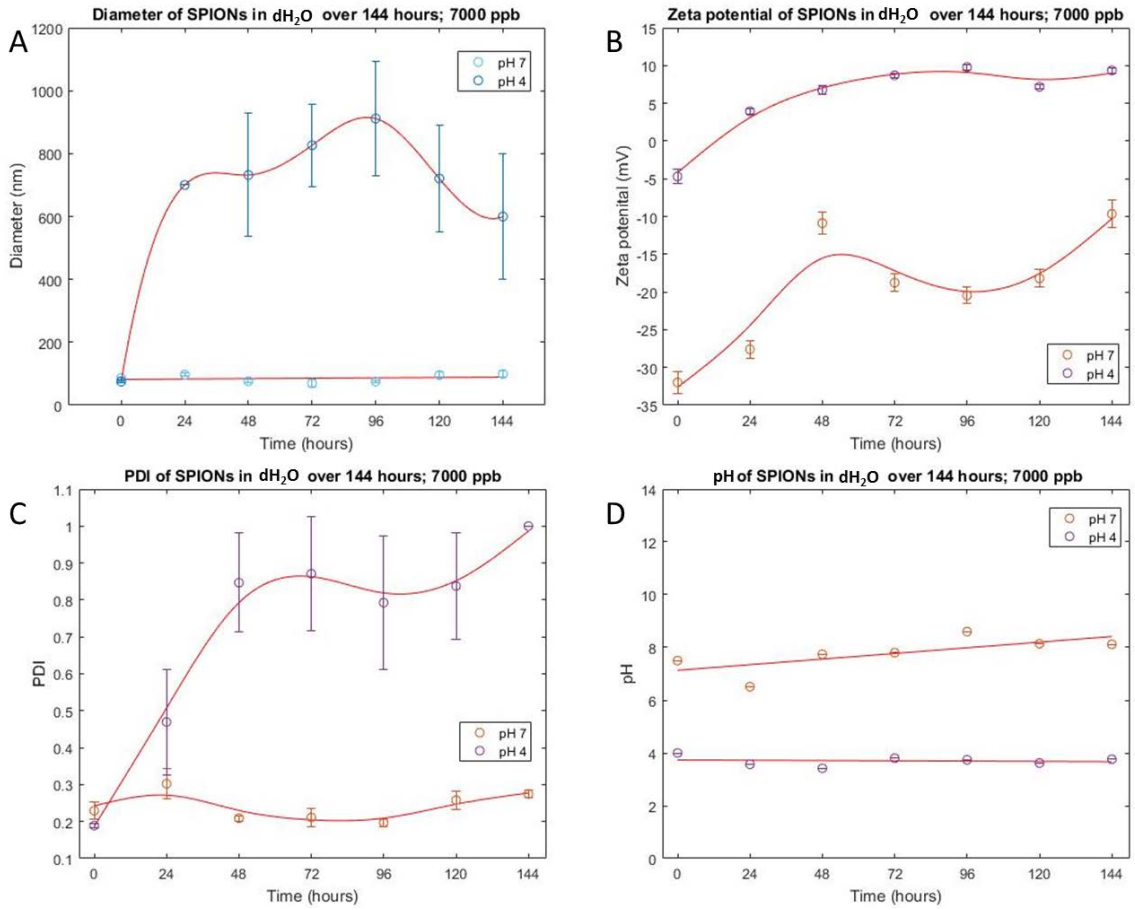

Figure 6.8: Test tube SPION dissolution study in dH_2O at pH 4 and 7. At pH 4, the diameter (nm) increased over the 144 hour time course, whereas at pH 7 the diameter remained consistent (A). Changes were observed in the Zeta potential (B), at pH 7 and pH 4 the zeta potentials become more positive over time. The PDI increased up to 1 at pH4 indicating an increase in the polydispersity (C). pH remained stable through the time course.

period of 144 hours when incubated at 37°C in dH_2O. The DLS peak intensity (of the largest peak) increased considerably at pH 4. The diameter of this peak was measured to be 75 nm +/- 4 nm at T=0, approaching a maximum at T=96 h of 911 nm +/- 181.5nm (M = 652 nm +/- 272 nm over the entire time course). However at pH 7 little change in the measured hydrodynamic diameter of the NP solution was observed over the time course (M = 85 nm +/- 11 nm over the entire time course) (Figure 6.8). The zeta potential is greatly influenced by the measured diameter, at pH 4 the zeta potential fluctuated between -4.7 mV +/- 0.95 mV and 9.8 mV +/- 0.4 (M = 5.9 mV +/- 5 mV over the time course). At pH 7 this fluctuation was even larger, ranging from -32 mV +/- 0.15 mV, to - 9 mV +/- 0.1.7 mV (M = -19.7 mV +/- 8.1 mV over the entire time course). The pH appeared to remain fairly stable in both experiments. At pH 7 the average pH was 7.77 +/- 0.7, and at pH 4 the average was 3.7 +/- 0.2 over the time course. Although there are changes in diameter recorded at pH 4, it is likely that the NPs in the solution are agglomerating, not dissolving. This indicates that pH alone is not sufficient to induce the dissolution of the SPIONs, in agreement with previous studies [168]. The parallel increase in polydispersity at pH 4 also suggests that the SPIONs are agglomerating (Figure 6.8). The carboxydextran coating is linked to the NP surface via multiple hydrogen bonds. At low pH, the carboxyl groups will become protonated [405]. The oxygen will become electro-negatively charged, and the hydrogen electro-positively charged due to the electron withdrawing effect of oxygen. Therefore electrostatic interactions between neighboring molecules could lead to agglomeration of NPs in this condition, which would explain the observed increase in diameter of the NPs within the solution (Figure 6.8).

Dissolution was also performed in the ALF using a pre-determined composition containing citrate, (Full composition - Appendix Section B.1) [390]. Arbab had previously postulated that after 96 hours SPIONs would have dissolved within lysosomal fluid [168]. Therefore, SPIONs (70 ppb) were incubated in ALF for 96 hours. It is worth noting that this concentration is significantly lower than that used in the experiments previously shown.

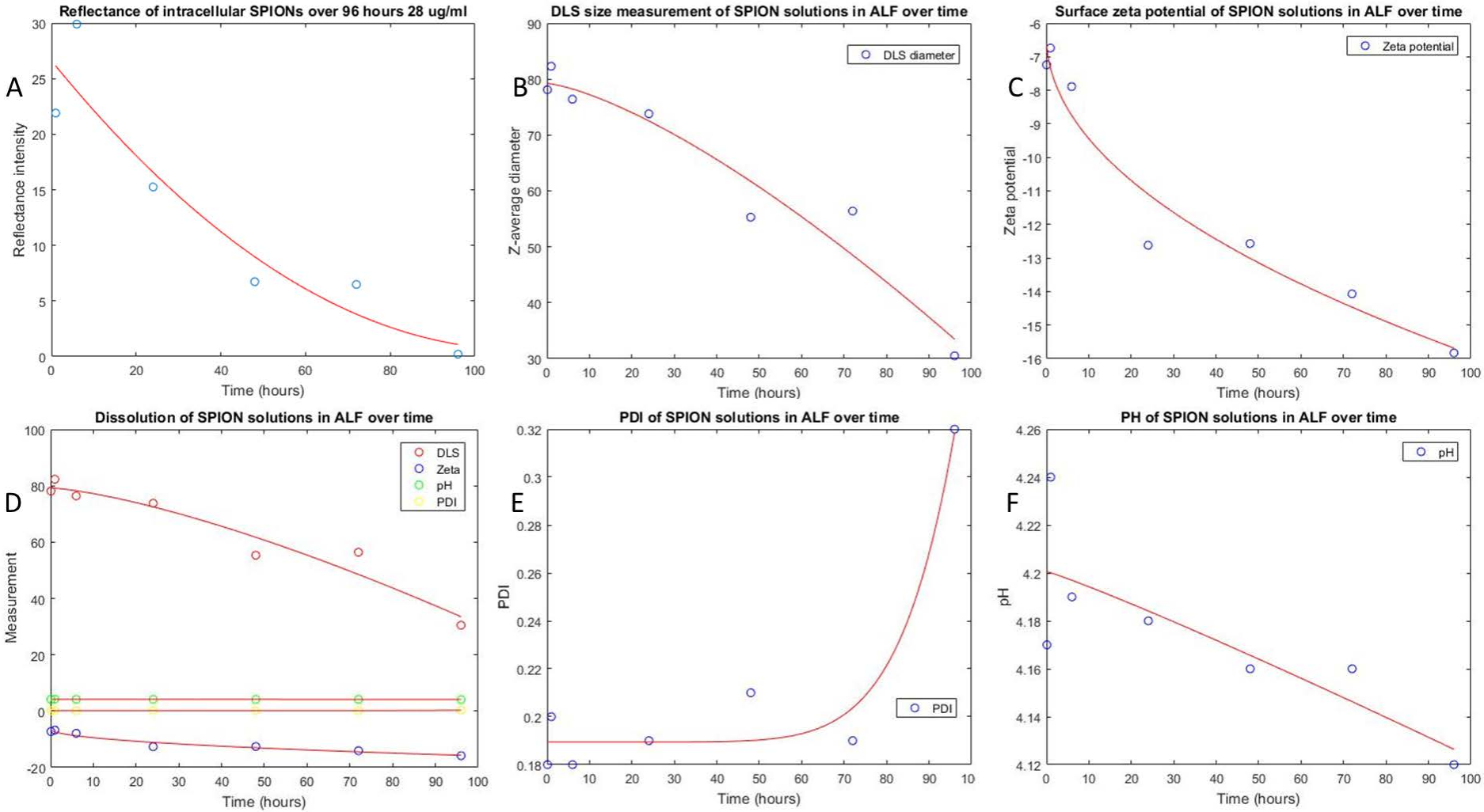

Figure 6.9: Dissolution of SPIONs in citrate containing ALF over 96 hour time course. A) A decrease in reflectance intensity is seen over time with RCM (N=1). A decrease in the diameter (nm) (B) and zeta potential (C) is also observed, and this is paralleled by an increase in the PDI (E) of the solution. Little change is observed in the pH of the solution.

This was largely due to the volume needed to reproduce the same concentration during the experimental time courses. To reproduce 280 µg/mL concentration used in previous cell studies, a volume of 1.8 mL NP stock solution would be necessary. Unfortunately, due to the availability of the SPION stock solution (clinical SPIONs directly purchased from endomagnetics) only a maximum of 20 mL available in total. Additionally, dissolution studies are often performed in the range of 5 ppb - 1000 ppb, for this reason a value in the upper half of this range was tested.The properties of the SPION solution at this concentration was determined; including diameter of the NPs, and Zeta potential, the PDI using the aforementioned techniques from Chapter 3. From Table 6.1, it can be seen that regardless of the difference in concentration, the parameters appear fairly consistent with those previously established in SCM and PBS from Chapter 3.

Solution	DLS	Zeta	PDI	pH
PBS	58.8 +/-3.9	-11+/-4.4	0.204 +/- 0.04	7.4 +/- 0.04
DMEM-SCM	65.05 +/- 5.0	-8+/-0.77	0.222 +/- 0.004	8.4 +/- 0.035
RPMI-SCM	65.7 +/- 3.6	-8+/-0.59	0.236 +/- 0.03	8.3 +/- 0.12
ALF	80.2 +/- 4.2	-11+/-4.7	0.263 +/- 0.03	4.1 +/- 0.015

Table 6.1: Summary of characterization of Sienna $^{+}$ SPION suspensions at T=0 in PBS and SCM and ALF. Summary of characterization of Sienna $^{+}$ SPIONs in different types of media. All suspensions are concentration of 280 ppb or 280 µg / mL at T = 0) except the ALF which contained 7000 ppb or 7 mg / mL.

The DLS, pH, Zeta potential and PDI were taken at 24 hour intervals following initial incubation (Figure 6.9). Decreases in the observed diameter were observed from T=0 (78.1 +/- 3.3 nm) to T=96 (30.5 +/- 4.4 nm) indicating dissolution of the NPs in solution (Figure 6.9). There was an observed increase in PDI from T=0 (0.18 +/- 0.0036) to T=96 (0.32 +/- 0.1) which indicates an increase in size distribution range (Figure 6.9). The zeta potential becomes more negative, from T=0 (-7.24 mV +/- 0.39 mV) to T=96 (-15.83 mV +/- 0.32 mV) indicating an increase in negative charge at the slipping plane of the NPs. This could indicate a reduction in steric stabilization of the solution that may coincide with breakdown of the surface carboxydextran coating. Within cells, the

dextran coating is thought to be degraded by the enzyme α-glucosidase [163]. However this enzyme is not present in the ALF, therefore Dextran could be broken down by acid hydrolysis [406].

Cells were also grown in MatTek dishes, and treated with SPIONs for 1 hour. Dishes were then fixed every 24 hours post incubation. Reflectance intensity was measured; this process involved automatic background subtraction to remove cell signal, and manual delineation. Manual delineation is necessary due to the high confluence of cells at later time points, complicating segmentation. A decrease in reflectance intensity was observed during the 96 hours (Figure 6.9). However, SPIONs and other NPs have been found to distribute to daughter cells during mitosis, which may be the reason for the visual decrease in reflectance intensity [138]. In a future experiment, cells could be incubated with a mitotic inhibitor, such as Vincristine, to negate this effect. Reflectance signal would then change dependant upon SPION accumulation and dissolution over time. It would be very interesting to try to monitor the loss of fluorescent dextran coating (or labeled corona), alongside a loss of reflectance intensity within lysosomal compartments. Such a study would have been investigated further had there been no time constraints for this work.

Taken together, the initial studies to assess dissolution indicate that SPIONs may be dissolving in the ALF solution which contains sodium citrate. It has been hypothesized that the combination of low pH and metallic chelate presence in the solution increases the dissolution of various NPs [168, 164]. Arbab *et al* saw evidence for the dissolution of PLL-SPIONs over 96 hours in these exposure conditions [168]. They also observed some undissolved SPIONs within membrane bound organelles in TEM images of treated cells. The methods of measuring the dissolution used up to this point in our studies are not definitive or quantitative. Therefore, dissolution studies were performed in conjunction with an additional step to quantify ion presence. This involved the centrifugal ultra-

filtration of the incubated solution at each time point to separate ions from intact NPs. The solutions containing ions was then subsequently digested with HNO_3 for elemental analysis. Different concentrations of SPION suspensions in ALF were monitored over the time course of 144 hours (or 7 days) from time 0, to Time = 144. The physicochemical properties were measured using the Zetasizer ZS Nano (DLS, zeta potential and PDI), and pH was measured. On each day, starting 24 hours post initial measurement, samples were prepared as described for elemental ICP-OES analysis. ICP-OES analysis provides quantification of the amount of Fe ions present in the sample. It is a powerful analytical technique that provides detection limits as low as 1 ppb. However, higher concentrations (7000 ppb and 700 ppb) were included to ensure dissolution of the SPIONs could be detected. A standard curve was generated using different concentrations of iron standards using the Fe 259.939 wavelength. This wavelength was selected as it resulted in the highest peak intensity (Figure 6.10).

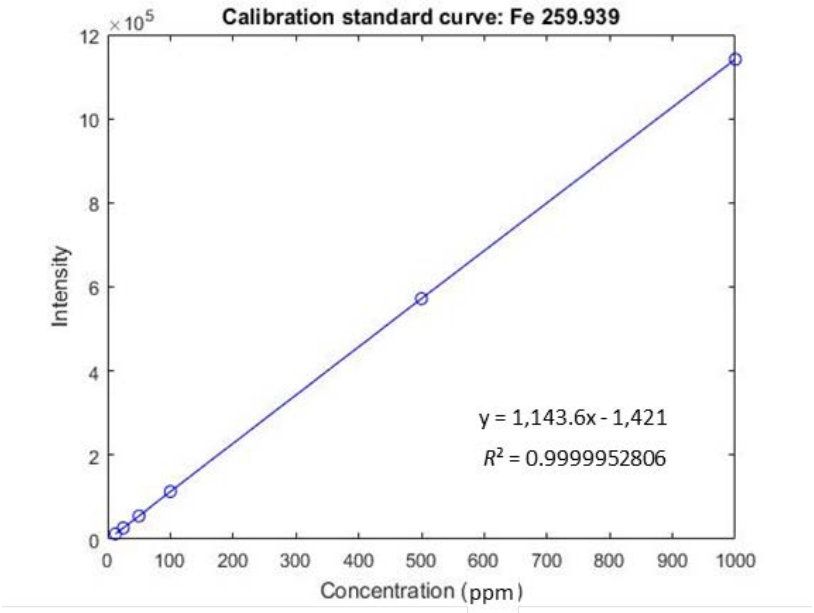

Figure 6.10: Calibration curve generated from ICP-OES analysis of iron standard solutions. The calibration curve is constructed from the analyses of 12.5, 25, 50, 100, 500, 1000 ppb solutions. The R^2 error is calculated to be 0.99 and the equation of the line is given.

Analyses were performed in triplicate, and the value given from the instrument represented an average of these repeats. The RSD% value was below 5% in all of the presented

results, which is acceptable for ICP-OES studies. One sample, C=70 ppb, T=24 hours, did not have a sufficiently acceptable RSD% value, (20.2%) and therefore was excluded. The Limit of Detection (LOD) was calculated using the standard addition method, and gave a value of 1.24 ppb. The Limit of Quantification (LOQ) was calculated based on the assumptions that the LOD is 3 times the SNR and the LOQ is 10 times the SNR, this gave a value of 4 ppb.

A time dependant increase in the amount of Fe ions present in the solutions was observed at each concentration of SPIONs incubated in the same ALF solution (Figure 6.11) [390, 277]. However full dissolution did not appear to occur as the curve did not plateau as would be expected at full dissolution. At 7000 ppb the curve started to plateau; therefore a longer time course may be necessary to determine the equilibrium. Interestingly in the study with 70 ppb starting concentration of SPIONs, the concentration of Fe ions measured at T=140 was higher than the starting concentration. This indicates that there may be some sort of spectral interference. Results obtained were normalized using the blank solution, due to the unusual matrix in which the ions were measured (the ALF solution) [390, 277]. However this solution contains numerous compounds, of which some spectral overlap may be occurring. The presence of calcium, citric acid and nitric acid could lead to spectral interference with the iron peak. It would be advantageous to determine this source of interference, and to extend the experimental time course. However, there is a clear increase in the presence of Fe ions over the time course in each study, regardless of starting concentration. This supports the conclusion that SPIONs are indeed dissolving in the low pH ALF solution. Subsequent isolation of lysosomal compartments from SPION treated cells over the same time courses (or longer) could be combined with elemental ICP-OES (or -MS) analysis and quantification. Isolation can be done easily with existing kits or centrifugation methods, or, due to the magnetic nature of the SPIONs, they could be isolated using magnetic separation [402, 403]. However, quantifications from different organelles could be complicated by the release of Fe from

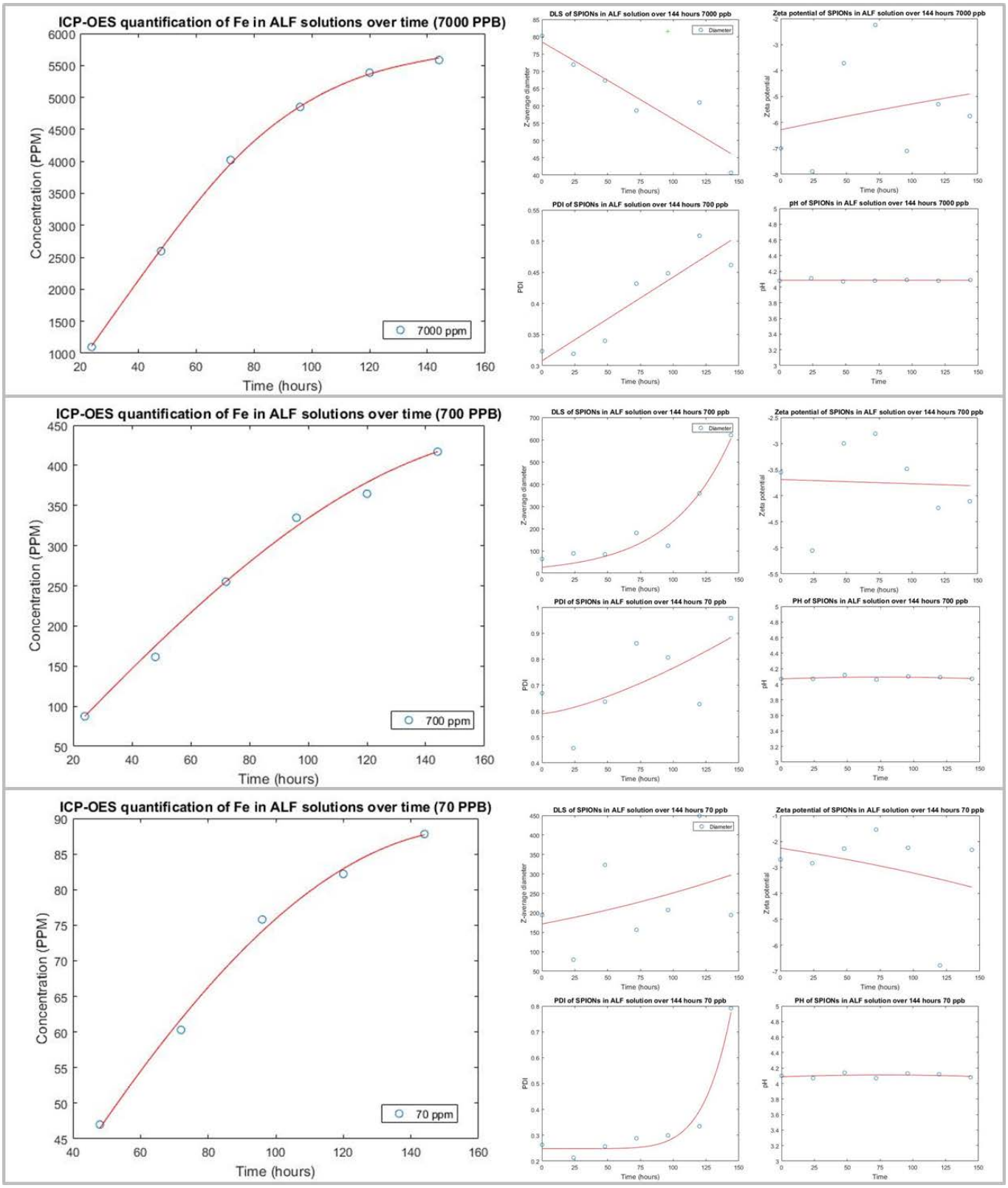

Figure 6.11: SPION dissolution studies performed in ALF at concentrations of 70 ppb, 700 ppb and 7000 ppb. ICP-OES analysis of the experimental time course (left). Increase in free iron is observed at all concentrations. The physicochemical properties for each time points are displayed (right). The results of DLS and zeta potential display no clear pattern between concentrations, indicating the complex nature of measuring NP dissolution. PDIs display an increase in each case, indicating changes in the polydispersity of the suspensions. The pH remains the same throughout.

the lysosomes into the cytoplasm, postulated to occur via divalent cation transport [168]. If organelles could be separated, and the rest of the cytoplasm retained, it may provide a value for the relative amounts of SPIONs and iron released in different areas of the cell. This could particularly benefit from techniques that discriminate between endogenous and exogenous iron.

Measurements of the DLS diameter and PDI, and the pH and Zeta potential were performed at each time point used for ICP-OES analysis (Figure 6.11). The corresponding graphs for DLS, PDI, Zeta and pH are displayed to the right of the ICP-OES curve (Figure 6.11). The results were very varied in terms of the observed effects, and did not display similar results to those in the first ALF experiment (70 ppb) in Figure 6.9. In all cases the PDI tends to increase, which would be expected as the SPIONs begin to dissolve, and the size distribution increases. The DLS diameter decreases in some cases (7000 ppb) and increases in others (700 ppb). In the case of 70 ppb it appears to be quite random. It is possible that the presence of different sized NPs leads to obscuring of the signal from smaller NPs. It is also possible that the dissolution of ions can lead to an increase in agglomeration of the exposed metal cores. The dissolution of SPIONs in these complex media likely results in a mixture containing various forms of partially dissolved SPIONs, ions and free dextran polymer, which can complicate results and invariably lead to different cellular effects [391]. The DLS data also influences the zeta potential measurement, as this is a measure of charge distributed across the SPION's surface. These studies indicate the complexity of dissolution studies, and the interplay between changes in physicochemical properties, whereby change in one property can alter others. More repeats of these experiments at longer time points will give a better indication on the dissolution process within the lysosome. An important consideration is the toxic effects of the intermediates formed during this dissolution process; not only the resultant free Fe that is released. It is likely that there is a complex interplay between the dissolution products and biological responses. Dissolution of the SPIONs in the exposure media, and

media that represents other fluids (such as within the lung and within the gastro environment) should also be investigated, to determine if dissolution occurs prior to cellular uptake, and could therefore also modulate unwanted effects.

6.3 Conclusion

The cellular, and indeed multicellular, toxicity associated with SPION exposure is likely linked directly to the concentration of the SPIONs internalized within the specific cell, the localization (and therefore potential interactions), and the form of the NPs [350]. This will in turn depend upon the processing of the NPs within the cell, the transport route it takes, the duration that the SPIONs are intact within the cell and the degradation timescale. Many drug delivery strategies require NPs to reach, or remain at, particular sites within the cell, and therefore understanding of the trafficking and biotransformation of NPs is important in ensuring success and safety. Sienna$^+$ SPIONs appear to follow a classical pathway that results in the lysosomal accumulation and subsequent degradation into free iron. This could be advantageous for some strategies, such as those that employ a pH modulated cleavage of drug bound cargo within the endo-lysosomal system [140]. Dissolution studies indicate that these SPIONs dissolve within citrate containing, low pH solutions. Physicochemical measurements indicated that a complex interplay exists between the different physical properties of these NP suspensions during the dissolution time course, which requires further investigation. Full dissolution was not observed, and spectral interference perhaps played a role in the resultant iron concentrations recorded by ICP-OES. Further method optimization is therefore required to determine the time scale for full dissolution in addition to determining the contribution of spectral overlap. Future studies including the isolation of intracellular organelles and endosomes, and subsequent quantification of iron would be interesting to confirm the localization of the NPs and any released iron within these compartments. This could be combined with analyses that can distinguish between exogenous and endogenous iron to give accurate conclusions [169].

6.4 Key findings

1. Sienna$^+$ SPIONs appear to traffic through the endo-lysosomal system, resulting in accumulation in the acidic lysosome compartment as earlier as 6 hrs. A portion appear to recycle to the cell surface.

2. Lysosomal accumulation is evident in MDA, HeLa, A549 and THP-1 cells.

3. Image processing can aid in determining the extent of SPION colocalization with various compartments and elemental quantification would provide absolute values for SPION presence.

4. SPIONs dissolve to free iron at low pH (4), in the presence of ALF. Citrate is suggested to be an important component in the dissolution of SPIONs and other NPs.

5. Dissolution leads to various changes in the physicochemical properties of SPIONs which requires further optimization and investigation.

CHAPTER 7

CONCLUSIONS AND FUTURE WORK

7.1 General conclusions

The field of NP research has exploded in recent years, due to the significant increase in incorporation of these materials into various aspects of every day life. Metal oxide NPs, such as SPIONs and cerium dioxide, have wide scale applications from investigative research and the inexpensive *in vivo* detection and screening of diseases such as cancer, to use in vehicle fuel efficiency (e.g. cerium dioxide NPs) [24, 407, 225]. Therefore the characterization of these NP and their interactions / effects, both during unwanted and intentional (medical) exposure, within organisms and the environment is a high priority. Understanding the cellular uptake and potential for toxicity of NPs is critical to ensure successful, effective and safe applications within these different fields.

NP can encompass a huge range of different preparation types, each with different properties that can lead to a variety of different effects within cellular systems and exposed organisms. Therefore it is necessary to thoroughly characterize these properties using standardized / harmonized methodologies, both in the synthesized form, and within potential biological exposure fluids [116, 123, 316]. Chapter 3 included characterizations of the relevant NP (Sienna$^+$ SPIONs, and in some cases cerium dioxide) under exposure conditions to determine properties such as surface charge, hydrodynamic size and disper-

sity. Preliminary investigation into the protein corona constituents was also performed following separation using a modified protocol involving the isolation stages suggested by Docter *et al*, with the exception of the use of a sucrose cushion as this was found to increase the isolation of proteins that were not associated with NP (i.e. in control samples) [288]. Future work within this section would include repetition of studies using different concentrations of FCS, and the inclusion of different types of serum, such as human serum to identify differences that occur due to different protein compositions and concentrations in media relevant to human exposure within biomedical applications. This would include post-cellular internalization corona studies, to determine constituents of the dynamic corona that evolves over time. Corona fingerprinting aims to identify the protein corona constituents, and combine this with other NP property information to produce models that can predict the cellular targeting, uptake, localization and effects of NP. Future intricate models that have multiple likelihood estimations including 1) fluid exposure constituents 2) NP properties 3) corona formation 4) Likelihood of cellular effects based on corona composition and physical properties, could aid *in silico* determination of the biological effects and outcomes of NP therapies. These could be used in a screening process to establish the likelihood of success or failure of drug candidates and therefore, if established, would be an indispensable tool within nanomedicine. However, such models would likely require extensive analysis of varieties of properties, and be specific to different core materials, in addition to requiring computational expertise to enable the modeling of various processes that may occur.

One primary aim within this thesis was to develop and optimize new tools for the visualization of these example NPs without the need of labeling due to the aforementioned problems with current methods such as fluorescent tagging. Reflectance imaging protocols were optimized and developed to illustrate the benefits these methodologies offer within the field of nanoresearch. Benefits include the relatively quick, inexpensive, label-free visualization of NP, resulting in high quality images that can be subsequently analysed

computationally as demonstrated in Chapters 4 and 5. In Chapter 4 metal oxide NPs, both cerium dioxide and SPIONs, were shown to introduce significant contrast into reflected light images; other NP that are not such good reflectors were also visualized (polystyrene core). The use of multiple NP with both R-SIM and RCM imaging methodologies provided validation for each instrument in the study of NPs comprised of different materials. Refinement of the imaging protocols, and the development of R-SIM as a complimentary (or stand alone) tool for investigating single samples will facilitate label free imaging of a wider range of NPs, improving throughput, technical capabilities and reducing time and cost [322]. Although the resolution of R-SIM does not approach that of TEM, the combination of reflectance image acquisition and subsequent correlation to ultrahigh resolution TEM imaging can increase the confidence in experimental conclusions and maximizes the information gained from a single prepared sample, as demonstrated here. Subsequent optimization of this correlative procedure would increase the range of NP that can be imaged under label-free conditions, and harmonization of sample preparation procedures could greatly simplify acquisitions (e.g. sample preparation routine to allow all imaging to be performed on TEM slotted grids).

The applications shown within this thesis highlight the value of these optimized reflectance methodologies to probe the important cellular interactions that occur during NP exposure within biological samples *in vitro* as presented in Chapters 5 and 6. The time and concentration dependence of uptake was established in multiple cancer cell types, benchmarked against the widely studied macrophage model. Important proteins were identified that may be instrumental in facilitating the internalization of these NP, particularly Cav1 and Pak1 in cancer cell lines. Calculations were performed to determine whether this was a result of internalization through fluid within the endosome (non-specific) or through membrane interactions. The expansion of these 2D cell culture studies into model systems that better represent multicellular organization is crucial to reduce unnecessary animal experiments. Reflectance imaging of 3D multicellular spheroids was performed, validating the

method for 3D exposure studies with these techniques. Continuation of these investigations may ultimately lead to more accurate conclusions regarding the behavior of NP within tissues, with the goal of ultimately improving the likelihood of success in subsequent translation to clinical trials and benefits. For example, despite increasing research into NP based therapies, few of these realize their full potential within a clinical setting [408, 409, 410]. In this way, reflectance microscopy may be influential in reducing the number of experiments that are continued into *in vivo* studies that have a limited chance of success in future clinical trials. These 3D spheroid models could act as a screening process for suitable NP treatments, to find those that can translocate through spheroids and localize to the desired organelle to highlight candidates for continuation into animal studies and eventual clinical trials. Refinement of the experimental procedures utilized in 2D cell cultures, such as siRNA inhibition or localization studies, to allow the application in 3D culture models could prove indispensable in this process. Imaging of tumor spheroids may be possible with R-SIM; this could be determined using correlative studies with the inclusion multiple modalities (such as RCM and TEM). Some of the available methods include slice and view technologies [411, 412]. Slice and view is a technique that allows SEM imaging followed by serial block face sectioning of a resin embedded tissue or cell sample within the microscope itself, allowing the acquisition of large amounts of high resolution 3D data. This would be very informative in terms of determining the localization of NP, and the sensitivity of reflectance imaging within tumor spheroids.

In Chapter 6, a relationship between intracellular NP location and the endo-lysosomal system / lysosomes was also identified using colocalization studies; although the best quantification method for these experiments are still often debated. The use of R-SIM increased confidence in the conclusions that the NP are localizing to within lysosomes following intracellular trafficking. Optimization of the imaging routines for R-SIM could greatly enhance colocalization studies providing more definitive conclusions and facilitating quantification of the amount of NP per lysosome and differentiation of cell populations

that internalize greater or fewer NPs. R-SIM, due to the increased resolution, could also be used to indicate the nature of internalized NP; as agglomerates, or as single NP. Optimization of live R-SIM could be instrumental in following this process over time and determining if NPs agglomerate due to the high internal lysosomal concentration following accumulation, in addition to the potential for monitoring degradation of NP cores and labeled coronas over time at high resolution.

Determination of these cellular interactions in Chapters 5 and 6 was greatly aided by computational processing to provide increased throughput, sample size and therefore number of experiments that can be performed (due to reduced analysis time). This enables relative quantifications between measured groups, however the next step involves the expansion into fully quantitative conclusions, in terms of internal NP concentration. Quantification of NP within cellular systems, and within specific compartments, is vital to determine the associated risk / benefits of NP within a biomedical context. Experiments can be correlated to analytical quantifications using a variety of instruments, such as ICP-OES and ICP-MS. ICP-OES was used in Chapter 6 to determine concentrations of iron in mimic fluids over time to ascertain the dissolution of SPIONs in the acidic lysosomal environment. Organelle isolation could be combined with elemental quantification to complement these examples of degradation and trafficking studies within the cell. Alternatively, the field of elemental imaging (such as MSI) is expanding rapidly, and imaging with light microscopy (and / or TEM) can be combined with studies that provide elemental image 'maps' of cellular or tissue samples. Recent success in the use of LA-ICP-MS on fixed cellular samples to gain quantitative insight into internalized NP highlight the potential to incorporate this type of analyses into the imaging experiments [183, 182]. These are exciting new directions towards NP characterization and detection. Identifying the same cell with label-free imaging, TEM, elemental quantification and the subsequent overlays could facilitate the development of NP-specific algorithms that can determine the absolute cellular accumulation of these NP applied to uptake concentration and NP degradation

over time. This would likely be a complicated task that would include a wide range of parameters that estimate, for e.g., NP that are not detected using microscopy and estimations of background from images. Series of validations using different concentrations and time points (to model changes in reflectance due to degradation i.e. with spICP-MS) could potentially facilitate complex, but accurate, analytical analyses from simple RCM experiments.

Although the discussed applications within this thesis are mainly directed towards nano-safety and nano-medicine, reflectance methods offer value for a broad range of investigations spanning multiple fields both *in vitro* and *in vivo*. RCM has been applied to the imaging of the focal contacts formed by cells attached to a surface, the morphology of red blood cells and the in vivo clinical diagnosis of a variety of pathologies, including skin, oral mucosa and cornea diseases to name a few [413, 414, 240, 415]. RCM offers non destructive methods to visualize live events and has been used to investigate the vesicle transport system in developing drosophila oocyte providing a real-time imaging method for innately reflective cellular constituents [248]. It is also well recognized that reflectance imaging can provide additional information in a variety of diagnostic or clinical experiments. Collection of the backscattered laser light from in vivo investigations has also allowed visualization of haemodynamic events and provides structural information to contextualize fluorescent signal [252, 103]. This emerging combination of two-photon fluorescence and RCM imaging allows the visualization of blood flow and anatomical tissue structure in regions such as the brain cortex [103]. Axonal myelin gives rise to contrast in the reflectance image, providing a means of monitoring axonal demyelination, a critical event in a host of neurodegenerative pathologies [252]. A novel methodology, termed *in vivo* microcartography, also employs this combination method to visualize the architecture and haemodynamics of in vivo tumor angiogenesis [254]. The availability of superresolution reflectance (R-SIM) could provide valuable additional information during many of these investigations involving reflective samples, providing higher resolution and

more precision and detail. Structured illumination has been applied for *in vivo* imaging investigations both in tissue diagnostics (using phantoms) and quality control [416, 417]. However widespread use of R-SIM will be increased with the appropriate modification of the reconstruction algorithm to minimize backgrounds effects in tissue, to allow better, more accurate signal reconstruction. This goal has been made more attainable in the past year due to the emergence of free-source scripts / implementations of the algorithm which were previously limited to commercial, non-modifiable software [331, 418]. Clearly reflectance imaging has a lot to offer across a host of different investigations, not limited to NP studies. Continued development of the imaging processes, particularly R-SIM, will lead to improved detection capabilities and increase the widespread use of this technique as a complimentary standard investigation.

7.2 Summary of thesis

The main aims within this thesis were to improve the methods available for the investigation of NP-cellular interactions, and to apply these in combination with existing methodologies to increase knowledge on NP interactions with cancer cell lines from both a safety and therapeutic benefit perspective. Figure 7.1 indicates the different aspects of work involved in each chapter and the techniques applied within and how these approaches were combined to address key questions regarding SPION uptake, trafficking and fate in different cell types. Chapter 3 focused on important characterizations of SPIONs based upon routinely used techniques including physicochemical characterizations of SPION solutions with the presence and absence of serum proteins (size, PDI, zeta potential), imaging (TEM) and identification of proteins associated with SPIONs. The limitations of existing imaging methodologies in the study of NPs, such as the effects of fluorescent labeling and diffraction limited resolution, and the advantages that visualization of spatial localization can offer in studies, increases the demand for new and optimized imaging routines. In Chapter 4, existing RCM methods were optimized and R-SIM imaging was

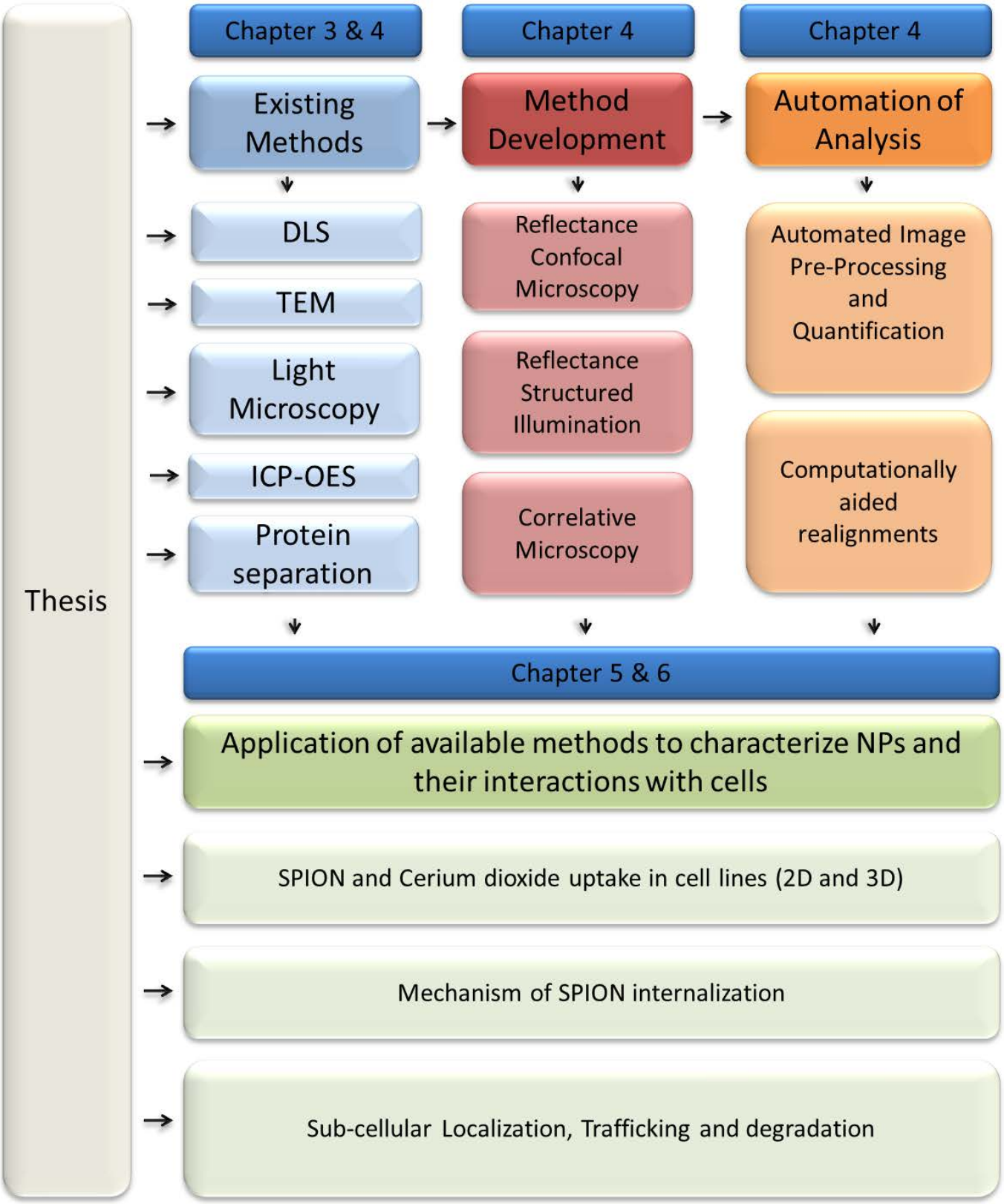

Figure 7.1: Flow chart showing the summary of work within each chapter of this thesis. The summary flow chart shows the main sections of work within this thesis and how they fit together into an integrated study advancing the state-of-the art.

introduced, offering a two fold increase in resolution - particularly advantageous for NP quantification and localization studies. Analysis routines were developed to enable the automated quantification of NP presence within cells via the different methodologies. Correlative procedures were also established for imaging the same sample with different reflectance methods and TEM, maximizing the information attainable from a single sample and allowing comparisons between the techniques for specific applications. Chapters 5 and 6 then made use of these optimized techniques, with a focus primarily on RCM due to its availability and high NP detection rates, utilizing the automated analysis presented in Chapter 3. This was used to determine NP uptake in four different cell lines, and, in combination with siRNA, to ascertain proteins that are involved in the uptake process. Chapter 5 also included preliminary work aimed at the translation of these studies into 3D culture models, and confirmation of the applicability of reflectance for imaging these 3D spheroid cultures was achieved. In the final results chapter, reflectance imaging methods were applied to SPION and cerium trafficking studies, and analysis methods were extended to include fluorescent segmentation and quantitative colocalization measures, determining the eventual fate of SPIONS and cerium dioxide NPs within cancer cells. Chapter 6 also included mock dissolution studies that simulated the lysosomal compartment within cells to model the degradative process of SPIONs within this fluid, utilizing analytical techniques such as ICP-OES. This thesis thus provided several important tools for the future assessment of the efficacy and safety of NPs for clinical use, enabling quantitative analysis of uptake route, subcellular localization and NP intracellular fate.

LIST OF REFERENCES

[1] Steffen Foss Hansen, Evan S Michelson, Anja Kamper, Pernille Borling, Frank Stuer-Lauridsen, and Anders Baun. Categorization framework to aid exposure assessment of nanomaterials in consumer products. *Ecotoxicology (London, England)*, 17(5):438–47, jul 2008.

[2] Johannes Loehr, Daniel Pfeiffer, Dirk Schüler, and Thomas M. Fischer. Magnetic guidance of the magnetotactic bacterium Magnetospirillum gryphiswaldense. *Soft matter*, 12(15):3631–5, 2016.

[3] Richard D Handy, Richard Owen, and Eugenia Valsami-Jones. The ecotoxicology of nanoparticles and nanomaterials: current status, knowledge gaps, challenges, and future needs. *Ecotoxicology (London, England)*, 17(5):315–25, jul 2008.

[4] M N Moore. Do nanoparticles present ecotoxicological risks for the health of the aquatic environment? *Environment International*, 32(8):967–976, 2006.

[5] Philip J Smith, Maude Giroud, Helen L Wiggins, Florence Gower, Jennifer A Thorley, Bjorn Stolpe, Julie Mazzolini, Rosemary J Dyson, and Joshua Z Rappoport. Cellular entry of nanoparticles via serum sensitive clathrin-mediated endocytosis, and plasma membrane permeabilization. *International journal of nanomedicine*, 7:2045–55, jan 2012.

[6] Piao Xu, Guang Ming Zeng, Dan Lian Huang, Chong Ling Feng, Shuang Hu, Mei Hua Zhao, Cui Lai, Zhen Wei, Chao Huang, Geng Xin Xie, and Zhi Feng Liu. Use of iron oxide nanomaterials in wastewater treatment: A review, 2012.

[7] Seung H Ko, Heng Pan, Costas P Grigoropoulos, Christine K Luscombe, Jean M J Fréchet, and Dimos Poulikakos. All-inkjet-printed flexible electronics fabrication on a polymer substrate by low-temperature high-resolution selective laser sintering of metal nanoparticles. *Nanotechnology*, 18(34):345202, aug 2007.

[8] Junfeng Zhang, Yevgen Nazarenko, Lin Zhang, Leonardo Calderon, Ki-Bum Lee, Eric Garfunkel, Stephan Schwander, Teresa D Tetley, Kian Fan Chung, Alexandra E

Porter, Mary Ryan, Howard Kipen, Paul J Lioy, and Gediminas Mainelis. Impacts of a nanosized ceria additive on diesel engine emissions of particulate and gaseous pollutants. *Environmental science & technology*, 47(22):13077–85, nov 2013.

[9] Simon P. Forster, Sandro Olveira, and Stefan Seeger. Nanotechnology in the market: promises and realities. *International Journal of Nanotechnology*, may 2011.

[10] Rod J. Aitken, M. Q. Chaudhry, A. B A Boxall, and M. Hull. Manufacture and use of nanomaterials: Current status in the UK and global trends. *Occupational Medicine*, 56(5):300–306, aug 2006.

[11] Anthony Seaton, Lang Tran, Robert Aitken, and Kenneth Donaldson. Nanoparticles, human health hazard and regulation. *Journal of the Royal Society, Interface / the Royal Society*, 7 Suppl 1(3):S119–29, feb 2010.

[12] Rodger. Duffin, Lang. Tran, A. Clouter, D. M. Brown, W. MacNee, V. Stone, and K. Donaldson. The Importance of Surface Area and Specific Reactivity in the Acute Pulmonary Inflammatory Response to Particles. *Annals of Occupational Hygiene*, 46(i):242–245, jan 2002.

[13] Rodger Duffin, Lang Tran, David Brown, Vicki Stone, and Ken Donaldson. Proinflammogenic effects of low-toxicity and metal nanoparticles in vivo and in vitro: highlighting the role of particle surface area and surface reactivity. *Inhalation toxicology*, 19(10):849–856, jan 2007.

[14] Mark R Miller. The role of oxidative stress in the cardiovascular actions of particulate air pollution. *Biochemical Society transactions*, 42(4):1006–11, aug 2014.

[15] Amy H. Auchincloss, Ana V. Diez Roux, J. Timothy Dvonch, Patrick L. Brown, R. Graham Barr, Martha L. Daviglus, David C. Goff, Joel D. Kaufman, and Marie S. O'Neill. Associations between recent exposure to ambient fine particulate matter and blood pressure in the multi-ethnic study of atherosclerosis (MESA). *Environmental Health Perspectives*, 116(4):486–491, 2008.

[16] Matthew C Stensberg, Rajtarun Madangopal, Gowri Yale, Qingshan Wei, Hugo Ochoa-Acuña, Alexander Wei, Eric S McLamore, Jenna Rickus, D Marshall Porterfield, and Maria S Sepúlveda. Silver nanoparticle-specific mitotoxicity in Daphnia magna. *Nanotoxicology*, 8(8):833–42, 2014.

[17] Health (HSE) and Sefety Executive. Review of the adequacy of current regulatory regimes to secure effective regulation of nanoparticles created by nanotechnology. page 22, 2006.

[18] REACH. REACH REGULATION (EC) No 1907/2006, 2006.

[19] Roger Strand and Kamilla Lein Kjølberg. Regulating Nanoparticles : The Problem of Uncertainty. *European Journal of Law and Technology*, 2(3):1–10, 2011.

[20] Morteza Mahmoudi, Shilpa Sant, Ben Wang, Sophie Laurent, and Tapas Sen. Superparamagnetic iron oxide nanoparticles (SPIONs): Development , surface modi fi cation and applications in chemotherapy. *Advanced Drug Delivery Reviews*, 63(1-2):24–46, 2011.

[21] Catherine A Schütz, Lucienne Juillerat-Jeanneret, Heinz Mueller, Iseult Lynch, and Michael Riediker. Therapeutic nanoparticles in clinics and under clinical evaluation. *Nanomedicine*, 8(3):449–467, mar 2013.

[22] Nathan Kohler, Conroy Sun, Jassy Wang, and Miqin Zhang. Methotrexate-modified superparamagnetic nanoparticles and their intracellular uptake into human cancer cells. *Langmuir : the ACS journal of surfaces and colloids*, 21(19):8858–64, sep 2005.

[23] Qimeng Quan, Jin Xie, Haokao Gao, Min Yang, Fan Zhang, Gang Liu, Xin Lin, Andrew Wang, Henry S Eden, Seulki Lee, Guixiang Zhang, and Xiaoyuan Chen. HSA coated iron oxide nanoparticles as drug delivery vehicles for cancer therapy. *Molecular pharmaceutics*, 8(5):1669–76, oct 2011.

[24] Santimukul Santra, Charalambos Kaittanis, Jan Grimm, and J Manuel Perez. Drug/dye-loaded, multifunctional iron oxide nanoparticles for combined targeted cancer therapy and dual optical/magnetic resonance imaging. *Small (Weinheim an der Bergstrasse, Germany)*, 5(16):1862–8, aug 2009.

[25] Yasuhiro Matsumura and H Maeda. A new concept for macromolecular therapeutics in cnacer chemotherapy: mechanism of tumoritropic accumulatio of proteins and the antitumor agents Smancs. *Cancer research*, 46(December):6387– 6392, 1986.

[26] Arun K. Iyer, Greish Khaled, Jun Fang, and Hiroshi Maeda. Exploiting the enhanced permeability and retention effect for tumor targeting, 2006.

[27] Mi Kyung Yu, Yong Yeon Jeong, Jinho Park, Sangjin Park, Jin Woong Kim, Jung Jun Min, Kyuwon Kim, and Sangyong Jon. Drug-loaded superparamagnetic iron oxide nanoparticles for combined cancer imaging and therapy in vivo. *Angewandte Chemie - International Edition*, 47(29):5362–5365, jul 2008.

[28] C J Li, Y Miyamoto, Y Kojima, and H Maeda. Augmentation of tumour delivery of macromolecular drugs with reduced bone marrow delivery by elevating blood pressure. *British journal of cancer*, 67(5):975–80, may 1993.

[29] Jessica Wright. Nanotechnology: Deliver on a promise. *Nature*, 509(7502):S58–9, may 2014.

[30] European Medicines Agency. WITHDRAWAL ASSESSMENT REPORT FOR SINEREM. 1, 2008.

[31] Chung Hang J. Choi, Christopher A. Alabi, Paul Webster, and Mark E. Davis. Mechanism of active targeting in solid tumors with transferrin-containing gold nanoparticles. *Proceedings of the National Academy of Sciences of the United States of America*, 107(3):1235–40, jan 2010.

[32] G. D. Byrne, M. C. Pitter, J. Zhang, F. H. Falcone, S. Stolnik, and M. G. Somekh. Total internal reflection microscopy for live imaging of cellular uptake of sub-micron non-fluorescent particles. *Journal of Microscopy*, 231(1):168–179, jul 2008.

[33] Kwangjae Cho, Xu Wang, Shuming Nie, Zhuo Chen, and Dong M Shin. Therapeutic nanoparticles for drug delivery in cancer, 2008.

[34] M. W. Freeman, A. Arrott, and J. H. L. Watson. Magnetism in Medicine. *Journal of Applied Physics*, 31(5):S404, aug 1960.

[35] Dmitri Artemov, Noriko Mori, Rajani Ravi, and Zaver M Bhujwalla. Magnetic resonance molecular imaging of the HER-2/neu receptor. *Cancer research*, 1(15):2723–2727, jun 2003.

[36] Qingxin Mu, Forrest M. Kievit, Rajeev J. Kant, Guanyou Lin, Mike Jeon, and Miqin Zhang. Anti-HER2/neu peptide-conjugated iron oxide nanoparticles for targeted delivery of paclitaxel to breast cancer cells. *Nanoscale*, 7(43):18010–4, 2015.

[37] Huan Li, Kai Yan, Yalei Shang, Lochan Shrestha, Rufang Liao, Fang Liu, Penghui Li, Haibo Xu, Zushun Xu, and Paul K. Chu. Folate-bovine serum albumin functionalized polymeric micelles loaded with superparamagnetic iron oxide nanoparticles

for tumor targeting and magnetic resonance imaging. *Acta Biomaterialia*, 15:117–126, 2015.

[38] Remon Bazak, Mohamad Houri, Samar El Achy, Serag Kamel, and Tamer Refaat. Cancer active targeting by nanoparticles: a comprehensive review of literature. *Journal of Cancer Research and Clinical Oncology*, 141:769–784, 2014.

[39] Andreas Wicki, Dominik Witzigmann, Vimalkumar Balasubramanian, and Jörg Huwyler. Nanomedicine in cancer therapy: Challenges, opportunities, and clinical applications, feb 2015.

[40] Eugene Mahon, Anna Salvati, Francesca Baldelli Bombelli, Iseult Lynch, and Kenneth A Dawson. Designing the nanoparticle-biomolecule interface for "targeting and therapeutic delivery", jul 2012.

[41] Aris Persidis. Cancer multidrug resistance. *Nature biotechnology*, 17(Supp):94–95, oct 1999.

[42] Michael M Gottesman, Tito Fojo, and Susan E Bates. Multidrug resistance in cancer: role of ATP-dependent transporters. *Nature reviews. Cancer*, 2(1):48–58, jan 2002.

[43] Eun Seong Lee, Kun Na, and You Han Bae. Doxorubicin loaded pH-sensitive polymeric micelles for reversal of resistant MCF-7 tumor. *Journal of Controlled Release*, 103(2):405–418, 2005.

[44] Rajesh Singh and James W Lillard. Nanoparticle-based targeted drug delivery, 2009.

[45] Morteza Mahmoudi, Abdolreza Simchi, Mohammad Imani, and Urs O. Hafeli. Superparamagnetic iron oxide nanoparticles with rigid cross-linked polyethylene glycol fumarate coating for application in imaging and drug delivery. *Journal of Physical Chemistry C*, 113(19):8124–8131, may 2009.

[46] Shahed Behzadi, Vahid Serpooshan, Ramin Sakhtianchi, Beate M??ller, Katharina Landfester, Daniel Crespy, and Morteza Mahmoudi. Protein corona change the drug release profile of nanocarriers: The "overlooked" factor at the nanobio interface. *Colloids and Surfaces B: Biointerfaces*, 123:143–149, 2014.

[47] Xiaohu Gao, Yuanyuan Cui, Richard M Levenson, Leland W K Chung, and Shuming Nie. In vivo cancer targeting and imaging with semiconductor quantum dots. *Nature Biotechnology*, 22(8):969–976, aug 2004.

[48] Hui Zhang, Jason E Fritts, and Sally A Goldman. Image segmentation evaluation: A survey of unsupervised methods. *Computer Vision and Image Understanding*, 110(2):260–280, 2008.

[49] J F Hainfeld, D N Slatkin, T M Focella, and H M Smilowitz. Gold nanoparticles: A new X-ray contrast agent. *British Journal of Radiology*, 79(939):248–253, mar 2006.

[50] Carlos Tassa, Stanley Y Shaw, and Ralph Weissleder. Dextran-coated iron oxide nanoparticles: A versatile platform for targeted molecular imaging, molecular diagnostics, and therapy, 2011.

[51] Qi Yang, Stephen W. Jones, Christina L. Parker, William C. Zamboni, James E. Bear, and Samuel K. Lai. Evading immune cell uptake and clearance requires PEG grafting at densities substantially exceeding the minimum for brush conformation. *Molecular Pharmaceutics*, 11(4):1250–1258, apr 2014.

[52] Hamed Arami, Amit Khandhar, Denny Liggitt, and Kannan M Krishnan. In vivo delivery, pharmacokinetics, biodistribution and toxicity of iron oxide nanoparticles. *Chem. Soc. Rev.*, 42(12):4906, 2015.

[53] Lin Yang, Huijuan Kuang, Wanyi Zhang, Zoraida P Aguilar, Yonghua Xiong, Weihua Lai, Hengyi Xu, and Hua Wei. Size dependent biodistribution and toxicokinetics of iron oxide magnetic nanoparticles in mice. *Nanoscale*, 7(2):625–636, 2015.

[54] Juergen Scheidler, Andreas F. Heuck, Werner Meier, and Maximilian F. Reiser. MRI of pelvic masses: Efficacy of the rectal superparamagnetic contrast agent Ferumoxsil. *Journal of Magnetic Resonance Imaging*, 7(6):1027–1032, nov 1997.

[55] Claire Corot, Philippe Robert, Jean Marc Idée, and Marc Port. Recent advances in iron oxide nanocrystal technology for medical imaging, dec 2006.

[56] Ansje S. Fortuin, Roger Bruggemann, Janine van der Linden, Ilia Panfilov, Bas Israel, Tom W J Scheenen, and Jelle O. Barentsz. Ultra-small superparamagnetic iron oxides for metastatic lymph node detection: Back on the block, apr 2017.

[57] Mehran Baghi, Martin G Mack, Jens Wagenblast, Markus Hambek, Jörg Rieger, Sotirios Bisdas, Wolfgang Gstoettner, Knut Engels, Thomas Vogl, and Rainald Knecht. Iron oxide particle-enhanced magnetic resonance imaging for detection of benign lymph nodes in the head and neck: How reliable are the results? *Anticancer Research*, 27(5 B):3571–3575, 2007.

[58] Lucia Santoro, Luigi Grazioli, Antonella Filippone, Emanuele Grassedonio, Giacomo Belli, and Stefano Colagrande. Resovist enhanced MR imaging of the liver: Does quantitative assessment help in focal lesion classification and characterization? *Journal of Magnetic Resonance Imaging*, 30(5):1012–1020, nov 2009.

[59] Wahajuddin and Sumit Arora. Superparamagnetic iron oxide nanoparticles: magnetic nanoplatforms as drug carriers. *International journal of nanomedicine*, 7:3445–71, jan 2012.

[60] Heike E Daldrup-Link, Anna Kaiser, Thomas M Link, Marcus Settles, Thomas Helbich, Martin Werner, Timothy P L Roberts, and Ernst J Rummeny. Comparison between gadopentetate and feruglose (Clariscan???)-enhanced MR-mammography: Preliminary clinical experience. In *Academic Radiology*, volume 9, pages S343–7. Elsevier, aug 2002.

[61] S M Hussain, K L Hess, J M Gearhart, K T Geiss, and J J Schlager. In vitro toxicity of nanoparticles in BRL 3A rat liver cells. In *Toxicology in Vitro*, volume 19, pages 975–983, 2005.

[62] Hanna L Karlsson, Johanna Gustafsson, Pontus Cronholm, and Lennart Möller. Size-dependent toxicity of metal oxide particles-A comparison between nano- and micrometer size. *Toxicology Letters*, 188(2):112–118, jul 2009.

[63] P F Hahn, D D Stark, J M Lewis, S Saini, G Elizondo, R Weissleder, C J Fretz, and J T Ferrucci. First clinical trial of a new superparamagnetic iron oxide for use as an oral gastrointestinal contrast agent in MR imaging. *Radiology*, 175(3):695–700, jun 1990.

[64] Stuart J. McLachlan, Marie R. Morris, Maria A. Lucas, Ricardo A. Fisco, Michael N. Eakins, Dennis R. Fowler, R. Bradley Scheetz, and Adeoye Y. Olukotun. Phase I clinical evaluation of a new iron oxide MR contrast agent. *Journal of magnetic resonance imaging : JMRI*, 4(3):301–7, may 1994.

[65] Arun Kumar, Prasanna K. Jena, Sumita Behera, Richard F. Lockey, Subhra Mohapatra, and Shyam Mohapatra. Multifunctional magnetic nanoparticles for targeted delivery. *Nanomedicine: Nanotechnology, Biology, and Medicine*, 6(1):64–69, 2010.

[66] Poornima Budime Santhosh and Nataša Poklar Ulrih. Multifunctional superparamagnetic iron oxide nanoparticles: Promising tools in cancer theranostics, 2013.

[67] Arati G. Kolhatkar, Andrew C. Jamison, Dmitri Litvinov, Richard C. Willson, and T. Randall Lee. Tuning the magnetic properties of nanoparticles, jul 2013.

[68] Margarethe Hofmann-amtenbrink, Heinrich Hofmann, Matsearch Pully, Chemin Jean Pavillard, Equine Hospital, and Vetsuisse Faculty Zurich. *Superparamagnetic nanoparticles for biomedical applications*, volume 661. 2009.

[69] Heather J. Shipley, Karen E. Engates, and Allison M. Guettner. Study of iron oxide nanoparticles in soil for remediation of arsenic. *Journal of Nanoparticle Research*, 13(6):2387–2397, jun 2011.

[70] Pragnesh N. Dave and Lakhan V. Chopda. Application of iron oxide nanomaterials for the removal of heavy metals, 2014.

[71] Dale L. Huber. Synthesis, properties, and applications of iron nanoparticles, may 2005.

[72] Reju Thomas, In-kyu Park, and Yong Yeon Jeong. Magnetic iron oxide nanoparticles for multimodal imaging and therapy of cancer. *International journal of molecular sciences*, 14(8):15910–30, 2013.

[73] CP Slichter. *Principles of magnetic resonance*. 1990.

[74] E. L. Hahn. Spin echoes. *Physical Review*, 80(4):580–594, nov 1950.

[75] Govind B Chavhan, Paul S Babyn, Bejoy Thomas, Manohar M Shroff, and E Mark Haacke. Principles, techniques, and applications of T2*-based MR imaging and its special applications. *Radiographics : a review publication of the Radiological Society of North America, Inc*, 29(62983):1433–1449, 2009.

[76] André Merbach, Lothar Helm, and Éva Tóth. *The Chemistry of Contrast Agents in Medical Magnetic Resonance Imaging: Second Edition*. John Wiley & Sons, Ltd, Chichester, UK, mar 2013.

[77] Jeff W. M. Bulte and Dara L. Kraitchman. Iron oxide MR contrast agents for molecular and cellular imaging, nov 2004.

[78] M. E. Bartolini, J Pekar, D. R. Chettle, F McNeill, A Scott, J Sykes, F. S. Prato, and G. R. Moran. An investigation of the toxicity of gadolinium based MRI contrast agents using neutron activation analysis. *Magnetic Resonance Imaging*, 21(5):541–544, 2003.

[79] Moshe Rogosnitzky and Stacy Branch. Gadolinium-based contrast agent toxicity: a review of known and proposed mechanisms, jun 2016.

[80] Frank G. Shellock and Emanuel Kanal. Safety of magnetic resonance imaging contrast agents. *J Magn Reson Imaging*, 10(3):477–84., sep 1999.

[81] Yi-xiang J Wang. Superparamagnetic iron oxide based MRI contrast agents: Current status of clinical application. *Quantitative imaging in medicine and surgery*, 1(1):35–40, 2011.

[82] Li Li, Wen Jiang, Kui Luo, Hongmei Song, Fang Lan, Yao Wu, and Zhongwei Gu. Superparamagnetic iron oxide nanoparticles as MRI contrast agents for non-invasive stem cell labeling and tracking, 2013.

[83] D D Stark, R Weissleder, G Elizondo, P F Hahn, S Saini, L E Todd, J Wittenberg, and J T Ferrucci. Superparamagnetic iron oxide: clinical application as a contrast agent for MR imaging of the liver. *Radiology*, 168(2):297–301, aug 1988.

[84] Peter Reimer, Martin Fiebich, Wolfgang Schima, Filip Deckers, and Christian Marx. Hepatic Lesion Detection and Characterization : Value of Nonenhanced MR Imaging , Superparamagnetic Iron Oxide enhanced MR Imaging , and Spiral CT ROC Analysis 1. *Radiology*, (2), 2000.

[85] Mukesh G Harisinghani, Jelle Barentsz, Peter F Hahn, Willem M Deserno, Shahin Tabatabaei, and Ralph Weissleder. new england journal. pages 2491–2499, 2003.

[86] Laura Johnson, Sarah E Pinder, and Michael Douek. Deposition of superparamagnetic iron-oxide nanoparticles in axillary sentinel lymph nodes following subcutaneous injection. pages 481–486, 2013.

[87] S.H. Choi, W.K. Moon, J.H. Hong, K.R. Son, Nariya Cho, B.J. Kwon, J.J. Lee, J.-K. Chung, H.S. Min, and S.H. Park. Lymph node metastasis: Ultrasmall superparamagnetic iron oxide-enhanced MR imaging versus PET/CT in a rabbit model. *Radiology*, 242(1):137–143, jan 2007.

[88] Y. X J Wang, S. M. Hussain, and G. P. Krestin. Superparamagnetic iron oxide contrast agents: Physicochemical characteristics and applications in MR imaging. *European Radiology*, 11(11):2319–2331, 2001.

[89] Stephan A. Schmitz, Matthias Taupitz, Susanne Wagner, Karl-Jürgen Wolf, Dirk Beyersdorff, and Bernd Hamm. Magnetic resonance imaging of atherosclerotic plaques using superparamagnetic iron oxide particles. *Journal of Magnetic Resonance Imaging*, 14(4):355–361, oct 2001.

[90] Alexander Neuwelt, Navneet Sidhu, Chien-An A Hu, Gary Mlady, Steven C Eberhardt, and Laurel O Sillerud. Iron-based superparamagnetic nanoparticle contrast agents for MRI of infection and inflammation. *AJR. American journal of roentgenology*, 204(3):W302–13, 2015.

[91] Catherine C Berry and Adam S G Curtis. Functionalisation of magnetic nanoparticles for applications in biomedicine. *Journal of Physics D: Applied Physics*, 36(13):R198–R206, 2003.

[92] Clare Hoskins, Yue Min, Mariana Gueorguieva, Craig Mcdougall, Alexander Volovick, Paul Prentice, Zhigang Wang, Andreas Melzer, Alfred Cuschieri, and Lijun Wang. Hybrid gold-iron oxide nanoparticles as a multifunctional platform for biomedical application. *???*, 10(1):1, 2012.

[93] Lihong Bu, Jin Xie, Kai Chen, Jing Huang, Zoraida P Aguilar, Andrew Wang, Kin Wai, Mei-sze Chua, Samuel So, Zhen Cheng, Henry S Eden, Baozhong Shen, and Xiaoyuan Chen. Assessment and comparison of magnetic nanoparticles as MRI contrast agents in a rodent model of human hepatocellular carcinoma. (November 2011), 2012.

[94] P Wust, B Hildebrandt, G Sreenivasa, B Rau, J Gellermann, H Riess, R Felix, and PM Schlag. Hyperthermia in combined treatment of cancer. *The Lancet Oncology*, 3(8):487–497, 2002.

[95] Andreas Jordan, Regina Scholz, Peter Wust, Horst Fähling, and Roland Felix. Magnetic fluid hyperthermia (MFH): Cancer treatment with AC magnetic field induced excitation of biocompatible superparamagnetic nanoparticles. *Journal of Magnetism and Magnetic Materials*, 201(1-3):413–419, 1999.

[96] A. Jordan, R. Scholz, P. Wust, H. Fähling, J. Krause, W. Wlodarczyk, B. Sander, Th. Vogl, and R. Felix. Effects of magnetic fluid hyperthermia (MFH) on C3H mammary carcinoma in vivo. *International journal of hyperthermia : the official*

journal of European Society for Hyperthermic Oncology, North American Hyperthermia Group, 13(6):587–605, jan 1997.

[97] Ingrid Hilger, Wilfried Andrä, Rudolf Hergt, Robert Hiergeist, Harald Schubert, and Werner Alois Kaiser. Electromagnetic heating of breast tumors in interventional radiology: in vitro and in vivo studies in human cadavers and mice. *Radiology*, 218(13):570–575, feb 2001.

[98] Jun Motoyama, Noriyuki Yamashita, Tomio Morino, Masashi Tanaka, Takeshi Kobayashi, and Hiroyuki Honda. Hyperthermic treatment of DMBA-induced rat mammary cancer using magnetic nanoparticles. *Biomagnetic research and technology*, 6(1):2, 2008.

[99] Feng Zhao, Ying Zhao, Ying Liu, Xueling Chang, Chunying Chen, and Yuliang Zhao. Cellular uptake, intracellular trafficking, and cytotoxicity of nanomaterials. *Small*, 7(10):1322–1337, 2011.

[100] Punit Kaur, Mark D Hurwitz, Sunil Krishnan, and Alexzander Asea. Combined hyperthermia and radiotherapy for the treatment of cancer, 2011.

[101] Bauke Anninga, Muneer Ahmed, Mieke Van Hemelrijck, Joost Pouw, David Westbroek, Sarah Pinder, Bennie Ten Haken, Quentin Pankhurst, and Michael Douek. Magnetic sentinel lymph node biopsy and localization properties of a magnetic tracer in an in vivo porcine model. *Breast Cancer Research and Treatment*, 141(1):33–42, aug 2013.

[102] M. Ahmed and M. Douek. The role of magnetic nanoparticles in the localization and treatment of breast cancer. *BioMed Research International*, 2013:1–11, 2013.

[103] J Gonzalez-Molina, J Riegler, P Southern, D Ortega, C C Frangos, Y Angelopoulos, S Husain, M F Lythgoe, Q A Pankhurst, and R M Day. Rapid magnetic cell delivery for large tubular bioengineered constructs. *Journal of the Royal Society, Interface / the Royal Society*, 9(76):3008–16, nov 2012.

[104] Lara Prosen, Sara Prijic, Branka Music, Jaka Lavrencak, Maja Cemazar, and Gregor Sersa. Magnetofection: A reproducible method for gene delivery to melanoma cells. *BioMed Research International*, 2013:1–11, 2013.

[105] Scott Goodwin, Caryn Peterson, Carl Hoh, and Craig Bittner. Targeting and retention of magnetic targeted carriers (MTCs) enhancing intra-arterial chemotherapy. *Journal of Magnetism and Magnetic Materials*, 194(1-3):132–139, apr 1999.

[106] Yi-Xiang J Wang. Current status of superparamagnetic iron oxide contrast agents for liver magnetic resonance imaging. *World journal of gastroenterology*, 21(47):13400–2, dec 2015.

[107] Neenu Singh, Gareth J.S. S Jenkins, Romisa Asadi, and Shareen H Doak. Potential toxicity of superparamagnetic iron oxide nanoparticles (SPION). *Nano Reviews*, 1:1–15, 2010.

[108] Yunli Shen, Zheyong Huang, Xuebo Liu, Juying Qian, Jianfeng Xu, Xiangdong Yang, Aijun Sun, and Junbo Ge. Iron-induced myocardial injury: An alarming side effect of superparamagnetic iron oxide nanoparticles. *Journal of Cellular and Molecular Medicine*, 19(8):2032–2035, 2015.

[109] Marco P Monopoli, Christoffer Åberg, Anna Salvati, and Kenneth A Dawson. Biomolecular coronas provide the biological identity of nanosized materials. *Nature Nanotechnology*, 7, 2012.

[110] Iseult Lynch and Kenneth A. Dawson. Protein-nanoparticle interactions. *Nano Today*, 3(1):40–47, 2008.

[111] Christine Grafe, Andreas Weidner, Moritz v d L??he, Christian Bergemann, Felix H Schacher, Joachim H Clement, and Silvio Dutz. Intentional formation of a protein corona on nanoparticles: Serum concentration affects protein corona mass, surface charge, and nanoparticle-cell interaction, jun 2015.

[112] L Vroman, AL Adams, GC Fischer, and PC Munoz. Interaction of high molecular weight kininogen, factor XII, and fibrinogen in plasma at interfaces. *Blood*, 55(1):156–159, jan 1980.

[113] Stefan Tenzer, Dominic Docter, Jörg Kuharev, Anna Musyanovych, Verena Fetz, Rouven Hecht, Florian Schlenk, Dagmar Fischer, Klytaimnistra Kiouptsi, Christoph Reinhardt, Katharina Landfester, Hansjörg Schild, Michael Maskos, Shirley K Knauer, and Roland H Stauber. Rapid formation of plasma protein corona critically affects nanoparticle pathophysiology. *Nature nanotechnology*, 8(10):772–81, 2013.

[114] M. Jansch, P. Stumpf, C. Graf, E. Rühl, and R. H. Müller. Adsorption kinetics of plasma proteins on ultrasmall superparamagnetic iron oxide (USPIO) nanoparticles. *International Journal of Pharmaceutics*, 428(1-2):125–133, 2012.

[115] Andre E Nel, Lutz Mädler, Darrell Velegol, Tian Xia, Eric M V Hoek, Ponisseril Somasundaran, Fred Klaessig, Vince Castranova, and Mike Thompson. Understanding biophysicochemical interactions at the nano-bio interface. *Nature materials*, 8(7):543–557, 2009.

[116] Martin Lundqvist, Johannes Stigler, Giuliano Elia, Iseult Lynch, Tommy Cedervall, and Kenneth A Dawson. Nanoparticle size and surface properties determine the protein corona with possible implications for biological impacts. *Proceedings of the National Academy of Sciences of the United States of America*, 105(38):14265–70, 2008.

[117] Usawadee Sakulkhu, Morteza Mahmoudi, Lionel Maurizi, Jatuporn Salaklang, and Heinrich Hofmann. Protein corona composition of superparamagnetic iron oxide nanoparticles with various physico-chemical properties and coatings. *Scientific reports*, 4:5020, may 2014.

[118] Zhou J Deng, Mingtao Liang, Istvan Toth, Michael J Monteiro, and Rodney F Minchin. Molecular interaction of poly(acrylic acid) gold nanoparticles with human fibrinogen. *ACS Nano*, 6(10):8962–8969, 2012.

[119] Angl Jedlovszky-Hajd, A, Francesca Baldelli Bombelli, Marco P. Monopoli, Etelka Tomb??cz, and Kenneth A. Dawson. Surface coatings shape the protein corona of SPIONs with relevance to their application in vivo. *Langmuir*, 28(42):14983–14991, oct 2012.

[120] Forrest M Kievit and Miqin Zhang. Surface engineering of iron oxide nanoparticles for targeted cancer therapy. *Accounts of Chemical Research*, 44(10):853–862, 2011.

[121] Malvern Instruments. Zeta potential - An introduction in 30 minutes, 2015.

[122] HORIBA Instruments. A Guidebook to Particle Size Analysis, 2014.

[123] Ayush Verma and Francesco Stellacci. Effect of surface properties on nanoparticle-cell interactions, jan 2010.

[124] Morteza Mahmoudi, Mohammad A Shokrgozar, Soroush Sardari, and Mojgan K Moghadam. Nanoscale Irreversible changes in protein conformation due to interaction with superparamagnetic iron oxide nanoparticles. pages 1127–1138, 2011.

[125] Carmen Vogt, Maria Pernemalm, Pekka Kohonen, Sophie Laurent, Kjell Hultenby, Marie Vahter, Janne Lehti??, Muhammet S Toprak, and Bengt Fadeel. Proteomics analysis reveals distinct corona composition on magnetic nanoparticles with different surface coatings: Implications for interactions with primary human macrophages. *PLoS ONE*, 10(10), 2015.

[126] Lars Thiele, Julia E. Diederichs, Regina Reszka, Hans P. Merkle, and Elke Walter. Competitive adsorption of serum proteins at microparticles affects phagocytosis by dendritic cells. *Biomaterials*, 24(8):1409–1418, 2003.

[127] H. Ryoung Kim, S. Gil, K. Andrieux, V. Nicolas, M. Appel, H. Chacun, D. Desmaële, F. Taran, D. Georgin, and P. Couvreur. Low-density lipoprotein receptor-mediated endocytosis of PEGylated nanoparticles in rat brain endothelial cells. *Cellular and Molecular Life Sciences*, 64(3):356–364, feb 2007.

[128] Tracy R. Daniels, Tracie Delgado, Gustavo Helguera, and Manuel L. Penichet. The transferrin receptor part II: Targeted delivery of therapeutic agents into cancer cells, 2006.

[129] Anna Salvati, Christoffer Åberg, Kenneth A. Dawson, Marco P. Monopoli, Christoffer Åberg, Anna Salvati, Kenneth A. Dawson, Christoffer Aberg, Anna Salvati, and Kenneth A. Dawson. Biomolecular coronas provide the biological identity of nanosized materials. *Nature Nanotechnology*, 7(12):779–786, dec 2012.

[130] Omid Veiseh, Jonathan W. Gunn, and Miqin Zhang. Design and fabrication of magnetic nanoparticles for targeted drug delivery and imaging, 2010.

[131] Sophie Laurent, Delphine Forge, Marc Port, Alain Roch, Caroline Robic, Luce Vander Elst, and Robert N Muller. Magnetic Iron Oxide Nanoparticles : Synthesis , Stabilization , Vectorization , Physicochemical Characterizations , and Biological Applications. pages 2064–2110, 2008.

[132] Sophie Laurent and Morteza Mahmoudi. Superparamagnetic iron oxide nanoparticles: Promises for diagnosis and treatment of cancer. *International Journal of Molecular Epidemiology and Genetics*, 2(4):367–390, 2011.

[133] Wei Wu, Zhaohui Wu, Taekyung Yu, Changzhong Jiang, and Woo-Sik Kim. Recent progress on magnetic iron oxide nanoparticles: synthesis, surface functional strategies and biomedical applications. *Science and Technology of Advanced Materials*, 16(2):023501, apr 2015.

[134] Camille C. Hanot, Young Suk Choi, Tareq B. Anani, Dharsan Soundarrajan, and Allan E. David. Effects of iron-oxide nanoparticle surface chemistry on uptake kinetics and cytotoxicity in CHO-K1 cells. *International Journal of Molecular Sciences*, 17(1):54, dec 2015.

[135] Adam J Cole, Allan E David, Jianxin Wang, Craig J Galbán, Hannah L Hill, and Victor C Yang. Polyethylene glycol modified, cross-linked starch-coated iron oxide nanoparticles for enhanced magnetic tumor targeting. *Biomaterials*, 32(8):2183–2193, mar 2011.

[136] Gaurav Sahay, Daria Y Alakhova, and Alexander V Kabanov. Endocytosis of nanomedicines, 2010.

[137] Amel Hanini, Alain Schmitt, Kamel Kacem, François Chau, Souad Ammar, and Julie Gavard. Evaluation of iron oxide nanoparticle biocompatibility. *International journal of nanomedicine*, 6:787–794, 2011.

[138] Julie Mazzolini, Ralf Weber, Hsueh-Shih Chen, Abdullah Khan, Emily Guggenheim, Robert Shaw, Kevin Chipman, Mark Viant, and Joshua Rappoport. Protein corona modulates uptake and toxicity of nanoceria via clathrin-mediated endocytosis e. *The Biological Bulletin*, 2016.

[139] Joanna Rejman, Volker Oberle, Inge S Zuhorn, and Dick Hoekstra. Size-dependent internalization of particles via the pathways of clathrin- and caveolae-mediated endocytosis. *The Biochemical journal*, 377(Pt 1):159–69, 2004.

[140] Jie Zhu, Lei Liao, Lina Zhu, Peng Zhang, Kai Guo, Jilie Kong, Chang Ji, and Baohong Liu. Size-dependent cellular uptake efficiency, mechanism, and cytotoxicity of silica nanoparticles toward HeLa cells. *Talanta*, 107:408–15, mar 2013.

[141] Philip J Smith, Maude Giroud, Helen L Wiggins, Florence Gower, Jennifer A Thorley, Bjorn Stolpe, Julie Mazzolini, Rosemary J Dyson, and Joshua Z Rappoport. Cellular entry of nanoparticles via serum sensitive clathrin-mediated endocytosis, and plasma membrane permeabilization. *International Journal of Nanomedicine*, 7:2045–2055, 2012.

[142] T F ROTH and K R PORTER. YOLK PROTEIN UPTAKE IN THE OOCYTE OF THE MOSQUITO AEDES AEGYPTI. L. *The Journal of cell biology*, 20:313–332, feb 1964.

[143] Gary J Doherty and Harvey T McMahon. Mechanisms of endocytosis. *Annual review of biochemistry*, 78:857–902, 2009.

[144] Longfa Kou, Jin Sun, Yinglei Zhai, and Zhonggui He. The endocytosis and intracellular fate of nanomedicines: Implication for rational design. *Asian Journal of Pharmaceutical Sciences*, 8(1):1–8, 2013.

[145] E YAMADA. The fine structure of the gall bladder epithelium of the mouse. *The Journal of biophysical and biochemical cytology*, 1(5):445–58, sep 1955.

[146] A M Fra, E Williamson, K Simons, and R G Parton. De novo formation of caveolae in lymphocytes by expression of VIP21-caveolin. *Proceedings of the National Academy of Sciences of the United States of America*, 92(19):8655–9, sep 1995.

[147] Sarah R. Elkin, Ashley M. Lakoduk, and Sandra L. Schmid. Endocytic pathways and endosomal trafficking: a primer, may 2016.

[148] Babak Razani, Scott E Woodman, and Michael P Lisanti. Caveolae: from cell biology to animal physiology. *Pharmacological reviews*, 54(3):431–467, sep 2002.

[149] Robert G. Parton and Mark T. Howes. Revisiting caveolin trafficking: the end of the caveosome. *The Rockefeller University Press J. Cell Biol*, 197(3):347–349, 2010.

[150] Robert G. Parton. Caveolae meet endosomes: A stable relationship?, 2004.

[151] Ivan R Nabi and Phuong U Le. Caveolae/raft-dependent endocytosis, may 2003.

[152] Nils Bohmer and Andreas Jordan. Caveolin-1 and CDC42 mediated endocytosis of silica-coated iron oxide nanoparticles in HeLa cells. *Beilstein Journal of Nanotechnology*, 6(1):167–176, jan 2015.

[153] Warren H Lewis. Pinocytosis by Malignant Cells. *The American Journal of Cancer*, pages 666–679, 1937.

[154] Jet Phey Lim and Paul A Gleeson. Macropinocytosis: an endocytic pathway for internalising large gulps. *Immunology and Cell Biology*, 89(8):836–843, 2011.

[155] Julia Dausend, Anna Musyanovych, Martin Dass, Paul Walther, Hubert Schrezenmeier, Katharina Landfester, and Volker Mailänder. Uptake mechanism of oppositely charged fluorescent nanoparticles in Hela cells. *Macromolecular Bioscience*, 8(12):1135–1143, dec 2008.

[156] Raymond S H Yang, Louis W Chang, Jui Pin Wu, Ming Hsien Tsai, Hsiu Jen Wang, Yu Chun Kuo, Teng Kuang Yeh, Chung Shi Yang, and Pinpin Lin. Persistent tissue kinetics and redistribution of nanoparticles, quantum Dot 705, in Mice: ICP-MS quantitative assessment. *Environmental Health Perspectives*, 115(9):1339–1343, 2007.

[157] Jing Li Gu, Hai Fei Xu, Ye Hua Han, Wei Dai, Wei Hao, Chun Yu Wang, Ning Gu, Hai Yan Xu, and Ji Min Cao. The internalization pathway, metabolic fate and biological effect of superparamagnetic iron oxide nanoparticles in the macrophage-like RAW264.7 cell. *Science China Life Sciences*, 54(9):793–805, 2011.

[158] Christoph Schweiger, Raimo Hartmann, Feng Zhang, Wolfgang J Parak, Thomas H Kissel, and Pilar Rivera_Gil. Quantification of the internalization patterns of superparamagnetic iron oxide nanoparticles with opposite charge. *Journal of Nanobiotechnology*, 10(1):28, 2012.

[159] Tiago Dos Santos, Juan Varela, Iseult Lynch, Anna Salvati, and Kenneth A. Dawson. Quantitative assessment of the comparative nanoparticle-uptake efficiency of a range of cell lines. *Small*, 7(23):3341–3349, 2011.

[160] Tiago dos Santos, Juan Varela, Iseult Lynch, Anna Salvati, and Kenneth A Dawson. Effects of transport inhibitors on the cellular uptake of carboxylated polystyrene nanoparticles in different cell lines. *PLoS ONE*, 6(9), 2011.

[161] Jaime Agudo-Canalejo and Reinhard Lipowsky. Critical particle sizes for the engulfment of nanoparticles by membranes and vesicles with bilayer asymmetry. *ACS Nano*, 9(4):3704–3720, 2015.

[162] Oshrat Harush-Frenkel, Nir Debotton, Simon Benita, and Yoram Altschuler. Targeting of nanoparticles to the clathrin-mediated endocytic pathway. *Biochemical and Biophysical Research Communications*, 353(1):26–32, 2007.

[163] Oleg Lunov, Tatiana Syrovets, Carlheinz Röcker, Kyrylo Tron, G. Ulrich Nienhaus, Volker Rasche, Volker Mailänder, Katharina Landfester, and Thomas Simmet. Lysosomal degradation of the carboxydextran shell of coated superparamagnetic iron oxide nanoparticles and the fate of professional phagocytes. *Biomaterials*, 31(34):9015–9022, 2010.

[164] Stefaan J H Soenen, Uwe Himmelreich, Nele Nuytten, Thomas R. Pisanic, Aldo Ferrari, and Marcel De Cuyper. Intracellular nanoparticle coating stability determines nanoparticle diagnostics efficacy and cell functionality. *Small*, 6(19):2136–2145, 2010.

[165] Lara K. Bogart, Arthur Taylor, Yann Cesbron, Patricia Murray, and Raphaël Lévy. Photothermal microscopy of the core of dextran-coated iron oxide nanoparticles during cell uptake. *ACS Nano*, 6(7):5961–5971, 2012.

[166] Maneesh Gujrati, Anthony Malamas, Tesia Shin, Erlei Jin, Yunlu Sun, and Zheng Rong Lu. Multifunctional cationic lipid-based nanoparticles facilitate endosomal escape and reduction-triggered cytosolic siRNA release. *Molecular Pharmaceutics*, 11(8):2734–2744, 2014.

[167] Andrew Elias and Andrew Tsourkas. Imaging circulating cells and lymphoid tissues with iron oxide nanoparticles. *Hematology / the Education Program of the American Society of Hematology. American Society of Hematology. Education Program*, pages 720–726, 2009.

[168] Ali S Arbab, Lindsey B Wilson, Parwana Ashari, Elaine K Jordan, Bobbi K Lewis, and Joseph A Frank. A model of lysosomal metabolism of dextran coated superparamagnetic iron oxide (SPIO) nanoparticles : implications for cellular magnetic resonance imaging. (July):383–389, 2005.

[169] Michael Levy, Nathalie Luciani, Damien Alloyeau, Dan Elgrabli, Vanessa Deveaux, Christine Pechoux, Sophie Chat, Guillaume Wang, Nidhi Vats, François Gendron, Cécile Factor, Sophie Lotersztajn, Alain Luciani, Claire Wilhelm, and Florence Gazeau. Long term in vivo biotransformation of iron oxide nanoparticles. *Biomaterials*, 32(16):3988–3999, jun 2011.

[170] Gayatri Bhasin, Hina Kauser, and Mohammad Athar. Iron augments stage-I and stage-II tumor promotion in murine skin. *Cancer Letters*, 183(2):113–122, sep 2002.

[171] Byeongsu Kwon, Eunji Han, Wonseok Yang, Wooram Cho, Wooyoung Yoo, Junyeon Hwang, Byoung Mog Kwon, and Dongwon Lee. Nano-Fenton Reactors as a New Class of Oxidative Stress Amplifying Anticancer Therapeutic Agents. *ACS Applied Materials and Interfaces*, 8(9):5887–5897, 2016.

[172] B Ankamwar, T C Lai, J H Huang, R S Liu, M Hsiao, C H Chen, and Y K Hwu. Biocompatibility of Fe(3)O(4) nanoparticles evaluated by in vitro cytotoxicity assays using normal, glia and breast cancer cells. *Nanotechnology*, 21(7):75102, feb 2010.

[173] Macarena Calero, Michele Chiappi, Ana Lazaro-Carrillo, María José Rodríguez, Francisco Javier Chichón, Kieran Crosbie-Staunton, Adriele Prina-Mello, Yuri Volkov, Angeles Villanueva, and José L Carrascosa. Characterization of interaction of magnetic nanoparticles with breast cancer cells. *Journal of Nanobiotechnology*, 13(1):16, 2015.

[174] Oleg Lunov, Tatiana Syrovets, Berthold Büchele, Xiue Jiang, Carlheinz Röcker, Kyrylo Tron, G Ulrich Nienhaus, Paul Walther, Volker Mailänder, Katharina Landfester, and Thomas Simmet. The effect of carboxydextran-coated superparamagnetic iron oxide nanoparticles on c-Jun N-terminal kinase-mediated apoptosis in human macrophages. *Biomaterials*, 31(19):5063–5071, 2010.

[175] Stefaan J. H. Soenen, Nele Nuytten, Simon F. De Meyer, Stefaan C. De Smedt, and Marcel De Cuyper. High intracellular iron oxide nanoparticle concentrations affect cellular cytoskeleton and focal adhesion kinase-mediated signaling. *Small*, 6(7):832–842, apr 2010.

[176] Jennifer A Tate, Alicia A Petryk, Andrew J Giustini, and P Jack Hoopes. In vivo biodistribution of iron oxide nanoparticles: an overview. *Proceedings of SPIE*, 7901:790117, feb 2011.

[177] K. G. Ljungström. Invited commentary: Pretreatment with dextran 1 makes dextran 40 therapy safer. *Journal of Vascular Surgery*, 43(5):1070–1072, 2006.

[178] Philippe Bourrinet, Howard H Bengele, Bruno Bonnemain, Anne Dencausse, Jean-Marc Idee, Paula M Jacobs, and Jerome M Lewis. Preclinical safety and pharmacokinetic profile of ferumoxtran-10, an ultrasmall superparamagnetic iron oxide magnetic resonance contrast agent. *Investigative radiology*, 41(3):313–324, mar 2006.

[179] Iker Montes-Burgos, Dorota Walczyk, Patrick Hole, Jonathan Smith, Iseult Lynch, and Kenneth Dawson. Characterisation of nanoparticle size and state prior to nanotoxicological studies. *Journal of Nanoparticle Research*, 12(1):47–53, jan 2010.

[180] Christopher Szakal, Lyubov Tsytsikova, David Carlander, and Timothy V. Duncan. Measurement methods for the oral uptake of engineered nanomaterials from human dietary sources: Summary and outlook, jul 2014.

[181] Anja Ostrowski, Daniel Nordmeyer, Alexander Boreham, Cornelia Holzhausen, Lars Mundhenk, Christina Graf, Martina C Meinke, Annika Vogt, Sabrina Hadam, J??rgen Lademann, Eckart Ruhl, Ulrike Alexiev, and Achim D Gruber. Overview about the localization of nanoparticles in tissue and cellular context by different imaging techniques, jan 2015.

[182] Daniela Drescher, Charlotte Giesen, Heike Traub, Ulrich Panne, Janina Kneipp, and Norbert Jakubowski. Quantitative imaging of gold and silver nanoparticles in single eukaryotic cells by laser ablation ICP-MS. *Analytical Chemistry*, 84(22):9684–9688, 2012.

[183] Daniela Drescher, Ingrid Zeise, Heike Traub, Peter Guttmann, Stephan Seifert, Tina Büchner, Norbert Jakubowski, Gerd Schneider, and Janina Kneipp. In situ characterization of SiO2 nanoparticle biointeractions using BrightSilica. *Advanced Functional Materials*, 24(24):3765–3775, jun 2014.

[184] Monika Perlovska Harvanova, Jana Jiravova, Jakub Malohlava, Katerina Barton Tomankova, Dagmar Jirova, and Hana Kolarova. Raman imaging of cellular uptake and studies of silver nanoparticles effect in BJ human fibroblasts cell lines. *International Journal of Pharmaceutics*, 528(1-2):280–286, 2017.

[185] Daniel Stucht, K Appu Danishad, Peter Schulze, Frank Godenschweger, Maxim Zaitsev, and Oliver Speck. Highest resolution in vivo human brain MRI using prospective motion correction. *PLoS ONE*, 10(7):e0133921, 2015.

[186] Stijn J M Van Malderen, Johannes T Van Elteren, and Frank Vanhaecke. Submicrometer Imaging by Laser Ablation-Inductively Coupled Plasma Mass Spectrometry via Signal and Image Deconvolution Approaches. *Analytical Chemistry*, 87(12):6125–6132, 2015.

[187] Lara J Gamble and C.R. Anderton. Secondary Ion Mass Spectrometry Imaging Tissue, Cells and Microbial Systems. *Microscopy Today*, 24(2):24–31, mar 2017.

[188] Michael A Robinson, Daniel J Graham, and David G Castner. ToF-SIMS depth profiling of cells: Z-correction, 3D imaging, and sputter rate of individual NIH/3T3 fibroblasts. *Analytical Chemistry*, 84(11):4880–4885, 2012.

[189] Geoffrey Tyler. ICP-MS, or ICP-AES and AAS?a comparison. 1994.

[190] Jason T Rashkow, Sunny C Patel, Ryan Tappero, and Balaji Sitharaman. Quantification of single-cell nanoparticle concentrations and the distribution of these concentrations in cell population. *Journal of the Royal Society, Interface / the Royal Society*, 11(94):20131152, may 2014.

[191] Daniel Hofmann, Stefan Tenzer, Markus B Bannwarth, and Claudia Messerschmidt. Mass Spectrometry and Imaging Analysis of Nanoparticle-Containing Vesicles Provide a Mechanistic Insight into Cellular Tra ffi cking. (Xx), 2014.

[192] Y P Kim, Hyun Kyong Shon, Seung Koo Shin, and Tae Geol Lee. Probing nanoparticles and nanoparticle-conjugated biomolecules using time-of-flight secondary ion mass spectrometry. *Mass Spectrom Rev*, 34(2):237–247, apr 2015.

[193] Andreas Limbeck, Patrick Galler, Maximilian Bonta, Gerald Bauer, Winfried Nischkauer, and Frank Vanhaecke. Recent advances in quantitative LA-ICP-MS analysis: challenges and solutions in the life sciences and environmental chemistry. *Analytical and bioanalytical chemistry*, 407(22):6593–6617, sep 2015.

[194] J Sabine Becker, Andreas Matusch, Christoph Palm, Dagmar Salber, Kathryn A Morton, and J Susanne Becker. Bioimaging of metals in brain tissue by laser ablation inductively coupled plasma mass spectrometry (LA-ICP-MS) and metallomics. 2009.

[195] Suming Chen, Caiqiao Xiong, Huihui Liu, Qiongqiong Wan, Jian Hou, Qing He, Abraham Badu-Tawiah, and Zongxiu Nie. Mass spectrometry imaging reveals the sub-organ distribution of carbon nanomaterials. *Nature nanotechnology*, 10(2):176–82, feb 2015.

[196] Chang Soo Kim, Xiaoning Li, Ying Jiang, Bo Yan, Gulen Y Tonga, Moumita Ray, David J Solfiell, and Vincent M Rotello. Cellular imaging of endosome entrapped small gold nanoparticles. *MethodsX*, 2:306–15, jan 2015.

[197] Katherine A Willets, Rp Van Duyne, and Richard P Van Duyne. Localized Surface Plasmon Resonance Spectroscopy and Sensing. *Annual Review of Physical Chemistry*, 58(1):267–297, 2007.

[198] T. Andrew Taton, Gang Lu, , and Chad A. Mirkin*. Two-Color Labeling of Oligonucleotide Arrays via Size-Selective Scattering of Nanoparticle Probes. 2001.

[199] W. Plieth, H. Dietz, A. Anders, G. Sandmann, A. Meixner, M. Weber, and H. Kneppe. Electrochemical preparation of silver and gold nanoparticles: Characterization by confocal and surface enhanced Raman microscopy. *Surface Science*, 597(1-3):119–126, 2005.

[200] Chrysafis Andreou, Volker Neuschmelting, Darjus-Felix Tschaharganeh, Chun-Hao Huang, Anton Oseledchyk, Pasquale Iacono, Hazem Karabeber, Rivka R Colen, Lorenzo Mannelli, Scott W Lowe, and Moritz F Kircher. Imaging of Liver Tumors Using Surface-Enhanced Raman Scattering Nanoparticles. *ACS nano*, 10(5):5015–26, may 2016.

[201] Francesco Masia, Wolfgang Langbein, Peter Watson, and Paola Borri. Four-wave mixing of gold nanoparticles for three-dimensional cell microscopy. In *CLEO/Europe - EQEC 2009 - European Conference on Lasers and Electro-Optics and the European Quantum Electronics Conference*, volume 34, pages 1816–8, jun 2009.

[202] Jordan Brocious and Eric O. Potma. Lighting up micro-structured materials with four-wave mixing microscopy, 2013.

[203] Hyunmin Kim, Garnett W. Bryant, and Stephan J. Stranick. Superresolution four-wave mixing microscopy. *Optics Express*, 20(6):6042, mar 2012.

[204] Gianluca Rago, Carolin M. Langer, Christian Brackman, James P.R. Day, Katrin F. Domke, Nathanael Raschzok, Christian Schmidt, Igor M. Sauer, Annika Enejder, Martina T. Mogl, and Mischa Bonn. CARS microscopy for the visualization of micrometer-sized iron oxide MRI contrast agents in living cells. *Biomedical Optics Express*, 2(9):2470, sep 2011.

[205] Emine U Saritas, Patrick W Goodwill, Laura R Croft, Justin J Konkle, Kuan Lu, Bo Zheng, and Steven M Conolly. Magnetic particle imaging (MPI) for NMR and MRI researchers. *Journal of Magnetic Resonance*, 229:116–126, apr 2013.

[206] Bernhard Gleich and Jürgen Weizenecker. Tomographic imaging using the nonlinear response of magnetic particles. *Nature*, 435(7046):1214–7, jun 2005.

[207] P Danhier, G De Preter, S Boutry, I Mahieu, P Leveque, J Magat, V Haufroid, P Sonveaux, C Bouzin, O Feron, R N Muller, B F Jordan, and B Gallez. Electron paramagnetic resonance as a sensitive tool to assess the iron oxide content in cells for MRI cell labeling studies. *Contrast Media and Molecular Imaging*, 7(3):302–307, 2012.

[208] Kim A Radermacher, Nelson Beghein, Sébastien Boutry, Sophie Laurent, Luce Vander Elst, Robert N Muller, Benedicte F Jordan, and Bernard Gallez. In vivo detection of inflammation using pegylated iron oxide particles targeted at E-selectin: a multimodal approach using MR imaging and EPR spectroscopy. *Investigative radiology*, 44(7):398–404, jul 2009.

[209] Oliviero L Gobbo, Friedrich Wetterling, Peter Vaes, Stephanie Teughels, Farouk Markos, Deirdre Edge, Christine M Shortt, Kieran Crosbie-Staunton, Marek W Radomski, Yuri Volkov, and Adriele Prina-Mello. Biodistribution and pharmacokinetic studies of SPION using particle electron paramagnetic resonance, MRI and ICP-MS. *Nanomedicine*, 10(11):1751–1760, 2015.

[210] Soren Nielsen, Erlend Arnulf Nagelhus, Mahmood Amiry-Moghaddam, Charles Bourque, Peter Agre, and Ole Petter Ottersen. Specialized Membrane Domains for Water Transport in Glial Cells: High-Resolution Immunogold Cytochemistry of Aquaporin-4 in Rat Brain. *J. Neurosci.*, 17(1):171–180, jan 1997.

[211] W Page Faulk and G Malcolm Taylor. Communication to the editors. *Immunochemistry*, 8(11):1081–1083, nov 1971.

[212] Andreas Elsaesser, Ashley Taylor, Gesa Staats de Yanés, George McKerr, Eun-Mee Kim, Eugene O'Hare, and C Vyvyan Howard. Quantification of nanoparticle uptake by cells using microscopical and analytical techniques. *Nanomedicine*, 5(9):1447–1457, 2010.

[213] Michał M Wójcik, Magdalena Olesińska, Michał Sawczyk, Józef Mieczkowski, and Ewa Górecka. Controlling the Spatial Organization of Liquid Crystalline Nanoparticles by Composition of the Organic Grafting Layer. *Chemistry (Weinheim an der Bergstrasse, Germany)*, 21(28):10082–8, 2015.

[214] Quentin Le Trequesser, Guillaume Devès, Gladys Saez, Laurent Daudin, Philippe Barberet, Claire Michelet, Marie-Hélène Delville, and Hervé Seznec. Single cell in situ detection and quantification of metal oxide nanoparticles using multimodal correlative microscopy. *Analytical chemistry*, 86(15):7311–9, aug 2014.

[215] Ajay Kumar Gupta and Mona Gupta. Synthesis and surface engineering of iron oxide nanoparticles for biomedical applications. *Biomaterials*, 26(18):3995–4021, 2005.

[216] Yang Yang, Huilan Chen, Bin Zhao, and Ximao Bao. Size control of ZnOnanoparticles via thermal decomposition of zinc acetate coated on organic additives. *Journal of crystal growth*, 263(1):447–453, 2004.

[217] Debra Gusnard and Robert H Kirschner. Cell and organelle shrinkage during preparation for scanning electron microscopy: effects of fixation, dehydration and critical point drying. *Journal of microscopy*, 110(1):51–57, 1977.

[218] Christian Mühlfeld, Barbara Rothen-Rutishauser, Dimitri Vanhecke, Fabian Blank, Peter Gehr, and Matthias Ochs. Visualization and quantitative analysis of nanoparticles in the respiratory tract by transmission electron microscopy. *Particle and fibre toxicology*, 4:11, jan 2007.

[219] D Bartczak, M-O Baradez, H Goenaga-Infante, and D Marshall. Label-free monitoring of the nanoparticle surface modification effects on cellular uptake, trafficking and toxicity. *Toxicology Research*, 4(1):169–176, 2015.

[220] Sergiy Patskovsky, Eric Bergeron, David Rioux, Mikaël Simard, and Michel Meunier. Hyperspectral reflected light microscopy of plasmonic Au/Ag alloy nanoparticles incubated as multiplex chromatic biomarkers with cancer cells. *The Analyst*, 139(20):5247–53, oct 2014.

[221] D. O. Shah W. Sigmund, H. El-Shall and B. M. Moudgil. *Particulate Systems in Nano- and Biotechnologies*. CRC Press, 2008.

[222] J K Sugden. Photochemistry of dyes and fluorochromes used in biology and medicine: some physicochemical background and current applications. *Biotechnic & histochemistry : official publication of the Biological Stain Commission*, 79(2):71–90, apr 2004.

[223] M. K. Quinn, N. Gnan, S. James, A. Ninarello, F. Sciortino, E. Zaccarelli, and J. J. McManus. How fluorescent labelling alters the solution behaviour of proteins. *Physical chemistry chemical physics : PCCP*, 17(46):31177–87, 2015.

[224] Katharina Böse, Marcus Koch, Christian Cavelius, Alexandra K Kiemer, and Annette Kraegeloh. A Correlative Analysis of Gold Nanoparticles Internalized by A549 Cells. *Particle & Particle Systems Characterization*, 31(4):439–448, 2014.

[225] Konstantin Sokolov, Michele Follen, Jesse Aaron, Ina Pavlova, Anais Malpica, Reuben Lotan, and Rebecca Richards-kortum. Real-Time Vital Optical Imaging of Precancer Using Anti-Epidermal Growth Factor Receptor Antibodies Conjugated to Gold Nanoparticles Advances in Brief Real-Time Vital Optical Imaging of Precancer Using Anti-Epidermal Growth Factor Receptor Antibodies Conj. *Cancer research*, 63(9):1999–2004, may 2004.

[226] A Rastar and ME Yazdanshenas. Theoretical Review of Optical Properties of Nanoparticles. *Fabrics & Fibers (...*, 2013.

[227] Colin J R Sheppard, X S Gan, Min Gu, and Maitreyee Roy. Signal-to-noise in confocal microscopes. *Handbook of Biological Confocal Microscopy*, (3):363–371, 1995.

[228] D Huang, E A Swanson, C P Lin, J S Schuman, W G Stinson, W Chang, M R Hee, T Flotte, K Gregory, and C A Puliafito. Optical coherence tomography. *Science (New York, N.Y.)*, 254(5035):1178–81, nov 1991.

[229] Haizhen Zhang, Qiuju Ji, Changjin Huang, Sulin Zhang, Bing Yuan, Kai Yang, and Yu-Qiang Ma. Cooperative transmembrane penetration of nanoparticles. *Scientific reports*, 5:10525, 2015.

[230] E J Ambrose. A surface contact microscope for the study of cell movements. *Nature*, 178:1194, 1956.

[231] E A Gibbs-Flournoy, P A Bromberg, T P Hofer, J M Samet, and R M Zucker. Darkfield-confocal microscopy detection of nanoscale particle internalization by human lung cells. *Particle and fibre toxicology*, 8(1):2, jan 2011.

[232] P. A. Temple. Total internal reflection microscopy: a surface inspection technique. *Applied optics*, 20(15):2656–64, aug 1981.

[233] Bo-Jui Chang, Shiuan Huei Lin, Li-Jun Chou, and Su-Yu Chiang. Subdiffraction scattered light imaging of gold nanoparticles using structured illumination. *Optics Letters*, 36(24):4773–4775, 2011.

[234] Milind Rajadhyaksha, Salvador González, James M. Zavislan, R. Rox Anderson, and Robert H. Webb. In vivo confocal scanning laser microscopy of human skin II: Advances in instrumentation and comparison with histology. *Journal of Investigative Dermatology*, 113(3):293–303, 1999.

[235] E. A. W. Wolberink, P. E J Van Erp, M. M. Teussink, P. C M Van De Kerkhof, and M. J. P. Gerritsen. Cellular features of psoriatic skin: Imaging and quantification using in vivo reflectance confocal microscopy. *Cytometry Part B - Clinical Cytometry*, 80 B(3):141–149, may 2011.

[236] Nicusor Iftimia, Gary Peterson, Ernest W Chang, Gopi Maguluri, William Fox, and Milind Rajadhyaksha. Combined reflectance confocal microscopy-optical coherence tomography for delineation of basal cell carcinoma margins: an ex vivo study. *Journal of Biomedical Optics*, 21(1):016006, 2016.

[237] Rahul Yadav, Kye-Sung Lee, Jannick P. Rolland, James M. Zavislan, James V. Aquavella, and Geunyoung Yoon. Micrometer axial resolution OCT for corneal imaging. *Biomedical Optics Express*, 2(11):3037, nov 2011.

[238] A S CURTIS. The Mechanism of Adhesion of Cells to Glass. a Study by Interference Reflection Microscopy. *The Journal of cell biology*, 20:199–215, feb 1964.

[239] H Verschueren. Interference reflection microscopy in cell biology: methodology and applications. *Journal of cell science*, 75:279–301, apr 1985.

[240] Chao Yin, Kin Liao, Hai Quan Mao, Kam W Leong, Ren Xi Zhuo, and Vincent Chan. Adhesion contact dynamics of HepG2 cells on galactose-immobilized substrates. *Biomaterials*, 24(5):837–850, 2003.

[241] Takahisa Matsuzaki, Kosaku Ito, Kentaro Masuda, Eisuke Kakinuma, Rumi Sakamoto, Kentaro Iketaki, Hideaki Yamamoto, Masami Suganuma, Naritaka Kobayashi, Seiichiro Nakabayashi, Takashi Tanii, and Hiroshi Y Yoshikawa. Quantitative Evaluation of Cancer Cell Adhesion to Self-Assembled Monolayer-Patterned Substrates by Reflection Interference Contrast Microscopy. *The Journal of Physical Chemistry B*, page acs.jpcb.5b11870, 2016.

[242] J. Bereiter-Hahn, C. H. Fox, and B. Thorell. Quantitative reflection contrast microscopy of living cells. *Journal of Cell Biology*, 82(3):767–779, 1979.

[243] Gabrielle De Wit, John S H Danial, Philipp Kukura, and Mark I Wallace. Dynamic label-free imaging of lipid nanodomains. *Proceedings of the National Academy of Sciences*, 2015(24):3–7, oct 2015.

[244] Jaime Ortega-Arroyo, Philipp Kukura, and R. Huang. Interferometric scattering microscopy (iSCAT): new frontiers in ultrafast and ultrasensitive optical microscopy. *Physical Chemistry Chemical Physics*, 14(45):15625, 2012.

[245] RA Zsigmondy. Richard Zsigmondy - Nobel Lecture: Properties of Colloids, 1926.

[246] Christopher Loo, Amanda Lowery, Naomi Halas, Jennifer West, and Rebekah Drezek. Immunotargeted nanoshells for integrated cancer imaging and therapy. *Nano Letters*, 5(4):709–711, 2005.

[247] Guy Cox and Colin J.R. Sheppard. Practical limits of resolution in confocal and non-linear microscopy. *Microscopy Research and Technique*, 63(1):18–22, jan 2004.

[248] Imre Gáspár and János Szabad. In vivo analysis of MTbased vesicle transport by confocal reflection microscopy. *Cell motility and the cytoskeleton*, 66(2):68–79, 2009.

[249] Peter Sandin, Laurence W Fitzpatrick, Jeremy C Simpson, and Kenneth A Dawson. High-speed imaging of Rab family small GTPases reveals rare events in nanoparticle trafficking in living cells. *ACS nano*, 6(2):1513–21, feb 2012.

[250] E. Abbe. Beiträge zur Theorie des Mikroskops und der mikroskopischen Wahrnehmung. *Archiv für Mikroskopische Anatomie*, 9(1):413–418, dec 1873.

[251] Chang Soo Kim, Xiaoning Li, Ying Jiang, Bo Yan, Gulen Y. Tonga, Moumita Ray, David J. Solfiell, and Vincent M. Rotello. Cellular imaging of endosome entrapped small gold nanoparticles. *MethodsX*, 2:306–315, 2015.

[252] Anna Letizia Allegra Mascaro, Irene Costantini, Emilia Margoni, Giulio Iannello, Alessandro Bria, Leonardo Sacconi, and Francesco S. Pavone. Label-free near-infrared reflectance microscopy as a complimentary tool for two-photon fluorescence brain imaging. *Biomedical Optics Express*, 6(11):4483, nov 2015.

[253] Salvador González, Robert Sackstein, Rox Rox Anderson, and Milind Rajadhyaksha. Real-time evidence of In Vivo leukocyte trafficking in human skin by reflectance confocal microscopy. *Journal of Investigative Dermatology*, 117(2):384–386, 2001.

[254] Mark P S Dunphy, David Entenberg, Ricardo Toledo-Crow, and Steven M. Larson. In vivo microcartography and subcellular imaging of tumor angiogenesis: A novel platform for translational angiogenesis research. *Microvascular Research*, 78(1):51–56, 2009.

[255] Lord Rayleigh. On the Theory of Optical Images, with special reference to the Microscope. *Journal of the Royal Microscopical Society*, 23(4):474–482, aug 1903.

[256] M. E. Verdat. *Leçons d'optique physique*, volume Vol 1. L'Imprimierie Imperiale, Paris, 1869.

[257] M G Gustafsson. Surpassing the lateral resolution limit by a factor of two using structured illumination microscopy. *Journal of microscopy*, 198(Pt 2):82–7, may 2000.

[258] M a Neil, Rimas Juskaitis, and Tony Wilson. Method of obtaining optical sectioning by using structured light in a conventional microscope. *Optics letters*, 22(24):1905–1907, 1997.

[259] W Denk, J. Strickler, and W. Webb. Two-photon laser scanning fluorescence microscopy. *Science*, 248(4951):73–76, apr 1990.

[260] E Hesper Rego, Lin Shao, John J Macklin, Lukman Winoto, Göran A Johansson, Nicholas Kamps-Hughes, Michael W Davidson, and Mats G L Gustafsson. Nonlinear structured-illumination microscopy with a photoswitchable protein reveals cellular structures at 50-nm resolution. *Proceedings of the National Academy of Sciences of the United States of America*, 109(3):E135–43, jan 2012.

[261] Lothar Schermelleh, Peter M Carlton, Sebastian Haase, Lin Shao, Lukman Winoto, Peter Kner, Brian Burke, M Cristina Cardoso, David A Agard, Mats G L Gustafsson, Heinrich Leonhardt, and John W Sedat. Subdiffraction multicolor imaging of the nuclear periphery with 3D structured illumination microscopy. *Science (New York, N.Y.)*, 320(5881):1332–6, jun 2008.

[262] Krzysztof Patorski, Maciej Trusiak, and Tomasz Tkaczyk. Optically-sectioned two-shot structured illumination microscopy with Hilbert-Huang processing. *Optics Express*, 22(8):9517, apr 2014.

[263] Emily J. Guggenheim, Iseult Lynch, and Joshua Z. Rappoport. Imaging In focus: Reflected light imaging: Techniques and applications. *The International Journal of Biochemistry & Cell Biology*, 83:65–70, 2017.

[264] Pascal De Boer, Jacob P Hoogenboom, and Ben N G Giepmans. Correlated light and electron microscopy : ultrastructure lights up ! review. 12(6), 2015.

[265] Alexandra V. Agronskaia, Jack A. Valentijn, Linda F. van Driel, Chris T W M Schneijdenberg, Bruno M. Humbel, Paul M P van Bergen en Henegouwen, Arie J. Verkleij, Abraham J. Koster, and Hans C. Gerritsen. Integrated fluorescence and transmission electron microscopy. *Journal of Structural Biology*, 164(2):183–189, 2008.

[266] L. H P Hekking, M. N. Lebbink, D. A M De Winter, C. T W M Schneijdenberg, C. M. Brand, B. M. Humbel, A. J. Verkleij, and J. A. Post. Focused ion beam-scanning electron microscope: Exploring large volumes of atherosclerotic tissue. *Journal of Microscopy*, 235(3):336–347, sep 2009.

[267] J A Rhodin and H Fujita. Capillary growth in the mesentery of normal young rats. Intravital video and electron microscope analyses. *Journal of submicroscopic cytology and pathology*, 21(1):1–34, jan 1989.

[268] Clemens Tscheka, Marius Hittinger, Claus Michael Lehr, Nicole Schneider-Daum, and Marc Schneider. Macrophage uptake of cylindrical microparticles investigated with correlative microscopy. *European Journal of Pharmaceutics and Biopharmaceutics*, 95(Pt A):151–155, sep 2015.

[269] Y Kaneko and P Walther. Comparison of ultrastructure of germinating pea leaves prepared by high-pressure freezing-freeze substitution and conventional chemical fixation. *Journal of electron microscopy*, 44(2):104–109, apr 1995.

[270] Lucy Collinson Perrine Paul-Gilloteaux, Xavier Heiligenstein, Martin Belle, Marie-Charlotte Domart, Banafshe Larijani and Graça Raposo & Jean Salamero. eC-CLEM: flexible multidimensional registration software for correlative microscopies. *Nature methods*, 4(2):101–103, 2017.

[271] C J Sheppard, Min Gu, Keith Brain, and Hao Zhou. Influence of spherical aberration on axial imaging of confocal reflection microscopy. *Applied optics*, 33(4):616–624, 1994.

[272] S. A. Haider, A. Cameron, P. Siva, D. Lui, M. J. Shafiee, A. Boroomand, N. Haider, A. Wong, M. Monici, C. Vonesch, F. Aguet, P. J. Verveer, M. Gemkow, T. M. Jovin, M. Riffle, T. N. Davis, M. S. Robbins, B. J. Hadwen, A. Pizurica, W. Philips, I. Lemahieu, M. Acheroy, F. Luisier, C. Vonesch, T. Blu, M. Unser, U. Bal, A. Lanza, S. Morigi, F. Sgallari, Y.-W. Wen, P. Perona, J. Malik, J. Ling, A. C. Bovik, Y.-L. You, M. Kaveh, J. Rajan, K. Kannan, M. Kaimal, A. A. Bindilatti, N. D. Mascarenhas, A. Danielyan, Y.-W. Wu, P.-Y. Shih, Y. Dembitskaya, A. Semyanov, J. M. Sanches, J. C. Nascimento, J. S. Marques, J. W. Yoon, M. Shafiee, J. C. Waters, J. Boulanger, J. Salmon, Z. Harmany, C.-A. Deledalle, R. Willett, M. Makitalo, A. Foi, M. Makitalo, A. Foi, Y. Le Montagner, E. D. Angelini, J.-C. Olivo-Marin, Y. Boykov, O. Veksler, R. Zabih, P. Erdös, A. Rényi, F. Murtagh, J.-L. Starck, A. Bijaoui, B. Zhang, J. Zerubia, J.-C. Olivo-Marin, and R. Bernardes. Fluorescence microscopy image noise reduction using a stochastically-connected random field model. *Scientific Reports*, 6:20640, feb 2016.

[273] Denis Ferraretti, Luca Casarotti, Giacomo Gamberoni, and Evelina Lamma. Spot detection in images with noisy background. In *Lecture Notes in Computer Science (including subseries Lecture Notes in Artificial Intelligence and Lecture Notes in Bioinformatics)*, volume 6978 LNCS, pages 575–584. Springer Berlin Heidelberg, 2011.

[274] I Smal, M Loog, and W Niessen. Quantitative comparison of spot detection methods in fluorescence microscopy. *IEEE Transactions on*, 2010.

[275] Hsueh-Shih Chen, Julie Mazzolini, Jon Ayers, Josh Rappoport, Jamie Lead, and Jon Preece. Synthesis and characterization of nano ceria for biological applications. In Shin Won Kang, Seung-Han Park, Luke P. Lee, Ki-Bong Song, and Yo Han Choi, editors, *Proceedings of SPIE - The International Society for Optical Engineering*, volume 8879, page 887910, may 2013.

[276] Marc Daigneault, Julie A Preston, Helen M Marriott, Moira K B Whyte, and David H Dockrell. The identification of markers of macrophage differentiation in PMA-stimulated THP-1 cells and monocyte-derived macrophages. *PloS one*, 5(1):e8668, 2010.

[277] Alison Motley, Nicholas A. Bright, Matthew N J Seaman, and Margaret S. Robinson. Clathrin-mediated endocytosis in AP-2-depleted cells. *Journal of Cell Biology*, 162(5):909–918, sep 2003.

[278] Joshua Z Rappoport and Sanford M Simon. Endocytic trafficking of activated EGFR is AP-2 dependent and occurs through preformed clathrin spots. *Journal of cell science*, 122(Pt 9):1301–5, may 2009.

[279] Shreyasi Thakur, Diego I. Cattoni, and Marcelo Nöllmann. The fluorescence properties and binding mechanism of SYTOX green, a bright, low photo-damage DNA intercalating agent. *European Biophysics Journal*, 44(5):337–348, 2015.

[280] Jean Christophe Olivo-Marin. Extraction of spots in biological images using multiscale products. *Pattern Recognition*, 35(9):1989–1996, 2002.

[281] Harald F. Krug. Nanosafety research-are we on the right track?, 2014.

[282] Chunbai He, Yiping Hu, Lichen Yin, Cui Tang, and Chunhua Yin. Effects of particle size and surface charge on cellular uptake and biodistribution of polymeric nanoparticles. *Biomaterials*, 31(13):3657–3666, 2010.

[283] Li Shang, Karin Nienhaus, and Gerd Ulrich Nienhaus. Engineered nanoparticles interacting with cells: size matters. *Journal of nanobiotechnology*, 12:5, jan 2014.

[284] Murali M. Yallapu, Neeraj Chauhan, Shadi F. Othman, Vahid Khalilzad-Sharghi, Mara C. Ebeling, Sheema Khan, Meena Jaggi, and Subhash C. Chauhan. Implications of protein corona on physico-chemical and biological properties of magnetic nanoparticles. *Biomaterials*, 46:1–12, 2015.

[285] Marc Thill, Andrzej Kurylcio, Rebekka Welter, Viviana van Haasteren, Britta Grosse, Gilles Berclaz, Wojciech Polkowski, and Nik Hauser. The Central-European SentiMag study: Sentinel lymph node biopsy with superparamagnetic iron oxide (SPIO) vs. radioisotope. *Breast*, 23(2):175–179, 2014.

[286] Joost J Pouw, Muneer Ahmed, Bauke Anninga, Kimberley Schuurman, Sarah E Pinder, Mieke Van Hemelrijck, Quentin A Pankhurst, Michael Douek, and Bennie ten Haken. Comparison of three magnetic nanoparticle tracers for sentinel lymph node biopsy in an in vivo porcine model. *International Journal of Nanomedicine*, 10:1235–1243, 2015.

[287] Peter Reimer and Thomas Balzer. Ferucarbotran (Resovist): a new clinically approved RES-specific contrast agent for contrast-enhanced MRI of the liver: properties, clinical development, and applications. *European radiology*, 13(6):1266–1276, 2003.

[288] Dominic Docter, Ute Distler, Wiebke Storck, Jörg Kuharev, Desirée Wünsch, Angelina Hahlbrock, Shirley K Knauer, Stefan Tenzer, and Roland H Stauber. Quantitative profiling of the protein coronas that form around nanoparticles. 2014.

[289] Tommy Cedervall, Iseult Lynch, Martina Foy, Tord Berggård, Seamas C. Donnelly, Gerard Cagney, Sara Linse, and Kenneth A. Dawson. Detailed identification of plasma proteins adsorbed on copolymer nanoparticles. *Angewandte Chemie - International Edition*, 46(30):5754–5756, jul 2007.

[290] C. Kisielowski, B. Freitag, M. Bischoff, H Van Lin, S. Lazar, G. Knippels, P. Tiemeijer, M Van Der Stam, S Von Harrach, M. Stekelenburg, M. Haider, S. Uhlemann, H. Müller, P. Hartel, B. Kabius, D. Miller, I. Petrov, E A Olson, T. Donchev, E A Kenik, A R Lupini, J. Bentley, S J Pennycook, I M Anderson, A M Minor, A K Schmid, T. Duden, V. Radmilovic, Q M Ramasse, M. Watanabe, R. Erni, E A Stach, P. Denes, U. Dahmen, H Muller, P. Hartel, B. Kabius, D. Miller, I. Petrov, E A Olson, T. Donchev, E A Kenik, A R Lupini, J. Bentley, S J Pennycook, I M Anderson, A M Minor, A K Schmid, T. Duden, V. Radmilovic, Q M Ramasse, M. Watanabe, R. Erni, E A Stach, P. Denes, and U. Dahmen. Detection of single atoms and buried defects in three dimensions by aberration-corrected electron microscope with 0.5-A information limit. *Microscopy and microanalysis the official journal of Microscopy Society of America Microbeam Analysis Society Microscopical Society of Canada*, 14(5):469–477, oct 2008.

[291] Angela Ariza de Schellenberger, Harald Kratz, Tracy D Farr, Norbert L??wa, Ralf Hauptmann, Susanne Wagner, Matthias Taupitz, J??rg Schnorr, and Eyk A Schellenberger. Labeling of mesenchymal stem cells for MRI with single-cell sensitivity. *International Journal of Nanomedicine*, 11:1517–1535, 2016.

[292] Malvern Instruments. Dynamic Light Scattering: An Introduction in 30 Minutes. 2014.

[293] Nicolas De Jaeger, Hugo Demeyere, Robert Finsy, Rik Sneyers, Jan Vanderdeelen, Paul van der Meeren, and Marc van Laethem. Particle Sizing by Photon Correlation Spectroscopy Part I: Monodisperse latices: Influence of scattering angle and concentration of dispersed material. *Particle & Particle Systems Characterization*, 8(1-4):179–186, 1991.

[294] Gaurav Sharma, Vamsi Kodali, Matthew Gaffrey, Wei Wang, Kevin R. Minard, Norman J. Karin, Justin G. Teeguarden, and Brian D. Thrall. Iron oxide nanoparticle agglomeration influences dose rates and modulates oxidative stress-mediated dose-response profiles in vitro. *Nanotoxicology*, 8(6):663–75, sep 2014.

[295] Peter Wick, Pius Manser, Ludwig K. Limbach, Ursula Dettlaff-Weglikowska, Frank Krumeich, Siegmar Roth, Wendelin J. Stark, and Arie Bruinink. The degree and kind of agglomeration affect carbon nanotube cytotoxicity. *Toxicology Letters*, 168(2):121–131, 2007.

[296] Jingkun Jiang, Günter Oberdörster, and Pratim Biswas. Characterization of size, surface charge, and agglomeration state of nanoparticle dispersions for toxicological studies. *Journal of Nanoparticle Research*, 11(1):77–89, jan 2009.

[297] Daniel M Golovko, Tobias Henning, Jan S Bauer, Marcus Settles, Thomas Frenzel, Artur Mayerhofer, Ernst J Rummeny, and Heike E Daldrup-Link. Accelerated stem cell labeling with ferucarbotran and protamine. *European Radiology*, 20(3):640–648, mar 2010.

[298] Ninell P Mortensen, Gregory B Hurst, Wei Wang, Carmen M Foster, Prakash D Nallathamby, and Scott T Retterer. Dyanmic development of the protein corona on silica nanoparticles: composition and role in toxicity. *Nanoscale*, 5(14):6372–6380, jul 2013.

[299] Peter Satzer, Frantisek Svec, Gerhard Sekot, and Alois Jungbauer. Protein adsorption onto nanoparticles induces conformational changes: Particle size dependency, kinetics, and mechanisms. *Engineering in Life Sciences*, 16(3):238–246, apr 2016.

[300] Zhenyu Wang, Kai Zhang, Jian Zhao, Xiaoyun Liu, and Baoshan Xing. Adsorption and inhibition of butyrylcholinesterase by different engineered nanoparticles. *Chemosphere*, 79(1):86–92, 2010.

[301] Deepak K Sharma, Amit Choudhury, Raman Deep Singh, Christine L Wheatley, David L Marks, and Richard E Pagano. Glycosphingolipids internalized via caveolar-related endocytosis rapidly merge with the clathrin pathway in early endosomes and form microdomains for recycling. *The Journal of biological chemistry*, 278(9):7564–72, feb 2003.

[302] S Honary and F Zahir. Effect of Zeta Potential on the Properties of Nano-Drug Delivery Systems - A Review (Part 2). *Tropical Journal of Pharmaceutical Research*, 12(2), may 2013.

[303] Angeles Villanueva, Magdalena Cañete, Alejandro G Roca, Macarena Calero, Sabino Veintemillas-Verdaguer, Carlos J Serna, María Del Puerto Morales, and Rodolfo Miranda. The influence of surface functionalization on the enhanced internalization of magnetic nanoparticles in cancer cells. *Nanotechnology*, 20(11):115103, mar 2009.

[304] Fabio Sonvico, Stéphane Mornet, Sébastien Vasseur, Catherine Dubernet, Danielle Jaillard, Jeril Degrouard, Johan Hoebeke, Etienne Duguet, Paolo Colombo, and Patrick Couvreur. Folate-conjugated iron oxide nanoparticles for solid tumor targeting as potential specific magnetic hyperthermia mediators: Synthesis, physicochemical characterization, and in vitro experiments. *Bioconjugate Chemistry*, 16(5):1181–1188, sep 2005.

[305] Catherine Cecilia Berry, Stephen Wells, Stuart Charles, Gregor Aitchison, and Adam S G Curtis. Cell response to dextran-derivatised iron oxide nanoparticles post internalisation. 25:5405–5413, 2004.

[306] N.S. Remya, S. Syama, A. Sabareeswaran, and P.V. Mohanan. Toxicity, toxicokinetics and biodistribution of dextran stabilized Iron oxide Nanoparticles for biomedical applications. *International Journal of Pharmaceutics*, 511(1):586–598, 2016.

[307] Upasna Gaur, Sanjeeb Kumar Sahoo, Tapas K De, Prahlad C. Ghosh, Amarnath Maitra, and P. K. Ghosh. Biodistribution of fluoresceinated dextran using novel nanoparticles evading reticuloendothelial system. *International Journal of Pharmaceutics*, 202(1-2):1–10, 2000.

[308] Karl Mandel and Frank Hutter. The magnetic nanoparticle separation problem. pages 485–487, 2012.

[309] Cafer T Yavuz, J T Mayo, William W Yu, Arjun Prakash, Joshua C Falkner, Sujin Yean, Lili Cong, Heather J Shipley, Amy Kan, Mason Tomson, Douglas Natel-

son, and Vicki L Colvin. Low-field magnetic separation of monodisperse Fe3O4 nanocrystals. *Science*, 314(5801):964–967, 2006.

[310] Sigma-aldrich. Sigma - ProteoSilver Silver Stain Kit protocol. pages 2–5.

[311] Biji T. Kurien and R. Hal Scofield. Common artifacts and mistakes made in electrophoresis. *Methods in Molecular Biology*, 869:633–640, 2012.

[312] Thomas Marshall and Katherine M Williams. Artifacts associated with 2-mercaptoethanol upon high resolution two-dimensional electrophoresis. *Analytical Biochemistry*, 139(2):502–505, jun 1984.

[313] Jonathan H Shannahan, Xianyin Lai, Pu Chun Ke, Ramakrishna Podila, Jared M Brown, and Frank A Witzmann. Silver Nanoparticle Protein Corona Composition in Cell Culture Media. *PLoS ONE*, 8(9), 2013.

[314] Masoud Rahman, Sophie Laurent, Nancy Tawil, L'Hocine Yahia, and Morteza Mahmoudi. Nanoparticle and protein corona. *Protein-Nanoparticle Interactions*, 15:21–44, 2013.

[315] Morteza Mahmoudi, Mohammad A Shokrgozar, Soroush Sardari, Mojgan K Moghadam, Hojatollah Vali, Sophie Laurent, and Pieter Stroeve. Irreversible changes in protein conformation due to interaction with superparamagnetic iron oxide nanoparticles. *Nanoscale*, 3(3):1127–1138, 2011.

[316] Parisa Foroozandeh and Azlan Abdul Aziz. Merging worlds of nanomaterials and biological environment: factors governing protein corona formation on nanoparticles and its biological consequences. *Nanoscale research letters*, 10(1):221, 2015.

[317] Carl D Walkey, Jonathan B. Olsen, Fayi Song, Rong Liu, Hongbo Guo, D. Wesley H Olsen, Yoram Cohen, Andrew Emili, and Warren C W Chan. Protein corona fingerprinting predicts the cellular interaction of gold and silver nanoparticles. *ACS Nano*, 8(3):2439–2455, 2014.

[318] D. Docter, D. Westmeier, M. Markiewicz, S. Stolte, S. K. Knauer, and R. H. Stauber. The nanoparticle biomolecule corona: lessons learned - challenge accepted? *Chemical Society reviews*, 44(17):6094–121, 2015.

[319] Stefan Tenzer, Dominic Docter, Susanne Rosfa, Alexandra Wlodarski, Jörg Kuharev, Alexander Rekik, Shirley K Knauer, Christoph Bantz, Thomas Nawroth,

Carolin Bier, Jarinratn Sirirattanapan, Wolf Mann, Lennart Treuel, Reinhard Zellner, Michael Maskos, Hansjörg Schild, and Roland H Stauber. Nanoparticle size is a critical physicochemical determinant of the human blood plasma corona: A comprehensive quantitative proteomic analysis. *ACS Nano*, 5(9):7155–7167, 2011.

[320] David B. Warheit. How meaningful are the results of nanotoxicity studies in the absence of adequate material characterization? *Toxicological Sciences*, 101(2):183–185, feb 2008.

[321] David J Smith. Chapter 1. Characterization of Nanomaterials Using Transmission Electron Microscopy. *Nanocharacterisation*, (37):1–29, 2015.

[322] Emily J. Guggenheim, Abdullah Khan, Jeremy Pike, Lynne Chang, Iseult Lynch, and Joshua Z. Rappoport. Comparison of Confocal and Super-Resolution Reflectance Imaging of Metal Oxide Nanoparticles. *PLOS ONE*, 11(10):e0159980, oct 2016.

[323] J P Heath and G A Dunn. Cell to substratum contacts of chick fibroblasts and their relation to the microfilament system. A correlated interference-reflexion and high-voltage electron-microscope study. *Journal of cell science*, 29:197–212, feb 1978.

[324] Colin J. R. Sheppard, M GU, and M ROY. SIGNAL-TO-NOISE RATIO IN CONFOCAL MICROSCOPE SYSTEMS. *JOURNAL OF MICROSCOPY-OXFORD*, 168(Part 3):209–218, dec 1992.

[325] H. NYQUIST. Certain Topics in Telegraph Transmission Theory. *Transactions of the American Institute of Electrical Engineers*, 47(2):617–644, 1928.

[326] Claude E Shannon. Communication_in_the_Presence_of_Noise. *Proc IRE*, 3(2):1–11, 1998.

[327] Andrew K Dunn, Colin Smithpeter, Ashley J Welch, and Rebecca Richards-Kortum. Sources of contrast in confocal reflectance imaging. *Applied Optics*, 35(19):3441–3446, 1996.

[328] X. J. Liang, A. Q. Liu, C. S. Lim, T. C. Ayi, and P. H. Yap. Determining refractive index of single living cell using an integrated microchip. *Sensors and Actuators, A: Physical*, 133(2 SPEC. ISS.):349–354, 2007.

[329] John M Murray. Chapter 18 - Practical Aspects of Quantitative Confocal Microscopy. *Digital Microscopy*, 114(0):427–440, 2013.

[330] Alison J North. Seeing is believing? A beginners guide to practical pitfalls in image acquisition. *The Journal of cell biology*, 172(1):9–18, jan 2006.

[331] Amit Lal, Chunyan Shan, and Peng Xi. Structured illumination microscopy image reconstruction algorithm. *IEEE Journal of Selected Topics in Quantum Electronics*, PP(99):1–1, 2016.

[332] James W. Cooley and John W. Tukey. An Algorithm for Machine Calculation of Complex Fourier Series. *Mathematics of Computation*, 19(90):297–&, apr 1965.

[333] Phuoc Long Truong, Xingyi Ma, and Sang Jun Sim. Resonant Rayleigh light scattering of single Au nanoparticles with different sizes and shapes. *Nanoscale*, 6(4):2307–15, feb 2014.

[334] Takumi Sannomiya, Juliane Junesch, Prayanka Rajendran, K Tiranathanagul, A Leelahavanichkul, and S Eiam-Ong. Imaging, Spectroscopy and Sensing With Single and Coupled Metallic Nanoparticles. *Journal of Optics Research*, 15(1):73, 2013.

[335] B. A. Veksler, A. Lemelle, I. S. Kozhevnikov, G. G. Akchurin, and I. V. Meglinski. Improving image quality in reflection confocal microscopy involving gold nanoparticles and osmotically active immersion liquids. *Optics and Spectroscopy*, 110(3):483–488, mar 2011.

[336] Derron Bishop, Ivana Nikić, Mary Brinkoetter, Sharmon Knecht, Stephanie Potz, Martin Kerschensteiner, and Thomas Misgeld. Near-infrared branding efficiently correlates light and electron microscopy. *Nature methods*, 8(7):568–570, 2011.

[337] Andriy Myronenko and Xubo Song. Point set registration: coherent point drift. *IEEE transactions on pattern analysis and machine intelligence*, 32(12):2262–75, dec 2010.

[338] Aurélien Rizk, Grégory Paul, Pietro Incardona, Milica Bugarski, Maysam Mansouri, Axel Niemann, Urs Ziegler, Philipp Berger, and Ivo F Sbalzarini. Segmentation and quantification of subcellular structures in fluorescence microscopy images using Squassh. *Nature protocols*, 9(3):586–96, feb 2014.

[339] J. B. MacQueen. *Some Methods for classification and Analysis of Multivariate Observations*. University of California Press, 1967.

[340] S. P. Lloyd. Least square quantization in PCM. *Bell Telephone Laboratories Paper*, 1957.

[341] H. Digabel and C. Lantuejoul. Iterative Algorithms. *Proceedings of the 2nd European Symposium Quantitative Analysis of Microstructures in Material Science*, pages 85–89, 1978.

[342] Dagmar A Kuhn, Dimitri Vanhecke, Benjamin Michen, Fabian Blank, Peter Gehr, Alke Petri-Fink, and Barbara Rothen-Rutishauser. Different endocytotic uptake mechanisms for nanoparticles in epithelial cells and macrophages. *Beilstein journal of nanotechnology*, 5(1):1625–36, jan 2014.

[343] Chung Yi Yang, Ming Fong Tai, Chih Peng Lin, Chen Wen Lu, Jaw Lin Wang, Jong Kai Hsiao, and Hon Man Liu. Mechanism of cellular uptake and impact of ferucarbotran on macrophage physiology. *PLoS ONE*, 6(9):e25524, sep 2011.

[344] Lars Matuszewski, Thorsten Persigehl, Alexander Wall, Wolfram Schwindt, Bernd Tombach, Manfred Fobker, Christopher Poremba, Wolfgang Ebert, Walter Heindel, and Christoph Bremer. Cell tagging with clinically approved iron oxides: feasibility and effect of lipofection, particle size, and surface coating on labeling efficiency. *Radiology*, 235(1):155–161, apr 2005.

[345] H E Daldrup-Link, M Rudelius, R a Oostendorp, M Settles, G Piontek, S Metz, H Rosenbrock, U Keller, U Heinzmann, E J Rummeny, J Schlegel, and T M Link. Targeting of hematopoietic progenitor cells with MR contrast agents. *Radiology*, 228(3):760–767, 2003.

[346] Francesco Cardarelli, Luca Digiacomo, Cristina Marchini, Augusto Amici, Fabrizio Salomone, Giuseppe Fiume, Alessandro Rossetta, Enrico Gratton, Daniela Pozzi, and Giulio Caracciolo. The intracellular trafficking mechanism of Lipofectamine-based transfection reagents and its implication for gene delivery. *Scientific reports*, 6(April):25879, may 2016.

[347] S. Bolte and F. P. Cordelieres. A guided tour into subcellular colocalisation analysis in light microscopy. *Journal of Microscopy*, 224(3):13–232, 2006.

[348] Jeremy A Pike, Iain B Styles, Joshua Z Rappoport, and John K Heath. Quantifying receptor trafficking and colocalization with confocal microscopy. *Methods*, 2017.

[349] Keiran S M Smalley, Mercedes Lioni, and Meenhard Herlyn. Life isn't flat: taking cancer biology to the next dimension. *In vitro cellular & developmental biology. Animal*, 42(8-9):242–247, 2006.

[350] Bella B. Manshian, Sebastian Munck, Patrizia Agostinis, Uwe Himmelreich, Stefaan J. Soenen, S. F. Hansen, A. Maynard, A. Baun, J. A. Tickner, E. C. Cho, Q. Zhang, Y. N. Xia, J. A. Kim, C. Aberg, A. Salvati, K. A. Dawson, A. M. Alkilany, C. J. Murphy, C. Medina, M. J. Santos-Martinez, A. Radomski, O. I. Corrigan, M. W. Radomski, L. Braydich-Stolle, S. Hussain, J. J. Schlager, M. C. Hofmann, J. C. Lai, I. Lynch, A. Salvati, K. A. Dawson, K. Peynshaert, C. D. Walkey, B. B. Manshian, I. Y. Kim, E. Joachim, H. Choi, K. Kim, G. Maiorano, D. Yoon, P. Rivera Gil, G. Oberdorster, A. Elder, V. Puntes, W. J. Parak, K. J. Ong, W. Lin, Y. W. Huang, X. D. Zhou, Y. Ma, S. Liu, L. Xu, T. Zhang, G. Ren, Z. Yang., S. J. Soenen, J. Rejman, W. J. Parak, B. Manshian, K. K. Comfort, E. I. Maurer, L. K. Braydich-Stolle, S. M. Hussain, M. Nazarenus, D. Docter, M. Lundqvist, C. Rocker, M. Potzl, F. Zhang, W. J. Parak, G. U. Nienhaus, M. Mahmoudi, M. Mahmoudi, M. Turabekova, S. J. Soenen, J. Demeester, S. C. De Smedt, K. Braeckmans, E. Chang, N. Thekkek, W. W. Yu, V. L. Colvin, R. Drezek, Ketkar-Atre, H. D. Summers, A. Nel, T. Xia, L. Madler, N. Li, F. T. Andon, B. Fadeel, Y. H. Luo, C. W. Lin, M. S. Jan, J. H. Kuo, J. Liu, D. J. Brayden, S. A. Cryan, K. A. Dawson, P. J. O'Brien, J. C. Simpson, S. Singh, A. E. Carpenter, A. Genovesio, C. Kirchner, S. J. Soenen, A. M. Derfus, W. C. W. Chan, S. N. Bhatia, F. Gagné, D. Maysinger, C. André, C. Blaise, M. Mahmoudi, J. Xue, P. Mishra, D. C. Chan, Z. Yang, J. J. Goronzy, C. M. Weyand, D. Liu, M. Gao, Y. Yang, Y. U. Qi, K. Wu, S. Zhao, Q. W. Wang, and H. Pi. High content analysis at single cell level identifies different cellular responses dependent on nanomaterial concentrations. *Scientific Reports*, 5:13890, sep 2015.

[351] Dong Ming Huang, Jong Kai Hsiao, Ying Chun Chen, Li Ying Chien, Ming Yao, Yin Kai Chen, Bor Sheng Ko, Szu Chun Hsu, Lin Ai Tai, Hui Ying Cheng, Shih Wei Wang, Chung Shi Yang, and Yao Chang Chen. The promotion of human mesenchymal stem cell proliferation by superparamagnetic iron oxide nanoparticles. *Biomaterials*, 30(22):3645–3651, 2009.

[352] H A Jeng and J Swanson. Toxicity of metal oxide nanoparticles in mammalian cells. *Journal of Environmental Science and Health Part a-Toxic/Hazardous Substances & Environmental Engineering*, 41(12):2699–2711, dec 2006.

[353] Saba Naqvi, Mohammad Samim, M. Z. Abdin, Farhan Jalees Ahmed, A. N. Maitra, C. K. Prashant, and Amit K. Dinda. Concentration-dependent toxicity of iron oxide nanoparticles mediated by increased oxidative stress. *International Journal of Nanomedicine*, 5(1):983–989, 2010.

[354] Heinz Mueller. Therapeutic nanoparticles in clinics and under clinical evaluation R eview. pages 449–467.

[355] Xinying Wu, Yanbin Tan, Hui Mao, and Minming Zhang. Toxic effects of iron oxide nanoparticles on human umbilical vein endothelial cells. *International Journal of Nanomedicine*, 5(1):385–399, 2010.

[356] Karin Müller, Jeremy N Skepper, Mihaly Posfai, Rikin Trivedi, Simon Howarth, Claire Corot, Eric Lancelot, Paul W Thompson, Andrew P Brown, and Jonathan H Gillard. Effect of ultrasmall superparamagnetic iron oxide nanoparticles (Ferumoxtran-10) on human monocyte-macrophages in vitro. *Biomaterials*, 28(9):1629–1642, mar 2007.

[357] Brian S Cummings, Lauren P Wills, and Rick G. Schnellmann. Measurement of Cell Death in Mammalian Cells. *Curr Protoc Phamacol*, 1(Lemasters 1999):1–30, sep 2004.

[358] Bruce L Roth, Martin Poot, Stephen T Yue, and Paul J Millard. Bacterial viability and antibiotic susceptibility testing with SYTOX green nucleic acid stain. *Applied and Environmental Microbiology*, 63(6):2421–2431, jun 1997.

[359] M.A. Lacaille-Dubois and H. Wagner. A review of the biological and pharmacological activities of saponins. *Phytomedicine*, 2(4):363–386, mar 1996.

[360] Kimberly J. Ong, Tyson J. MacCormack, Rhett J. Clark, James D. Ede, Van A. Ortega, Lindsey C. Felix, Michael K M Dang, Guibin Ma, Hicham Fenniri, Jonathan G C Veinot, and Greg G. Goss. Widespread nanoparticle-assay interference: Implications for nanotoxicity testing. *PLoS ONE*, 9(3):e90650, mar 2014.

[361] Alessandra Spano, Sergio Barni, Vittorio Bertone, Luigi Sciola, Scienze Biomediche, and Università Sassari. Changes on lysosomal compartment during PMA-induced differentiation of THP-1 monocytic cells : Influence of type I and type IV collagens. *Advances in Bioscience and Biotechnology*, 2013(August):8–18, 2013.

[362] Helinor J Johnston, Manuela Semmler-Behnke, David M Brown, Wolfgang Kreyling, Lang Tran, and Vicki Stone. Evaluating the uptake and intracellular fate of polystyrene nanoparticles by primary and hepatocyte cell lines in vitro. *Toxicology and Applied Pharmacology*, 242(1):66–78, jan 2010.

[363] Jade Dungao Trono, Kazue Mizuno, Noritaka Yusa, Takehisa Matsukawa, Kazuhito Yokoyama, and Mitsuru Uesaka. Size, concentration and incubation time dependence of gold nanoparticle uptake into pancreas cancer cells and its future application to X-Ray Drug Delivery System. *Journal of radiation research*, 52(1):103–109, 2011.

[364] Adny H. Silva, Enio Lima, Marcelo Vasquez Mansilla, Roberto D. Zysler, Horacio Troiani, Mary Luz Mojica Pisciotti, Claudriana Locatelli, Juan C. Benech, Natalia Oddone, Vinícius C. Zoldan, Evelyn Winter, André A. Pasa, and Tânia B. Creczynski-Pasa. Superparamagnetic iron-oxide nanoparticles mPEG350- and mPEG2000-coated: Cell uptake and biocompatibility evaluation. *Nanomedicine: Nanotechnology, Biology, and Medicine*, 12(4):909–919, 2016.

[365] L B Thomsen, T Linemann, K M Pondman, J Lichota, K S Kim, R J Pieters, G. M. Visser, and T Moos. Uptake and transport of superparamagnetic iron oxide nanoparticles through human brain capillary endothelial cells. *ACS Chemical Neuroscience*, 4(10):1352–1360, 2013.

[366] Isabelle Raynal, Philippe Prigent, Sophie Peyramaure, Abderrahim Najid, Cécile Rebuzzi, and Claire Corot. Macrophage endocytosis of superparamagnetic iron oxide nanoparticles: mechanisms and comparison of ferumoxides and ferumoxtran-10. *Invest Radiol*, 39(1):56–63, jan 2004.

[367] Jong Ah Kim, Christoffer Åberg, Anna Salvati, and Kenneth A Dawson. Role of cell cycle on the cellular uptake and dilution of nanoparticles in a cell population. 2012.

[368] Ivanov. *Exocitosis and Endocytosis*, volume 440. 2008.

[369] Dries Vercauteren, Roosmarijn E Vandenbroucke, Arwyn T Jones, Joanna Rejman, Joseph Demeester, Stefaan C De Smedt, Niek N Sanders, and Kevin Braeckmans. The use of inhibitors to study endocytic pathways of gene carriers: optimization and pitfalls. *Molecular therapy : the journal of the American Society of Gene Therapy*, 18(3):561–569, 2010.

[370] Lei Li, Tao Wan, Min Wan, Bei Liu, Ran Cheng, and Rongying Zhang. The effect of the size of fluorescent dextran on its endocytic pathway. *Cell Biology International*, 39(5):531–539, may 2015.

[371] Oleg Lunov, Vitalii Zablotskii, Tatiana Syrovets, Carlheinz Röcker, Kyrylo Tron, G Ulrich Nienhaus, and Thomas Simmet. Modeling receptor-mediated endocytosis

of polymer-functionalized iron oxide nanoparticles by human macrophages. *Biomaterials*, 32(2):547–555, 2011.

[372] S Matveev, D R van der Westhuyzen, and Eric J Smart. Co-expression of scavenger receptor-BI and caveolin-1 is associated with enhanced selective cholesteryl ester uptake in THP-1 macrophages. *Journal of lipid research*, 40(9):1647–54, sep 1999.

[373] Peter Gargalovic and Ladislav Dory. Caveolin-1 and caveolin-2 expression in mouse macrophages: High density lipoprotein 3-stimulated secretion and a lack of significant subcellular co-localization. *Journal of Biological Chemistry*, 276(28):26164–26170, jul 2001.

[374] C J Fielding and Phoebe E Fielding. Intracellular cholesterol transport. *Journal of lipid research*, 38(8):1503–21, aug 1997.

[375] Haifei Xu, Wei Dai, Yehua Han, Wei Hao, Fei Xiong, Yu Zhang, and Ji-Min Cao. Differential internalization of superparamagnetic iron oxide nanoparticles in different types of cells. *Journal of nanoscience and nanotechnology*, 10(11):7406–7410, nov 2010.

[376] Thomas Schlorf, Manuela Meincke, Elke Kossel, C C C Gluer, Olav Jansen, and Rolf Mentlein. Biological Properties of Iron Oxide Nanoparticles for Cellular and Molecular Magnetic Resonance Imaging. *International Journal of Molecular Sciences*, 12(1):12–23, dec 2011.

[377] Leshuai W Zhang and Nancy A. Monteiro-Riviere. Mechanisms of quantum dot nanoparticle cellular uptake. *Toxicological Sciences*, 110(1):138–155, 2009.

[378] Evelina Miele, Gian Paolo Spinelli, Ermanno Miele, Federica Tomao, and Silverio Tomao. Albumin-bound formulation of paclitaxel (Abraxane® ABI-007) in the treatment of breast cancer. *International Journal of Nanomedicine*, 4:99–105, 2009.

[379] J E Fox and David R. Phillips. Inhibition of actin polymerization in blood platelets by cytochalasins. *Nature*, 292(5824):650–2, aug 1981.

[380] C. Lamaze, L. M. Fujimoto, H. L. Yin, and S. L. Schmid. The Actin Cytoskeleton Is Required for Receptor-mediated Endocytosis in Mammalian Cells. *Journal of Biological Chemistry*, 272(33):20332–20335, aug 1997.

[381] Stephanie E A Gratton, Patricia A Ropp, Patrick D Pohlhaus, J Christopher Luft, Victoria J Madden, Mary E Napier, and Joseph M DeSimone. The effect of particle design on cellular internalization pathways. *Proceedings of the National Academy of Sciences of the United States of America*, 105(33):11613–8, aug 2008.

[382] C Wilhelm, C Billotey, J Roger, J N Pons, J. C. Bacri, and F Gazeau. Intracellular uptake of anionic superparamagnetic nanoparticles as a function of their surface coating. *Biomaterials*, 24(6):1001–1011, 2003.

[383] Brad Larson. 3D Cell Culture: A Review of Current Techniques, 2015.

[384] Yukie Yoshii, Atsuo Waki, Kaori Yoshida, Anna Kakezuka, Maki Kobayashi, Hideo Namiki, Yusei Kuroda, Yasushi Kiyono, Hiroshi Yoshii, Takako Furukawa, Tatsuya Asai, Hidehiko Okazawa, Juri G Gelovani, and Yasuhisa Fujibayashi. The use of nanoimprinted scaffolds as 3D culture models to facilitate spontaneous tumor cell migration and well-regulated spheroid formation. *Biomaterials*, 32(26):6052–6058, 2011.

[385] Keyang Huang, Huili Ma, Juan Liu, Shuaidong Huo, Anil Kumar, Tuo Wei, Xu Zhang, Shubin Jin, Yaling Gan, Paul C Wang, Shengtai He, Xiaoning Zhang, and Xing Jie Liang. Size-dependent localization and penetration of ultrasmall gold nanoparticles in cancer cells, multicellular spheroids, and tumors in vivo. *ACS Nano*, 6(5):4483–4493, 2012.

[386] Nicole S. Bryce, Binh T. T. Pham, Nicole W. S. Fong, Nirmesh Jain, Eh Hau Pan, Renee M. Whan, Trevor W. Hambley, and Brian S. Hawkett. The composition and end-group functionality of sterically stabilized nanoparticles enhances the effectiveness of co-administered cytotoxins. *Biomater. Sci.*, 1(12):1260–1272, aug 2013.

[387] Rainer Tietze, Stefan Lyer, Stephan Dürr, and Christoph Alexiou. Nanoparticles for cancer therapy using magnetic forces. *Nanomedicine*, 7(3):447–457, mar 2012.

[388] Don N Ho, Nathan Kohler, Aruna Sigdel, Raghu Kalluri, Jeffrey R Morgan, Chenjie Xu, and Shouheng Sun. Penetration of endothelial cell coated multicellular tumor spheroids by iron oxide nanoparticles. *Theranostics*, 2(1):66–75, 2012.

[389] Lennart Treuel, Xiue Jiang, and Gerd Ulrich Nienhaus. New views on cellular uptake and trafficking of manufactured nanoparticles. *Journal of The Royal Society Interface*, 10(82), 2013.

[390] Larissa V. Stebounova, Ethan Guio, and Vicki H. Grassian. Silver nanoparticles in simulated biological media: A study of aggregation, sedimentation, and dissolution. *Journal of Nanoparticle Research*, 13(1):233–244, jan 2011.

[391] Superb K. Misra, Agnieszka Dybowska, Deborah Berhanu, Samuel N. Luoma, and Eugenia Valsami-Jones. The complexity of nanoparticle dissolution and its importance in nanotoxicological studies. *Science of the Total Environment*, 438:225–232, nov 2012.

[392] Cecilia Bucci, Robert G. Parton, Ian H. Mather, Henk Stunnenberg, Kai Simons, Bernard Hoflack, and Marino Zerial. The small GTPase rab5 functions as a regulatory factor in the early endocytic pathway. *Cell*, 70(5):715–728, sep 1992.

[393] Yan Feng, Barry Press, and Angela Wandinger-Ness. Rab 7: An important regulator of late endocytic membrane traffic. *Journal of Cell Biology*, 131(6 I):1435–1452, dec 1995.

[394] Oliver Ullrich, Sigrid Reinsch, Sylvie Urbé, Marino Zerial, and Robert G Parton. Rab11 regulates recycling through the pericentriolar recycling endosome. *Journal of Cell Biology*, 135(4):913–924, nov 1996.

[395] K. W. Dunn, M. M. Kamocka, and J. H. McDonald. A practical guide to evaluating colocalization in biological microscopy. *AJP: Cell Physiology*, 300(4):C723–C742, jan 2011.

[396] Thibault Lagache, Vannary Meas-Yedid, and Jean Christophe Olivo-Marin. A statistical analysis of spatial colocalization using Ripley's K function. In *Proceedings - International Symposium on Biomedical Imaging*, number 1, pages 896–901, 2013.

[397] Melike Lakadamyali, Michael J Rust, and Xiaowei Zhuang. Ligands for clathrin-mediated endocytosis are differentially sorted into distinct populations of early endosomes. *Cell*, 124(5):997–1009, mar 2006.

[398] Tsai-Hua Chung, Jong-Kai Hsiao, Ming Yao, Szu-Chun Hsu, Hon-Man Liu, and Dong-Ming Huang. Ferucarbotran, a carboxydextran-coated superparamagnetic iron oxide nanoparticle, induces endosomal recycling, contributing to cellular and exosomal EGFR overexpression for cancer therapy. *RSC Advances*, 5:89932–89939, 2015.

[399] Chung Yi Yang, Ming Fong Tai, Chih Peng Lin, Chen Wen Lu, Jaw Lin Wang, Jong Kai Hsiao, and Hon Man Liu. Mechanism of cellular uptake and impact of ferucarbotran on macrophage physiology. *PLoS ONE*, 6(9):e25524, 2011.

[400] C Bucci, P Thomsen, P Nicoziani, J McCarthy, and B van Deurs. Rab7: a key to lysosome biogenesis. *Molecular biology of the cell*, 11(2):467–80, feb 2000.

[401] Phillip A Vanlandingham and Brian P Ceresa. Rab7 regulates late endocytic trafficking downstream of multivesicular body biogenesis and cargo sequestration. *Journal of Biological Chemistry*, 284(18):12110–12124, 2009.

[402] Adam P. Rofe and Paul R. Pryor. Purification of lysosomes using supraparamagnetic iron oxide nanoparticles (SPIONs). *Cold Spring Harbor Protocols*, 2016(4):338–342, apr 2016.

[403] Mathew W. Walker and Emyr Lloyd-Evans. A rapid method for the preparation of ultrapure, functional lysosomes using functionalized superparamagnetic iron oxide nanoparticles. *Methods in Cell Biology*, 126:21–43, 2015.

[404] Yang Li, Wen Zhang, Junfeng Niu, and Yongsheng Chen. Surface-coating-dependent dissolution, aggregation, and reactive oxygen species (ROS) generation of silver nanoparticles under different irradiation conditions. *Environmental Science and Technology*, 47(18):10293–10301, sep 2013.

[405] Mariagrazia Di Marco, Claudia Sadun, Marc Port, Irene Guilbert, Patrick Couvreur, and Catherine Dubernet. Physicochemical characterization of ultrasmall superparamagnetic iron oxide particles (USPIO) for biomedical application as MRI contrast agents, 2007.

[406] Arno Max Basedow, Klaus Heinrich Ebert, and Hanns Josef Ederer. Kinetic Studies on the Acid Hydrolysis of Dextran. *Macromolecules*, 11(4):774–781, 1978.

[407] Barry Park, Kenneth Donaldson, Rodger Duffin, Lang Tran, Frank Kelly, Ian Mudway, Jean-Paul Morin, Robert Guest, Peter Jenkinson, Zissis Samaras, Myrsini Giannouli, Haris Kouridis, and Patricia Martin. Hazard and risk assessment of a nanoparticulate cerium oxide-based diesel fuel additive - a case study. *Inhalation toxicology*, 20(6):547–66, apr 2008.

[408] Frank Alexis, Eric M. Pridgen, Robert Langer, and Omid C. Farokhzad. Nanoparticle technologies for cancer therapy, 2010.

[409] Ruth Duncan and Rogerio Gaspar. Nanomedicine(s) under the microscope, 2011.

[410] Vincent J Venditto and Francis C Szoka. Cancer nanomedicines: So many papers and so few drugs!, 2013.

[411] Richard M. Langford. Focused ion beams techniques for nanomaterials characterization, jul 2006.

[412] Winfried Denk and Heinz Horstmann. Serial block-face scanning electron microscopy to reconstruct three-dimensional tissue nanostructure. *PLoS Biology*, 2(11):e329, nov 2004.

[413] M Rajadhyaksha, M Grossman, D Esterowitz, R H Webb, and R R Anderson. In vivo confocal scanning laser microscopy of human skin: melanin provides strong contrast. *The Journal of investigative dermatology*, 104(6):946–52, jun 1995.

[414] Piergiacomo Calzavara-Pinton, Caterina Longo, Marina Venturini, Raffaella Sala, and Giovanni Pellacani. Reflectance confocal microscopy for in vivo skin imaging, nov 2008.

[415] C J Koester, J D Auran, H D Rosskothen, G J Florakis, and R B Tackaberry. Clinical microscopy of the cornea utilizing optical sectioning and a high-numerical-aperture objective. *Journal of the Optical Society of America. A, Optics and image science*, 10(7):1670–9, jul 1993.

[416] Yuzhen Lu, Richard Li, and Renfu Lu. Structured-illumination reflectance imaging (SIRI) for enhanced detection of fresh bruises in apples. *Postharvest Biology and Technology*, 117:89–93, 2016.

[417] Tomasz Tkaczyk, Mohammed Rahman, Vivian Mack, Konstantin Sokolov, Jeremy Rogers, Rebecca Richards-Kortum, and Michael Descour. High resolution, molecular-specific, reflectance imaging in optically dense tissue phantoms with structured-illumination. *Optics express*, 12(16):3745–3758, aug 2004.

[418] Marcel Müller, Viola Mönkemöller, Simon Hennig, Wolfgang Hübner, and Thomas Huser. Open-source image reconstruction of super-resolution structured illumination microscopy data in ImageJ. *Nature Communications*, 7:10980, mar 2016.

Appendices

APPENDIX A

Published papers

Emily J Guggenheim, Iseult Lynch, Joshua Z. Rappoport. *Imaging in focus: Reflected light imaging: Techniques and applications.* The international journal of biochemistry & cell biology. 2016.

Emily J Guggenheim, Abdullah Khan, Jeremy Pike, Lynne Change, Iseult Lynch, Joshua Z. Rappoport. *Confocal and super-resolution reflectance imaging of metal oxide nanoparticles inside cells.* PloSONE. 2016.

Julie Mazzolini, Ralf Weber, Hseuh-Shih Chen, Abdullah Khan, **Emily J Guggenheim**, Robert Shaw, James Chipman, Mark Viant, Joshua Z. Rappoport. *Protein corona modulates uptake and toxicity of nanoceria via clathrin mediated endocytosis.* The Biological Bulletin, (Issue TBC). 2016.

APPENDIX B

B.1 Methods

B.1.1 Bacterial transformation

1 µL of the required cDNA construct was added to 50 µL MAX efficiency Escherichia Coli (E.Coli) DH5α competent bacterial cells (Invitrogen, UK) and kept on ice for 30 mins. DH5α were then heat shocked at 42°C for 45 seconds, followed by incubation on ice for a further 2 mins. SOC (Super Optimal broth with Catabolic repression) media 500 µL was then added, and the E.Coli incubated at 37°C in a shaking incubator for 1.5 hours. E.Coli (125 µL) were then spread onto agar plates containing Kanamycin (Kan) or Ampicillin (Amp), dependant on specific resistance, using a disposable plastic spreader under sterile conditions. Plates were then inverted and incubated overnight at 37°C. On the following day, a single colony was picked with a pipette tip and added to 2 mL Lutria Broth (LB) containing Kan (50 µl /mL) or AMP (100 µg/mL) in 14 mL snap cap round bottom tubes (Falcon, UK) and incubated at 37℃ for 8 hours in a shaking incubator. 200 µL of the bacteria was then added to 100 mL of antibiotic containing LB in a suitable container and incubated for 12-16 hours at 37°C in a shaking incubator. Bacteria were centrifuged at 5000 rpm at 4°C in 50 mL plastic centrifuge tubes (Falcon, UK) using a bench-top centrifuge (3K10 Centrifuge, Sigma, UK). The pellet was then dried and lysed immediately for purification with a Qiagen Plasmid Maxi-Prep Kit (Qiagen, UK) as per

the manufacturers protocol. Eluted DNA was dissolved in 1 mL endotoxin-free ultrapure water and stored at -20°C. DNA concentration was ascertained using a U1800 model spectrophotometer (Digilab Hitachi) prior to DNA transfections.

B.1.2 Dissolution studies

Full composition of artificial lysosomal fluid is listed in B.1.

Table B.1: Composition of artificial lysosomal fluid solution

Artificial lysosomal fluid
NaCl (3.210 g), NaOH (6.000 g), citric acid (20.800 g), CaCl2 (0.097 g), NaH2PO4_7H2O (0.179 g), NaSO4 (0.039 g), MgCl2_6H2O (0.106 g), glycerine (0.059 g), sodium citrate dehydrate (0.077 g), sodium tartrate dehydrate (0.090 g), sodium lactate (0.085 g), sodium pyruvate (0.086 g), formaldehyde (1.000 mL).

B.1.3 Western Blot Buffers and Protocol

Buffers

Lysis buffer - 1% Triton X

Triton X (10%) (Sigma-Aldridge, UK) solution was made. This was made by addition of 100 µL TritonX100 solution to 9ml of PBS, addition of a roche protease inhibitor and vortexing thoroughly.

To make up 50mL of 12.5% solution of acrylamide gel, the following was combined. dH_20, (16.1mL); Tris HCl (12.5 mL); 10% SDS (0.5 mL) and Bis Acrylamide (20.8 mL). Just prior to gel setting, APS (0.5 mL)and TEMED (0.075 mL) were added to solidify the gel.

0.5M pH Tris-HCL 60.57g of Tris (Fisher Scientific) dissolved in 1L distilled water. 5M HCl was used to obtain the correct pH using a Basic Denver pH meter (Denver Instru-

ments).

Ammonium Persulphate 10% Ammonium Persulphate (APS): 1 g of APS was dissolved in 10 mL dH_2O frozen in 1 mL aliquots.

10% SDS

10% Sodium Dodecyl Sulphate (SDS) was made up by dissolving 10 g of SDS in 100 mL of dH_2O.

10X running buffer

10X Running buffer was made with 144 g of Glycine (Fisher Scientific), 30g Tris, 4g SDS made up to 1L in dH_2O.

1X running buffer

1X running buffer was made by diluting 100ml of 10X Running buffer in of 900 mL of dH_2O.

10X transfer buffer

10X Running buffer was made with 144 g of Glycine (Fisher Scientific), 30g Tris, made up to 1L in dH_2O.

1X transfer buffer

1X running buffer was made by diluting 100ml of 10X transfer buffer in of 900 mL of dH_2O.

10X TBS

200 mL of 1M Tris-HCl (pH 7.5), 300 mL of 5M NaCl made upto 1L in dH_2O - 5M HCl was used to obtain the correct pH.

5M NaCl

292.2g NaCl (Fisher Scientific, UK) dissolved dH_2O.

TBST

1X TBST buffer was made by diluting 100 mL of 10X TBS with 900 mL dH_2O with 1 mL of Tween20 (Sigma-Aldridge, UK). In order to pipette Tween20,a P1000 pipette tip was used with the end cut off. The remnants of Tween20 were removed from the tip by ejecting the tip into the solution after addition.

Marvil solution

To make up the 5% marvil solution, 10g Marvil skimmed milk powder was dissolved in 200 mL 1XTBST.

Sample buffer 3X

Tris (1M, pH 6.8, 8.8 mL;Fisher Scientific) was combined with 6g SDS, 15 mL βmercaptoethanol (Sigma-Aldridge, UK), 30mL Glycerol with 100 mL hdH_2O. Bromophenol blue was added and sample buffer mixed thoroughly.

Western blot protocol

Western blots were performed using the Mini-Protean Tetra Electrophoresis System (Bio-Rad). All buffers and solutions were made as described above. Prior to use, all equipment, including combs, glass plates and mini-glass plates were washed with ethanol (70%). The plates were inserted into the holder and placed in a casting frame (BioRad). Resolving gel (12.5%) was pipetted into the cassette, ethanol was poured on top to ensure the gel

set level, and then it was left to set for 15 minutes. Excess ethanol was blotted off using blotting paper, then, approximately 4 mL of the stacking gel was added on top of the set resolving gel, and the comb was inserted into the gel. This was left to set for 20 minutes. Then the gel cassette was placed inside the electrode chamber, with the wells facing inward, and placed inside the gel running tank. The tank, and the inside of the chamber was then filled with running buffer to the 2 gel or 4 gel line. In the first lane, 15 µL of ColorbandPlus protein ladder was added. Then 20 µL of sample was added to each lane in the gel. The gels were then run at 180V for approximately 90 minutes using a power pack (PowerPack Basic Supply - BioRad). Once the dye reached the bottom of the gel, the electrical current was removed and the gels taken from the cassette The stack was then removed. Gels were then set up to for transfer to PVDF membrane. The PVDF membrane was first activated in a weighing boat using 100 methanol. The transfer sandwich was then stacked as follows: Cassette clear plastic side down, sponge, 2x filter paper, PVDF membrane, gel, 2x filter paper, and a sponge. A stripette was used to flatten the sandwich prior to closing to remove any air bubbles. The casette was placed in the transfer container and ice cold transfer buffer added to the 4 gel line in the tank. The gel was then transferred for 90 minutes at 400mA. Following transfer, the membranes were removed and blocked in 5% milk solution (20 mL). Membranes were then probed overnight at 4_oC with the specific primary antibody. Membranes were then washed 4x with TBST, and probed with the secondary antibody. Following secondary antibody, the membranes were blotted dry and imaged using the odysea IR-detection system.

Corona isolation

NP protein corona was isolated using a centrifugation protocol. First NP were incubated with SCM, PBS or C-SCM. Following incubation, solutions were centrifuged for 20 minutes at 4 °C at 15,3000g. The supernatant was aspirated and the pellet resuspended in 1 mL of PBS. This procedure was repeated 3 more times. Following the final pellet, 100 µl

SDS sample buffer was added. Samples were then heated for 5 mins at 95 °C to denture the proteins and remove them from the NP surface. The NPs were then pelleted by a final centrifugation of 15 minutes at RT and 15,300 g. The supernatant was transferred to a new tube and stored at -20 until the gel was run.

B.1.4 Correlative Image Acquisition

Images were taken on a Nikon A1R inverted confocal microscope (Nikon Corp, Japan). To set up the reflectance optical configuration in NIS elements the first dichroic mirror was set to B520/80 to allow light transmission, the fourth channel was set up for reflectance using the 488 nm laser, and all channel light paths were set to through. CTO was excited using the 561 nm laser and the 405 nm laser was used for DAPI imaging. Where present, lysosomal stain was excited using a 561 nm laser and cytoplasm stain (CTRD) replaced CTO, and was excited using the 640 nm laser. Grid squares were visualized and located using a 10X Plan apo 0.45 NA objective. Grid squares for imaging were picked based on certain criteria including central location within the grid and sparse cell density. Z-stacks from the coverslip to the top of the cell at a step size of 200 nm were acquired using a 60X apo 1.4 NA or a 100X apo 1.49 NA objective. Entire grid squares were imaged using large image capture (0.6mm squared) and stitching or single cells, picked based upon distinctive features and shapes for identification in subsequent imaging modalities, were imaged.

Following, or prior to, RCM imaging cells mounted in PBS or Vectashield were imaged with reflectance Structured Illumination Microscopy (SIM) (N-SIM, Nikon Corp., Japan) with an EM-CCD camera iXon3 DU-897E (Andor Technology Ltd.). To facilitate R-SIM a half mirror was placed in the light path by utilizing a filter cube that contains a half-mirror in place of the dichroic. The 488 nm laser was used to illuminate the sample using 2D-SIM imaging. CTO was excited using a 561 nm laser. Where present lysosomal stain was excited using a 561 nm laser and cytoplasm stain (CTRD) replaced CTO, and was excited using the 640 nm laser. First, the grid square was located on a 10X Plan apo

0.45 NA objective and the area of interest centered The objective was switched to the 100X apo 1.49 NA and images were acquired either as entire grid squares (by use of the X-Y multipoint acquisition) or single cells were picked based on confocal location using the previously acquired images. Due to the high magnification and small field of view, acquisition of 0.5 mm2 in 15 focal planes using the N-SIM leads to acquisition, reconstruction and stitching times totaling over 24 hours; the final reconstruction provides a large amount of high resolution data, but also regions of blank reconstructed space where no cells are localized. Acquiring Z-stacks (200 nm Z-step) of individual cells provides a time efficient data acquisition, allowing reconstruction parameters to be tailored on a per cell basis, improving the finally reconstructed images. Z-stacks of the cells were therefore acquired to facilitate alignment with the correct plane in other modalities (RCM and TEM) with a step of 200 nm. Images were reconstructed using NIS elements SIM reconstruction software.

Acquiring RCM data first minimizes photobleaching effects in the fluorescence channels that can occur during SIM acquisitions. Glass bottom Petri dishes with an etched alphanumeric grid pattern allow successful cell relocation across modalities. A region of interest can be located using a low magnification objective lens (10X), followed by a high magnification acquisition of the specific region (RCM: 100X/100X. SIM: 100X). Z-stack acquisitions provide 3D information from RCM and R-SIM; however, the optical thickness of sections obtained will differ between modalities. The theoretical optical thickness in RCM is 480 nm, whereas for SIM it is 685 nm. However, while RCM utilizes pinhole optics to exclude out of focus light from optical sections, SIM suffers from out of plane haze due to the wide-field illumination path employed. Acquiring Z-stacks (200 nm Z-step) of individual cells provides a time efficient data acquisition, allowing reconstruction parameters to be tailored on a per cell basis, improving the finally reconstructed images.

B.1.4.1 TEM Processing

Following light microscopy, cells were washed with 0.1 M PB buffer before a second fixation with 2.5% Gluteraldehyde / 2% para-formaldehyde (EMS, Hatfield, Pennsylvania) in 0.1 M Cacodylate Buffer (CB) (1h overnight) then washed with 3 x 0.1 M CB buffer. Cells were then stained with 2% osmium tetroxide (OsO4) (EMS, Hatfield, Pennsylvania) (1 hour) followed with 3 x dH2O washes. Cells were then fixed with uranyl acetate (1 hour) followed by washing with 3 x dH2O. Cells were then dehydrated with a series of ethanol washes x 2 (50%, 60%, 70%, 80%, 90% and 100%) before infiltration with 50:50 absolute alcohol:EmBed 812 (1 hour). EmBed 812 was made up as per the standard protocol for hard resin (EMS, Hatfield, Pennsylvania). Two subsequent infiltrations were performed (45 min) with EmBed 812 alone, before inverting and mounting on resin-filled embedding BEEM capsules (EMS, Hatfield, Pennsylvania) with care taken to remove all bubbles from within the capsule. Samples were then baked overnight at 60C in an oven (Thelco Laboratory Apparatus by Precision Scientific Co., India). Coverslips were separated from BEEM capsules by plunging into liquid nitrogen, and samples were then allowed to re-equilibrate with room temperature. The area of interest (0.5 mm2) was visualized, and trimmed and isolated with a sharp single edge razor blade (EMS, Hatfield, Pennsylvania) under a light microscope (Leica Ultra-cut UCT, Leica Microsystems Inc., IL, USA). Following trimming, 70 nm or 150 nm serial sections were cut using a Diatome diamond knife (EMS, Hatfield, Pennsylvania). Sections were then collected onto 200 mesh copper (Cu) grids or slotted grids (EMS, Hatfield, Pennsylvania) that had been pre-treated with alcohol. Samples were then stored for staining. Grids containing sections were stained by inverting on top of small blobs of 2% uranyl acetate (10 minutes) (EMS, Hatfield, Pennsylvania) inside petri dishes; grids were then washed with dH2O and air dried before repeating this step with Reynolds lead citrate (CaCO3 crystals used to remove air from within the chamber). Following this, grids were washed with dH2O and left to dry before TEM imaging.

B.2 Supplementary results

B.2.1 Chapter 3

Table 1. Compilation of the size distribution parameters obtained by different measurement methods.

Method	Quantity	Size					Reference
		$\overline{d}_{1,V}$ (nm)	$\frac{\Delta d_1}{\overline{d}_{1,V}}$ (nm)	$\overline{d}_{2,V}$ (nm)	$\frac{\Delta d_2}{\overline{d}_{2,V}}$ (nm)	$\overline{d}_{3,V}$ (nm)	
TEM	d	5					[7]
TEM	d	4.7(3)	0.30(3)				this study
PCS	d_h					60	[7]
PCS	d_h					61	[9]
PCS+A4F	d_h			30		62	[10]
SAXS+A4F	d_s	10	0.24	20	0.16		[10]
MRX	d_C					53(3)	this study
MRX	d_C					54(2)	[7]
M(H)	d_m	4.9(1)	0.53(1)	23.2(3)	0.21(1)		this study
MRX	d_m			16(2)	0.28(2)		this study

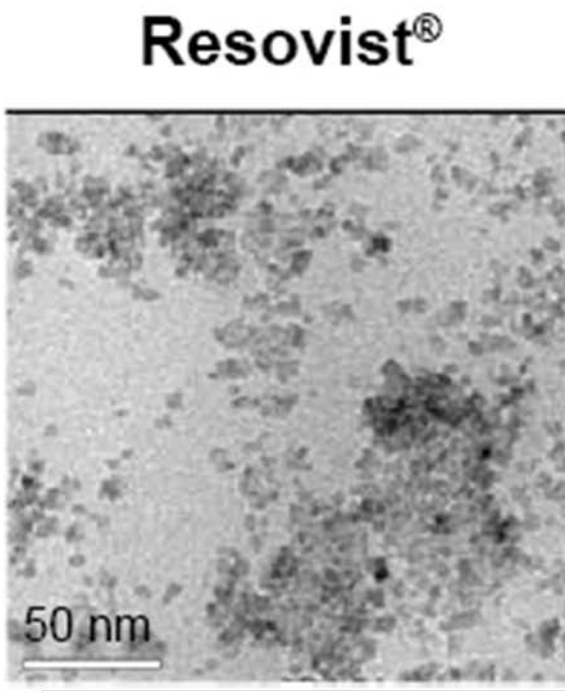

Figure B.1: Size and imaging data for resovist / ferucarbotran Size and imaging data for resovist / ferucarbotran from Buzug *et al* and De Schellenberger *et al*. Buzug *et al*provide their own measurements of the TEM core along with other measurements taken from the given references in this article relating to the properties (size) of resovist as analysed by PCS and TEM. These parameters match those determine in Chapter 3. De Schellenberger *et al* sow TEM imaging of resovist which resemble the TEM taken within Chapter 3 of Sienna$^+$.

MW (KDA)	SCM + NP	C.SCM (alone not isolated)	C.SCM+NP	Treated from cells
10.8		Spleen trypsin inhibitor I		
11.2		Apolipoprotein A2		
11.9				CXC motif chemokine 6
15.2	Hemoglobin subunit alpha	Hemoglobin subunit alpha		
16.2			Cystatin-S	
17.6	Interleukin-2			
19.9			beta-lactoglobulin	beta-lactoglobulin
19.9	beta-lactoglobulin		beta-lactoglobulin	
20.2				coatomer subunit zeta
21.4	kappa casein		kappa casein	kappa casein
21.4			Alipoprotein D	
23.2			alpha-1 acid glycoprotein	
24.4	Trypsin		Trypsin	Trypsin
24.5	Alpha S1 casein		Alpha S1 casein	Alpha S1 casein
24.6			GTPase IMAP family member	GTPase IMAP family member
25.1	Beta Casein		Beta Casein	Beta Casein
25.5			matrix protein	
26	Alpha S2 ceasin		Alpha S2 ceasin	Alpha S2 ceasin
28.3	collectic 11			
36			Alipoprotein E	
37.1	Phosphoribosylformylglycinamidine cyclo-ligase			
38.2			3-isopropylmalate dehydrogenase	
38.4	Alpha 2HS Glycoprotein	Alpha-2-HS-glycoprotein	Alpha 2HS Glycoprotein	Alpha 2HS Glycoprotein
38.6			Annexin A2	
39.2		NADH-ubiquinone oxidoreductase		
41.41	F-box only protein			
41.6	Protein NDRG1			
41.7	Actin		Actin	Actin
42.1			succinyl coa ligase	
42.6	Feutin-B	Feutin-B		
44.9	5-azacitidine-induced protein 2			
45.3	plasma serine protease inhibitor		plasma serine protease inhibitor	
46.1	Alpha-1 antiproteinase		Alpha-1 antiproteinase	
46.2			pigment epithelial derived factor	
46.8			eukaryotic initiation factor 4a	
48				Transcription factor AP-2-alpha
50.1			elongation factor 1	elongation factor 1
51.1			Clusterin	

Table B.2: Full list of identified protein corona constituents of SPION solutions incubated with SCM, C.SCM, and following cell treatment This table shows the first part of the table presenting each of the identified proteins within the corona of NPs following treatment, corona isolation, PAGE separation, and LC MS/MS analysis.

51.7	Factor XIIa inhibitor		Factor XIIa inhibitor	
52.2	HemoPexin			
52.3	antithrombin-III			
53.3			Fibrinogen	
53.5	Alpha -1B-glycoprotein			
53.7			lipopolysacharride binding protein	
53.7				Vimentin
54.7	Alpha-2-antiplasmin			
56.3	Phosphatidylinositol-glycan biosynthesis class W protein			
56.9			trna-guanine methyl transferase	
57.6	non structural protein 1			
59.6				Amine oxidase
67.1	coagulation factor XII			
68.5			alpha feto-protein	
68.7			kininogen-2	
68.8	C4b-binding protein alpha chain			
69.2	Serum Albumin	Serum Albumin	Serum Albumin	Serum Albumin
70.3			heatshock 70kda protein	
70.5	Prothrombin			
70.6	VLC acyl-CoA dehydrogenase			
76.6	complement C1s subcomponent			
77.7	Serotransferrin	Serotransferrin	Serotransferrin	
78.1	lactotransferrin		lactotransferrin	lactotransferrin
78.4				lutropin-choriogonadotropic hormone receptor
80.7	Gelsolin		Gelsolin	
80.7	Neurolysin			
81			phosphatidylinositol	
81.8			haemoglobin subunit beta	
81.8			junction plakoglobin	
85.3	Complement factor b			
93	Complement component C7			
101.4			inter-alpha trypsin inhbitor heavy chain H1	
101.8			Complement C4	
129.5			thrombospondin-1	
140.3			Complement factor H	
146.5			synaptojanin-1	
167.5			alpha 2 macroglobule	
248.8			coagulation factor 5	
272	Fibronectin		Fibronectin	
327	tRNA nuclease CdiA			
16.8 - 18.8	Lyzozyme C		Lyzozyme C	Lyzozyme C
59-63	Keratin (I and II)		Keratin (I and II)	Keratin (I and II)

Table B.3: Full list of identified protein corona constituents of SPION solutions incubated with SCM, C.SCM, and following cell treatment cont. This table shows the second part of the table presenting each of the identified proteins within the corona of NPs following treatment, corona isolation, PAGE separation, and LC MS/MS analysis.

B.2.2 Chapter 4

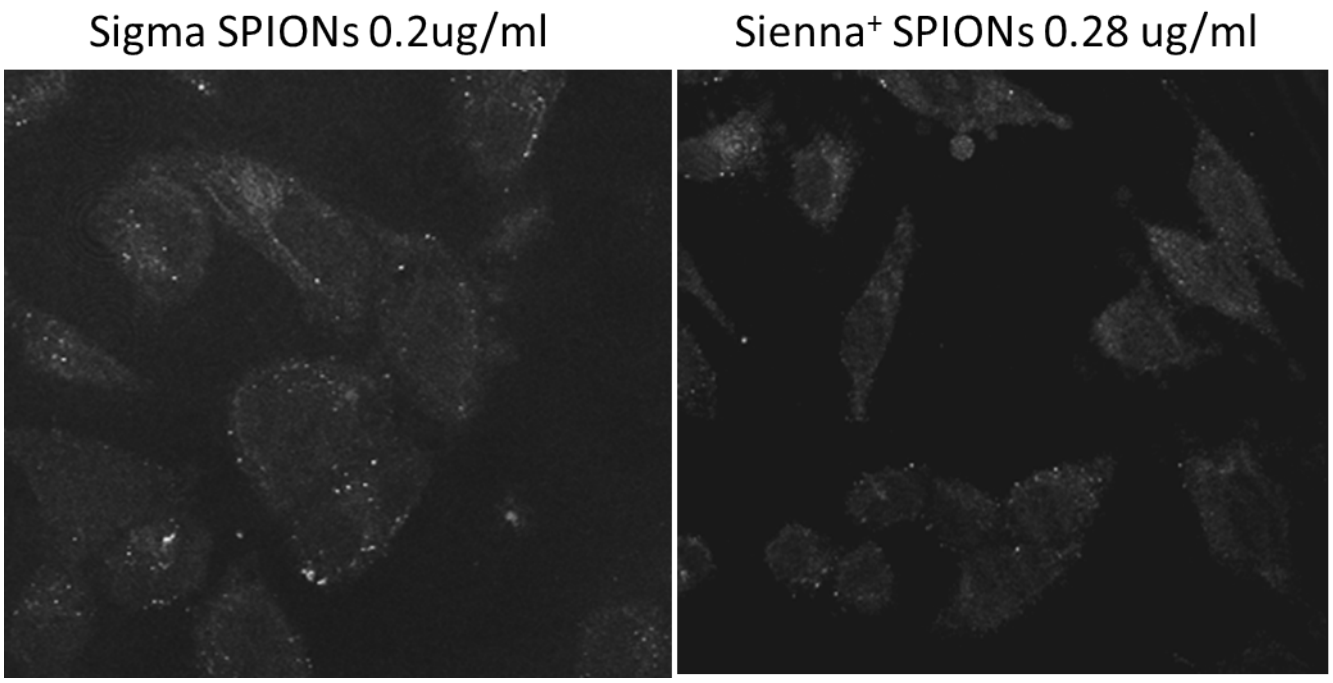

Figure B.2: Reflectance confocal images of Sigma SPIONs and Sienna+ SPIONs. Sienna+ SPIONs do not generate as much reflectance signal as SPIONs with a larger, more spherical core.

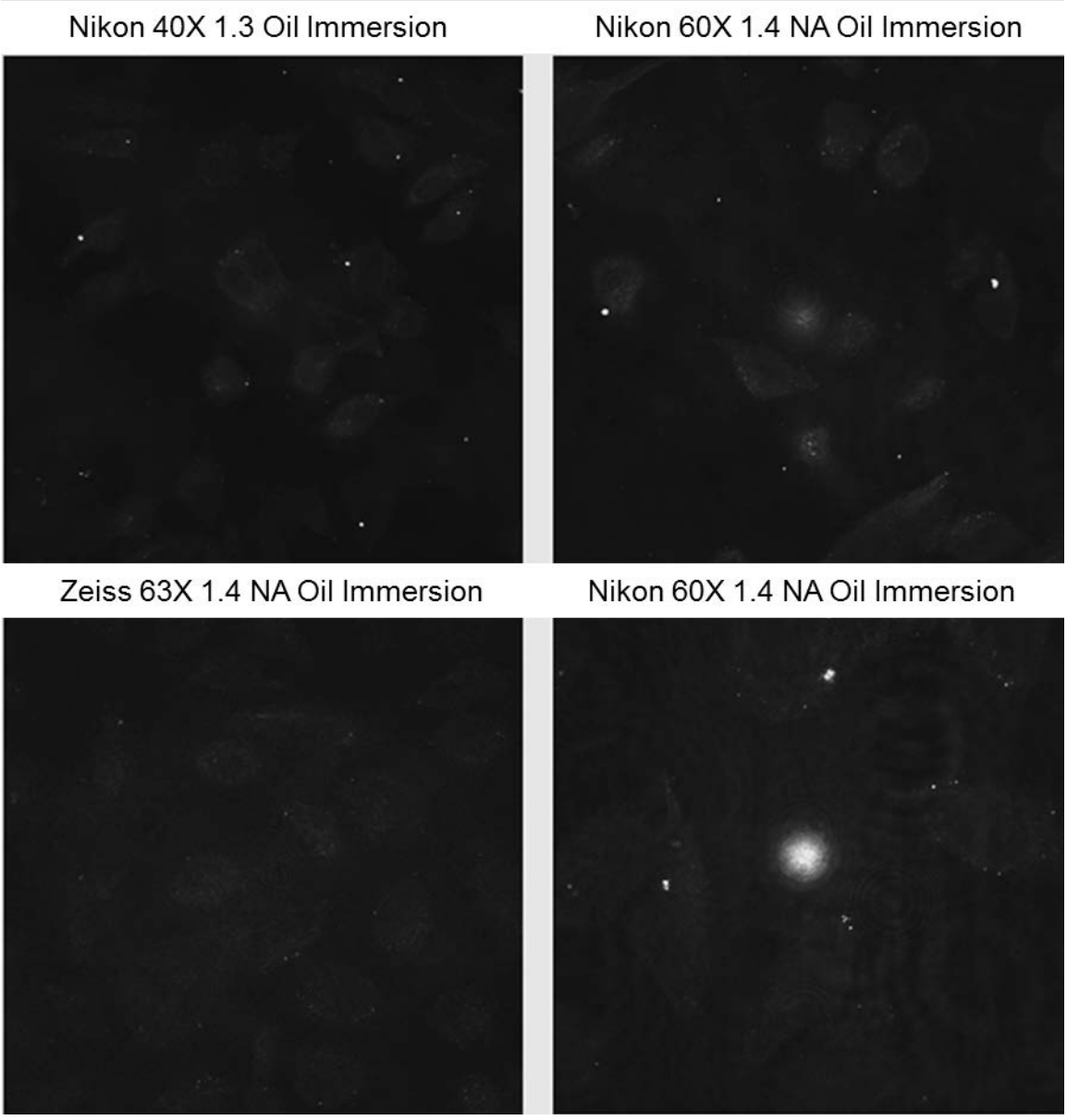

Figure B.3: Comparison of reflectance images obtained using different objectives on the Nikon A1R and the Zeiss LSM710. Different microscopes and microscope objectives give rise to different levels of contrast in reflectance mode, this figure shows differences between them and indicated the higher contrast on the Nikon A1R.

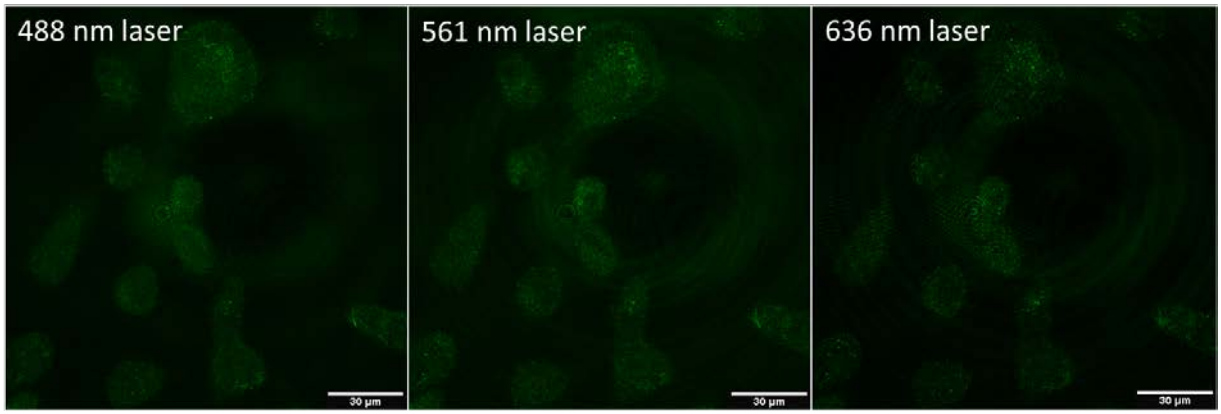

Figure B.4: Example reflectance images acquired of NP inside cells when different lasers were tested. Increasing wavelength of laser line used to acquire reflectance images leads to increases in background reflectance and an apparent decrease in SNR.

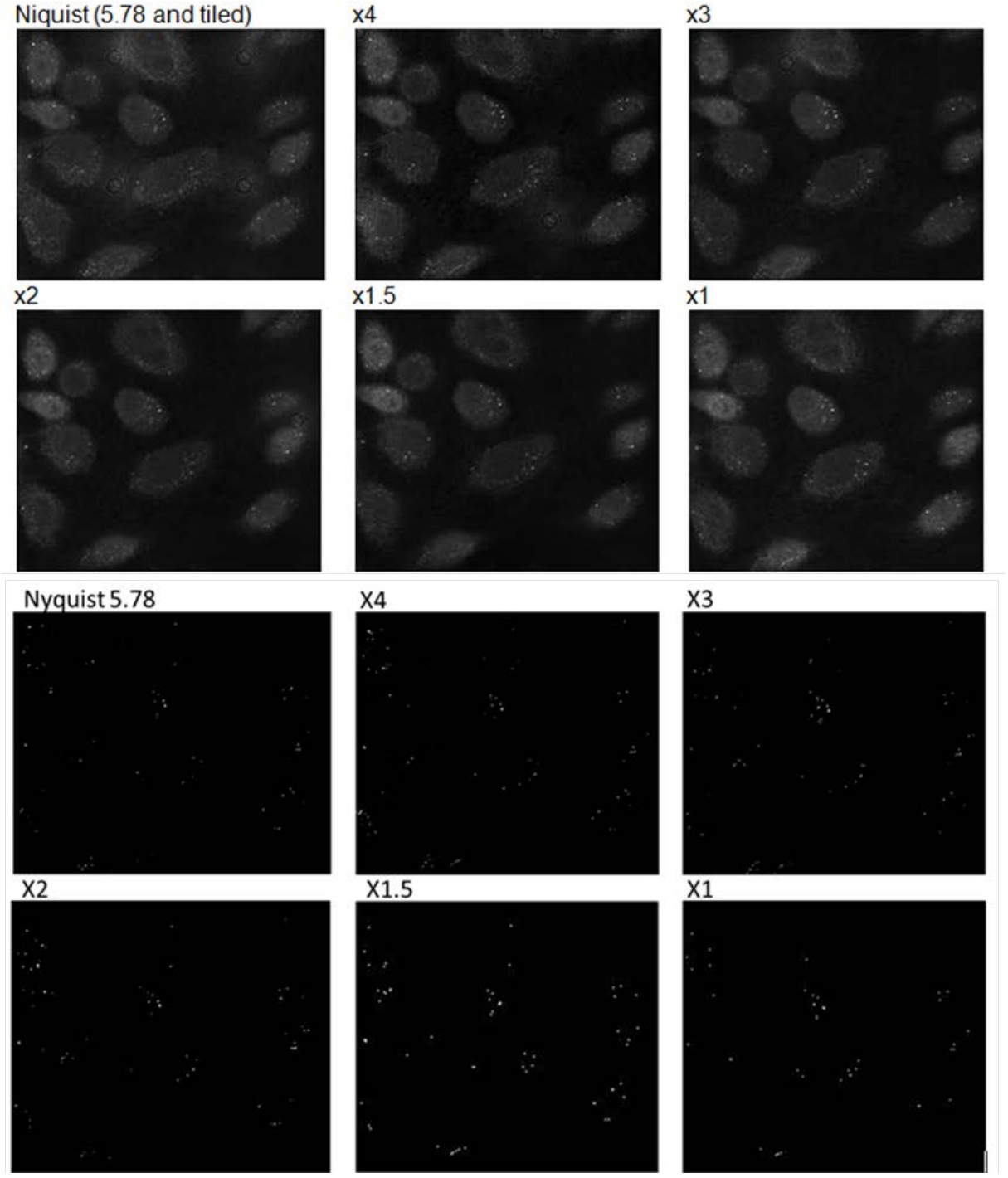

Figure B.5: The effect of optically decreased FOV on the 40X objective on the Nikon A1R for the detection of NP. Qualitatively image contrast and resolution increase with decreasing field of view towards the Nyquist criteria. However artifact increases, therefore a trade-off is observed. When manually counted there appears to be 63 regions of signal determined from the Nyquist image. This indicates the artifact might effect the detection of NP at very small FOV.

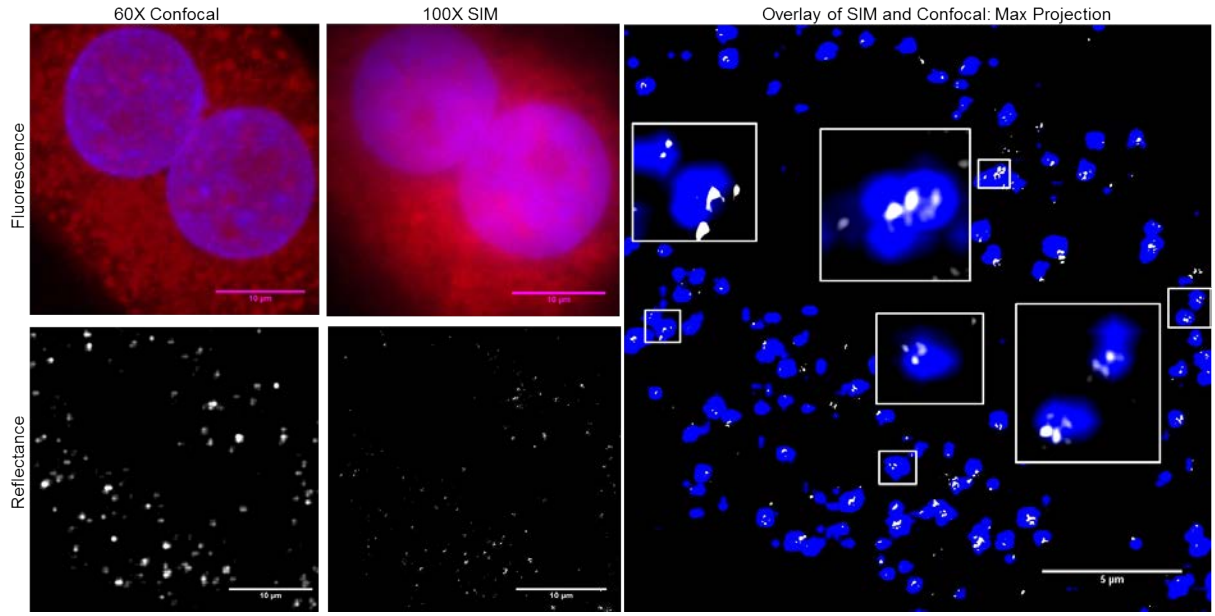

Figure B.6: Comparison of RCM (60X 1.4 NA) and R-SIM (100X 1.49 NA) .Maximum intensity Z-projection images of a HeLa cell treated with cerium dioxide NPs, acquired with RCM (60X 1.40 NA) and SIM reflectance (100X 1.49 NA). RCM imaging volume is 8.4 m and SIM 6.8 m. Images show CTO (red) cytoplasmic stain, DAPI (blue) nuclear stain and NP signal (grey). Overlay of the cerium dioxide NP regions shows particles detected on RCM (blue) and SIM (grey). White boxes display a sample of regions where RCM detects one spot and SIM detects multiple spots, illustrating the enhanced resolution of SIM.

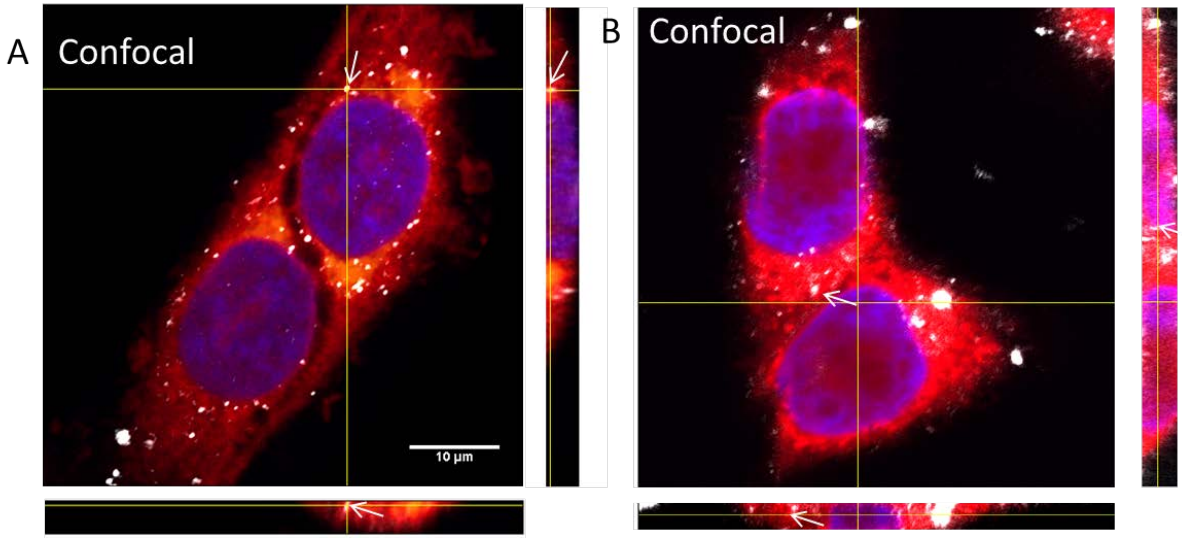

Figure B.7: Figure showing slices through Z, Y and Z to indicate the internalized particles within cells using confocal. This figure shows an example cell indicating that particles are internalized and not present at the cell surface (A). The corresponding single section and Z views of a cell shown in Figure 4.9 (B) indicating that no particles are present in the nucleus and particles are present inside cells

.

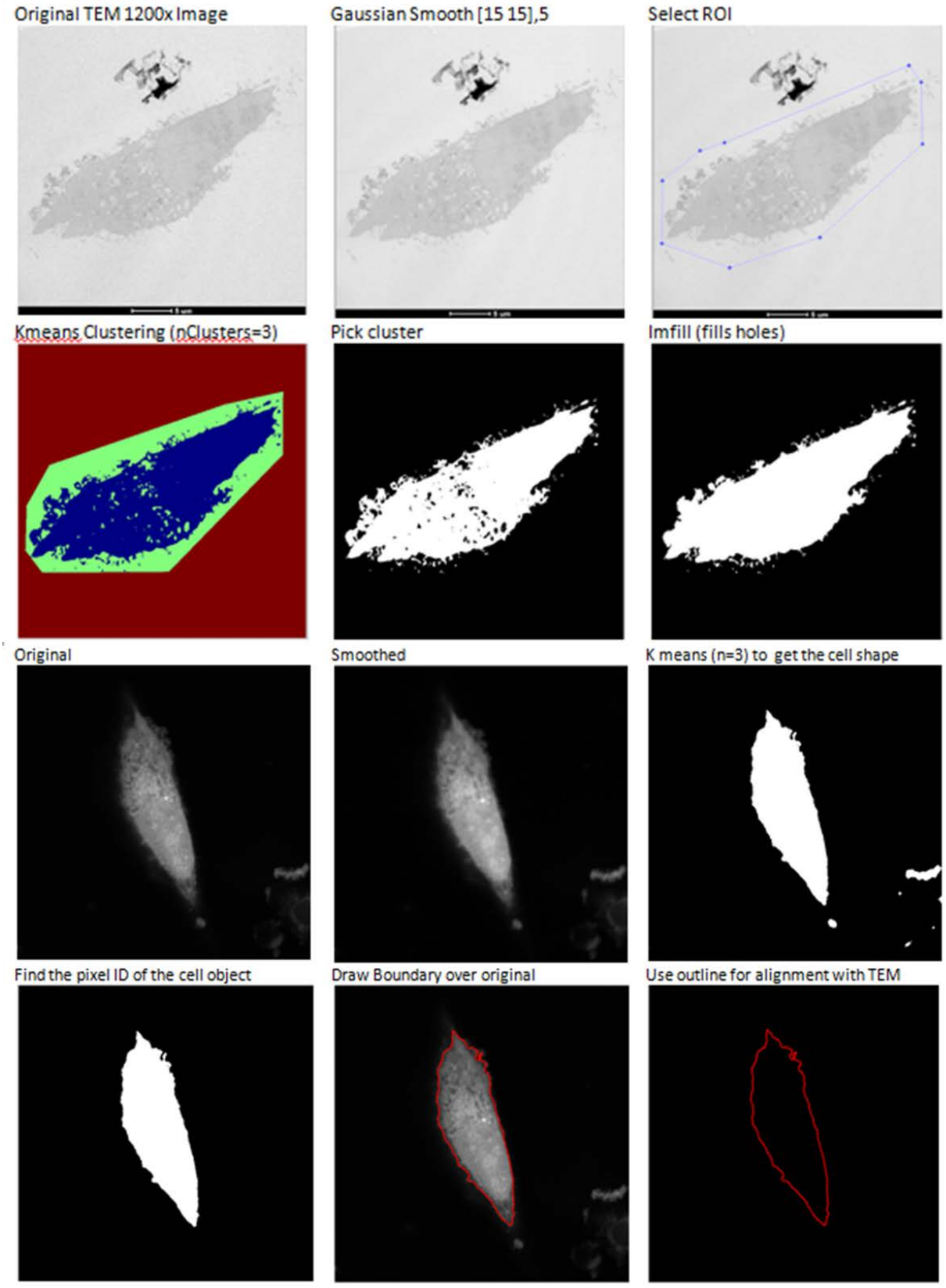

Figure B.8: Examples of the automated segmentation of TEM images for use with realignment methods. Similar processing methods can be applied to those used for RCM including smoothing, background subtraction and then K-means clustering

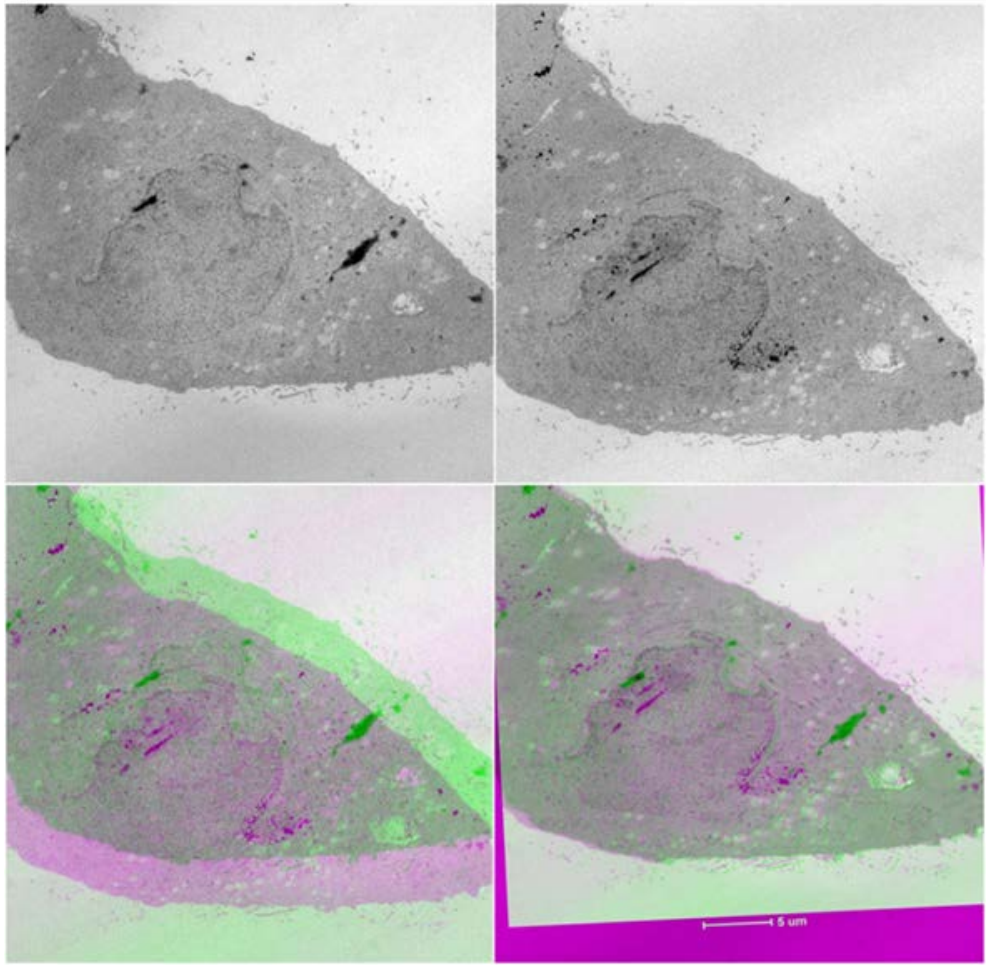

Figure B.9: Example realignment of TEM sections using automated MATLAB processing. TEM sections were automatically realigned using built in imregister function. The top images show the slices pre-realignment separately, and the bottom left image shows the initial overlay of the two slices. Following imregister realignment, the two slices overlay very well, as seen in the bottom right figure.

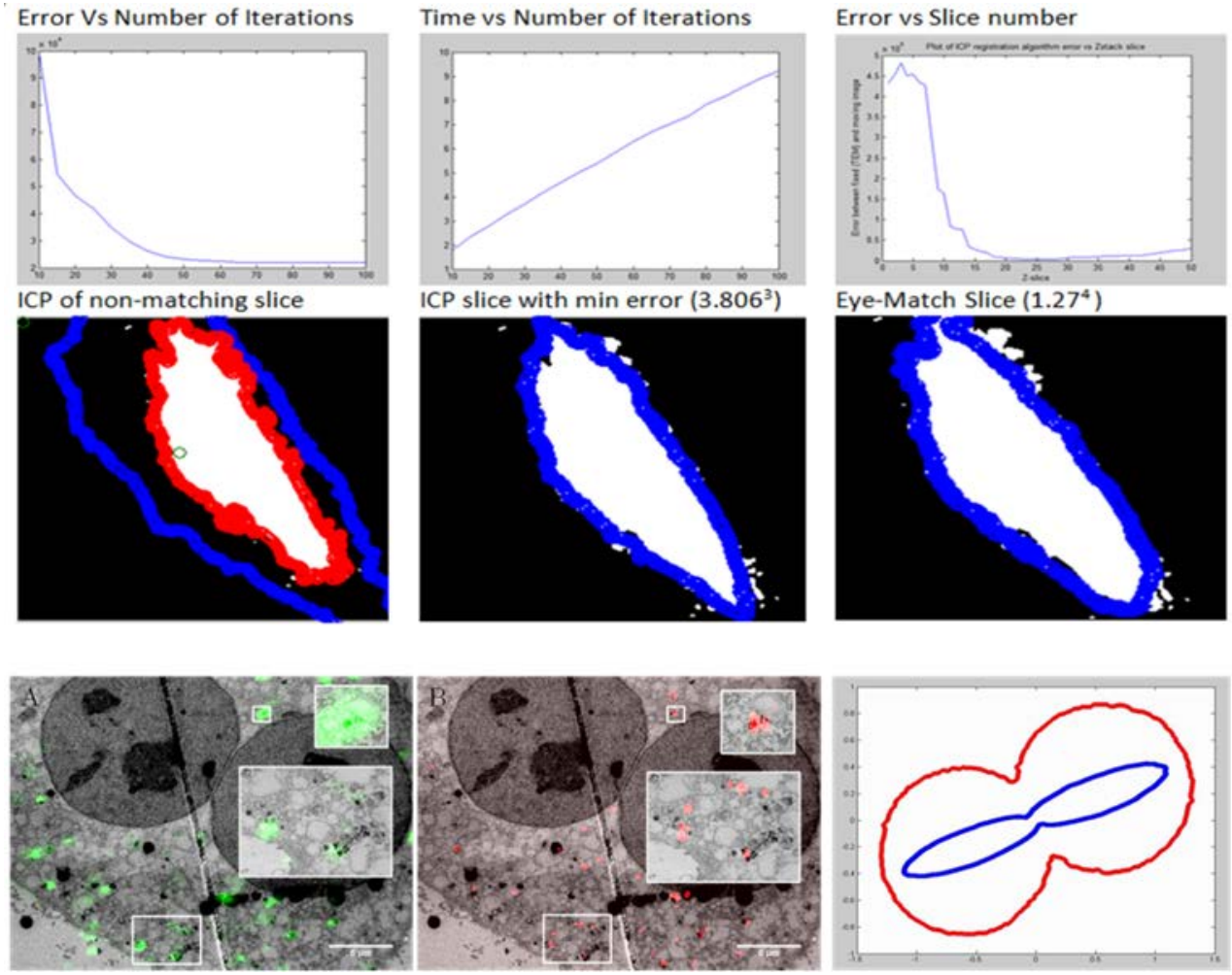

Figure B.10: Example of the automated ICP algorithm and CPD algorithm to determine co-aligning planes. The top images show the parameters of ICP algorithm, the error of fit decreases with the number of ICP iterations, the time also increases with iteration number as would be expected. The error of the fit (confocal to TEM) is also shown on the top right, indicating a clear maxima where the ICP converges to the correct TEM matching slice of the Z-stack. The CPD algorithm (bottom row) realigns segmented nuclei from TEM and confocal images, without user input. The method of registration is shown as a snapshot at the bottom right, and the result of realignment on both SIM and confocal images is shown (bottom middle and left respectively)

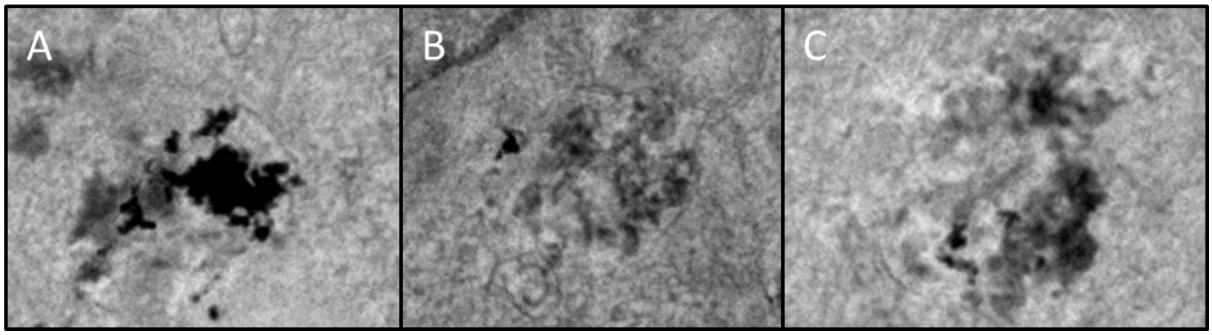

Figure B.11: TEM images showing regions of electrodensity in HeLa cell treated with cerium dioxide NPs. Images showing NPs within HeLa cells (A) and regions where no NPs are detected but electron density appears to be observed at low magnification (B and C).

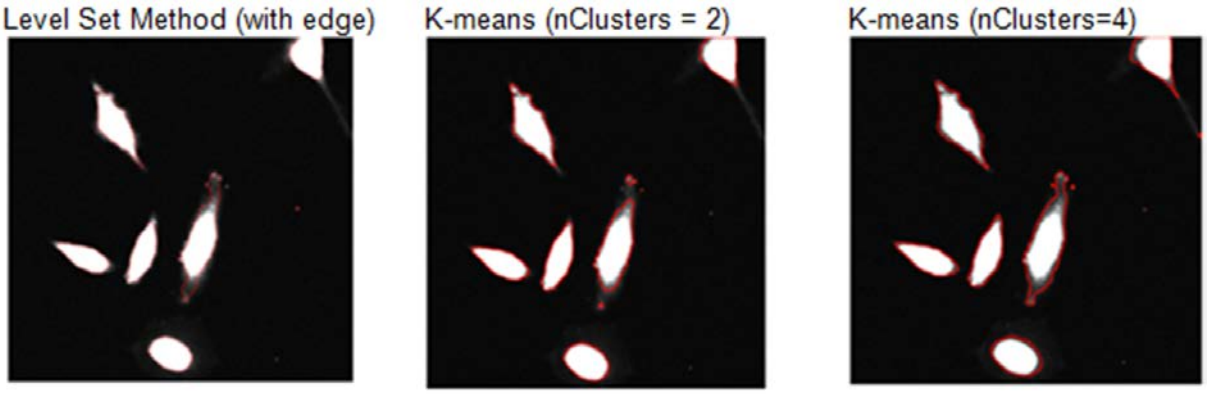

Figure B.12: Example of different methods for cell segmentation. Different methods lead to different levels of segmentation with different associated advantages and disadvantages, including accuracy of segmentation, and computational expense.

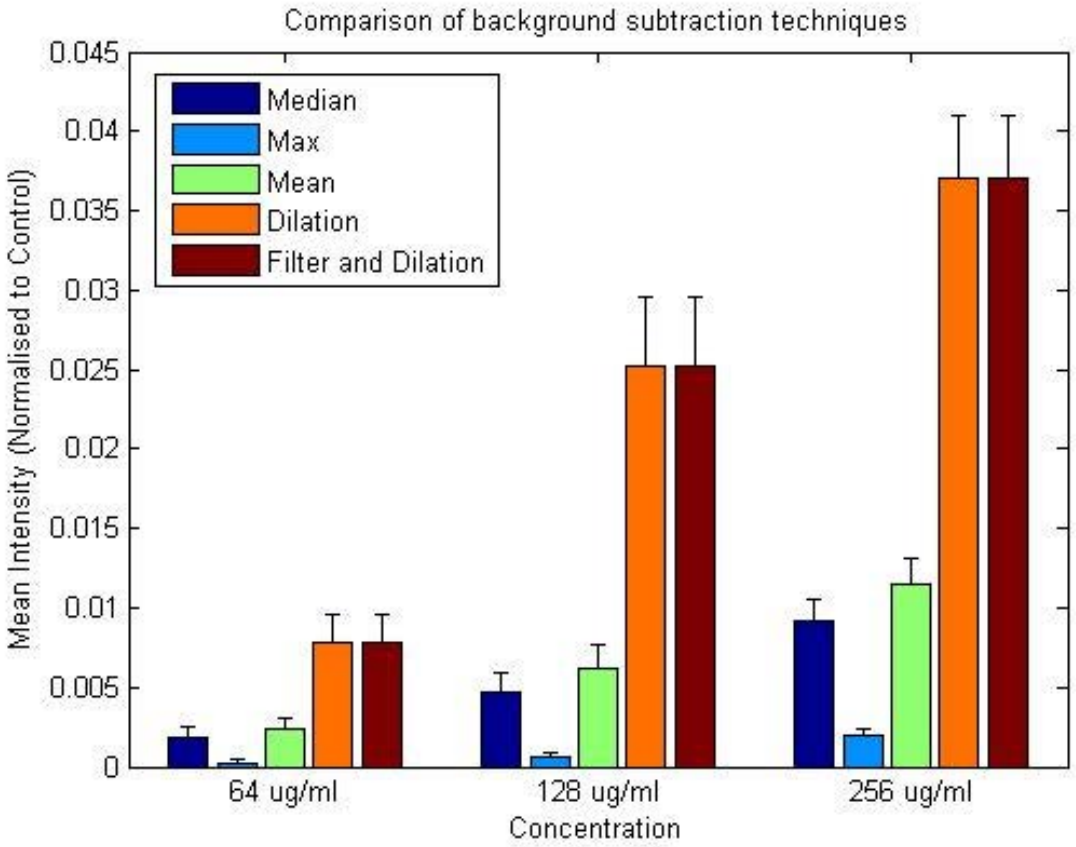

Figure B.13: Example of different background subtraction methods for signal preservation. Different background subtraction methods lead to different levels of signal loss and preservation. The least signal is lost using background subtraction of the image itself followed by k-means clustering

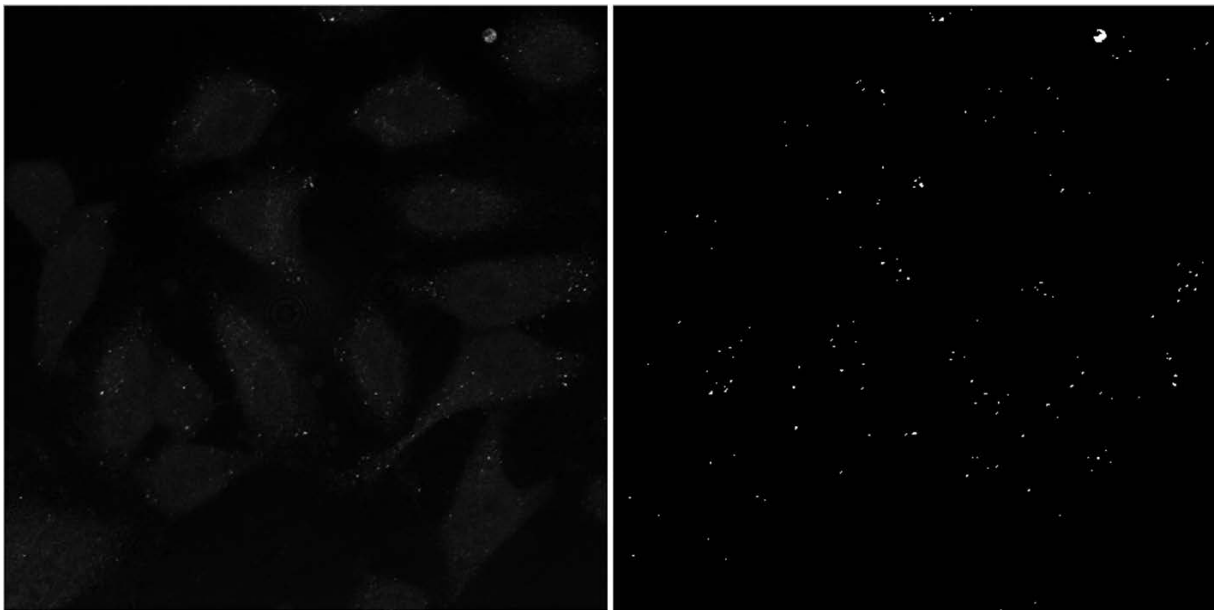

Figure B.14: Example of the success of the K-means segmentation on an example RCM image. Example of the success of the K-means clustering algorithm with a cluster number of 3 for segmenting high intensity nanoparticle signal from low intensity background reflectance.

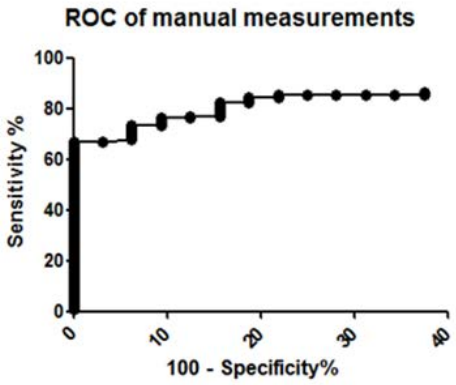

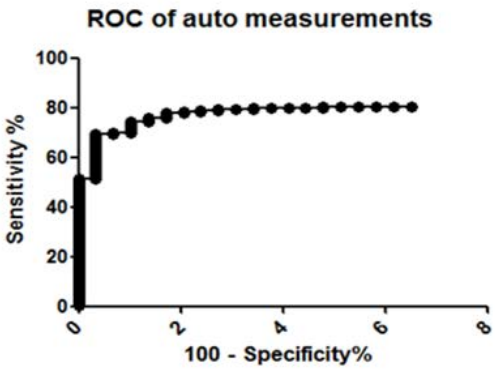

	Area	SD	
Manual	0.8803	0.02789	
Automatic	0.8928	0.01318	
Z=	-0.06168		
Z=	0.06168		
p value=	0.95082		

Figure B.15: ROC curves for manual and automatic analysis methods. ROC curves show similar sensitivity and specificity for both manual and automatic methods, and no statistically significant difference is observed.

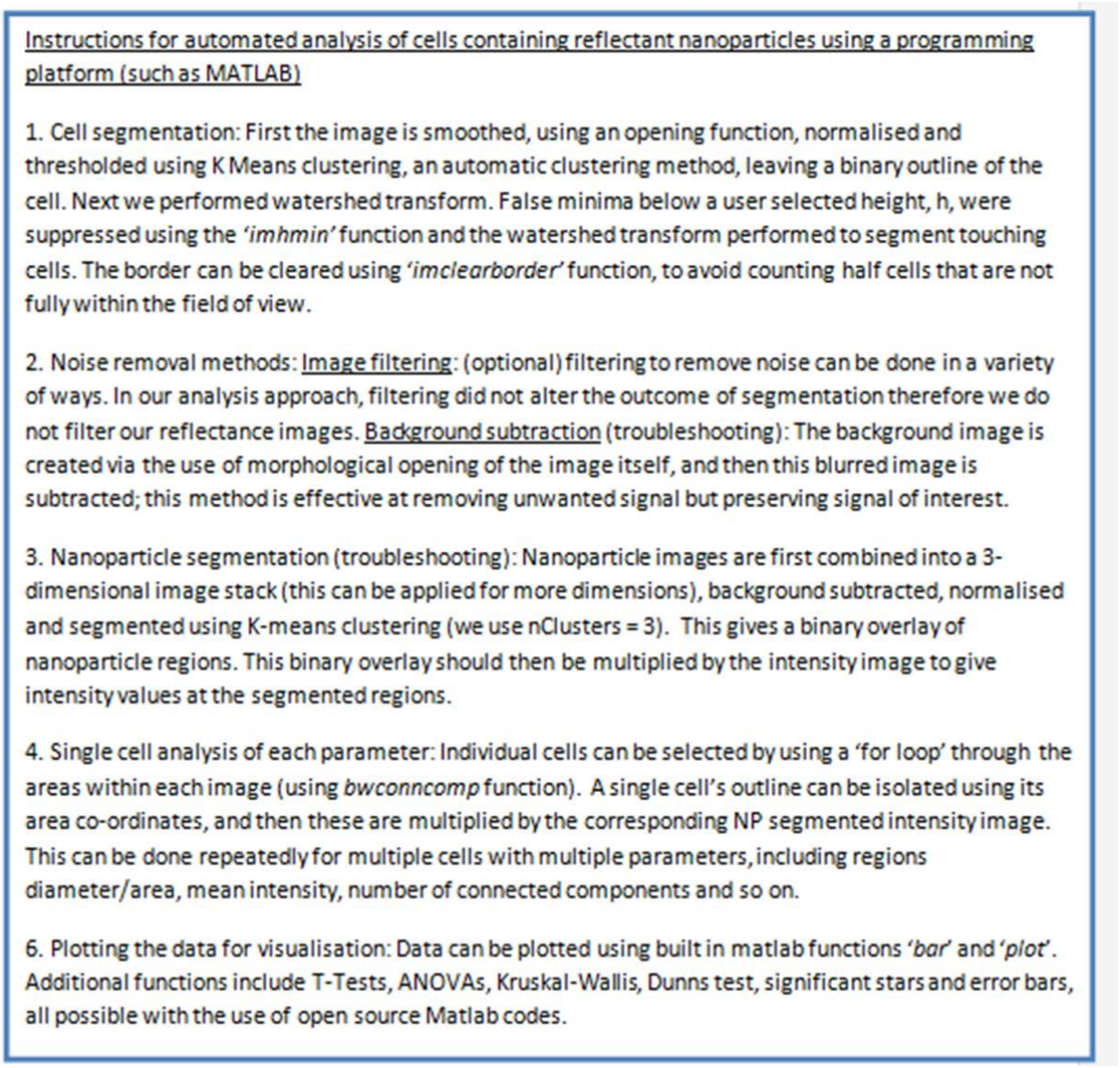

Figure B.16: Instructions for the automated analysis in stages.

Setting up the analysis routine

Install bioformats (Loci tools) into a folder that is in your file path in matlab. Load image data set with bfopen function. Bfopen is part of Loci tools and works for any image file format. Critical Step: Channel order needs to remain the same across all images. The channels will be located in the MetaData in the same order they were saved, so if a channel was acquired first, it will be channel 1. Additionally, consistent labelling to allow sorting of data for visualisation of groups graphically is helpful (i.e. 280 ug mL 60 mins

001; 280 ug ml 60 mins 002; 280 ug ml 15 mins 001).

Create for loops for the following steps, to loop through all of the images in your dataset, so that analysis can be performed on all images one after the other, to save repetitive analysis steps that increase computational time (see example MATLAB code). *Critical step: All channels must be linked together by the index i. Large numbers of images will be processed and they must all correspond to the same i to ensure correct images are recombined in later stages and to get meaningful results.*

1. CTO channel processing: Apply a smoothing filter to the image (we suggest Gaussian [3 3], 05) to remove the effects of noise.

2. Normalize the image, then perform K-means clustering on the filtered image, this gives N number of clusters (user selected N). The last or second to last cluster will give the best binary outline for the cells dependent upon CTO stain intensity.

3. Post segmentation steps may be required, such as filling in black holes within the segmented cell, using the imfill built in function, in addition to the removal of small objects that are not cells, using the bwareaopen built in function. *Critical Step: it is important to check in the first few stages that the segmentations are providing accurate results. This can be done by doing overlays of the segmented image outline onto the original image.* 4. Locate the nanoparticle image from the MetaData.

5. We suggest subtracting the background at this stage, prior to segmentation. Morphological dilation (using a disk with structuring element size 3) creates an estimate of the local background, and then this background can be subtracted from the original image. The result is the background subtracted image.

6. Segment the nanoparticles. We input the processed images into a 3D stack of all the

images from our dataset. Load each 512 by 512 image into a different channel of the stack (for e.g. 3Dstack(:,:,i)=NPImage). The stack should then be normalized as a whole and the K-means clustering algorithm performed. The number of clusters generally refers to the number of expected groups of pixels (for e.g. we except 1) nanoparticle signal, 2) cell background signal and 3) noise/background that is not cell or nanoparticle, therefore we adopt an nClusters=3.

7. The segmentation result is a binary image of areas that correspond to high intensity regions (nanoparticles). This can be combined (multiplied) with the original (background subtracted) NP image to give pixel intensity values to the image, leaving a segmented image with no background effects.
Critical step: Controls must be included; this segments nanoparticles using controls as a comparison, and also gives an indication of the success (i.e. nanoparticle spots should not be detected in the controls.

8. Use the function *bwconncomp* to find the object details in the Cell outlines mask (created in 22). CC=Bwconncomp gives the number of objects (CC.NumObjects) and the pixel co-ordinates of these objects (CC.PixelIdxList). Use these co-ordinates to create a new image of the same size with only one object (i.e. one cell). Another for loop can be used here to loop through all the objects (using k=1:size(CC.NumObjects).

9. Create a new image using the co-ordinates of one of the objects in the cell. The function NewImage=FALSE(M,N) creates an MxN matrix of zeroes (e.g. FALSE(size(CellTrackerImage)). This image is currently blank, add the co-ordinates of the kth object (e.g. NewImage(CC.PixelIdxListk)=true;). The NewImage now contains only one object.

10. Multiple this single cell image with the segmented nanoparticle image, to get a single cell with segmented nanoparticle regions. This image still has pixel values out-

side of the cell (despite them being 0, this will skew results). Using the NewImage, all pixels that are NOT part of this object can be disregarded from this Image: (NewNPImage(NewImage==0)=[];).

11. We now have single cell pixel values, with pixel values inside the cell only, and containing segmented nanoparticle regions. Multiple parameters can be assessed at this stage. These include: Cell area, Mean intensity, Number of connected components, Connected component area, Connected component diameter. Caution: Increased parameters increase computational time.

12. This is repeated for every cell, in every image, in every group of data. This can be as fully automated as required (by the use of multiple for loops within for loops: see example code).

13. Cell data can then be grouped based on sample. We use a naming system that is also linked with i to sort the data into groups.

14. Data can be visualized graphically using the built in bar function. Other open source visualized plot tools exist to allow error bars and significant stars.

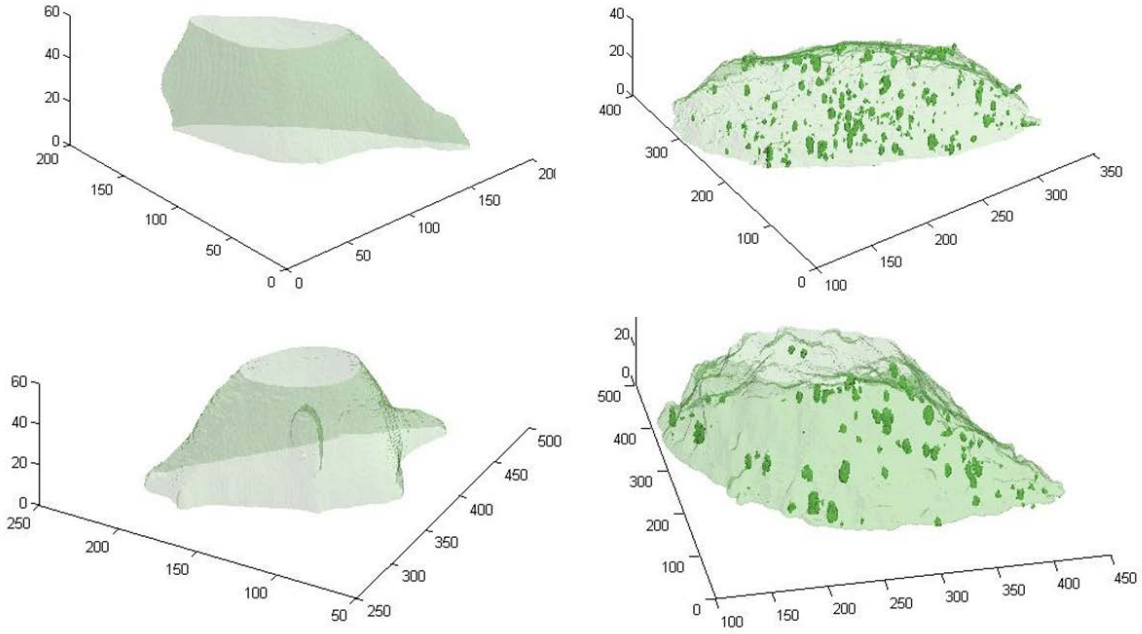

Figure B.17: Example of the use of the analysis method extended to 3D images.. Segmentation of both cell and NPs use exactly the same method, and overlays can be visualized using MATLAB. The left hand image shows control HeLa cells and the right hand shows cerium dioxide treated HeLa cells. Following this similar connected components and mean intensity analysis can be applied to the data.

B.2.3 Chapter 5

A titration was done at different concentrations of Wav2 siRNA. This titration indicated that in wave2 siRNA treated cells the expression of Wav2, compared to Tub, increased (Figure B.18). This increase in wave2 expression was also observed with the treatment of cells with NSC siRNA (Figure B.18). This may reflect a cellular stress response to the wave2 siRNA treatment, but more studies would be necessary to validate this conclusion. For these reasons the use of wave2 in these experiments was ceased.

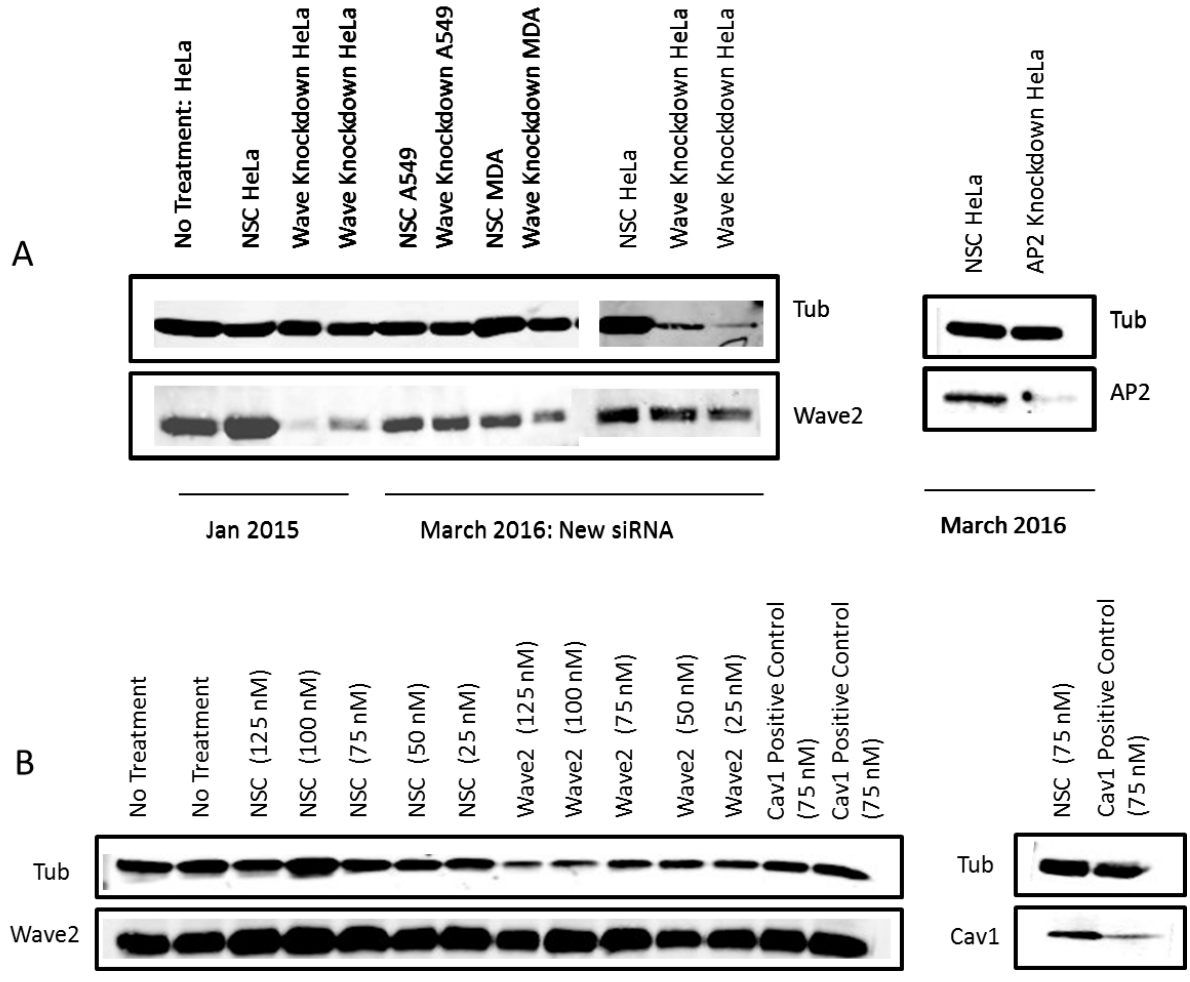

Figure B.18: Wave2 siRNA appears to lead to unpredictable expression levels of wave2 protein. A) initially wave2 expression appeared to decrease upon treatment with wave2 siRNA. However subsequent studies were unable to reproduce this knockdown (B) At every concentration tested within the manufacturers identified range. Positive knockdowns done alongside indicated the success of AP2 and cav-1 siRNA, validating the experimental procedure itself.

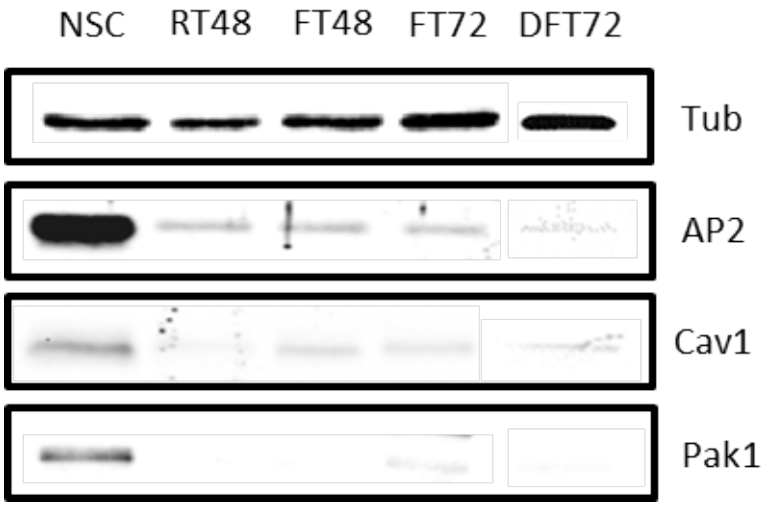

Figure B.19: Protocol to achieve highest transfection efficiency. Double knockdown with 72 hours led to an increased transfection efficiency in HeLa cells when compared to 72 hours single transfection, and reverse and forward transfection for 48 hours.

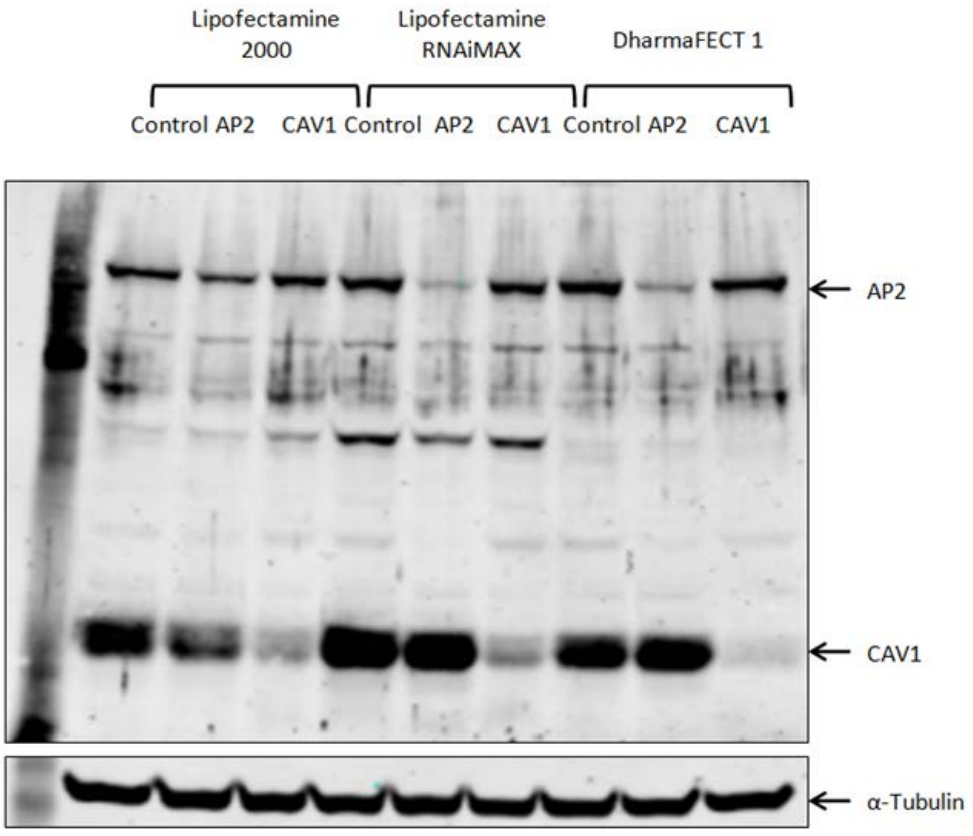

Transfection Reagent	AP2 (% knockdown)	CAV1 (% knockdown)
Lipofectamine 2000	40.45	68.00
Lipofectamine RNAiMax	79.91	83.69
Dharmafect	73.17	91.51

Figure B.20: RNAi max gives superior transfection efficiency in HeLa cells.

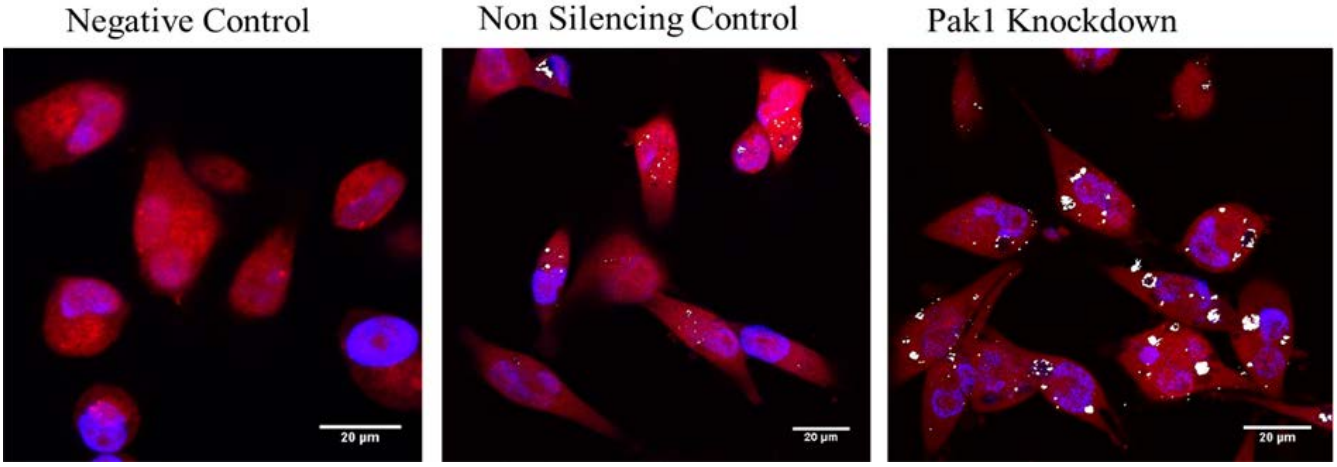

Figure B.21: Vacuoles appear to form in MDA cells treated with Pak-1 siRNA. Vacuole formation appears to be induced following the siRNA inhibition of Pak1 in MDA cells. This is an effect not observed when MDA cells were treated with AP2 or Cav1 siRNA, thus invalidating conclusions from this condition. NSC and Pak1 images show NP treated cells, the negative control is untreated.

B.2.4 Chapter 6

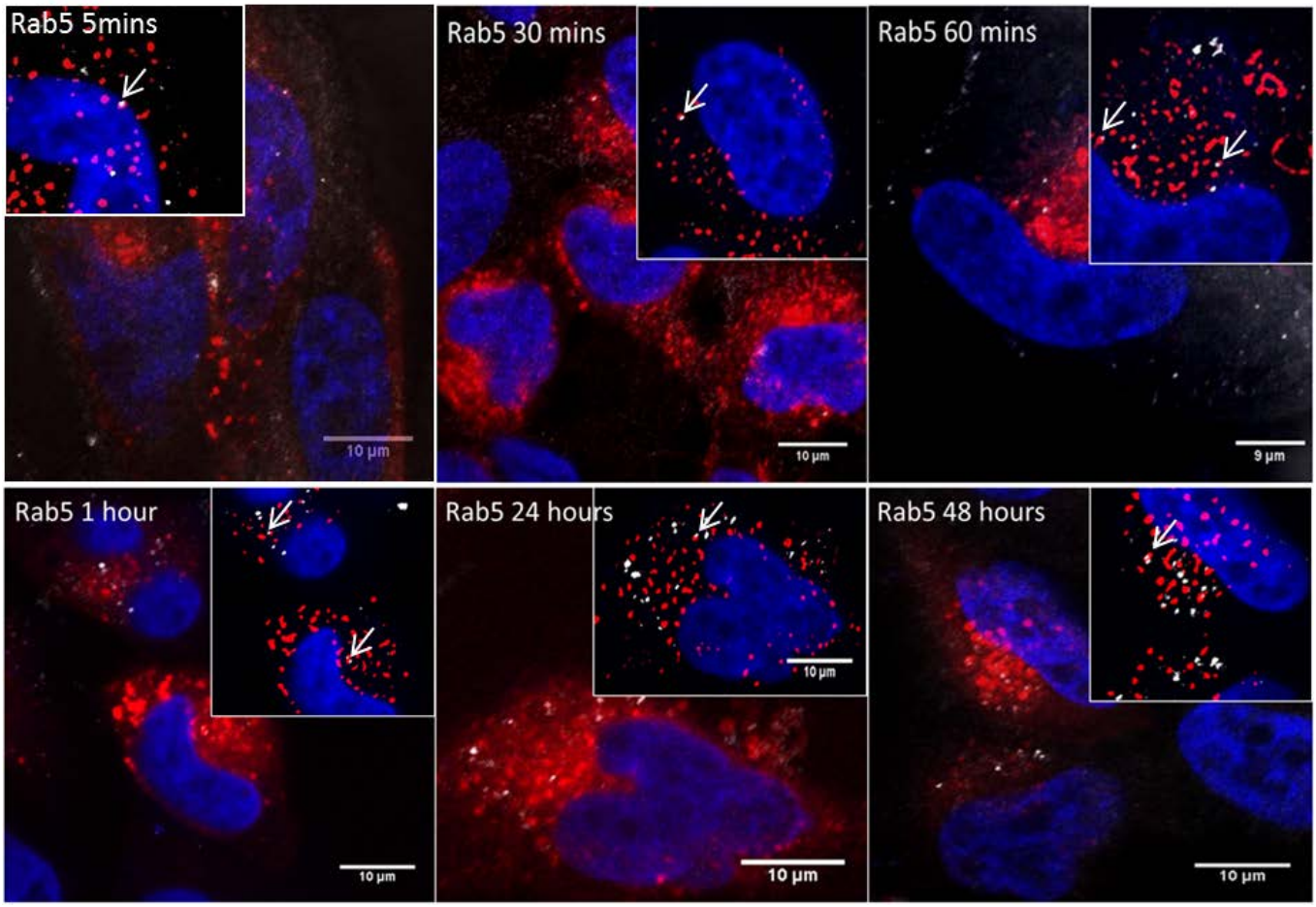

Figure B.22: Example images of intracellular SPIONs and Rab5-mRFP stain showing colocalization at different time points SPIONs appear to colocalize with Rab positive structures at earlier time points, and less so at later time points.

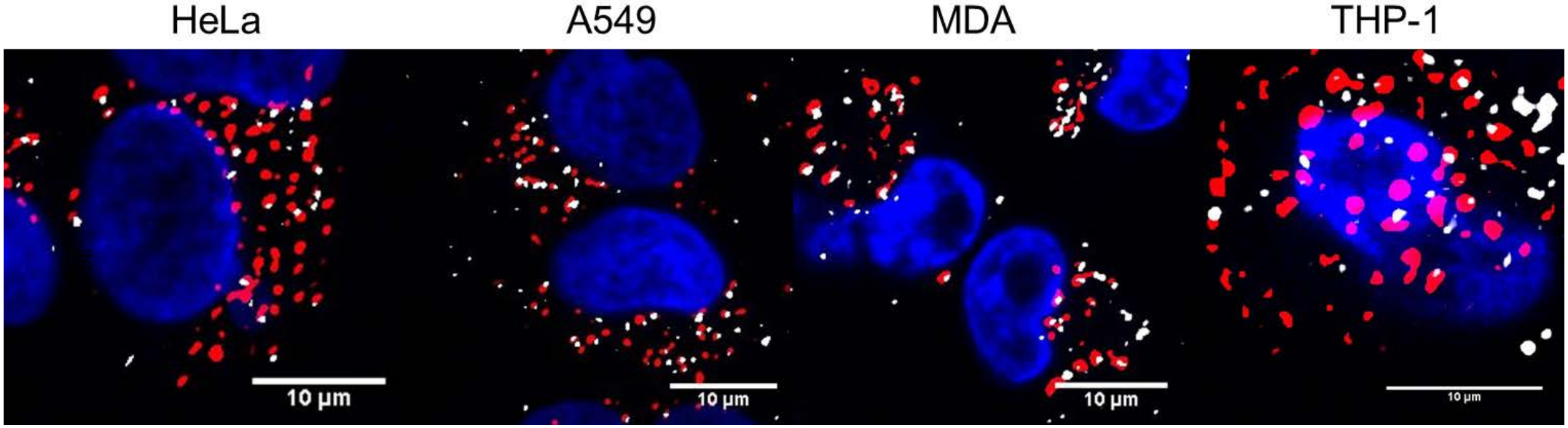

Figure B.23: Example images of intracellular SPIONs 24 hours post treatment and the lysosome in HeLa, A549, MDA and THP-1 cells. At 24 hours post incubation with SPIONs, all cell lines show a high degree of colocalization between SPIONs and lysosomal regions.